Technical Report

TR-10-50

Radionuclide transport report for the safety assessment SR-Site

Svensk Kärnbränslehantering AB

December 2010

Svensk Kärnbränslehantering AB
Swedish Nuclear Fuel
and Waste Management Co

Box 250, SE-101 24 Stockholm
Phone +46 8 459 84 00

ISSN 1404-0344
SKB TR-10-50

Radionuclide transport report for the safety assessment SR-Site

Svensk Kärnbränslehantering AB

December 2010

Keywords: SKBdoc 1266928, Advection, Colloid, COMP23, Corrosion, Deterministic calculation, Far field, FARF31, Isostatic load, MARFA, Near field, Pinhole, Probabilistic calculation, Radionuclide release, Radionuclide transport, Shear load.

Preface

This document compiles radionuclide transport calculations of a KBS-3 repository for the safety assessment SR-Site. The SR-Site assessment supports the licence application for a final repository at Forsmark, Sweden.

The following persons have had the main responsibilities for specific subject areas: James Crawford, Kemakta Konsult AB, Sweden (geosphere processes and site characteristics), Christina Greis, SKB and Maria Lindgren, Kemakta Konsult AB, Sweden (near- and far-field calculations with COMP23 and FARF31), Scott Painter, Los Alamos National Lab, US (far-field calculations with MARFA) and the undersigned (methodology, sensitivity analyses and analytical calculations).

The report has been reviewed by Jordi Bruno, Amphos, Spain; Alan Hooper, Alan Hooper Consulting Limited, UK; Ivars Neretnieks, Royal Institute of Technology, Sweden; and Mike Thorne, Mike Thorne and Associates Ltd, UK.

Stockholm, December 2010

Allan Hedin
Project leader SR-Site

Summary

The safety assessment SR-Site is undertaken to assess the safety of a geologic repository at the Forsmark site. The assessment supports SKB's licence application for a final repository for spent nuclear fuel at Forsmark. The results of the assessment are documented in the SR-Site Main report and supporting documents. This report describes calculations of radionuclide release and transport for the proposed repository at Forsmark and compares the resulting radiological doses to applicable regulatory limits. Release and transport in several additional scenarios that help illustrate barrier function are also described. Site characteristics and processes affecting release and transport are also described.

The dominant processes responsible for geosphere radionuclide transport include advection through networks of fractures, diffusion in intact host rock adjacent to fractures, ion exchange and surface complexation reactions on mineral surfaces within the host rock, radionuclide decay and in-growth of daughter radionuclides, and radionuclide sorption onto clay colloids that may be generated in the buffer material under some conditions. The SR-Site project has developed a comprehensive strategy for representing flow in fractures and engineered features of the repository (described elsewhere). The outputs of that flow modelling activity, which represent inputs to the transport modelling described here, are advective travel times and flow-related transport resistance parameters for individual transport pathways and flow rates at individual deposition holes. Model uncertainties related to the representation of flow are addressed by considering multiple conceptual models of the discrete fracture network based on different degrees of correlation between fracture transmissivity and length. Multiple realisations of the discrete fracture network are included to address uncertainties associated with the stochastic generation of fracture networks. Steady flow and chemical conditions for the present day are used in the transport calculations for SR-Site; variant simulations and screening analyses allowing transient flow and chemical conditions demonstrate that the steady approximation is an adequate representation. Sorption processes are represented by equilibrium sorption partitioning coefficients with appropriately defined probability distributions instead of detailed modelling of ion-exchange and surface-complexation reactions.

Two scenarios for which canister failures and subsequent radionuclide release cannot be ruled out are identified in SR-Site. The two scenarios are failure of the copper canister by corrosion and by earthquake-induced shear movements in fractures intersecting the canister positions. Two additional hypothetical scenarios (a growing pinhole failure and failure due to isostatic load) are also analysed to illustrate barrier functions although the analyses discussed in the SR-Site main report led to the conclusion that the canister failure modes associated with these scenarios can be ruled out. Important near-field processes are dependent on the release scenario, but generally include dissolution of the fuel matrix and corrosion of structural parts of the fuel assemblies and control rods, precipitation/dissolution of secondary radionuclide-bearing minerals, and sorption onto clay buffer and backfill material. Diffusion in the buffer material is the primary transport mechanism if the buffer material remains in place; otherwise, advection is the primary transport mechanism in the near field.

Probabilistic calculations of radionuclide release and transport demonstrate that the mean releases from the engineered barrier system give rise to doses below the dose corresponding to the regulatory risk limit. The dose-equivalent releases are also significantly below estimates of dose corresponding to background concentrations of uranium and radium. The releases are small because the geosphere and engineered barrier system protect the canisters by providing favourable hydrological and geochemical environments, thus resulting in small probability of failure for a few canisters and negligible probability of failure for the vast majority of canisters. In the shear-failure scenario, sorption on buffer material also attenuates radionuclide release.

Radionuclide release from the engineered barrier system is further attenuated by the geosphere. The geosphere attenuation is approximately a factor of 3 for the corrosion scenario (central case conditions). The attenuation is relatively modest in the central corrosion case because the canisters that are most likely to fail are associated with flow paths with modest retention. Geosphere attenuation is stronger for variant modelling cases that result in larger releases from the engineered barrier system. Thus, in addition to protecting the canisters and limiting releases, the geosphere also reduces

uncertainty in the estimated doses by attenuating the dose for variant cases that have larger release from the engineered barrier system. For all probabilistic cases considered, the mean annual effective dose is at least an order of magnitude smaller than the dose corresponding to the risk limit. For the central corrosion case, the peak of the mean annual effective dose is estimated to be 0.18 μSv/year. For comparison, the dose corresponding to the risk limit is approximately 14 μSv/year and the dose corresponding to typical background radiation is approximately 1,000 μSv/year.

Sorption to mobile clay colloids is an uncertain process that is handled pessimistically in SR-Site by neglecting a range of potential mitigating processes. When this process is included, the geosphere is not a significant barrier to radionuclide transport for the brief periods in which high colloid concentrations are possible. However, these periods are brief and the small near-field release rates are sufficient to keep dose-equivalent releases below the dose corresponding to the risk limit.

Results of simplified analytical models are in good agreement with results obtained with the numerical models. The agreement enhances confidence in the dose equivalent release calculations presented here for two reasons. First, the comparison provides an important quality assurance check on the numerical modelling of dose equivalent releases. Second, it demonstrates that potential doses are controlled by relatively simple processes that are straightforward to understand and model.

Sammanfattning

Säkerhetsanalysen SR-Site görs för att analysera säkerheten för ett geologiskt förvar i Forsmark. Analysen ligger till grund för SKB:s ansökan om att uppföra ett slutförvar för använt kärnbränsle i Forsmark. Resultatet av säkerhetsanalysen dokumenteras i SR-Sites huvudrapport och huvudreferenser samt i stödjande rapporter. Den här rapporten utgör en av huvudreferenserna och beskriver beräkningar av frigörelse och transport av radionuklider för det föreslagna förvaret i Forsmark och jämför beräknad radiologisk dos med den dos som motsvarar myndigheternas riskkriterium. Frigörelse och transport beskrivs också för flera så kallade restscenarier som hjälp för att illustrera betydelsen av enskilda barriärer och barriärfunktioner. Dessutom beskrivs platskaraktäristik och processer som påverkar frigörelse och transport.

De viktigaste processerna som påverkar radionuklidtransporten i geosfären är advektion genom nätverk av sprickor, diffusion i intakt bergmatris intill sprickor, jonbytes- och ytkomplexeringsreaktioner på mineralytor i bergmatrisen, radioaktivt sönderfall och inväxt av dotternuklider. SR-Site projektet har utvecklat en omfattande strategi för att modellera vattenflöde i sprickor och tekniska barriärer. Utdata från vattenflödesmodelleringen i form av advektiv gångtid och flödesrelaterade tranportmotståndsparametrar för individuella transportvägar och flödeshastigheter i individuella deponeringshål används som indata till transportmodelleringen. Modellosäkerheter relaterade till beräkningen av vattenflödet omhändertas genom att beakta flera konceptuella modeller av det diskreta spricknätverket baserat på olika grad av korrelation mellan spricktransmissivitet och sprickstorlek. Flera realiseringar av det diskreta spricknätverket har använts för att beakta osäkerheten till följd av den stokastiska genereringen av spricknätverken. Konstant flöde och konstanta kemiska förhållanden motsvarande dagens situation används huvudsakligen i transportberäkningarna i SR-Site. Variationsfall samt beräkningar med varierande flöde och kemiska förhållanden visar att approximationen med konstanta förhållanden är adekvat. Sorptionsprocesser representeras med jämviktssorptionskoefficienter med lämpligt definierade sannolikhetsfördelningar i stället för detaljerad modellering av jonbytes- och ytkomplexeringsreaktioner.

I SR-Site identifieras två scenarier för vilka det inte kan uteslutas att kapselns isolering går förlorad och att radionuklider frigörs. De två scenarierna är korrosion av kopparkapseln och kapselskador till följd av jordskalvsinducerade skjuvrörelser i sprickor som korsar kapselpositionen. Två hypotetiska restscenarier (växande initialt pinnhål och skada på grund av isostatisk last) analyseras också för att belysa barriärernas funktion, även om analysen som beskrivs i SR-Sites huvudrapport leder till slutsatsen att dessa båda kapselskador kan uteslutas. Viktiga närzonsprocesser är scenarioberoende, men generellt omfattar de upplösning av bränslematrisen och korrosion av metall i bränsleboxarna och i styrstavar, utfällning/upplösning av sekundära mineraler som innehåller radionuklider samt sorption på bentoniten i buffert och tunnelåterfyllning. Diffusion i buffertmaterialet är den primära transportmekanismen, om buffertmaterialet är kvar, annars är advektion den primära transportmekanismen i närzonen.

Probabilistiska beräkningar av frigörelse och transport av radionuklider visar att medelutsläppet från de tekniska barriärerna är lägre än den dos som motsvarar myndigheternas riskkriterium. Utsläppet är också betydligt lägre än dosen från bakgrundskoncentrationer av uran och radium. De låga utsläppen beror på att geosfären och de tekniska barriärerna skyddar kapslarna genom att tillhandahålla en gynnsam hydrologisk och geokemisk miljö, som resulterar i en låg sannolikhet för skador på ett fåtal kapslar och försumbar sannolikhet för skador på en majoritet av kapslarna. I skjuvscenariot bidrar också sorption på buffertmaterial till en dämpning av radionuklidutsläppet.

Radionuklidfrigörelsen från de tekniska barriärerna dämpas ytterligare av geosfären, vilket medför en minskning med ungefär en faktor tre för korrosionsscenariot (centralfallet). Dämpningen är relativt begränsad i det centrala korrosionsfallet på grund av att de kapslar som har högst sannolikhet att skadas är sammankopplade med flödesvägar med ringa retention. Geosfärens dämpning är större för beräkningsfall som resulterar i högre utsläpp från de tekniska barriärerna. Förutom att skydda kapslarna och begränsa utsläppen, reducerar geosfären alltså också osäkerheter i de uppskattade doserna genom att dämpa dosen mer för de fall som har högre utsläpp från de tekniska barriärerna. För alla probabilistiska fall som beaktats är den effektiva årliga medeldosen åtminstone en storleksordning

lägre än dosen som motsvarar SSM:s riskkriterium. För det centrala korrosionsfallet är den högsta årliga effektiva dosen beräknad till 0,18 µSv/år. Som jämförelse är dosen som motsvarar riskkriteriet ungefär 14 µSv/år och dosen som motsvarar typisk bakgrundsstrålning omkring 1 000 µSv/år.

Sorption på mobila lerkolloider är en process av osäker omfattning som hanteras pessimistiskt i SR-Site genom att försumma ett antal för säkerheten gynnsamma delprocesser. Då denna process inkluderas, är geosfären inte en signifikant barriär mot radionuklidtransport under de kortvariga perioder då höga kolloidkoncentrationer är möjliga. Dessa perioder är dock kortvariga och utsläppstakten från närzonen är tillräckligt låg för att hålla dosekvivalenta utsläpp under dosen som motsvarar myndigheternas riskkriterium.

Resultat av beräkningar med förenklade analytiska modeller stämmer väl överens med resultat från de numeriska modellerna. Överrensstämmelsen stärker tilltron till de dosekvivalenta utsläppsberäkningarna av två anledningar. Dels ger jämförelsen en viktig kvalitetskontroll av den numeriska modelleringen av dosekvivalenta utsläpp och dels visar den att potentiella doser kontrolleras av relativt enkla processer som är okomplicerade att förstå och modellera.

Contents

1 Introduction

The safety assessment project SR-Site is undertaken by SKB to assess the safety, as defined in applicable Swedish regulations, of a potential geologic repository for spent nuclear fuel. The results of that assessment are documented in the SR-Site **Main report**[1] and supporting documents. The **Main report** forms part of SKB's license application to construct and operate a repository at Forsmark based on the KBS-3V concept.

Calculations of radionuclide release, transport and dose consequences for different scenarios and cases are important components of the safety assessment SR-Site. This report quantitatively describes such calculations for all scenarios contributing to the calculated risk for the proposed Forsmark repository and compares the resulting radiological annual doses to applicable regulatory limits. The report also summarises transport assessments for residual scenarios that were selected to illustrate performance of the repository barrier systems. As described in the Section 2.5.12 of the **Main report**, this report is one of 16 main references for the SR-Site **Main report** and is referred to as the **Radionuclide transport report**.

The SR-Site project team has developed an 11-step process for the SR-Site safety assessment (Figure 2-2 of the **Main report**). This report focuses on Step 10, Analyses of Selected Scenarios with Respect to Isolation and Retardation. In addition, transport-related aspects of Step 2a, Description of Initial Site State and Step 7, Definition and Analyses of Reference Evolution are also described.

Several scenarios that have the potential to cause radionuclide mobilisation and release from the engineered barrier system are identified in Chapter 11 of the **Main report**. The current report analyses consequences of the two scenarios identified as the most risk significant: canister failure due to corrosion and canister failure due to shear load. In the 'canister failure due to corrosion' scenario (called briefly the corrosion scenario below) canisters fail as a result of enhanced corrosion due to advective conditions in the deposition hole following the loss of buffer through erosion. In the 'canister failure due to shear load' scenario, canisters fail due to earthquake-induced secondary shear movement along fractures intersecting the canister position. Details of the two scenarios are discussed in the **Main report**. In addition, several residual scenarios that help understand geosphere barrier function are also analysed.

In addition to the analyses of selected scenarios, this report also briefly summarises site characteristics that affect radionuclide transport. Further, several radionuclide transport/retention processes that are not explicitly included in SR-Site but require further analyses are discussed.

Some aspects of radionuclide transport are discussed in the **Main report** and are not discussed here, including dose to non-human biota, risk summation, and gas-phase transport.

---

[1] To improve readability, abbreviated names in bold font are used here to refer to the SR-Site **Main report** and its main references. Full report names are provided in the reference list.

2 Processes and site characteristics affecting transport

The migration of solutes through fractured rock is dependent on a number of processes and variables. These are outlined in the **Geosphere process report** and can generally be categorised as being either geological (i.e. relating to microstructural properties of the rock), hydrogeological (i.e. relating to flow), or hydrochemical in nature (i.e. relating to groundwater chemistry). Although the migration of solutes can also be related to a broader class of reactive transport processes governing groundwater composition, in this chapter the focus is primarily on features and processes of importance for the transport of radionuclides from canister positions in the repository to the biosphere.

In this context, geological factors of importance relate primarily to the existence of a hydraulically connected fracture system traversing the repository volume as well as the flow-wetted surface and microporous structures both immediately adjacent to fracture surfaces and within the deep rock matrix. Although there is considerable overlap in the ontological description of features and processes that are considered geological and those categorised as being hydrogeological, both are important for the overall description of radionuclide transport processes. Hydrochemical features include the groundwater chemistry parameters that govern the solubilities of radionuclides and influence the chemical reactions of nuclides with geological materials lining flowpaths through the near field, far field, and biosphere. Hydrochemical features, although more precisely differentiated than geological or hydrogeological entities in this description, are still strongly dependent on the couplings between geology, flow and chemical reactions involving other non-nuclide groundwater chemical constituents. The following sections give an overview of the main features.

2.1 Flow

Groundwater flow is a primary control on radionuclide migration in the subsurface. The groundwater flow system at Forsmark has been studied extensively and is described in detail in Section 10.3.6 of the **Main report** and supporting documents. At present, flow at Forsmark is primarily vertically upward from the repository to a shallow bedrock aquifer associated with large, nearly horizontal fractures/sheet joints because of the effects of a local topography-driven flow cell, then horizontally in the shallow bedrock aquifer to discharge locations at topographic lows /Follin 2008/.

The existence of flow in fractured rock, its spatial distribution, and temporal variability are strongly governed by the geological characteristics of the site and hydraulic boundary conditions. In some situations, flow may be relatively evenly distributed throughout the available flow space, although in-situ observations suggest (e.g. /Abelin et al. 1991a, b, 1994/) that it is more likely to be channelised to varying degrees. Channelised flow can arise spontaneously on the level of regional fault structures and more local scale heterogeneous fracture networks where water flow preferentially follows the path of least resistance in connected hydraulic features. A comprehensive modelling approach is used in SR-Site to represent the effects of such channelling at Forsmark. The modelling approach uses a combination of discrete fracture network (DFN), continuous porous medium (CPM), and equivalent continuum porous medium (ECPM) models. The latter class of models represents flow in fractured rock by upscaling a DFN representation to a CPM representation. Models of flow during the temperate period use nested DFN/ECPM models with explicit CPM representation of tunnels, boreholes and near-surface soil layers. Modelling of flow during the glacial and periglacial periods has been carried out using ECPM representations without explicit representation of the repository engineered features.

Regardless of how the flow modelling is carried out, flow-related input to transport calculations is limited to three parameters: equivalent flow rate at the canister Q_{eq}, the advective travel time t_w, and the flow-related transport resistance F. Definitions for these “flow triplet” parameters may be found in /Joyce et al. 2010/.

The flow triplets vary spatially and by realisation of the stochastically generated DFN. The Q_{eq} varies by canister location, release path (see Section 3.3), and DFN realisations. The t_w and F parameters are properties of the flowpath connecting a near-field release location to a geosphere discharge location. Thus, a unique pair of t_w and F is required for each combination of DFN realisation, canister location, near-field release path, and flow path through the geosphere. Depending on the transport code being used (3.6), spatial variability of t_w and F along the flow path may also be represented (e.g. element by element in a finite element representation of the flow). Cumulative distributions of F for different realisations of the hydrological model are found in /Joyce et al. 2010/. Within each realisation, the F values associated with different deposition holes span a large range.

The flow and transport modelling approach used in SR-Site represents spatial variability and channelling phenomena down to the level of individual fractures. Channelling phenomena can occur at even smaller scales because of physical features such as enlarged fracture intersections or within-fracture variability in fracture aperture. Channelling at the sub-fracture scale is not represented in SR-Site. Technical bases for neglecting within-fracture channelling are discussed in Section 2.1.1 and Appendix A.

Future glacial cycles are expected to have significant effect on groundwater flow /**Climate report**/. For most of the transport scenarios analysed here and in the **Main report**, these effects are ignored and steady temperate-period flow and chemical conditions are assumed. Selected modelling cases presented later in this report are used to assess the impacts of climate variability and show that the temperate-period results provide a reasonable approximation to peak mean annual dose. Section 2.1.2 describes how flow evolution on a glacial cycle is represented in those selected modelling cases.

2.1.1 Spatial variability and the nature of channelised flow

On the scale of single fractures, the existence of a heterogeneous transmissivity field may result in the merging of flow lines in high velocity regions of the fractures. Owing to the limited spatial extent of these regions, this merging may decrease the flow-related transport resistance (F-factor) of certain parts of the fracture relative to the estimate representing the average flow smeared evenly over the whole fracture surface. As shown by /Cvetkovic et al. 1999/ increasing amounts of fracture-scale heterogeneity results in a broadening of the F-factor and advective travel time distribution and an increasing statistical average of these variables. Although an increasing average implies enhanced retardation, this does not apply to the fast flowpaths in the fracture, which are of most relevance for safety assessment calculations. When considering the fracture as a whole, broadening of the F-factor and advective travel time distribution implies both a greater frequency of fast flowpaths together with a greater frequency of slow flowpaths at the expense of middling flowpaths. Furthermore, this does not consider the location or extent of the solute source nor the setting in which individual fractures reside (i.e. in a heterogeneous three dimensional network of connected structures). For this reason it is important to not only consider heterogeneity on the level of individual fractures, but also effects arising on the larger scale of the fracture network itself which also includes consideration of hydraulic boundary conditions and source term locations relevant for the solute transport under consideration.

Calculations made by /Painter 2006/ indicate that internal variability in transport aperture and transmissivity has only a minor effect on the estimated flow-related transport resistance (F-factor) and the advective travel time provided the internal variability is not greater than the fracture-to-fracture variability. One cause of the insensitivity is a “choke-point effect” caused by the fact that fluid can enter and leave a fracture only on limited areas, thereby constraining the flowpath geometries. The overall effect of fracture-to-fracture transmissivity variability and hydraulic connectivity are referred to collectively as network scale effects in this report. In cases where the network scale variability was less than the internal fracture variability, more severe channelling resulted in a greater frequency of fast flowpaths with reduced F-factors. Although these calculations were made for non-contacting fractures, similar results are likely for fractures with asperity contacts since the flow naturally tends to seek out the path of least resistance. This does not necessarily mean that flow channelling is unimportant but merely that the effect in many cases may be weak in relation to the impact of network scale stochastic variability.

The problem remains, however, how to adequately account for flow channelling in safety assessment calculations when it is not possible to make large scale hydrogeological simulations with sufficiently well resolved spatial variability (i.e. on the level of individual fractures) to adequately capture important flow channelling phenomena. Since the flow in sparse, heterogeneous fracture networks tends to be governed by network scale effects, the issue essentially boils down to estimating the effective flow-wetted surface that channelised flow makes contact with in individual fractures. In the previous SR-Can safety assessment /SKB 2006a/ this was handled by a heuristic assumption that the F-factor should be pessimistically reduced by a factor of ten relative to that estimated based on average fracture transmissivities and the assumption of flow contact with entire fracture surfaces. This was not based on any specific quantitative reasoning, but primarily on subjective expert judgement under the assumption that the bulk of the flow might only contact about 10% of the total fracture surface area.

In the present SR-Site safety assessment, the F-factor is not reduced by a factor of ten as was done previously since this is considered to be an unnecessarily pessimistic assumption for three reasons. First, fracture-to-fracture variability is generally larger than within-fracture variability in aperture. Second, fluid can only enter and leave fractures on limited area, significantly constraining the meander of flowlines /Painter 2006/. Third, substantial portions of the non-contacting fracture surface area outside of the dominant flow channels may still be accessible by diffusion within the fracture pore space and thus provide additional surface area for radionuclides to interact with the rock matrix. While this type of transverse dispersion can usually be neglected on the timescale of tracer tests performed in fractured rock, it is of great significance at safety assessment timescales where rates of diffusive mass transfer can become commensurate with the rate of advective transport. On balance this means that non-scaled F-factor ranges can often be assumed for transport calculations even in the presence of significantly channelised flow without introducing large errors provided a set of reasonable conditions can be fulfilled. Calculations detailing the conditions under which this assumption is considered reasonable are presented in Appendix A.

2.1.2 Evolution of flow over a glacial cycle

Understanding of climate evolution at the Forsmark site is described in detail in the **Climate report**. Future glacial cycles will have a significant effect on groundwater flow and chemistry. For most of the transport scenarios analysed here and in the **Main report**, these effects are ignored and steady temperate-period flow and chemical conditions are assumed. Selected modelling cases presented later in this report are used to assess the impacts of climate variability and show that the temperate-period results provide a reasonable approximation to peak mean annual dose.

In those selected modelling cases that include unsteady conditions, a pessimistic abstraction of the groundwater flow field evolution is used in place of the full details of the flow and chemical evolution during a glacial cycle. A simplification of the glacial cycle is developed in the **Climate report** to support the abstraction, see Figure 2-1. The simplified cycle has two temperate periods, three periglacial periods, two glacial periods, and two submerged periods in the 120 kyr cycle. It is noted that the summed percentages of each climate period coincides with the corresponding percentages for the original, non-simplified cycle. In the abstraction, the cycle repeats 8 times in the 1 million year assessment period of interest. Table 2-1 provides times for each flow change in the first 120 kyr cycle.

Detailed simulations of transient flow during a glacial cycle have been undertaken /Vidstrand et al. 2010/. These simulations show that both the direction and magnitude of groundwater flow are affected by the glacial cycle. As an alternative to representing the full details of transient groundwater flow fields in the transport simulations, a pessimistic bounding abstraction is developed. The abstraction includes changes in flow magnitude, but uses pathlines from the temperate period /Joyce et al. 2010/ and ignores changes in flow direction. This abstraction is pessimistic because it greatly overestimates the vertical component of the flow velocity compared with detailed simulations /Vidstrand et al. 2010/, and also ignores lengthening of the flow paths that may occur during some of the climate periods.

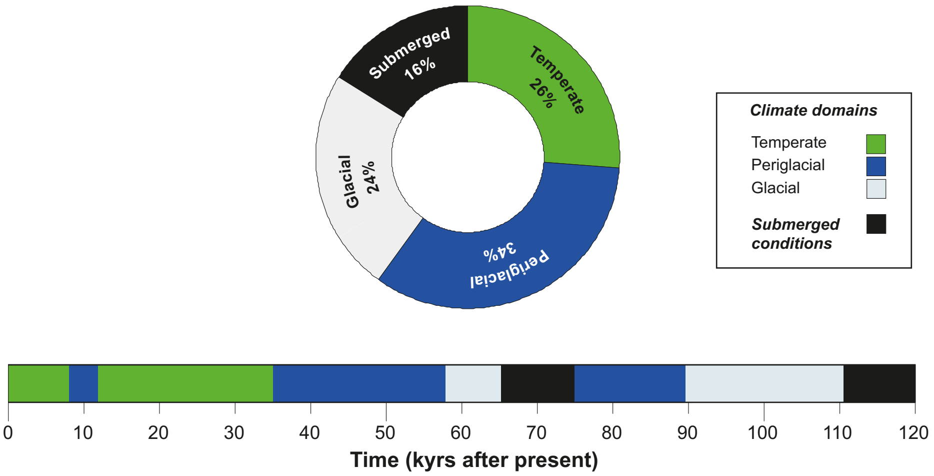

***Figure 2-1.** Simplified glacial cycle for use in the geosphere transport assessment /**Climate report**/.*

Table 2-1. Duration of each climate period in the simplified 120 kyr cycle. The percentage of each accumulated period is also indicated.

Period	Calendar time (kyrs)	Duration (kyrs)	Accumulated duration (kyrs)
Temperate	0–8	8	8
Periglacial	8–12	4	4
Temperate	12–35	23	8+23=31 (26%)
Periglacial	35–58	23	4+23=27
Glacial	58–65	7	7
Submerged	65–75	10	10
Periglacial	75–89	14	27+14=41 (34%)
Glacial	89–111	22	7+22=29 (24%)
Submerged	111–120	9	10+9=19 (16%)

The glacial periods summarised in Figure 2-1 and Table 2-1 need to be further subdivided into advancing, glacial maximum, and retreating phases because the groundwater velocity will be very different in these three phases. For the advancing ice sheet, it takes 366 years for the ice sheet to move between ice front locations I and IV, see /Vidstrand et al. 2010/ for details. For the retreating ice sheet it takes 61 years to move between ice front locations IV and I. As an approximation, it is judged that when the ice front is beyond these ice front locations, the influence of the ice front on the repository will be small, i.e., conditions close to periglacial or submerged will prevail. However, even beyond these times, there is some influence, even if not comparable to the peak, see Figure 2-2, which shows the Darcy flux at repository depth within the repository footprint (measurement locality 2 in /Vidstrand et al. 2010/). Specifically, during the ice advance, the increase in Darcy flux relative to temperate conditions prevails approximately for 2,000 years. It is decided to represent the glacial advancing period as having duration of 1,800 years, which is much longer than the time to move between ice front locations I and IV, but slightly shorter than the time 2,000 years. The more rapid retreating phase is modelled as having duration of 300 years; i.e., the ratio in duration between advance and retreat phases is maintained. It is also noted that the increase in Darcy flux during the advancing phase is smaller than during the retreating phase. This is due to the fact that the advancing phase is characterised by permafrost in front of the ice sheet, whereas the retreating ice sheet is warm based such that no permafrost is present, see /Vidstrand et al. 2010/ for details.

Flow scaling factors for each climate domain are obtained from the calculated Darcy flux distributions at deposition hole locations in the super-regional groundwater flow model of /Vidstrand et al. 2010/. In Figure 6-18 of /Vidstrand et al. 2010/, the maximum, median, and minimum Darcy flux distributions are shown normalised by the temperate period value. The normalised median values from Figure 6-18 of /Vidstrand et al. 2010/ and the duration of each flow epoch from Table 2-1 are used to obtain time-dependent flow factors (Figure 2-3). In developing the flow factors, the glacial state with a 2-km tongue of permafrost was assumed for the glacial advancing period, and the glacial state without permafrost was assumed for the glacial retreating phase. The latter assumption is regarded as slightly pessimistic because the fluxes in the glacial case without permafrost of /Vidstrand et al. 2010/ were developed for an advancing ice sheet but applied here for a retreating ice sheet. In the far-field calculations with MARFA, the advective travel time and flow-related transport resistance for the temperate period are inversely scaled by the values in Figure 2-3 to obtain corresponding values for other stages in the glacial cycle.

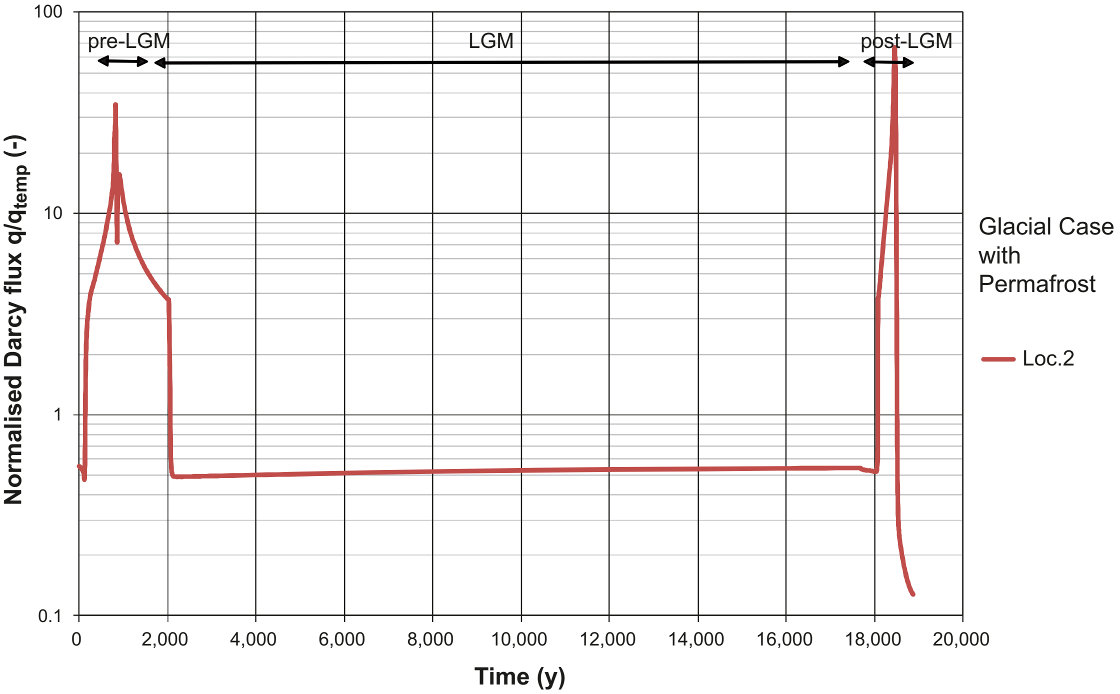

Figure 2-2. *Change in Darcy flux relative to the temperate period as the ice sheet advances and retreats over the repository location. Figure is modified after Figure G-12 (Appendix G) of /Vidstrand et al. 2010/.*

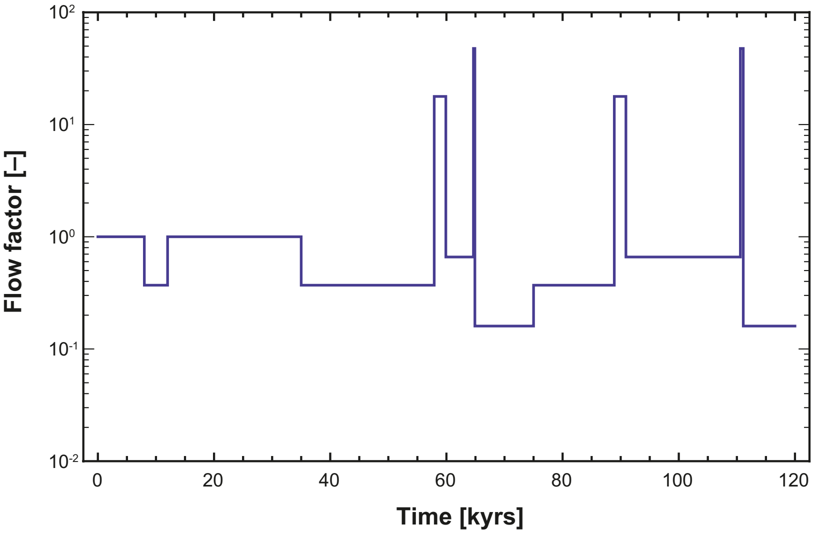

Figure 2-3. *Flow scaling factors for one glacial cycle (of eight during 1 million years) for use in far-field radionuclide transport simulations. The spikes at the end of the two glacial periods have duration of 300 years (not resolved on this scale). The scaling factor is defined relative to the Darcy flux in the temperate period and is used to adjust both advective travel time and flow-related transport resistance.*

2.2 Chemistry

A broad overview of chemical processes of relevance for SR-Site is given in the **Geosphere process report**. In this section, chemical processes of specific importance for radionuclide migration in the far field are described. The chemical composition of groundwater and the reactions between aqueous solutes is of great importance for understanding the sorption processes that give rise to the transport retardation effects modelled in SR-Site.

Although the partitioning of nuclides between the aqueous and surface sorbed phases is treated in a simple fashion using a linear isotherm (K_d) approach, it is important to remember that the conditional K_d value is simply the ratio of immobilised and dissolved solute that is specific for a particular solid phase composition, water chemistry, and solute concentration and does not rely on any particular mechanistic argumentation regarding underlying sorption processes. In SR-Site, the term sorption is used to describe adsorption processes involving ion-exchange and surface complexation. Ion-exchange refers to the electrostatic interactions of dissolved solutes with permanently charged sites of minerals, usually phyllosilicates. Surface complexation, however, refers to the interactions of dissolved solutes with surface reactive groups on mineral surfaces. Inner sphere surface complexation involves covalent bonding of solutes to these reactive groups, whereas outer-sphere surface complexation refers to the electrostatic interaction of solutes with the reactive groups.

By their very nature, surface reactive groups are sensitive to the groundwater composition, in particular pH, and the relative abundance of binding sites is therefore strongly dependent on groundwater chemistry. Nuclides sorbed by way of ion-exchange or outer sphere surface complexation are sensitive to ionic strength since the electrostatic interactions are weak and they can easily be displaced by competing solutes. Nuclides that form inner sphere surface complexes are typically considered less sensitive to ionic strength on account of their stronger bonds with the surface.

Direct and indirect competitive effects involving other dissolved species in groundwater influence sorption of nuclides. Direct effects involve the presence of other groundwater solutes that, owing to their much higher concentration, compete against nuclides for a limited number of sorption sites even if they sorb less strongly than the migrating nuclide. Reactive ligands in solution such as carbonate and hydroxyl ion also compete with sorption sites to bind radionuclides in the form of aqueous complexes. This is an example of an indirect competive effect. In general the free concentration of a solute makes up a variable part of the total dissolved concentration of a substance. The distribution of a nuclide between its various complexed forms (i.e. its speciation) has a strong influence on the overall magnitude of sorption.

There are a number of different ligands present in groundwater that may influence the speciation of radionuclides. Chief among these are hydroxyl ions (involved in hydrolysis), carbonate, and to a lesser extent chloride. Depending on redox conditions, the presence of sulphate or sulphide may also play a role in radionuclide speciation. Certain nuclides are highly sensitive to redox potential and can switch between largely immobile forms under reducing conditions to relatively more mobile forms under oxidising conditions. The redox potential at which a transition is thermodynamically possible from reduced to oxidised forms is also influenced by pH and carbonate concentration.

The two key variables that govern a large portion of radionuclide speciation are the pH and carbonate concentration (or equivalent partial pressure of carbon dioxide). These are considered to be of primary relevance for the sorption of many of the radionuclides in SR-Site, particularly those that sorb by way of a surface complexation mechanism. For solutes that sorb principally by ion-exchange or outer-sphere surface complexation, the concentration of competing solutes given by the total dissolved solids (TDS) or ionic strength is a key variable influencing sorption. Redox speciation is considered separately in SR-Site owing to the overwhelmingly strong control that it exerts on the mobility of certain radionuclides (principally, U, Np, Tc, and Pu).

2.2.1 Spatial variability of groundwater chemistry

The spatial distribution of groundwater composition at different times in the temperate phase of repository evolution is shown in Figure 2-4 for 2,000 years, and in Figure 2-5 for 9,000 years.

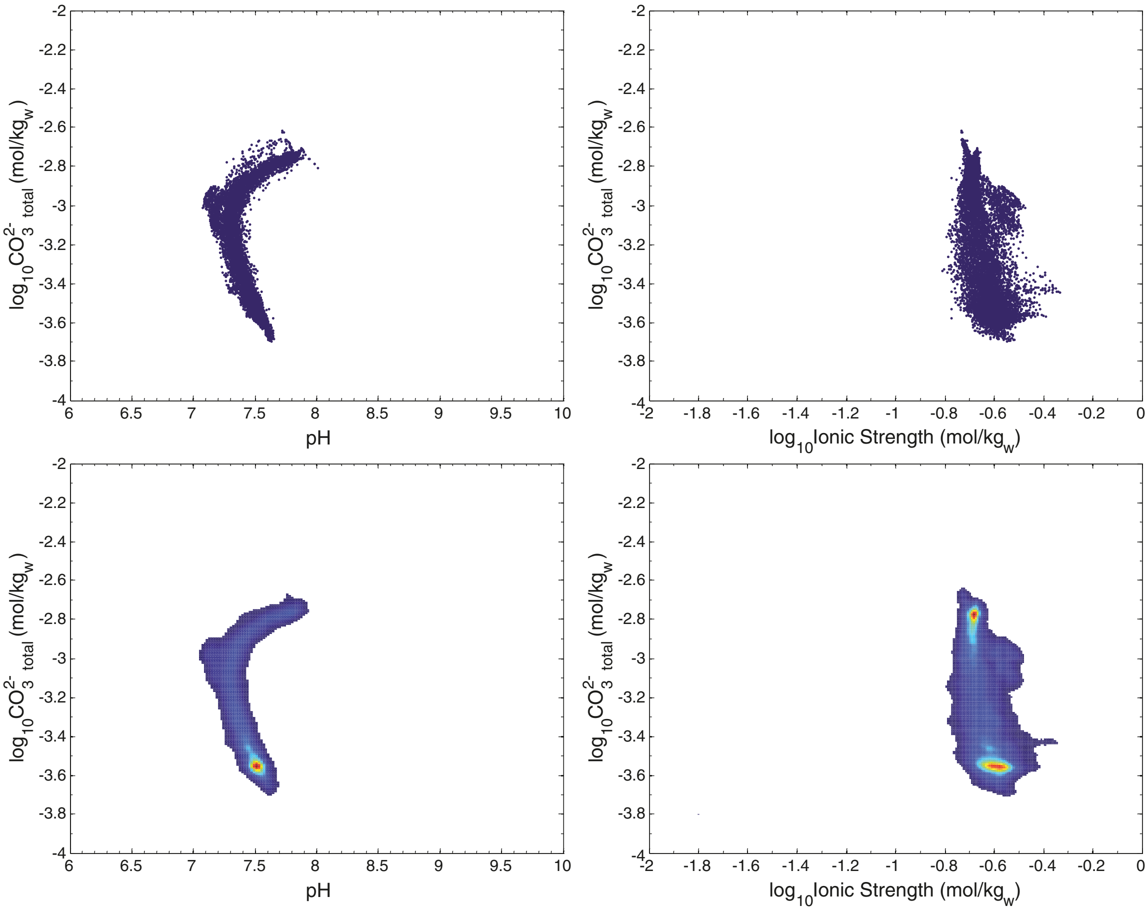

Figure 2-4. Distribution of groundwater compositions at 2,000 years in the temperate phase of repository evolution. Data are given for total carbonate versus pH (left hand side), and total carbonate vs. ionic strength (corresponding to the data calculated by /Salas et al. 2010/ and stored on SKB's trac database). The data are visualised in scatterplot form (top) and as a smoothed 2D histogram (bottom).

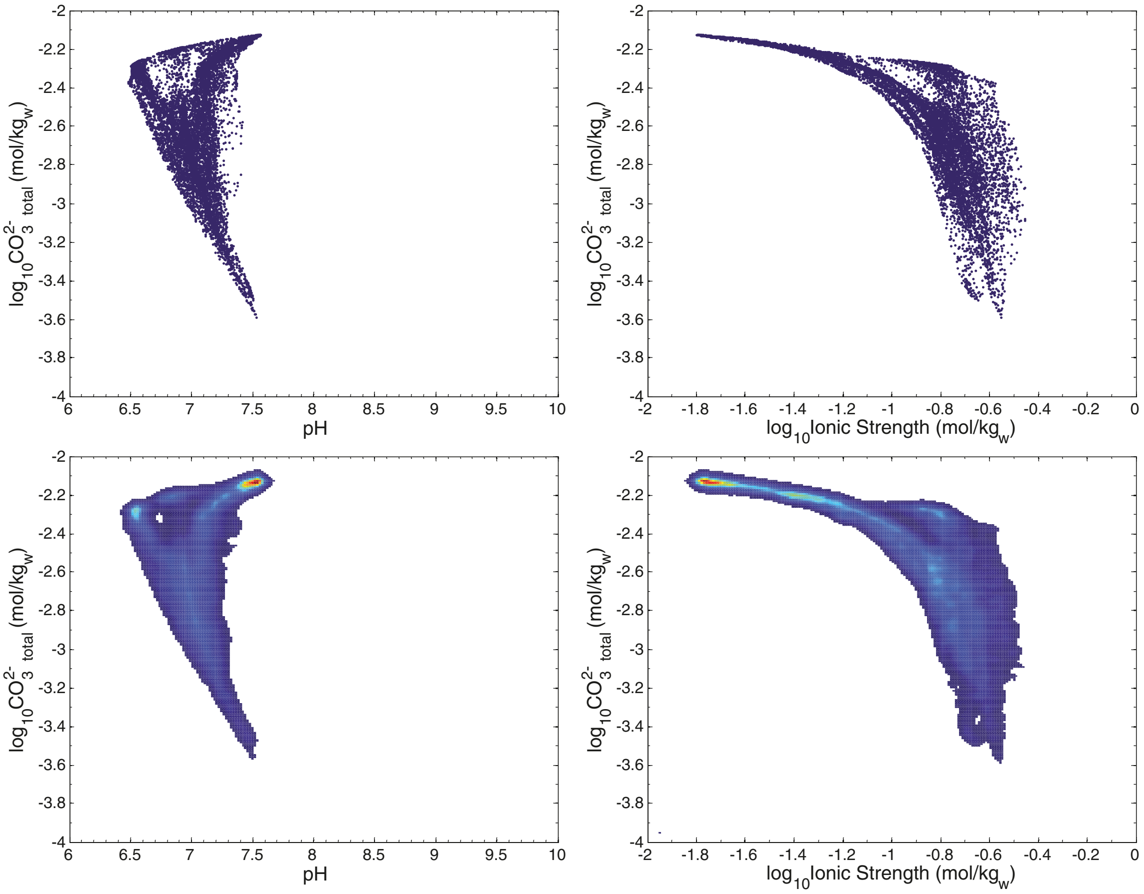

Figure 2-5. Distribution of groundwater compositions at 9,000 years in the temperate phase of repository evolution. Data are given for total carbonate versus pH (left hand side), and total carbonate vs. ionic strength (corresponding to the data calculated by /Salas et al. 2010/ and stored on SKB's trac database). The data are visualised in scatterplot form (top) and as a smoothed 2D histogram (bottom).

2.2.2 Evolution of groundwater chemistry over a glacial cycle

The evolution of groundwater chemistry over time is described in some detail in the **Main report** and only a brief overview of the most salient features is given here. Over a glacial cycle the changes in groundwater chemistry are driven by different processes: infiltration of meteoric water in combination with land uplift during the temperate period (*interglacial*), alternating pulses of dilute, glacial melt water and deep saline groundwater during the glacial advance and retreat (*periglacial*), and nearly stagnant conditions when a stable ice sheet exists over the repository. During various parts of the glacial phase, permafrost may also extend to a significant depth in the rock and prevent the flow of water.

The temperate period is characterised by a slow freshening of the groundwater surrounding the repository over many thousands of years under the influence of infiltrating meteoric water. During this period, the groundwater evolves towards lower pH levels and higher carbonate concentrations. This is also likely to result in a steady increase in the redox potential over time. The intruding meteoric water displaces saline water in the fracture system and mixes by diffusive exchange with stagnant water in the rock matrix.

During the ice-front advance, the large hydraulic gradient near the advancing front of the ice margin results in dilute glacial meltwater being forced to great depth in the rock before exiting downstream of the advancing front although still short of the repository location. The meltwater comes in part from water under the ice itself held in a liquid state by isostatic pressure and partly from water draining from the surface of the ice through moulins near the ice margin. The disturbance in hydrogeological conditions displaces the existing saline water in the fracture system forcing it downwards and forwards. This results in saline upconing of deep brine groundwater to shallower depths in the repository vicinity. As the ice margin approaches and passes over the repository, the flows are partly reversed and meltwater may penetrate the repository environment. Since the hydraulic connectivity of the fracture system and conductivity of the rock is very heterogeneous, some recharge flowpaths experience very large and rapid changes in groundwater chemistry, whereas others are hardly affected. Generally it is the flowpaths characterised by high Darcy fluxes and low F-factors that experience the greatest changes.

After the ice margin has passed, the flow gradually decreases until at some point nearly stagnant conditions are achieved owing to the extremely low hydraulic gradients under the main part of the ice sheet and the influence of permafrost, which reduces inflows to the groundwater system. The large mass of ice on top of the land mass simultaneously pushes down on the crust, which has an influence on hydraulic conductivity of the rock. During this phase of the repository evolution, flows are much reduced relative to the temperate phase and flowpaths are longer to the discharge locations downstream of the ice front. Salt stored in the rock matrix begins to diffuse back out into the diluted fracture water and slowly restores salinity in the fracture system.

As the ice front begins to retreat, a similar sequence of processes is set in motion although in reverse. In this case, the newly re-established saline groundwater in the fracture system is rapidly flushed out by the forced intrusion of meltwater in the vicinity of the ice front. After the retreating ice front passes over the repository location, additional episodes of saline upconing may occur. After the ice front has retreated even further, the saline conditions typical of the temperate period becomes slowly re-established. At this time, the isostatic load of the ice will depress the crust and result in the repository site being inundated with marine water and under sea level.

The subsequent uplift of the crust due to glacial rebound will slowly change the shoreline location and topographic elevation of the land relative to the sea. The slowly changing topographical conditions and shoreline results in the repository eventually becoming an inland location. The slowly evolving hydrogeological situation then results in a gradual freshening of groundwater in the repository environment due to infiltrating meteoric water and a return to temperate conditions.

Although this paints a broad picture of the main sequence of events characterising an individual glacial cycle, it is important to also consider that such cycles can be expected to reoccur with a predetermined periodicity and possibly deepening intensity with time as described in the **Climate report**. There may also be transients (e.g. stadial and interstadial periods) and shorter glacial/interglacial periods over the total 120 ka timespan of the full glacial cycle. In the radionuclide transport calculations, however, a much simpler tableau of glacial evolution is considered as indicated in Figure 2-1.

2.3 Background levels of naturally occurring radionuclides

A number of nuclides belonging to naturally occurring U-series decay chains are present in the groundwater at Forsmark. To place in context the mean annual effective doses calculated later in this report, it is useful to have an estimate of the corresponding dose from the naturally occurring radionuclides.

Activities of U-238, U-234, Th-230, Ra-226, and Rn-222 (belonging to the U-238 decay chain) have been measured during the site investigations as well as Th-232, Ra-228, Th-228 (belonging to the Th-232 decay chain), and U-235 /Laaksoharju et al. 2008/. If one excludes Rn-222, the largest contributors to the natural background activity in Forsmark groundwater are Ra-226, U-238, and U-234. These nuclides are shown in Figure 2-6 as a function of sampling depth. Generally it is found that Ra-226 activities are greatest at depth with a slight decrease towards the surface. The opposite behaviour is observed for U with the lowest activities found at depth with a steady increase towards the surface. Both these trends are in broad qualitative agreement with the understanding of groundwater chemistry at the site. The groundwater activity of Ra, for example, is well correlated with TDS (more so with Ca concentration) indicating a geochemical control by way of ion-exchange or possibly solid solution involving calcite. Barite, which forms solid solutions with Ra, does not appear to be present in significant amounts in Forsmark fracture minerals, an observation which

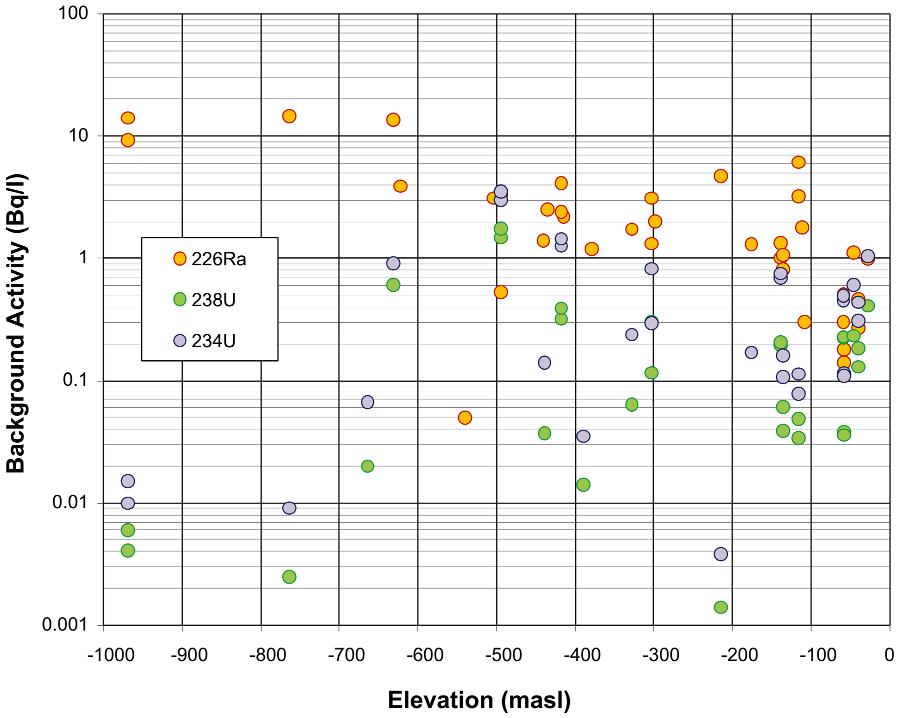

Figure 2-6. *Typical background activities of the main naturally occurring radionuclides of interest in groundwater at the Forsmark site /Laaksoharju et al. 2008/ (numerical values are taken from the SKB SIMON database). Rn-222 is neglected on account of its gaseous form and consequent rapid dilution in the biosphere (it is also neglected in the calculation of far-field dose rates calculated in SR-Site owing to its low relative contribution to radiological risk).*

is consistent with the only weak correlation between dissolved Ba and Ra concentrations at the site. The decreasing trend of U activities with depth appears to be coupled to the decreasing redox potential and carbonate concentration at increasing depths. Most sampled groundwaters at Forsmark have a U-234/U-238 isotope ratio between 2–3 /Sandström et al. 2008/.

Assuming that the arithmetic average of sampled nuclide activities can be taken to be approximately representative of the situation existing at 2000 AD in the corrosion scenario (central case), a comparative estimate of far-field release rates arising from these naturally occurring nuclides can be made. The release rate (Bq/yr) of naturally occurring nuclides can be estimated by multiplying the arithmetic average of the measured groundwater activities $\overline{A}_i$ (Bq/m^3) with the discharge flux v_{ex} (m^3/m^{2}yr) and surface area a_{ex} (m^2) for release:

$$\mathrm{N}_i \approx \overline{A}_i \cdot v_{ex} \cdot a_{ex} \qquad 2\text{-}1$$

Since the naturally occurring background of dissolved nuclides is not restricted to the local or even the regional scale model area, the total release rate depends on the landscape surface area assumed to make the calculation. In order to make a relevant comparison with the anthropogenic dose rates, some reference area needs to be assumed. For the purposes of SR-Site, the most appropriate reference area is the predicted area for hypothetical nuclide release from the repository. The particle tracking calculations used to estimate surface exit locations in the central case are used to estimate this area in this analysis. The surface exit locations at 2000 AD for all realisations of the hydrogeological semi-correlated case (cf. Table 4-1) are shown in Figure 2-7. The relevant surface area was estimated by binning the particle release locations into a 2D histogram with 40 m × 40 m cells and calculating the area of occupied cells.

The arithmetic mean of the groundwater activity is deemed an appropriate measure of groundwater activity since the total release of nuclides represents a summation of groundwater activities originating from many different flowpaths. In accordance with this, the standard error of the mean activity

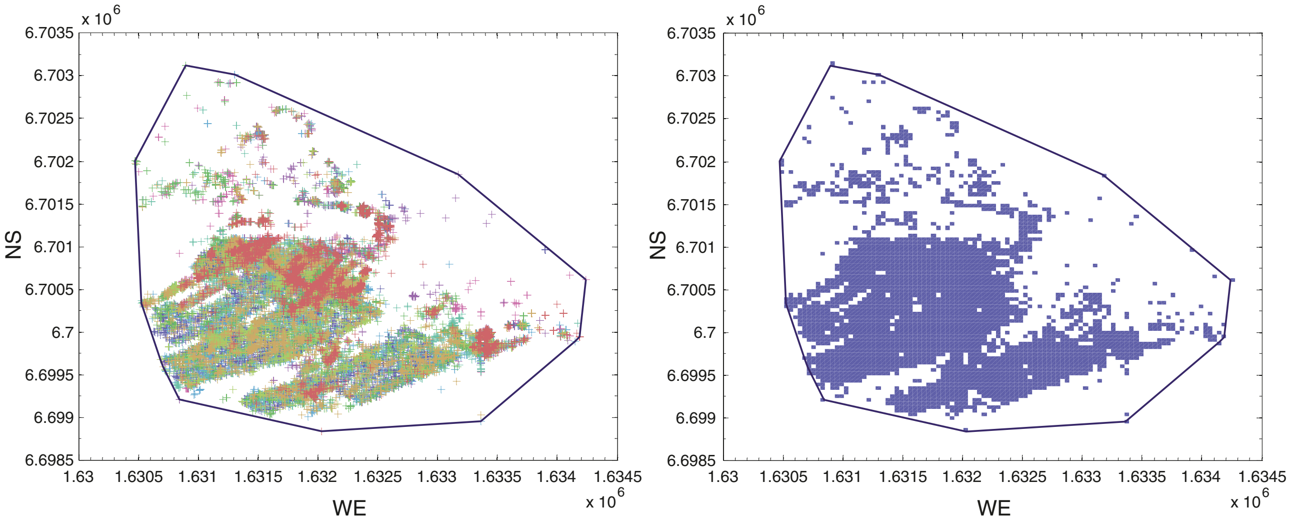

Figure 2-7. *Particle exit locations at 2000 AD for all realisations of the hydrogeological semi-correlated case (left). The approximate footprint of particle release locations for all simulations taken together as an ensemble is also shown (right) where particles are sorted into a 2D histogram of 40 m × 40 m cells. The convex hull of the full set of release locations is also shown as a reference (blue outline).*

is deemed the relevant measure of uncertainty. The individual realisations of the hydrogeological model, however, may be considered as all equally valid with regard to estimated release area. This means that the variance of the estimated area between realisations must be treated as a data uncertainty rather than a measure of variability, given that in reality there should be only one true value of the release area for a given set of boundary conditions.

Since the release area estimate is based on only a limited number of realisations, it is necessary to calculate an expanded range of uncertainty that explicitly takes the limited sample size into account. If it is assumed that the uncertainty of the estimated area can be modelled as a lognormally distributed variable, then the correct form of the expanded uncertainty range is given by the student-t distribution. A lognormal measure of the uncertainty is considered appropriate in this case since the variation of the particle release area between realisations is sufficiently large that it would imply negative areas if treated as a normally distributed uncertainty. Based on nine realisations of the hydrogeological model, the release area and its expanded uncertainty range are therefore estimated to be $(1.9\pm1.7)\cdot10^6$ m^2. If, on the other hand, the ensemble of particle release locations from all realisations were to be considered together, the estimated release area would be $4.1\cdot10^6$ m^2.

The average groundwater discharge in a 5×5 km area surrounding the Forsmark site is given by /Follin et al. 2007/ as roughly 2.6 mm/yr at an elevation of –100 m. This, however, is only a very approximate estimate since the upward discharge varies with depth and one ideally would need to consider that the discharge rate to the surface consists of water originating from different depths representing different advective recharge histories and most likely different hydrochemical compositions (see Figure 2-8). A large proportion of the upwards flow in the upper 100 m, for example, derives from local flow cells that do not necessarily penetrate very deeply into the bedrock and therefore may not carry representative amounts of naturally occurring nuclides. Based on the depth dependent discharge fluxes calculated by /Follin et al. 2007/, less than 1% of the upward water flux at an elevation of –100 m originates from repository depth and only about 13% originates from elevations less than –200 m. Water sampled at elevations above –100 m is generally more dilute than groundwaters sampled at greater depths owing to the larger turnover of water in the shallower flow cells. Assuming, however, that the average groundwater activity measured at the site and depicted in Figure 2-6 is reasonably representative of the upwelling groundwater at an elevation of about –100 m then an approximate order of magnitude estimate of the natural background nuclide flux can be made. This assumes that none of the naturally occurring activity originating from shallow flow cells contributes in a meaningful way to the overall nuclide flux.

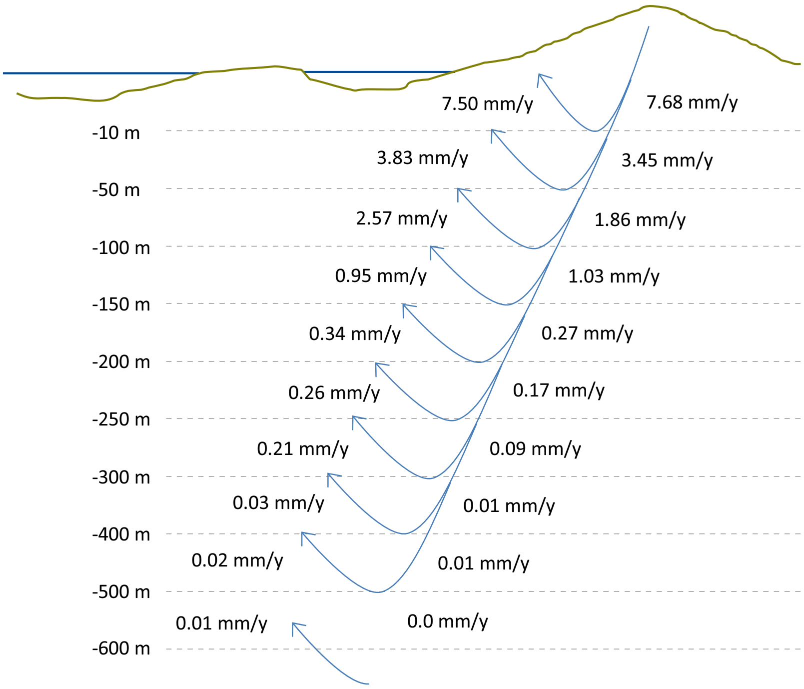

Figure 2-8. *Average vertical groundwater fluxes over a 5 km × 5 km surface area at different elevations at the Forsmark site as calculated by /Follin et al. 2007/. Since the surface discharge represents a mix of groundwaters with different advective histories, the upward flux at –100 m is chosen arbitrarily as being approximately representative of water carrying the average nuclide activity based on the data in Figure 2-6.*

Table 2-2 gives the mean groundwater activity (Bq/m^3), the estimated mean flux (Bq/m^{2}yr), and estimated mean release of natural background activity (Bq/yr) calculated for U-238, U-234, and Ra-226 at the Forsmark site. Since the mean release (Equation 2-1) is equal to the product of several variables with either normal or lognormally distributed uncertainties, it also has a lognormal uncertainty distribution. The estimated mean release and associated confidence interval given in Table 2-2 implicitly assumes this.

Table 2-2 Summary of natural background activities of naturally occurring radionuclides (U-238, U-234, and Ra-226) estimated flux to the surface, and total release rate within the same release footprint as the semi-correlated case far-field transport calculations.

		Mean activity (Bq/m^3)	Mean flux (Bq/m^{2}yr)	Mean release (Bq/yr)
U-238	Mean	94.1±31.5	$(2.42±0.81)\cdot10^{-1}$	$(4.7±4.6)\cdot10^{5}$
	CI (95%)	47 – 169	0.12 – 0.43	$5.73\cdot10^{4}$ – $1.68\cdot10^{6}$
U-234	Mean	243±78	$(6.24±2.02)\cdot10^{-1}$	$(1.21±1.18)\cdot10^{6}$
	CI (95%)	125 – 429	0.32 – 1.1	$1.52\cdot10^{5}$ – $4.31\cdot10^{6}$
Ra-226	Mean	1,530±325	3.94±0.84	$(7.61±7.02)\cdot10^{6}$
	CI (95%)	995 – 2,260	2.56 – 5.81	$1.18\cdot10^{6}$ – $2.62\cdot10^{7}$

2.4 Transport and retention processes

The migration of radionuclides in fractured rock is controlled by a variety of processes including advection and dispersion in water flowing through fractures, diffusion in the water in the pore space of the rock matrix, sorption processes, mineral precipitation/dissolution reactions, and interactions with colloids /**Geosphere process report**/. The **Geosphere process report** further identifies the dominant mechanisms as advection/dispersion in flowing water in fractures, diffusion in the water-filled pore space of the rock matrix, and sorption onto mineral grains. These processes are generally modelled using the advection dispersion equation in the fractures coupled with a Fickian model for matrix diffusion and a linear model for sorption in the rock matrix. Similar processes govern the movement of radionuclides out of the canisters and through the buffer material with the main difference being that precipitation/dissolution may be important within the canister for some radionuclides. Generally, these modelling simplifications of what is in reality a complex, coupled reactive transport process are justified on the basis that the transported radionuclides are extremely dilute, trace components within the groundwater /**Geosphere process report**/. However, a few neglected processes require some additional discussion, which is given in the following subsections.

2.4.1 Non-linear sorption processes

A number of different non-linearities can influence the retardation of transported radionuclides. The most direct effect is intrinsic non-linearity where sorptivity is limited by the finite number of binding sites available for sorption. This is most frequently formalised in the Langmuir isotherm where the amount of solute sorbed as a proportion of the aqueous concentration decreases with increasing surface loading up to a maximum monolayer sorption capacity. Where there are multiple surface sites with different reactive characteristics and maximum sorption capacities, the Freundlich isotherm is sometimes used as an approximation. Multicomponent, Langmuirian non-linear behaviour also arises where there is competition between different groundwater constituents for a limited number of binding sites. These types of intrinsic non-linearities are explicitly represented in thermodynamic models of ion exchange and surface complexation.

In many cases, the concentrations of migrating radionuclides are sufficiently low that intrinsic non-linearities do not need to be considered and conditional K_d values appropriate for extremely dilute nuclide concentrations can be assumed. This is frequently the case for radionuclides with strong solubility controls governing the near-field source term. In these cases, although retention in the immediate vicinity of the source may feature strongly non-linear characteristics a transition to approximately linear behaviour is expected after a short migration distance as the release is diluted by the retarded advective transport. The retardation effect achieved over the bulk of the subsequent migration path can then be characterised by approximately linear sorption over the relevant concentration range, all other things being equal.

Even when nuclide concentrations are not dilute, the conditional K_d value may be considered effectively constant if the approximately static background concentration of naturally occurring isotopes establishes the appropriate region of the non-linear sorption isotherm where the conditional K_d value is evaluated. This is particularly relevant for radioelements such as Cs, Ra, U, Sr, Th, and to a lesser extent the naturally occurring rare earth counterparts of the trivalent actinides and lanthanides. Provided the transported concentration of anthropogenic nuclides does not exceed the background levels, the assumption of sorption linearity is an acceptable approximation.

Intrinsic non-linearity is considered relatively straightforward to handle since it is always possible to establish a relevant concentration range over which a conditional K_d value can be defined that pessimistically overpredicts radiological consequences. More important non-linearities, however, relate to the impact of variable groundwater chemistry on the magnitude of the conditional K_d value. Selection of an appropriate K_d value therefore requires careful consideration of the ranges of groundwater chemistry that might be encountered and their spatial and temporal variability. As outlined in /Crawford 2010/ the K_d data supplied for SR-Site are associated with large uncertainties. A large proportion of this uncertainty relates to variable or uncertain contact solution compositions used in laboratory sorption measurements and how these relate to projected groundwater compositions in SR-Site.

At present it is not possible to quantitatively relate changes in sorptivity with evolving groundwater chemistry for many of the safety relevant nuclides. This is largely due to the lack of sufficiently detailed, multidimensional data sets of unambiguous sorption data for granitic rock types. Also, at any given time the concentration of major groundwater constituents can vary by two or more orders of magnitude throughout the repository volume. As outlined in Section 2.2.1 and 2.2.2 the spatially variable groundwater compositional profile also evolves over time under the influence of the prevailing hydrogeological boundary conditions. Fast flowpaths featuring low F-factors can be expected to exhibit greater temporal changes in chemical composition than slower flowpaths featuring higher F-factors. Since groundwater chemistry is not resolved on the level of individual flowpaths through the rock, a detailed knowledge of how groundwater composition influences the conditional K_d value would not necessarily give narrower bounds of uncertainty for radionuclide transport and it is only possible to speculate on the average impact of changing groundwater compositions throughout the repository volume as a whole. More detailed discussion concerning the neglect of non-linear sorption processes and its justification for the purposes of SR-Site in the presence of evolving groundwater chemistry can be found in /Crawford 2010/.

2.4.2 Precipitation and dissolution in the far field

Although precipitation and dissolution processes are considered to be of central importance for determining the source terms for solubility limited nuclides in the spent fuel canisters, these processes are typically disregarded in the far-field transport modelling. Over long time scales it is conceivable that pure phase precipitates of solubility limited nuclides will form outside the canister deposition holes in the near field. The further mobilisation of these nuclide enrichment zones along a migration path is limited by the groundwater flow and solubility equilibria governing the aqueous concentration of the nuclide in contact with the pure phase. For the redox sensitive radioelements, U in particular, the groundwater redox buffering effect arising from the presence of the enrichment zone itself may result in self-limiting transport dynamics which could conceivably give rise to roll front behaviour not dissimilar to that observed in some natural analogues. Immediately downstream of such mineralisations, however, the concentration of the nuclide will be diluted to below the solubility limit by various other retention processes and no longer controlled by pure phase solubility equilibrium. In these locations, the aqueous concentration will instead be governed by solid solutions with fracture filling minerals (discussed in Section 2.4.3) as well as ion exchange and surface complexation with fracture minerals. These processes may be considered to occur in addition to the diffusion and sorption on rock matrix microsurfaces assumed in transport calculations. This is a particularly relevant consideration if the abundance of potential co-precipitating fracture minerals along a flowpath is such that they have a lower overall retention capacity than the sorptive surfaces that can be effectively equilibrated in the rock matrix on the timescale of transport (as the scoping calculations detailed in Appendix B indeed suggest).

The retardation effect that these retention processes impose on the migrating nuclide causes further dilution of the nuclide until it reaches a concentration whereby sorption can be regarded as approximately linear both within the rock matrix and the advective pore space. This hierarchy of retardation processes and the continuous transition from highly non-linear sorption to approximately linear behaviour over a short distance from the repository is one of the main justifications for the assumption of intrinsically linear sorptivity in the far field as already outlined in Section 2.4.1. In an overwhelming majority of studied cases, the natural analogues used to support understanding of radionuclide migration behaviour in the near field and far field exhibit these characteristics outlined above (i.e. a hierarchy of processes active in different parts of the geosphere with increasing distance from the spent fuel analogue). Specific examples of these used in support of the corrosion scenario are discussed in more detail in the **Main report**.

The background concentrations of naturally occurring nuclides and non-active counterparts of anthropogenic radioelements, however, in many cases may be governed by solubility equilibria (in particular, U and Th). Deep within the rock matrix, recoil processes due to U-series radioactive decay lead to the accumulation of various U, Th, and Ra isotopes in the pore water until secular equilibrium is attained. Microprecipitates of secondary U(IV) and Th(IV) phases are likely to govern U and Th concentrations in the aqueous phase deep inside the rock matrix. On the other hand, and assuming that solid solution forming minerals such as calcite and barite are absent from the rock matrix, the pore water concentration of Ra is likely to be governed by ion-exchange sorption.

Porewater concentrations of rare earth element (REE) counterparts of the trivalent lanthanides and actinides are unlikely to be pure phase solubility limited owing to their extremely low concentrations. The background concentrations of these solutes are therefore largely expected to reflect the effect of surface complexation sorption involving mineral surfaces in the rock matrix.

In the immediate vicinity of fracture surfaces, solubility limiting phases may be absent in which case the formation of solid solutions with ferric oxyhydroxides and hematite as well as ion-exchange/surface complexation sorption will instead control U and Th availability (concentrations of REE are also expected to be influenced by this). Near the fracture surfaces, however, the interplay between redox buffering due to the weathering of ferrous minerals and the redox potential of flowing groundwater (together with the groundwater pH and pCO_2) govern the redox status of the predominant form of U in the groundwater. Amongst the redox sensitive radionuclides, U is particularly sensitive to groundwater composition and there is considerable evidence from U-series disequilibrium that U has been mobilised as U(VI) and re-deposited as relatively immobile U(IV) many times in the Forsmark fracture system over geological timescales ($\geq$ 1 Ma) /Sandström et al. 2008/.

The solubility equilibria governing the aqueous phase concentrations of U and Th deep within the rock matrix coupled with additional surface reactive processes and matrix diffusion near and at the fracture surfaces sets the relevant groundwater concentration range for conditional K_d evaluation even though precipitation and dissolution of these solutes is not directly modelled in far-field transport calculations.

2.4.3 Sorptive interactions with fracture minerals

Secondary minerals in the form of fracture coatings lining the advective flow space are expected to sorb migrating nuclides (both naturally occurring and anthropogenic). Although the term sorption has been used consistently throughout the SR-Site reports to refer specifically to ion exchange and surface complexation, the description is extended here to also include surface reactions involving solid solutions with minerals such as calcite, barite, and ferric oxides. There are many different types of minerals present in fracture coatings at the Forsmark site. The most important of these from a perspective of potential nuclide retention, are calcite, hematite, chlorite, and other clay minerals (referred to here as a group although including illite, smectites, and various mixed layer clays).

Chlorite and clay minerals are expected to sorb nuclides by ion exchange and surface complexation interactions whereas calcite and hematite can additionally form solid solutions with migrating nuclides. Although precipitation/dissolution equilibrium is typically neglected in safety assessment on account of the extremely low concentration of transported nuclides (outlined already in Section 2.4.2), solid solutions are extremely relevant for far-field transport processes in the geosphere on account of the fact that, unlike pure phase equilibria, such processes are active already at very low nuclide concentrations.

Generally, the retention processes involving fracture-filling minerals are considered to give an additional transport retardation effect over and above that estimated by the customary handling of retardation by matrix diffusion and sorption on rock matrix microsurfaces. For the central case where static groundwater compositions and flow trajectories are assumed, it is pessimistic to neglect these additional retardation processes because they only serve to lower far-field doses. Throughout the glacial cycle, however, groundwater chemistry is expected to change and in certain situations the neglect of the additional retention processes in the fracture minerals could potentially have negative radiological consequences for the far-field doses. This has been handled in SR-Site by screening calculations of possible changes in solute retention on fracture filling materials as a function of evolving groundwater chemistry, as discussed in Section 2.4.4.

2.4.4 Consequences of neglected retention processes and temporal changes in groundwater chemistry

The neglect of sorption on fracture minerals lining the advective pore space is generally expected to be a cautious assumption given that retention is relatively stronger in the fracture minerals than in the rock matrix. If fracture surface retention processes were to be included in the safety assessment modelling this would give additional retardation of the early breakthrough of transported radionuclides. The fracture minerals that would be expected to contribute most to the enhanced retardation are chlorite and other clay minerals, calcite, and (although to a lesser extent due to low abundance) hematite.

Since the quantity of such minerals lining the fracture space is limited, however, the retention capacity is small and only significant for flowpaths where the retardation effect arising due to matrix diffusion and sorption on rock matrix microsurfaces is weak. On account of the fracture minerals being distributed in a thin layer that is in direct contact with the flowing water, equilibrium sorption can be reasonably assumed for ion-exchange and surface complexation reactions on the timescale of transport.

Based on the statistical abundances of fracture minerals hosted in flow-bearing fractures at Forsmark /Löfgren and Sidborn 2010/, estimates have been made of the additional retardation effect arising due to equilibrium sorption on fracture minerals. On average, there are about 6–14 g of calcite, 2–5 g of chlorite, and 1–2 g of clay minerals per square metre of fracture area in typical flow bearing fractures at Forsmark. Given that the matrix retardation is approximately proportional to the square of the F-factor, the additional retardation due to sorption on fracture minerals is mostly negligible for flowpaths featuring F-factors greater than 10^4–10^5 yr/m. Although only an estimate, this range may be considered to be an approximately representative transition region that depends additionally on the strength of sorption both in the rock matrix and on fracture minerals. For flowpaths featuring very low F-factors, on the other hand, nuclide retention on fracture minerals is expected to have a much larger impact on the overall transport retardation (for details see Appendix B). For this reason, the neglect of fracture mineral retention processes is considered a pessimistic assumption in the central case transport modelling for SR-Site.

This reasoning assumes, however, that the evolving groundwater composition does not change in such a way that might lead to a sudden pulse-like release of surface sorbed nuclides under elevated flow conditions, which might occur periodically during a glacial cycle. In a model without explicit consideration of fracture mineral retention, nuclides are sequestered to a greater extent in the rock matrix rather than in association with the fracture minerals where they might be more easily mobilised. For some nuclides this might lead to far-field dose rates being underestimated.

In order to address this issue, consideration has been given to the potential for remobilisation to occur during the glacial IIa (saline upconing) and IVa (glacial meltwater penetration) time domains. These events are thought to be representative of the largest deviations expected from the conditions established during the temperate phase of repository evolution, which comprises the central case. These time domains are also characterised by significantly higher flowrates and lower F-factors than the temperate phase hydrogeological conditions. Cross plots of the main hydrochemical parameters influencing sorption are shown in Figure 2-9 as an aid to understanding relative changes in sorptivity of nuclides at different times in response to evolving groundwater chemistry.

Here, the impact of changing groundwater chemistry is considered simultaneously for phyllosilicate fracture minerals (i.e. chlorite and clay) and the rock matrix since the primary sorption mechanisms of ion-exchange and surface complexation are the same in each case. A change in groundwater composition, for example, that gives rise to a decrease in rock matrix sorptivity might also be reasonably inferred to give a similar although not necessarily proportionate decrease in sorptivity for fracture filling minerals that feature similar sorption mechanisms.

Fracture calcite, on the other hand, must be considered separately since it may form solid solutions with migrating nuclides. Since calcite does not typically occur within the rock matrix itself, this process is not considered to be a relevant mechanism of nuclide retention in the rock matrix and is therefore not modelled. In order to properly account for the full range of retention processes that might occur in association with fracture minerals, however, one would therefore also need to consider the possible role of solid solution formation with calcite (and possibly barite in the case of Ra-226). For this reason, detailed scoping calculations have been made on the impact of evolving groundwater chemistry on retention by solid solution (see Appendix B).

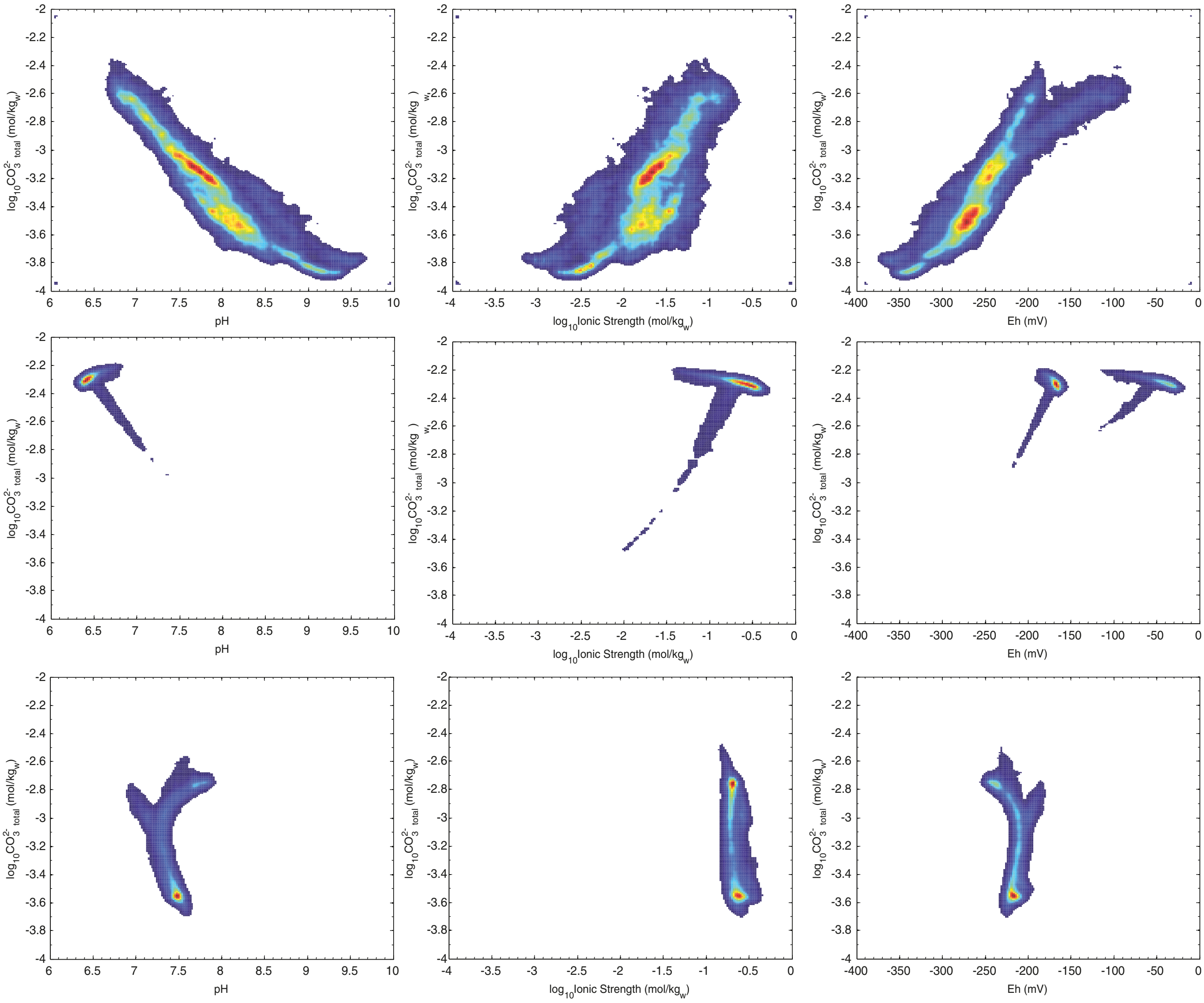

Figure 2-9. *Comparative plots of groundwater master variables influencing sorption. Data are shown for the hydrochemical reference case at 3,000 years (bottom row), glacial IIa case (centre row), and glacial IVa cases (top row) in the form of 2D histogram plots (log$_{10}$ space). In each case the total carbonate concentration is plotted versus pH (left), ionic strength (centre), and Eh (right). The plots correspond to the data calculated by /Salas et al. 2010/ and stored on SKB's trac database.*

Since the different sorption mechanisms respond in different ways to evolving groundwater chemistry, they are each considered separately in the following discussions. The overall impact of changing groundwater chemistry on far-field dose rates, however, needs careful consideration of all relevant sorption mechanisms simultaneously in the context of the prevailing hydrogeological situation. This must also be considered in the context of the inventory of nuclides that are actually sorbed by fracture minerals relative to that sequestered in the rock matrix. Since the fracture minerals have a limited capacity for nuclide retention relative to the rock matrix, the impact of remobilisation is generally not expected to be large even in cases where it might be reasonably expected to occur.

Impact of evolving groundwater chemistry on ion-exchanging nuclides

For nuclides that sorb by an ion-exchange mechanism (or whose sorption is otherwise strongly influenced by ionic strength), K_d values are chosen to reflect the most unfavourable groundwater compositions expected. The groundwater compositions existing at 2,000–3,000 years during the temperate time domain represent the peak groundwater salinity. Since sorption of these nuclides is negatively affected by elevated ionic strength, the hydrochemical conditions existing at this time are therefore used as a basis for the recommended rock matrix K_d values in the central case. For these particular solutes (Cs, Sr, and Ra), groundwater chemistry transfer factors are calculated with the aid of a simplified ion-exchange model to account for ionic strength effects during this time domain /Crawford 2010/. In the case of Ni, which exhibits a weak ionic strength dependency, groundwater chemistry correction factors are calculated on the basis of a power law regression model relating apparent K_d with ionic strength. Although slightly higher peak salinities are expected during the glacial IIa domain, this only occurs during brief transient periods and is not considered representative of the conditions prevailing during most of the repository evolution.

The correction implied by the chemistry transfer factor is very small relative to the level of overall uncertainty in the uncorrected K_d data sets. Counterintuitively, the solutes that are most strongly influenced by ionic strength on account of their weak sorptivity are also given smaller correction factors than more strongly sorbing solutes that are less affected by ionic strength. This is due to the larger underlying data uncertainty in the case of the more weakly sorbing solutes which tends to drown out the systematic trends that can be quantitatively related to evolving groundwater salinity. This should not be taken to mean that ionic strength is less important for the weakly sorbing solutes, but rather that the effect is more difficult to quantify for weakly sorbing solutes relative to the more strongly sorbing solutes.

It must also be remembered that since the changes in groundwater composition are not resolved on the level of individual migration paths, extrapolation to the groundwater situations existing at different times must consider the statistical distribution of spatially variable groundwater compositions throughout the entire repository volume which, in itself, introduces additional statistical dispersion in the calculation of K_d uncertainty ranges. It is therefore important when discussing the impact of evolving groundwater chemistry to distinguish between the true impact of ionic strength on the sorption process as it actually occurs from the impact that is statistically quantifiable for modelling purposes. Changes in groundwater salinity are therefore likely to have a much more profound local impact on sorptivity than has been quantified in the K_d recommendation. Since the K_d data are recommended for relatively saline conditions, this means that the strength of sorption will be pessimistically underestimated during the bulk of repository evolution.

Higher salinities encountered during the glacial IIa domain could result in a mobilisation of nuclides that are sensitive to ionic strength and give far-field dose rates higher than predicted by the transport modelling. Essentially, this would mean that radionuclide mass flux during the low-salinity phases of repository groundwater evolution would be overestimated and the radionuclide mass flux during the transitory saline glacial IIa phase would be underestimated. The nuclide most strongly influenced by this (and which has the largest potential impact on far-field dose rates) is Ra-226. However, the landscape dose conversion factor for Ra-226 is almost 3 orders of magnitude lower during the glacial periods compared with the interglacial period /Avila et al. 2010/, thus easily overwhelming any potential effects of underestimating salinity during the glacial IIa period.

Although not strictly considered to be an ion-exchanging solute, Ni-59 might also be affected by evolving salinity on account of its apparent sensitivity to ionic strength. Given that Ni-59 contributes much less to far-field dose rates, however, any variation in sorptive retention due to evolving groundwater composition is not expected to make a meaningful contribution to the overall picture of risk. Moreover, the landscape dose factor for Ni-59 is more than 3 orders of magnitude smaller during the glacial period as compared with the interglacial period /Avila et al. 2010/.

During the glacial IVa period, decreased groundwater ionic strength would typically result in enhanced sorptivity both in the fracture minerals and in the rock matrix, which is pessimistically neglected.

Impact of evolving groundwater chemistry on surface-complexing nuclides

For nuclides that sorb by way of a surface complexation mechanism, it was judged not feasible at this time to make quantitative predictions of how changing groundwater chemistry might affect the magnitude of sorption. This is largely due to a lack of suitable mechanistic models describing the sorption of nuclides in association with granitic rock. At the same time, it is acknowledged that relatively sophisticated surface complexation models do indeed exist for sorption of nuclides in association with fracture filling minerals such as illite and smectite. Similarly to the quantification of ionic strength effects, however, even a very detailed mechanistic model would be unlikely to give a much reduced span of K_d uncertainty owing to the large spatial variability of groundwater compositions existing throughout the repository volume at any given time. In spite of this, it is still possible to make a relatively detailed qualitative account of how changes in groundwater chemistry might affect sorptivity based upon the well-known behaviour of model systems comprised of single minerals.

For surface complexing nuclides, groundwater pH, carbonate concentration (or pCO_2), and redox potential (Eh) are considered to be the most important master variables influencing sorption. In general, lower pH levels and higher carbonate concentrations are expected to result in reduced sorptivity of cationic nuclides by way of changes in the relative abundance of negatively charged surface binding sites as well as increased aqueous phase complexation by carbonate. For anionic nuclides one would generally expect the opposite behaviour with regard to pH changes (although this mostly concerns hematite, which has a relatively high point of zero charge). In most cases, however, the sorption of anions is negligible owing to a higher abundance of negative surface charge at prevailing groundwater pH and because their sorption is also subject to competition from other anionic groundwater constituents.

Redox potential also has a very strong influence on the predominant state of the redox sensitive nuclides that mostly sorb by surface complexation mechanisms. Higher Eh can imply a transition from relatively immobile reduced forms to more mobile oxidised forms that, in some cases, could imply the possibility of remobilisation during the glacial IVa period. Carbonate also plays an important role in redox speciation by altering the threshold at which transitions between predominantly reduced and oxidised forms can take place. Of the redox sensitive solutes, Pu and Np are not expected to be influenced by this on account of the Eh being well below their respective thresholds for transition from reduced to oxidised speciation for all conceivable groundwater situations predicted during the glacial cycle. U and Tc, on the other hand, may experience a transition to predominantly oxidised speciation during the glacial IVa period. The predominant redox speciation of U, however, is sufficiently uncertain even during the temperate time period that both oxidised and reduced speciation cases are propagated in SR-Site. This is due to the fact that the Eh and carbonate concentration ranges predicted during the temperate phase are such that the predominance of the U(IV) form cannot be strictly guaranteed at all times throughout the repository volume.

Although less mobile, the reduced U(IV) form is considered to be the more pessimistic assumption in the central case since it represents a more concentrated secondary source of the Ra-226 daughter nuclide. As already noted for Ra-226, any changes in the relative sorptivity of U which might give rise to remobilisation must also be considered in the context of the lower landscape dose factors during the periods of remobilisation. For this reason remobilisation scenarios affecting U transport in the far field are not considered to be of great significance to the overall picture of radiological risk. Notwithstanding this, however, sensitivity calculations are made with low U sorptivity as a variant of the central corrosion case in Section 4.5.4 and to assess the possible role of periodic transitions to low U sorptivity during the full glacial cycle in Section 4.5.7.

It should also be noted that the ranges of uncertainty recommended for K_d data implicitly include the full range of spatial and temporal variability expected in groundwater compositions. Although this means that nuclide dose rates are likely to be pessimistically overestimated during the temperate time domain, this does not necessarily inform the discussion of possible remobilisation of nuclides due to changing groundwater chemistry during the glacial IIa and IVa periods. Based on the relative trends of pH and carbonate concentration depicted in Figure 2-9, however, a decrease in sorptivity is expected during the glacial IIa domain on account of higher carbonate concentrations and reduced pH relative to the temperate time period. Groundwater conditions during the glacial IVa domain are more heterogeneous with a much broader range of pH and carbonate concentrations than are predicted to exist during the temperate time domain. On average, however, the carbonate concentration is higher although the pH is also slightly higher implying a mixed impact on sorptivity.

Impact of evolving groundwater chemistry on retention by solid solution

In Appendix B, detailed scoping calculations have been made with the aim of approximately quantifying retention by solid solution during the temperate time domain as well as likely impacts that changes in groundwater chemistry might bring about. In these calculations, the retention of nuclides as solid solutions in association with calcite (and barite in the case of Ra-226) has been cast in a conditionally constant K_d framework. Although there are known situations in which a conditionally constant K_d description may not be an appropriate means of modelling transport retardation by solid solution, the approach is justified for the purpose of making scoping calculations through the application of a series of simplifying assumptions that are considered reasonable for the physicochemical boundary conditions describing the geosphere environment in SR-Site. Although only a small number of solutes (Ra, Am, Ni, U(IV), U(VI)) representing a range of different sorption chemistries are considered in the calculations, more general conclusions concerning impacts on the retardation of other nuclides may then be drawn by invoking appropriate geochemical analogies. In order to be consistent with the corresponding discussion for retention by ion-exchange and surface complexation, equivalent K_d values are derived for the groundwater compositions existing at 3,000 years in the temperate time domain as a hydrochemical reference case.

The scoping calculations indicate that equilibrium retention by solid solutions with calcite varies considerably amongst the different nuclides studied. In some cases the retention capacity is of similar magnitude (Am and Ni) or larger (Ra) than that of the chlorite and clay minerals, although in other cases the retention by solid solution is estimated to be considerably smaller than that of the chlorite and clay minerals (U(IV) and U(VI)). Groundwater chemistry correction factors defined in a similar fashion to that outlined previously for ion-exchanging nuclides indicate that retention is generally higher under most of the glacial cycle relative to the hydrochemical reference case with the exception of the glacial IIa time domain where retention by calcite solid solution appears to decrease slightly relative to the hydrochemical reference case. On the other hand, retention appears to be significantly enhanced during the glacial IVa time domain, which suggests that remobilisation scenarios are unlikely for solid solutions involving calcite. The considerable increase in retention by calcite during glacial IVa also suggests that possible decreases in sorptivity predicted for the surface complexing nuclides in association with chlorite and other clay minerals may be at least partially offset in some cases. This would certainly appear to be the case for trivalent actinides and lanthanides by way of geochemical analogy with Am.

Although barite has not been identified in quantifiable amounts in the fracture system at Forsmark its presence might be reasonably inferred from the only slight oversaturation of barite apparent in the groundwater compositions measured at the site /Crawford 2010/. Calculations indicate that as little as 1 mg/m^2 of barite would be sufficient to represent a larger retention capacity for Ra than that of the other fracture minerals. Calculation of chemistry correction factors for radiobarite indicate that retention of Ra is considerably reduced during the glacial IIa and IVa time domains relative to the hydrochemical reference case. If barite were the only mineral likely to form solid solutions with Ra, this would imply the potential for remobilisation during the glacial IIa and IVa periods. Interestingly, the decrease in retention by barite is offset by a corresponding increase in retention by calcite and the chlorite/clay mineral group during the glacial IVa period. If the amount of barite is much less than about 1 mg/m^2, the net effect would be an increase in retention during glacial IVa although still a slight decrease in retention during glacial IIa. As already noted, however, the landscape dose conversion factors are significantly lower during the glacial periods. The radiological consequences of remobilisation scenarios of anthropogenic Ra-226 therefore appear to be minor.

Although equilibrium sorption on fracture minerals can generally be assumed for ion-exchange and surface complexation sorption mechanisms, this is not necessarily always the case for solid solution retention processes on account of the kinetic effects related to the uptake process. In the scoping calculations, both equilibrium sorption and kinetically limited modes of solute uptake are therefore considered. It is concluded, however, that there is sufficient uncertainty concerning rates and actual mechanisms of kinetic rates of solute uptake at this time that the notion of equilibrium sorption by solid solution formation is not a prudent assumption for safety assessment modelling. The retention of radionuclides as solid solutions in association with calcite or barite may therefore be significantly less than that estimated on the basis of the equilibrium assumption.

2.5 Summary of geosphere non-flow related data

The movement of solutes through fractured rock depends on several parameters, which are discussed in detail in the **Data report** and supporting documents. Parameters related to the rock matrix – the effective diffusivity, diffusion available porosity, and sorption partitioning coefficient – are summarised briefly here. These data are site specific, depending on the geological settings and groundwater composition.

Flow-related parameters (e.g. the F-factor) are specific to the modelling case addressed. Data for the flow triplet parameters (Q_{eq}, t_w, F) are therefore discussed on a case-by-case basis where appropriate in Chapters 3 to 6. Near-field parameters related to the properties of buffer and backfill material can be found in the **Data report** and supporting documents. Other parameters related to the conceptualisation of radionuclide release and conversion of radionuclide mass discharge to a radiological dose rate are discussed in the following chapter.

2.5.1 Diffusion-available porosity

The diffusion available porosity is discussed in the **Data Report**. Based on consideration of the dominant rock type in the repository volume, a flowpath average porosity of 0.18% is recommended for use in SR-Site calculations. This recommended value is reduced relative to the measured laboratory value to account for the possible biasing effect of mechanical damage incurred during drilling and core extraction. The applied scaling factor of 0.8 is based on comparison of water saturation porosities with microcrack volume (porosity) measurements made in triaxial compression tests using site-specific rock samples.

2.5.2 Effective diffusivity

The handling of effective diffusivity and data used in SR-Site is discussed in the **Data report**. Based on the analysis documented there, a flowpath average effective diffusivity is recommended for use in transport calculations. For the purposes of SR-Site, the effective diffusivity recommended for cations and neutral species is assumed to have a lognormally distributed uncertainty with the following characteristics:

$$\log_{10} D_e = -13.7 \pm 0.25 \qquad 2\text{-}2$$

For anionic radionuclides, the recommended distribution is:

$$\log_{10} D_e = -14.2 \pm 0.25 \qquad 2\text{-}3$$

It should be noted that the standard error of the estimate given in Equations 2-2 and 2-3 relate to uncertainty rather than spatial variability and the estimates are considered to be already averaged. Since radionuclides may be present in a number of different speciated forms depending on groundwater chemistry, there is the possibility that cationic, anionic and neutral forms may exist contemporaneously. Because the safety assessment codes only allow for the assignment of a single effective diffusivity per nuclide this means that a judgement must be made for which effective diffusivity is to be used. Table 2-3 summarises the assumed speciation of different elements and redox species of importance for SR-Site.

Table 2-3. Dominant speciated forms estimated for elements and redox states at pH 8 and for saline groundwater (5,190 mg/l Cl^-, 22 mg/l HCO^{3-}) approximately representative of current conditions at repository depth. Carbonate complexed forms may take on greater significance in groundwater of more meteoric character. In situations where there is doubt concerning the most likely speciation, the anionic form might be considered a more cautious choice.

Element	Dominant species	Status
Cs(I)	Cs^+	Cation
Ra(II)	Ra^{2+}	Cation
Sr(II)	Sr^{2+}	Cation
Eu(III)	$EuCO_3^+$	Cation
Ho(III)	$HoCO_3^+$	Cation
Sm(III)	$SmCO_3^+$	Cation
Ac(III)	$AcCO_3^+$	Cation
Am(III)	$AmCO_3^+$	Cation
Cm(III)	$CmCO_3^+$	Cation
Np(IV)	$Np(OH)_4$	Neutral
Np(V)	NpO_2^+, $NpO_2CO_3^-$	Cation/Anion (carbonate dependent)
Pa(IV)	$Pa(OH)_4$	Neutral
Pa(V)	$PaO_2(OH)$	Neutral
Pu(III)	$PuOH^{2+}$, Pu^{3+}	Cation
Pu(IV)	$Pu(OH)_4$	Neutral
Pu(V)	PuO_2^+	Cation
Pu(VI)	$PuO_2(CO_3)_2^{2-}$, PuO_2CO_3	Anion
Th(IV)	$Th(OH)_3CO_3^-$	Anion
U(IV)	$U(OH)_4$	Neutral
U(VI)	$UO_2(CO_3)_3^{4-}$, $UO_2(CO_3)_2^{2-}$	Anion
Ni(II)	Ni^{2+}, $NiCl^+$	Cation
Zr(IV)	$Zr(OH)_5^-$	Anion
Ag(I)	$AgCl_2^-$, $AgCl_4^{3-}$, $AgCl_3^{2-}$	Anion
Cd(II)	$CdCl^+$, Cd^{2+}, $CdCl_2$	Cation
Pb(II)	$PbCO_3$, $PbCl^+$, $PbOH^+$, Pb^{2+}	Cation
Pd(II)	$Pd(OH)_2$	Neutral
Mo(VI)	MoO_4^{2-}	Anion
Nb(V)	NbO_3^-, $Nb(OH)_5$	Anion
Tc(IV)	$TcO(OH)_2$	Neutral
Tc(VII)	TcO_4^-	Anion
C(IV)	HCO_3^{3-}	Anion
C(-IV)	CH_4 (or organic acids)	Neutral
Cl(-I)	Cl^-	Anion
I(-I)	I^-	Anion
Se(-II)	HSe^-	Anion
Se(IV)	$HSeO_3^-$, SeO_3^{2-}	Anion
Se(VI)	SeO_4^{2-}	Anion
Sn(IV)	$Sn(OH)_2$	Neutral

2.5.3 Rock matrix sorptivity

K_d data recommended for use in SR-Site are based in part on site specific data obtained during the Forsmark and Laxemar site investigations, and in part on data contained in the open scientific literature. These data are documented in /Crawford 2010/ and the **Data report**. The data are corrected to account for biases due to differences in sorptive surface area and cation exchange capacity (CEC) of the crushed rock types used in laboratory investigations relative to the intact site specific rock assumed as a reference material for transport calculations (Forsmark metagranite).

In the small number of cases (Cs, Sr, Ra, Ni) where an ionic strength dependency has been quantified, data have been selected for the most unfavourable groundwater compositions expected which corresponds to roughly 2,000–3,000 years in the temperate case /Salas et al. 2010/. Generally, the overall uncertainty of the underlying data sets dominate and the correction implied by temporal changes in groundwater composition gives rise to only very small differences in the recommended values. Although salinity is slightly less on average at 3,000 years than 2,000 years, the difference is sufficiently small as to be statistically insignificant for the estimation of corrected K_d values. For elements where it is not feasible to quantitatively estimate the impact of spatially and temporally variable groundwater composition on sorptivity, K_d data representing a range of contact water compositions are combined to give an uncertainty range that is thought to reasonably represent the diversity of hydrochemical conditions expected. The conditional K_d values recommended for use in SR-Site in most cases represent a relatively large span of contact water compositions and experimental conditions. Although there may be some bias in the sampled parameter space for certain nuclides, the recommended data capture as much of the groundwater compositional uncertainty as is reasonably possible to achieve. In many cases it is likely that the uncertainty distributions represent a broader parameter space than is predicted for SR-Site groundwater compositions.

Recommended data for geosphere transport calculations

Sorption K_d data recommended for use in SR-Site for radionuclide migration calculations in the geosphere at the Forsmark site are summarised in Table 2-4. The data are given in the form of lognormal distributions characterised by a mean (μ) and standard deviation (σ) and implicitly include the combined impact of uncertainty as well as spatial and temporal variability. The median of the K_d uncertainty distribution may be taken to be the best estimate value for central case deterministic calculations. Since uncertainty rather than variability is expected to make the dominant contribution to the statistical dispersion of the recommended K_d data ranges it is not possible to estimate a meaningful flowpath average for the geosphere. For stochastic simulations, it was recommended that the lognormal distributions be sampled uniformly between the 2.5% and 97.5% percentiles specified as the lower and upper K_d limits in the table.

K_d values are given for the predominant redox species considered most likely for the groundwater compositions existing during the temperate phase of groundwater evolution. For all redox sensitive nuclides except U, the reduced species is predominant. Pu is assumed to be present in the trivalent state even though a mixed Pu(III,IV) state is possible. Since Pu(III) is assigned a slightly lower K_d interval than Pu(IV), this may be considered cautious with regard to model parameterisation. At later times during the temperate phase, reduced U(IV) speciation cannot be guaranteed and it is likely that U(VI) is predominant in parts of the repository environment. Owing to this uncertainty, both U(IV) and U(VI) cases have been propagated forward in the transport calculations. For times greater than 9,000 y in the temperate case, the trend to increasing carbonate concentration and decreasing Eh owing to infiltration of meteoric water may give more weakly reducing conditions, although this is principally an issue for U redox speciation.

Table 2-4. Recommended sorption partitioning coefficient, K_d values for use in SR-Site simulations of the Forsmark site. The predominant species for redox sensitive elements are highlighted in bold text. Values are given for the best estimate (median), parameters for the lognormal distribution (μ and σ), as well as lower and upper limits corresponding to the 2.5% and 97.5% percentiles, respectively.

Radionuclide (Redox State)	Best estimate K_d (m^3/kg)	$\log_{10}K_d$ – μ	$\log_{10}K_d$ – σ	Lower K_d limit (m^3/kg)	Upper K_d limit (m^3/kg)
Ac(III)	$1.48\cdot10^{-2}$	–1.83	0.72	$5.74\cdot10^{-4}$	$3.83\cdot10^{-1}$
Ag(I)	$3.49\cdot10^{-4}$	–3.46	0.51	$3.46\cdot10^{-5}$	$3.52\cdot10^{-3}$
Am(III)	$1.48\cdot10^{-2}$	–1.83	0.72	$5.74\cdot10^{-4}$	$3.83\cdot10^{-1}$
C, HCO_3^-	0.0	–	–	0.0	0.0
C, CH_4	0.0	–	–	0.0	0.0
C, $-CO_2H$	0.0	–	–	0.0	0.0
Cd(II)	$1.10\cdot10^{-3}$	–2.96	0.65	$5.97\cdot10^{-5}$	$2.04\cdot10^{-2}$
Cl(-I)	0.0	–	–	0.0	0.0
Cm(III)	$1.48\cdot10^{-2}$	–1.83	0.72	$5.74\cdot10^{-4}$	$3.83\cdot10^{-1}$
Cs(I)	$3.49\cdot10^{-4}$	–3.46	0.51	$3.46\cdot10^{-5}$	$3.52\cdot10^{-3}$
Eu(III)	$1.48\cdot10^{-2}$	–1.83	0.72	$5.74\cdot10^{-4}$	$3.83\cdot10^{-1}$
H(I)	0.0	–	–	0.0	0.0
Ho(III)	$1.48\cdot10^{-2}$	–1.83	0.72	$5.74\cdot10^{-4}$	$3.83\cdot10^{-1}$
I(-I)	0.0	–	–	0.0	0.0
Mo(VI)	0.0	–	–	0.0	0.0
Nb(V)	$1.98\cdot10^{-2}$	–1.70	0.64	$1.11\cdot10^{-3}$	$3.53\cdot10^{-1}$
Ni(II)	$1.10\cdot10^{-3}$	–2.96	0.65	$5.97\cdot10^{-5}$	$2.04\cdot10^{-2}$
Np(IV)	**$5.29\cdot10^{-2}$**	**–1.28**	**0.65**	**$2.84\cdot10^{-3}$**	**$9.84\cdot10^{-1}$**
Np(V)	$4.13\cdot10^{-4}$	–3.38	0.74	$1.48\cdot10^{-5}$	$1.15\cdot10^{-2}$
Pa(IV)	$5.92\cdot10^{-2}$	–1.23	0.48	$6.76\cdot10^{-3}$	$5.18\cdot10^{-1}$
Pa(V)	**$5.92\cdot10^{-2}$**	**–1.23**	**0.48**	**$6.76\cdot10^{-3}$**	**$5.18\cdot10^{-1}$**
Pb(II)	$2.52\cdot10^{-2}$	–1.60	0.56	$2.05\cdot10^{-3}$	$3.10\cdot10^{-1}$
Pd(II)	$5.20\cdot10^{-2}$	–1.28	0.83	$1.22\cdot10^{-3}$	2.21
Pu(III)	**$1.48\cdot10^{-2}$**	**–1.83**	**0.72**	**$5.74\cdot10^{-4}$**	**$3.83\cdot10^{-1}$**
Pu(IV)	$5.29\cdot10^{-2}$	–1.28	0.65	$2.84\cdot10^{-3}$	$9.84\cdot10^{-1}$
Pu(V)	$9.14\cdot10^{-3}$	–2.04	0.60	$6.19\cdot10^{-4}$	$1.35\cdot10^{-1}$
Pu(VI)	$9.14\cdot10^{-3}$	–2.04	0.60	$6.19\cdot10^{-4}$	$1.35\cdot10^{-1}$
Ra(II)	$2.42\cdot10^{-4}$	–3.62	0.41	$3.87\cdot10^{-5}$	$1.51\cdot10^{-3}$
S(-II)	0.0	–	–	0.0	0.0
Se(-II)	**$2.95\cdot10^{-4}$**	**–3.53**	**0.55**	**$2.50\cdot10^{-5}$**	**$3.48\cdot10^{-3}$**
Se(IV)	$2.95\cdot10^{-4}$	–3.53	0.55	$2.50\cdot10^{-5}$	$3.48\cdot10^{-3}$
Se(VI)	$2.95\cdot10^{-4}$	–3.53	0.55	$2.50\cdot10^{-5}$	$3.48\cdot10^{-3}$
Sm(III)	$1.48\cdot10^{-2}$	–1.83	0.72	$5.74\cdot10^{-4}$	$3.83\cdot10^{-1}$
Sn(IV)	$1.59\cdot10^{-1}$	–0.80	0.28	$4.51\cdot10^{-2}$	$5.58\cdot10^{-1}$
Sr(II)	$3.42\cdot10^{-6}$	–5.47	0.99	$3.84\cdot10^{-8}$	$3.05\cdot10^{-4}$
Tc(IV)	**$5.29\cdot10^{-2}$**	**–1.28**	**0.65**	**$2.84\cdot10^{-3}$**	**$9.84\cdot10^{-1}$**
Tc(VII)	0.0	–	–	0.0	0.0
Th(IV)	$5.29\cdot10^{-2}$	–1.28	0.65	$2.84\cdot10^{-3}$	$9.84\cdot10^{-1}$
U(IV)	**$5.29\cdot10^{-2}$**	**–1.28**	**0.65**	**$2.84\cdot10^{-3}$**	**$9.84\cdot10^{-1}$**
U(VI)	**$1.06\cdot10^{-4}$**	**–3.97**	**0.66**	**$5.53\cdot10^{-6}$**	**$2.05\cdot10^{-3}$**
Zr(IV)	$2.13\cdot10^{-2}$	–1.67	0.35	$4.48\cdot10^{-3}$	$1.02\cdot10^{-1}$

3 Conceptualisation of transport processes and conditions within SR-Site

The three hydrogeological models (semi-correlated, uncorrelated and fully correlated) described by /Joyce et al. 2010/ form the base for the calculations. The hydrogeological calculations are performed for different climate conditions. Temperate conditions at the time 2000 AD are assumed to provide adequate representations of near-field and far-field conditions at Forsmark for the purpose of estimating radionuclide release and transport. This approximation is relaxed in a few selected variant modelling cases to evaluate its adequacy.

The EFPC criterion has been applied for most of the calculation cases, i.e. canister positions intersected by fractures that also intersect the entire tunnel perimeter have been discarded. This means that those deposition holes have been filtered from the results of the transport calculations.

3.1 Selection of radionuclides

The selection of radionuclides is based on radiotoxicity, inventory, half-life and shared solubility. The selection is further described in Appendix D. Some of the selected, short-lived nuclides were omitted in cases where they would have decayed to insignificance at the time of the start of the calculation.

The following 23 fission and activation products were selected: Ag-108m, C-14, Cd-113m, Cl-36, Cs-135, Cs-137, Eu-152, H-3, Ho-166m, I-129, Mo-93, Nb-93m, Nb-94, Ni-59, Ni-63, Pd-107, Se-79, Sm-151, Sn-121m, Sn-126, Sr-90, Tc-99 and Zr-93.

The following 22 decay chain nuclides (ordered by chain) were selected: Pu-240, U-236, Th-232, Cm-245, Am-241, Np-237, U-233, Th-229, Cm-246, Am-242m, Pu-242, Pu-238, U-238, U-234, Th-230, Ra-226, Pb-210, Am-243, Pu-239, U-235, Pa-231 and Ac-227. Some nuclides with short half-lives in comparison to their progeny were only included by adding their initial inventory to that of their progen. This applies to e.g. Cm-244, Pu-241, Cm-243 and Pa-233.

3.2 Radionuclide release from the fuel

The following contributions to the outward transport from the fuel can be distinguished.

- The instantaneously accessible fraction of radionuclides, IRF, that is assumed to rapidly dissolve in the water void volume and be subsequently released from the canister. This gives rise to a pulse of uncertain duration, the uncertainty stemming from e.g. uncertainties in the detailed development of the canister failure through which the IRF is made accessible.
- A contribution from the corrosion of metal parts in the fuel assemblies and the congruent release of radionuclides embedded in the metal parts. These inventories are collectively called the corrosion release fraction, abbreviated CRF.
- A contribution from fuel dissolution and the congruent release of radionuclides embedded in the fuel matrix.
- Elemental solubilities as a limit for radionuclide release. If the solubility limit is reached, the concentration of the dissolved nuclide in the water does not increase further.

3.2.1 Release of instantaneous release fraction

As soon as a continuous water pathway has been formed the instant release fraction of the inventory dissolves in the water in the canister void.

In the corrosion scenario the IRF is assumed to rapidly dissolve and be subsequently flushed from the canister. Since these nuclides are in general non-sorbing and since the flow related retardation properties in the geosphere are poor for the flow paths associated with the deposition positions in question, they are generally released as pulses of durations of tens of years from the geosphere to the biosphere. The release of the IRF is calculated separately, see Section 4.1.3.

3.2.2 Release of activation products in metal parts

The inventory of activation products in the metal parts of the fuel assemblies has normally been assigned to the instantaneously accessible fraction (for example in SR-Can, SKB 2006a), since it has been considered unnecessary to develop a model for the metal parts as nuclides in these are dispersed during transport through the near field and far field. However, in the corrosion scenario this assumption would lead to unrealistically high peaks in the releases of e.g. Ni-59 and Nb-94. Therefore, corrosion of metal parts of the fuel assemblies is included in the near-field model, with corrosion rates given in the **Data report,** Section 3.2. The fraction of the inventory for which corrosion of metal parts determines the release rate is called the corrosion release fraction, CRF. The CRF is given in the **Data report**, Section 3.2, in the same manner as other fractions of the inventory.

3.3 Near-field transport and retention

After failure the canister is not assumed to provide any transport resistance except in the growing pinhole scenario.

There is no transport resistance at all in the near field in the corrosion scenario. The release is assumed to occur with the water flow in the deposition hole.

In all scenarios, but the corrosion scenario, the nuclides are sorbed with varying efficiency in the buffer and the diffusion and sorption properties determine the time for diffusion through the buffer to the rock at release path Q1, i.e. a fracture intersecting the deposition hole. In the shear load scenario the shear is assumed to increase the fracture transmissivity significantly. The Q_{eq} value for the intersecting fracture is, therefore, assumed to be sufficiently high that it does not contribute to the transport resistance in the near field. In the two hypothetical residual scenarios, isostatic load and growing pinhole, the limited flow in the fractures intersecting the deposition hole contributes to the transport resistance through the Q_{eq} value. Thermally induced spalling is assumed to have occurred in the wall of the deposition hole. This implies, that the transport resistance at the interface at Q1 is lower than if spalling is not included.

In the growing pinhole scenario two additional exits from the near field are included: an excavation damaged zone, EDZ, in the floor of the deposition tunnel (if such a zone is assumed to exist), Q2, and a fracture intersecting the deposition tunnel, Q3. The radionuclide transport is assumed to occur by diffusion in the buffer and backfill in the deposition hole and by diffusion and advection in the deposition tunnel. The nuclides are sorbed with varying efficiency in the buffer and backfill and the water flow, the diffusion and sorption properties in the backfill determine the time for diffusion through the buffer and backfill to the rock at release paths Q1, Q2 and Q3. The advective flow in the deposition tunnel and the boundary conditions for the near field at Q1, Q2 and Q3 are determined in the hydrogeological calculations. In the section describing the near-field model COMP23 (Section 3.6.1) more details are given and in Figure 3-1 the modelled system in the pinhole scenario including the three release paths Q1, Q2 and Q3 is shown. A detailed description of the discretisation, diffusion resistances and boundary conditions used in COMP23 in the different scenarios is given in Appendix G.

3.4 Geosphere transport and retention

In SR-Site, solute transport in the geosphere is conceptualised to occur by advective flow along discrete migration paths where retention is caused by matrix diffusion and equilibrium sorption on rock matrix microsurfaces /**Geosphere process report**/. For modelling purposes these processes are assumed to be reversible and linear thereby implying a Fickian formulation of matrix diffusion characterised by an effective diffusivity, D_e, that can vary spatially along a flowpath depending upon the local microstructural properties of the rock. The effective diffusivity of specific solutes in the rock depends upon the geometric structure and connectivity of the rock matrix porosity, which is conceptualised to consist of both microfractures and grain boundary porosity. The handling of effective diffusivity and data used in SR-Site are discussed in the **Data report**.

In a similar fashion, the sorptive properties of the rock are modelled based on the assumption of a constant linear partitioning coefficient, K_d, which also can vary spatially along a flowpath depending on the local mineralogy of the rock and porewater chemistry. The residence time distribution of a solute subject to advective transport and retardation by matrix diffusion and linear sorption is a function of the master variables D_e, K_d and the F-factor. In SR-Site, the diffusive mass transfer to the rock matrix is furthermore assumed to be one-dimensional and perpendicular to the advective flowpath along which the radionuclide is transported.

3.5 Biosphere representation

The biosphere is mainly represented by multiplying the radionuclide releases from the near field or from the geosphere by an appropriate dose conversion factor (LDF).

The so obtained doses, or, in the case of the near field, dose equivalent releases, are the main calculation end-points in the consequence calculations presented in this report. The conversion to dose is done to obtain a convenient measure of the impact of the releases, where also a total measure is obtained as the summed dose.

For the shear load scenario with early failure the use of LDF values overestimates the doses in this time perspective since i) the LDF is a pessimistic upper bound on releases occurring continuously over an entire interglacial period taking into account accumulation whereas a large part of the interglacial period has elapsed without any releases when the repository is sealed and ii) it is not meaningful to use the LDF concept for a radionuclide that decays to insignificance over an interglacial period, since the concept is based on a continuous releases over the period.

Basic Landscape Dose Conversion Factors (LDF)

The Basic Landscape Dose Conversion Factors, LDF, have been used for estimating doses for scenarios characterised by nearly constant release rates during a long-term period. The LDF values are therefore derived from simulations using constant unit release rates during the whole simulation period. LDF values are calculated for the different climate conditions, e.g. interglacial, periglacial, glacial and submerged. The used values are the maximum values (over time and objects) obtained from the transient modelling. For all radionuclide transport cases the values for interglacial conditions are used, except in the cases assessing influence of varying climate where also values for periglacial, glacial and submerged conditions are used. The highest doses from a constant release rate from the repository are expected under temperate conditions when humans are exposed to radionuclides that have accumulated in a wetland that has been converted to arable land, and when contaminated well water is utilised by human inhabitants and livestock. Hence, the LDFs for the interglacial period are the maximum values applicable during the reference glacial cycle. The interglacial period, i.e. the period from deglaciation to the onset of periglacial conditions, cf. Figure 4-35 in the **Climate report**, is represented by climate conditions similar to those of today and is, in accordance with the reference glacial cycle, assumed to prevail for 18,400 years (i.e. from –9000 to 9400 AD) and include both submerged and temperate conditions. The LDF values used include the influence of exposure from a well. The details of how the LDF values have been derived are given in the SR-Site **Main report**, Section 13.2 and in /Avila et al. 2010/. The interglacial-period LDF values used are given in Table 3-7; see the **Data report** for LDF values for other climate domains.

Dose Conversion Factors for pulse releases (LDF pulse)

In the corrosion scenario the instant release fraction, IRF, are generally released as pulses of durations of tens of years from the geosphere to the biosphere, see further 4.1.3. The basic LDF values (previous section) are not applicable for pulse releases, since the former are derived from simulations with a constant release rate during long-term periods, whereas pulse releases will, by definition, take place during a relatively short time period. Hence, the derivation of LDF pulse values has been done by performing simulations for a release of 1Bq to the landscape during a short time period. The duration of the release period has been varied from 1 to 1,000 years and simulations have been carried out for pulse releases occurring at different times within an interglacial period. Studies of the effect of the starting time of the releases and the duration of the pulse have shown very little influence of these factors in the derived Dose Conversion Factors. In Table 3-7 values of the LDF pulse are presented for those radionuclides that occur in pulse releases. The values are the maximum annual effective doses calculated for 1-year pulses released at 9000 BC, 3500 AD and 9400 AD.

Distributed LDF

There are also a few cases, calculated for illustrative purposes, see Section 6.2.3 and Section 6.5, where a large number of canisters are assumed to fail. In such cases, LDF values calculated for a release spread over the landscape objects according to the distribution of release locations over time during the modelled interglacial period are applied, rather than the basic LDF values where the landscape object yielding the highest dose is pessimistically used to represent the biosphere. These LDF values are referred to as distributed LDF.

Time dependent biosphere

In a few cases of relatively early releases, the basic LDF values would represent an overestimation of the dose consequences, again since a steady state release situation is far from established. In some of these cases, time dependent releases are transferred to the same biosphere model as used for the derivation of LDF values and a time dependent dose, taking into account both the temporal variation of the release and the development of the landscape, is obtained.

3.6 Models used

Calculations of radionuclide release and transport rely on three primary computer codes COMP23, FARF31 and MARFA. The codes are described in Section 3.6.1, 3.6.2 and 3.6.3, respectively. The codes are further described in the SR-Site **Model summary report**. In addition, all three codes require information derived from groundwater velocity fields calculated by the ConnectFlow code /Joyce et al. 2010/. A summary of the transport model chain is given in Section 3.6.4.

In addition to the numerical codes an analytical model for both near-field and far-field calculations is used. A short description of the model is given in Section 3.6.5 and a more detailed description is given in the SR-Site **Model summary report**.

3.6.1 COMP23

COMP23 /Romero 1995, Cliffe and Kelly 2006, Kelly and Cliffe 2006/ is a compartment code used for radionuclide migration calculations in the near field (the canister and the engineered systems). The code was initially developed as NUCTRAN /Romero 1995/ and was subsequently incorporated into the SKB safety assessment calculation framework Proper as the submodel COMP23. Proper is a collection of codes used for migration and consequence calculations through the near field, the far field and the biosphere and uses standardised methods to transfer data and results between the different submodels. In SR-Site, an implementation of the COMP23 model written in Matlab/Simulink is used for the near-field migration calculations. This implementation of COMP23 is also called Compulink /Vahlund and Hermansson 2006/.

COMP23 has been used by SKB in the SR 95 /SKB 1995/, the SR 97 /Lindgren and Lindström 1999, SKB 1999/, SR-Can interim /SKB 2004/ and the SR-Can /SKB 2006a/ assessments of a final repository of the KBS-3 type. A closely related code, NUCTRAN/NUCFLOW, (which originate from the same source but allows for multiple sources opposed to COMP23 which only handles single sources) was used in the SAFE assessment of the SFR repository for operational waste /Lindgren et al. 2001/.

COMP23 models processes related to radionuclide release and transport in the canister interior, the buffer and the deposition tunnel backfill. These incorporate the processes radioactive decay, metal corrosion (modelled as a constant metal corrosion rate), fuel dissolution, dissolution of gap inventory (modelled as an instantaneous release), speciation of radionuclides (i.e. dissolution/precipitation of nuclides with shared elemental solubilities), diffusion and sorption in the buffer and advection, diffusion and sorption in the deposition tunnel backfill. It also handles the release of radionuclides to different exit paths from the near field.

COMP23 is a multiple-path model that calculates transient nuclide transport in the near field of a repository by use of a network of coupled resistances and capacitances in analogy with an electrical circuit network. Analytical solutions, instead of fine discretisation, at sensitive zones, for example at the exit point of a small canister hole and at the entrance to fractures, are embedded to enhance calculation speed.

Figure 3-1 shows the canister, deposition hole and the deposition tunnel backfill and how these are modelled by COMP23 in the growing pinhole scenario. Three exits from the near field are included: a fracture intersecting the deposition hole at the vertical position of the canister lid, denoted Q1, an excavation damaged zone, EDZ, in the floor of the deposition tunnel (if such a zone is assumed to exist), Q2, and a fracture intersecting the deposition tunnel, Q3. In the hydrogeological modelling, the number of fractures intersecting a deposition hole and the properties of these fractures are determined statistically based on the DFN description of the rock. If more than one fracture intersects a deposition hole, the transport capacity of the several fractures are added and pessimistically assigned to the single fracture, Q1, modelled by COMP23. The equivalent flow rate through Q2 is also calculated as an integral part of the hydrogeological modelling. The flow rate in the deposition tunnel and the distance to the nearest Q3 fracture through which radionuclides are released to the geosphere from the tunnel are given by the hydrogeological modelling. Transport by advection and diffusion in the tunnel is included in the near-field simulations and the computational domain is extended in the downstream direction to include the Q3 fracture. All needed results from the hydrogeological modelling are transferred to COMP23 through the ptb-files from ConnectFlow.

Effects of spalling in deposition holes are treated by a modification of the equivalent flow rates for the transport path Q1, see Appendix G.

Advective conditions in the buffer, as in the corrosion scenario, are simply treated by equating the outflux from the canister interior compartment with the release to Q1. The release paths Q2 and Q3 are not modelled when advective conditions are assumed in the buffer since releases to Q1 completely dominate over those to Q2 and Q3 for such cases.

Further details of the discretisation, diffusion resistances and boundary conditions used in the different scenarios are described in Appendix G.

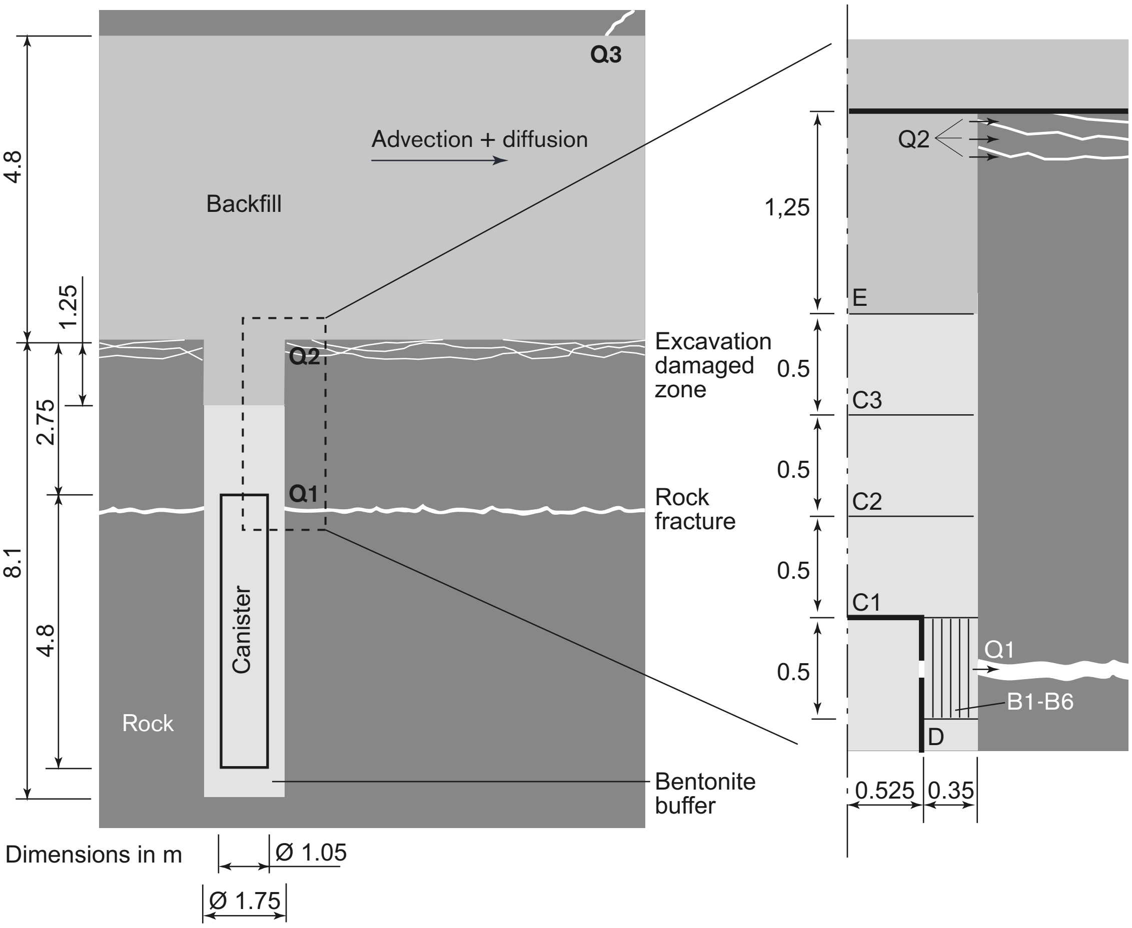

Figure 3-1. COMP23 model, for the growing pinhole scenario, with details of its model representation as compartments B1–B6, C1–C3, D and E. The transport paths Q1, Q2 and Q3 to a fracture intersecting the deposition hole, to the excavation damaged zone, and to a fracture intersecting the deposition tunnel, respectively, are also shown.

3.6.2 FARF31

FARF31 /Norman and Kjellbert 1990, Lindgren et al. 2002, Elert et al. 2004/ is a code used for radionuclide migration calculations in the far field, i.e. the geosphere.

FARF31 has been employed already in earlier assessments, e.g. SR 97 /Lindgren and Lindström 1999/ and SR-Can /SKB 2006a/.

FARF31 is based on a model with a one-dimensional advection-dispersion equation along a, possibly curved, stream tube coupled to a pure diffusion equation in the direction perpendicular to the centroid of the stream tube, for a number of radionuclides. Chain decay and in-growth are included in the model. The concept of a stream tube can be compared to the combined effect of a large number of individual fractures all sharing the same inlet and outlet.

The governing equations are solved in the Laplace domain using the advective travel time in the longitudinal direction as the independent variable to obtain a unit response function, which is subsequently convoluted with the input function to obtain the output function. A detailed description of the solution method can be found in /Norman and Kjellbert 1990/.

It is noted that the equations are expressed in terms of accumulated travel time rather than distance along the flow path. This feature makes it easy to calculate travel times in a stand-alone groundwater flow model, and subsequently radionuclide transport in a decoupled fashion.

FARF31 was originally developed to be used with a groundwater flow model adopting a continuum representation of the rock. In SR-Site, groundwater flow is primarily modelled through a discrete fracture network (DFN) where individual fractures are represented explicitly. Here, the conceptualisation of a migration path is slightly different than in a continuum-based groundwater flow model. Rather than macroscopic stream-tubes encompassing both rock and flow paths, the equation now describes flow paths through the actual open pore space, i.e., through the connected fracture network. However, the governing equations are identical for the two conceptualisations. The entities calculated in the DFN-based groundwater flow models are the advective travel time (t_w) and flow-related transport resistance (F) along flow paths.

3.6.3 MARFA

The computer code MARFA /Painter and Mancillas 2009/ uses a particle-based Monte Carlo method to simulate the transport of radionuclides in fractured or unfractured geologic media. MARFA was specifically designed to integrate with the safety assessment workflow used by SKB. Version 3.2.2 and earlier versions accept pathline trajectories from the ConnectFlow code /Serco 2008/ in the form of ConnectFlow ptv-files. The pathline trajectories represent transport pathways. MARFA then solves radionuclide transport along the pathways using a time-domain particle method. With this method, particles are advanced along a pathway using deterministic spatial displacements and random transit times for each step. Testing and experience with the code demonstrate that the code is computationally efficient and extremely robust. Limited and unlimited matrix diffusion, equilibrium sorption, longitudinal dispersion, decay, and in-growth are represented. MARFA supports full spatial variability for all pathway properties, decay chains of any length, and full temporal variability in radionuclide source strength. The code reports radionuclide release rates (breakthrough) at the pathway endpoints.

Validation tests for MARFA are described in the MARFA Version 3.2.2 User's Manual /Painter and Mancillas 2009/. Additional comparisons between MARFA and FARF31 were also undertaken to provide further confidence in the MARFA results for SR-Site parameter ranges (Appendix C).

Note that in a stochastic framework with multiple realisations, COMP23 and FARF31 must be executed once for each realisation, but MARFA need to be run only once with parameters for all pathway realisations as input. With multiple pathway realisations, MARFA calculates an ensemble mean breakthrough. The Monte Carlo nature of the algorithm ensures that an unbiased statistical estimate of the ensemble mean is obtained even when too few particles are used to accurately calculate breakthrough for each pathway realisation. Moreover, the statistical uncertainty in the ensemble mean is greatly reduced relative to that of individual realisations, a property of the method with significant advantages in terms of computational efficiency.

3.6.4 Summary of the transport model chain

Model linkages and data flows differ somewhat depending on whether far-field transport is modelled with MARFA or FARF31. Data flows and model linkages for FARF31 and MARFA are shown in Figure 3-2 and Figure 3-3, respectively.

FARF31, with its integrated description of the transport pathway, requires only global information about each pathway from ConnectFlow. The required information – the flow-related transport resistance factor F and advective travel time t_w along each pathway – is contained in ConnectFlow ptb-files. The ptb-files also contain the third component of the so-called flow triplets, the equivalent flow rate Q_{eq} at the canister. Q_{eq} is required by COMP23.

MARFA accommodates a spatially resolved (segmented) description of the transport pathway and thus accepts ConnectFlow ptv-files, which contain F and t_w parameters and a rocktype descriptor for each segment in each segmented pathway.

MARFA and FARF31 both calculate radionuclide release rates in terms of moles of radionuclides per time per each realisation. These release rates are then converted to effective doses by simply multiplying with the Dose Conversion Factors (LDFs) and averaged to get mean annual releases. A description of the work done for developing the LDFs is provided in /Avila et al. 2010/.

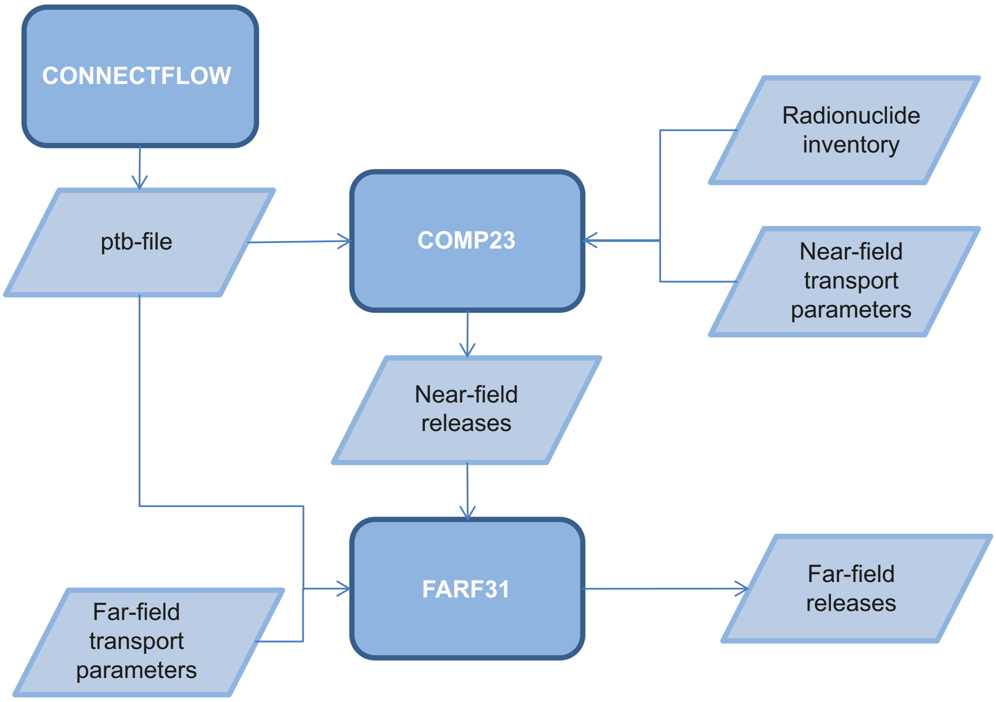

Figure 3-2. *Model linkages and data flows for radionuclide transport simulations using FARF31.*

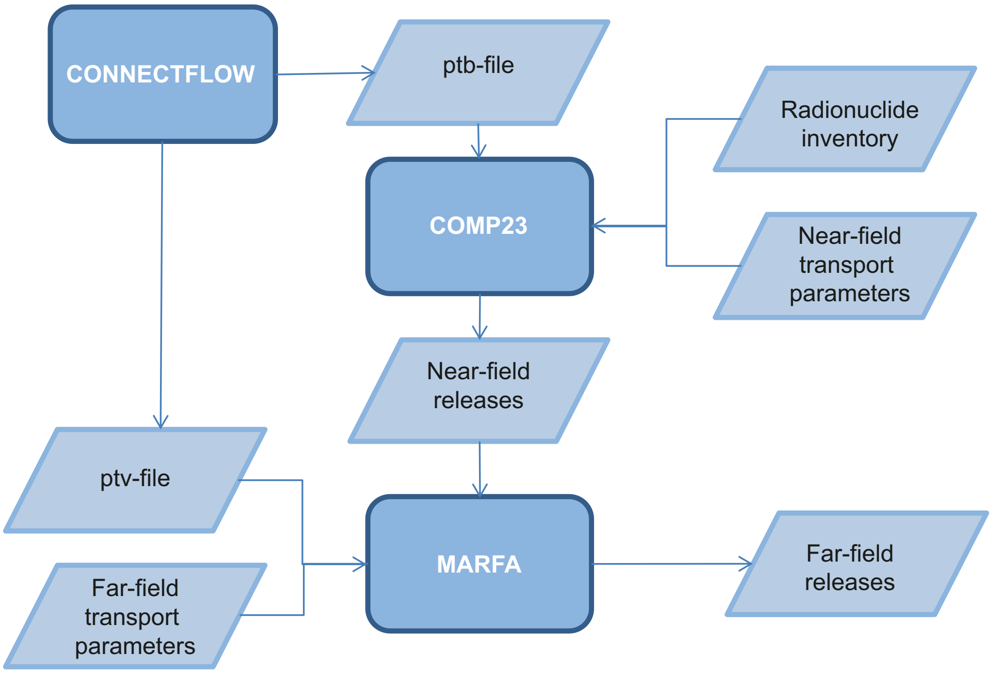

Figure 3-3. *Model linkages and data flows for radionuclide transport simulations using MARFA.*

The potential role of bentonite colloids in facilitating transport of certain radionuclides is addressed in variant modelling cases using MARFA. For those variants, the data flow shown in Figure 3-3 is modified slightly. Specifically, in the colloid-facilitated transport variant, the output of COMP23 is further processed to partition radionuclides between colloid-associated and dissolved states. The model for that partitioning process is described later in this report. The implementation of the partitioning model is not through compiled software but relies on Mathematica™ scripts.

3.6.5 Analytical models

Analytical simplified versions of the near-field and far-field transport models have been developed /Hedin 2002b/. These models use the same input data as the corresponding numerical models and doses are calculated using the same LDF values as in the numerical approach. The models may be executed probabilistically and yield results in good agreement with the deterministic and probabilistic calculation cases in the SR 97 assessment /Hedin 2002b, SKB 2004/. In the SR-Can assessment they were shown to be in good agreement for the corrosion scenario, for the shear load scenario and for releases from a pinhole failure of the canister /SKB 2006a/. A single realisation with the analytical models executes in around 0.1 second on a 2 GHz Personal Computer, making them well suited for probabilistic calculations. The corresponding calculation time for the numerical models is of the order of 10 seconds.

The analytical models have been benchmarked against the numerical models for several calculation cases in this report. The roles of the analytical models are to i) quickly and preliminarily evaluate calculation cases to be used in the planning of the transport calculations, ii) serve as one of several quality assurance measures of the numerical calculations by identifying potential differences in results obtained with the analytical and numerical models and seeking explanations for these (are they due to modelling errors or to differences in the nature of the models?), and iii) demonstrating an understanding of the nature of the models facilitated by the simple nature of the analytic models.

3.6.6 Input data to the transport models

Detailed discussions of data sources and data qualification methods can be found in the **Data report**. Unless otherwise noted, parameters required in the radionuclide transport calculations presented in this **Radionuclide transport report** are taken from the **Data report**. Specific sections of the **Data report** relevant to radionuclide transport calculations are as follows: parameters required to model spent fuel mobilisation are discussed in Chapter 3; buffer and backfill data required to model radionuclide migration in the near field are described in Section 5.3; flow related and non-flow related migration properties are found in Section 6.7 and 6.8, respectively; landscape dose factors are discussed in Section 7.2. Additional discussions of parameters and parameter summaries are also provided in this report, as needed, to facilitate a self-contained reading.

For some modelling cases, input parameters are required that are outside the scope of the **Data report**. Input parameters required for those cases are documented here. The specific parameters are colloid concentrations for modelling cases that consider colloid-facilitated transport (Sections 4.5.6 and 4.5.8) and flow scaling factors for cases that considered the effects of unsteady flow (Sections 4.5.7 and 4.5.8). In addition, one set of modelling cases (Section 6.4) that used a hypothetical residual scenario to illustrate certain barrier functions of the geosphere was completed before SR-Site data were finalised. Assumed parameters for those modelling cases are summarised in Appendix H.

3.7 Summary of all data used

Hydrogeological data related to flow and transport, obtained from the modelling reported in /Joyce et al. 2010/ are transferred to the calculations through the ptb/ptv-files. Three fracture size/transmissivity correlation functions are considered yielding three variants of the hydrogeological DFN model. Several cases/realisations are available for each variant of the hydrogeological model, see Table 3-1. The ptb-files and ptv-files are archived at SKB, see Table 3-8. All hydrogeological cases used in the radionuclide release calculations are for the time 2000 AD.

Almost all data are qualified in the SR-Site **Data report** and therefore is only a short summary of the input given in this section. Table 3-2 gives a summary of the data used.

The numerical dose estimates are dependent on the radionuclide inventory assumed. Sensitivity to the assumed inventory and implications of using an average inventory in the calculations are discussed in detail in Appendix E. The inventories for most nuclides that contribute significantly to dose vary by less than a factor of 1.5. The exception is Ag-108m, which has negligible inventory in BWR canisters and a PWR inventory that is a factor of 4 higher than the assumed average. However, Ag-108m contributes significantly to the total dose only in the shear failure case with early failure and in hypothetical cases used to illustrate barrier function. Most of the dose-contributing radionuclides are single radionuclides and hence the doses are directly scaled to the inventories. Although the dose from Ra-226 is dependent of the inventories of its precursor radionuclides, U-238, Pu-238, U-234 and Th-230, none of those radionuclides differ more than a factor of two between different canisters.

Table 3-1. Hydogeological realisations used in the radionuclide transport calculations /Joyce et al. 2010/.

Hydrogeological DFN model	Realisations
Semi-correlated model	Base case and 10 additional realisations at 2000 AD
	Crown space
	No EDZ
	EDZ with transmissivity of 10^{-7} m^2/s
	EDZ with transmissivity of 10^{-6} m^2/s
Uncorrelated model	Base case and 5 additional realisations
Fully correlated model	Base case and 5 additional realisations

Table 3-2. Input data for the probabilistic calculations for the corrosion, shear load, isostatic load and pinhole scenarios.

Parameter name	Parameter	Unit	Data	NF/FF	Data report section and symbol
HALFLIFE	Half-life	yr	Constants	NF/FF	3.1 $t_{½}$
FPC, EFPC	Criteria for exclusion of deposition holes		Corrosion: Used to select deposition holes, given in ptb-files Shear load: Not used Isostatic load: same as corrosion Pinhole: same as corrosion	NF/FF	
Near-field geometry			See Appendix G, Table G-1	NF	
Number of failed canisters			See each case	NF	
INVENTORY	Radionuclide inventory	mol	Constant. Data for average canister calculated from all fuel assemblies	NF	3.1
FDMC	Fuel conversion time	yr	Log-triangular (10^6, 10^7,10^8 yr)	NF	3.3
IRF	Instant release fraction of inventory	–	Data for average canister. Normal distributions for Cl, Cs, I, Se. Triangular distributions for Sr, Ni, Nb, Mo Tc, Pd, Sn. 100% for H, Ag. Single value for Cd	NF	3.2 *IRF*
CRF	Corrosion release fraction of inventory	–	Data for average canister. Double triangular distributions for C, Cl, Ni, Se, Mo, Zr, Tc, Sn-121m, U-233. 100% for Nb-94. Single value for Nb-93m	NF	3.2 *CRF*
TCORR	Corrosion time	yr	Log-triangular (10^2, 10^3, 10^4 yr)	NF	3.2 t_{corr}
TFAILURE	Time for failure	yr	Corrosion: As calculated with the corrosion model, see each case. Shear load: See each case Isostatic load: 10,000 years and 100,000 years (postulated) Pinhole: Initial failure (postulated)	NF	
TDELAY	Delay time for onset of radionuclide transport*	yr	Corrosion: 0 years Shear load: 100 years Isostatic load: 0 years Pinhole: 1,000 years	NF	4.2 t_{delay}
TLARGE	Time for large canister defect	yr	Corrosion: Same as time for failure Shear load: Same as time for failure Isostatic load: Same as time for failure Pinhole: 10,000 yr (postulated)	NF	4.2 t_{large}
ADELAY, ALARGE	Canister defect sizes	m	Corrosion: Unlimited at the time for failure Shear load: Unlimited at the time for failure Isostatic load: Unlimited at the time for failure Pinhole: Between onset and TLARGE: 2 mm radius penetrating pinhole. After TLARGE: Unlimited.	NF	4.2 r_{defect}
CSOL	Solubility limits	mol/m³	Calculated distributions based on distributions of several groundwater compositions, see Appendix F Corrosion: Not used (except in one alternative case “including solubility limits in the near field”) Shear load: Calculated distributions Isostatic load: Calculated distributions Pinhole: Calculated distributions	NF	3.4
KDB	Buffer sorption partitioning coefficients	m³/kg	Corrosion: Not used Shear load: Log triangular distributions Isostatic load: Log triangular distributions Pinhole: Log triangular distributions	NF	5.3 K_d
DEB	Buffer effective diffusivities	m²/s	Corrosion: Not used Shear load: Distributions Isostatic load: Distributions Pinhole: Distributions	NF	5.3 D_e
EPSB	Buffer porosities (diffusion available porosity)	–	Corrosion: Not used Shear load: Anions: Triangular (0.13, 0.18, 0.24) Minor changes in Data report; Cations: Triangular (0.43, 0.44, 0.47) Minor changes in Data report Isostatic load: same as shear load Pinhole: same as shear load	NF	5.3 ε

RHO for material 2	Buffer density (density of the solid particles)	kg/m^3	Corrosion: Not used Shear load: Constant = 2,780 kg/m^3 Isostatic load: Constant = 2,780 kg/m^3 Pinhole: Constant = 2,780 kg/m^3	NF	5.1 ρ_s
KDBF	Backfill sorption partitioning coefficients	m^3/kg	Corrosion: Not used Shear load: Not used Isostatic load: Log triangular distributions Pinhole: Log triangular distributions	NF	5.3 K_d
DEBF	Backfill effective diffusivities	m^2/s	Corrosion: Not used Shear load: Log triangular distributions Isostatic load: Log triangular distributions Pinhole: Log triangular distributions	NF	5.3 D_e
EPSBF	Backfill porosity (diffusion available porosity)	–	Corrosion: Not used Shear load: Anions: triangular (0.13, 0.18, 0.26) Cations: triangular (0.44, 0.46, 0.48) Isostatic load: same as shear load Pinhole: same as shear load	NF	5.3 ε
RHO for material 3	Backfill density (density of the solid particles)	kg/m^3	Corrosion: Not used Shear load: Constant = 2,780 kg/m^3 Isostatic load: Constant = 2,780 kg/m^3 Pinhole: Constant = 2,780 kg/m^3	NF	5.1 ρ_s
QEQ_1	Equivalent flow from deposition hole to fracture(s) intersecting deposition hole	m^3/yr	Corrosion: Not used Shear load: 1 m^3/yr Isostatic load: given in ptb-files (QEQ) Pinhole: given in ptb-files (QEQ)	NF	6.7 Q_{eq1}
QEQ_2	Equivalent flow to EDZ	m^3/yr	Corrosion: Not used Shear load: Not used Isostatic load: given in ptb-files (QEQ) Pinhole: given in ptb-files (QEQ)	NF	6.7 Q_{eq2}
QEQ_3	Equivalent flow to fractures intersecting deposition tunnel	m^3/yr	Corrosion: Not used Shear load: Not used Isostatic load: given in ptb-files (QEQR) Pinhole: given in ptb-files (QEQR)	NF	6.7 Q_{eq3}
LR_TUN_3	Path length to the first fracture in tunnel	m	Corrosion: Not used Shear load: Not used Isostatic load: given in ptb-files (LR_TUN) Pinhole: given in ptb-files (LR_TUN)	NF	
TRAPP_3* LR_TUN_3/ TR_TUN_3	Darcy flux in the deposition tunnel (Porosity*Path length/travel time)	m/yr	Corrosion: Not used Shear load: Not used Isostatic load: Calculated from porosity (TRAPP), path length (LR_TUN) and travel time (TR_TUN) given in ptb-files Pinhole: same as Isostatic load	NF	
U0_1	Darcy flux at deposition hole	m^3/m^2,yr	Corrosion: Used to calculate the flow in the deposition hole, given in ptb-files (U0) Shear load: Not used Isostatic load: Used for spalling, given in ptb-files (U0) Pinhole: Used for spalling, given in ptb-files (U0)	NF	6.7 *q/U0*
FLEN	Length of largest fracture intersecting deposition hole	m	Corrosion: Not used Shear load: Not used Isostatic load: Used for spalling, given in ptb-files (FLEN) Pinhole: Used for spalling, given in ptb-files (FLEN)	NF	
Wzone	Width of spalling zone	m	Corrosion: Not used Shear load: Not used Isostatic load: Used for spalling, Constant = 0.5 m Pinhole: Used for spalling, Constant = 0.5 m	NF	6.5 W_{zone}
Lzone	Length of spalling zone	m	Corrosion: Not used Shear load: Not used Isostatic load: Used for spalling, Constant = 8 m Pinhole: Used for spalling, Constant = 8 m	NF	6.5 L_{zone}
dzone	Thickness of spalling zone	m	Corrosion: Not used Shear load: Not used Isostatic load: Used for spalling, Constant = 0.1 m Pinhole: Used for spalling, Constant = 0.1 m	NF	6.5 d_{zone}

epszone	Porosity of spalling zone	–	Corrosion: Not used Shear load: Not used Isostatic load: Used for spalling, Constant = 0.02 Pinhole: Used for spalling, Constant = 0.02	NF	6.5 ε_{zone}
Dp	Diffusion coefficient in spalling zone (damaged zone)	m^2/s	Corrosion: Not used Shear load: Not used Isostatic load: Used for spalling, Constant = 10^{-11} m^2/s. Calculated from $Dp=Dw/\tau^2$ according to /Neretnieks et al. 2010/. τ is given in the Data report. Pinhole: same as isostatic load	NF	6.5
RHO for material 1	Water density	kg/m^3	Constant = 1,000 kg/m^3	NF	
Dw	Diffusivity in water	m^2/s	Corrosion: Not used Shear load: Not used Isostatic load: Constant = 10^{-9} m^2/s. Used for calculation of the diffusivity in spalling zone Pinhole: Constant = 10^{-9} m^2/s. Used for calculation of the resistance in the hole in the pinhole scenario and for calculation of the diffusivity in spalling zone	NF	6.8 D_w
KDR	Rock sorption partitioning coefficients	m^3/kg	Corrosion: Truncated log-normal distributions Shear load: Not used Isostatic load: Truncated log-normal distributions Pinhole: Truncated log-normal distributions	FF	6.8 K_d
DER	Rock effective diffusivities	m^2/s	Corrosion: Log normal distributions, mean values anions: $2.1\cdot10^{-7}$ m^2/yr, cations: $6.6\cdot10^{-7}$ m^2/yr Shear load: Not used Isostatic load: same as corrosion Pinhole: same as corrosion	FF	6.8 D_e
EPSR	Rock porosities (diffusion available porosity)	–	Corrosion: Constant = 0.0018 Shear load: Not used Isostatic load: Constant = 0.0018 Pinhole: Constant = 0.0018	FF	6.8 ε
	Rock density (solid density)	kg/m^3	Corrosion: Constant = 2,700 kg/m^3 Shear load: Not used Isostatic load: Constant = 2,700 kg/m^3 Pinhole: Constant = 2,700 kg/m^3	FF	6.4 ρ
F_1, F_2, F_3	Rock transport resistance for paths beginning at Q1, Q2 and Q3	yr/m	Corrosion: given in ptb-files (F) Shear load: Not used Isostatic load: given in ptb-files (F) Pinhole: given in ptb-files (F)	FF	6.7 F
TW_1, TW_2, TW_3	Rock advective travel time for paths beginning at Q1, Q2 and Q3	yr	Corrosion: given in ptb-files (TW) Shear load: Not used Isostatic load: given in ptb-files (TW) Pinhole: given in ptb-files (TW)	FF	6.7 t_w
PE	Rock Peclet number	–	Corrosion: Constant = 10 Shear load: Not used Isostatic load: Constant = 10 Pinhole: Constant = 10	FF	6.7 Pe
DPEN	Max. penetration depth in rock matrix	m	Corrosion: Constant = 12.5 Shear load: Not used Isostatic load: Constant = 12.5 Pinhole: Constant = 12.5	FF	6.7 L_D
LDF	Biosphere LDF factors	Sv/y per Bq/y	Constant. Calculated LDF values, see Table 3-7.	FF	7.2 LDF
KDC	Colloid sorption coefficients	m^3/kg	Corrosion: Only used in calculations including colloids Buffer sorption coefficients, KDB, are used Shear load: Not used Isostatic load: Not used Pinhole: Not used	FF	
	Concentration of suspended colloids	kg/m^3	Corrosion: Only used in calculations including colloids 10 mg/litre and 10 g/litre Shear load: Not used Isostatic load: Not used Pinhole: Not used	FF	

* Time between canister failure and the establishment of a continuous water pathway from the fuel to the exterior of the canister.

3.7.1 Probabilistic input data

The software @risk (the risk analysis add-in for excel, version 5.0.1, Palisade Corporation) was used to generate input data to the transport calculations when the **Data report** recommended a distribution. Also correlations recommended in the Data report were used. In all simulations Latin hypercube was used as the sampling type and 6,916 iterations were run. Each data table from the **Data report** was analysed separately with @risk. The simulation results were transferred to Matlab files (.mat files) and these files were always used as input to COMP23 and FARF31. Each line number in the .mat files forms a unique set of input data for a single calculation and in this section it is called a realisation.

The variants of the corrosion case, including cases addressing best available technique (BAT), had different numbers of realisations depending on how many possible failure times the case was holding. Each failure time was iterated 50 times (see Section 4.4.4 about convergence) so the total number of realisations in each case was the number of failure times multiplied by 50. The input files containing 6,916 realisations were always used starting from realisation 1 in the input file and ending at the realisation number. For corrosion variants with less than 6,916 realisations the procedure is not fully consistent with Latin hypercube sampling, i.e. the advantage of the Latin hypercube is not fully used. However, this is not expected to create any biases. In a few corrosion variants, the number of realisations was greater than 6,916 and in these calculations the input datasets were re-run from the beginning as many times as needed to calculate up to the realisation number in demand. Again, this procedure is not fully consistent with Latin hypercube sampling but is not expected to create biases in the results.

All variants of the shear load cases were run with exactly 6,916 realisations except for the case with a failure at 100,000 years, which was run with 1,000 realisations. This case had an input data set with 1,000 simulations sampled by Latin hypercube.

All variants of the isostatic load case and the pinhole cases were run with exactly 6,916 realisations, i.e. the optimal spread of data sampled by Latin hypercube is used.

3.7.2 Deterministic input data

The deterministic input data set consists of median values from the probabilistic input data sets of 6,916 iterations, see Table 3-3 and Table 3-4. All variables were the same in all different calculation cases except for the transport parameters (U0, QEQ, FLEN, TW, F, TRAPP, LR_TUN and TR_TUN). These parameters change with the hydrogeological case for the shear cases, the isostatic load cases and the pinhole cases. The semi-correlated base case is used for the shear load, isostatic load, the base case and the no spalling case of the pinhole scenario. The rest of the pinhole cases had specific hydrogeological cases.

Near-field transport parameters are median values after excluding the special cases of OKFLAG=1, FPC>0 and EFPC>4, see Table 3-5. The only exception is in the shear load scenario where QEQ always is assumed to be high and set to 1 m^3/yr both in the probabilistic and deterministic calculations. OKFLAG=1 represents paths where the particle failed to start due to no fracture or low velocity. Excluding FPC>0 means that deposition holes are excluded due to background fractures or deformation zone fractures. Excluding EFPC>4 means that canister positions intersected by fractures that also intersect the entire tunnel perimeter have been discarded.

The far-field transport parameters are median values after excluding OKFLAG=1, 2, 3 and 4, FPC>0 and EFPC>4, see Table 3-6. OKFLAG 2, 3, 4 indicates that the particle tracing in the hydrogeological calculations failed to compleate.

For the corrosion scenario the transport parameters change with the hydrogeological case and the results from the erosion/corrosion model and the parameters used in the deterministic calculations are always those connected to the earliest failure time, see Section 4.3.

The LDF-values used for both deterministic and probabilistic calculations are given in Table 3-7.

Table 3-3. Median values of D_e, K_d and ε used in the deterministic near-field and far-field calculations. ε rock is not in the table since it is constant, $1.80\cdot10^{-3}$ (–), for all nuclides.

	D_e buffer (m^2/yr)	D_e backfill (m^2/yr)	D_e rock (m^2/yr)	K_d buffer (m^3/kg)	K_d backfill (m^3/kg)	K_d rock (m^3/kg)	ε buffer (–)	ε backfill (–)
Ac-227	$4.20\cdot10^{-3}$	$5.00\cdot10^{-3}$	$6.30\cdot10^{-7}$	5.20	5.20	$1.5\cdot10^{-2}$	0.45	0.46
Ag-108m	$4.20\cdot10^{-3}$	$5.00\cdot10^{-3}$	$6.30\cdot10^{-7}$	0.00	0.00	$3.5\cdot10^{-4}$	0.45	0.46
Am-241	$4.20\cdot10^{-3}$	$5.00\cdot10^{-3}$	$6.30\cdot10^{-7}$	$2.50\cdot10^{1}$	$2.50\cdot10^{1}$	$1.5\cdot10^{-2}$	0.45	0.46
Am-242m	$4.20\cdot10^{-3}$	$5.00\cdot10^{-3}$	$6.30\cdot10^{-7}$	$2.50\cdot10^{1}$	$2.50\cdot10^{1}$	$1.5\cdot10^{-2}$	0.45	0.46
Am-243	$4.20\cdot10^{-3}$	$5.00\cdot10^{-3}$	$6.30\cdot10^{-7}$	$2.50\cdot10^{1}$	$2.50\cdot10^{1}$	$1.5\cdot10^{-2}$	0.45	0.46
C-14	$4.20\cdot10^{-3}$	$5.00\cdot10^{-3}$	$6.30\cdot10^{-7}$	0.00	0.00	0.0	0.45	0.46
Cd-113m	$4.20\cdot10^{-3}$	$5.00\cdot10^{-3}$	$6.30\cdot10^{-7}$	$6.60\cdot10^{-2}$	$6.60\cdot10^{-2}$	$1.1\cdot10^{-3}$	0.45	0.46
Cl-36	$2.50\cdot10^{-4}$	$3.10\cdot10^{-4}$	$2.00\cdot10^{-7}$	0.00	0.00	0.0	0.18	0.19
Cm-245	$4.20\cdot10^{-3}$	$5.00\cdot10^{-3}$	$6.30\cdot10^{-7}$	$2.50\cdot10^{1}$	$2.50\cdot10^{1}$	$1.5\cdot10^{-2}$	0.45	0.46
Cm-246	$4.20\cdot10^{-3}$	$5.00\cdot10^{-3}$	$6.30\cdot10^{-7}$	$2.50\cdot10^{1}$	$2.50\cdot10^{1}$	$1.5\cdot10^{-2}$	0.45	0.46
Cs-135	$8.40\cdot10^{-3}$	$9.90\cdot10^{-3}$	$6.30\cdot10^{-7}$	$3.10\cdot10^{-2}$	$3.10\cdot10^{-2}$	$3.5\cdot10^{-4}$	0.45	0.46
Cs-137	$8.40\cdot10^{-3}$	$9.90\cdot10^{-3}$	$6.30\cdot10^{-7}$	$3.10\cdot10^{-2}$	$3.10\cdot10^{-2}$	$3.5\cdot10^{-4}$	0.45	0.46
Eu-152	$4.20\cdot10^{-3}$	$5.00\cdot10^{-3}$	$6.30\cdot10^{-7}$	5.20	5.20	$1.5\cdot10^{-2}$	0.45	0.46
H-3	$4.20\cdot10^{-3}$	$5.00\cdot10^{-3}$	$6.30\cdot10^{-7}$	0.00	0.00	0.0	0.45	0.46
Ho-166m	$4.20\cdot10^{-3}$	$5.00\cdot10^{-3}$	$6.30\cdot10^{-7}$	5.20	5.20	$1.5\cdot10^{-2}$	0.45	0.46
I-129	$2.50\cdot10^{-4}$	$3.10\cdot10^{-4}$	$2.00\cdot10^{-7}$	0.00	0.00	0.0	0.18	0.19
Mo-93	$2.50\cdot10^{-4}$	$3.10\cdot10^{-4}$	$2.00\cdot10^{-7}$	0.00	0.00	0.0	0.18	0.19
Nb-93m	$4.20\cdot10^{-3}$	$5.00\cdot10^{-3}$	$6.30\cdot10^{-7}$	3.10	3.10	$2.0\cdot10^{-2}$	0.45	0.46
Nb-94	$4.20\cdot10^{-3}$	$5.00\cdot10^{-3}$	$6.30\cdot10^{-7}$	3.10	3.10	$2.0\cdot10^{-2}$	0.45	0.46
Ni-59	$4.20\cdot10^{-3}$	$5.00\cdot10^{-3}$	$6.30\cdot10^{-7}$	$6.60\cdot10^{-2}$	$6.60\cdot10^{-2}$	$1.1\cdot10^{-3}$	0.45	0.46
Ni-63	$4.20\cdot10^{-3}$	$5.00\cdot10^{-3}$	$6.30\cdot10^{-7}$	$6.60\cdot10^{-2}$	$6.60\cdot10^{-2}$	$1.1\cdot10^{-3}$	0.45	0.46
Np-237	$4.20\cdot10^{-3}$	$5.00\cdot10^{-3}$	$6.30\cdot10^{-7}$	$3.90\cdot10^{1}$	$3.90\cdot10^{1}$	$5.3\cdot10^{-2}$	0.45	0.46
Pa-231	$4.20\cdot10^{-3}$	$5.00\cdot10^{-3}$	$6.30\cdot10^{-7}$	3.10	3.10	$5.9\cdot10^{-2}$	0.45	0.46
Pb-210	$4.20\cdot10^{-3}$	$5.00\cdot10^{-3}$	$6.30\cdot10^{-7}$	$4.90\cdot10^{1}$	$4.90\cdot10^{1}$	$2.5\cdot10^{-2}$	0.45	0.46
Pd-107	$4.20\cdot10^{-3}$	$5.00\cdot10^{-3}$	$6.30\cdot10^{-7}$	5.10	5.10	$5.2\cdot10^{-2}$	0.45	0.46
Pu-238	$4.20\cdot10^{-3}$	$5.00\cdot10^{-3}$	$6.30\cdot10^{-7}$	$3.90\cdot10^{1}$	$3.90\cdot10^{1}$	$1.5\cdot10^{-2}$	0.45	0.46
Pu-239	$4.20\cdot10^{-3}$	$5.00\cdot10^{-3}$	$6.30\cdot10^{-7}$	$3.90\cdot10^{1}$	$3.90\cdot10^{1}$	$1.5\cdot10^{-2}$	0.45	0.46
Pu-240	$4.20\cdot10^{-3}$	$5.00\cdot10^{-3}$	$6.30\cdot10^{-7}$	$3.90\cdot10^{1}$	$3.90\cdot10^{1}$	$1.5\cdot10^{-2}$	0.45	0.46
Pu-242	$4.20\cdot10^{-3}$	$5.00\cdot10^{-3}$	$6.30\cdot10^{-7}$	$3.90\cdot10^{1}$	$3.90\cdot10^{1}$	$1.5\cdot10^{-2}$	0.45	0.46
Ra-226	$4.20\cdot10^{-3}$	$5.00\cdot10^{-3}$	$6.30\cdot10^{-7}$	$1.10\cdot10^{-3}$	$1.10\cdot10^{-3}$	$2.4\cdot10^{-4}$	0.45	0.46
Se-79	$2.50\cdot10^{-4}$	$3.10\cdot10^{-4}$	$2.00\cdot10^{-7}$	0.00	0.00	$3.0\cdot10^{-4}$	0.18	0.19
Sm-151	$4.20\cdot10^{-3}$	$5.00\cdot10^{-3}$	$6.30\cdot10^{-7}$	5.20	5.20	$1.5\cdot10^{-2}$	0.45	0.46
Sn-121m	$4.20\cdot10^{-3}$	$5.00\cdot10^{-3}$	$6.30\cdot10^{-7}$	$3.90\cdot10^{1}$	$3.90\cdot10^{1}$	$1.6\cdot10^{-1}$	0.45	0.46
Sn-126	$4.20\cdot10^{-3}$	$5.00\cdot10^{-3}$	$6.30\cdot10^{-7}$	$3.90\cdot10^{1}$	$3.90\cdot10^{1}$	$1.6\cdot10^{-1}$	0.45	0.46
Sr-90	$4.20\cdot10^{-3}$	$5.00\cdot10^{-3}$	$6.30\cdot10^{-7}$	$1.10\cdot10^{-3}$	$1.10\cdot10^{-3}$	$3.4\cdot10^{-6}$	0.45	0.46
Tc-99	$4.20\cdot10^{-3}$	$5.00\cdot10^{-3}$	$6.30\cdot10^{-7}$	$3.90\cdot10^{1}$	$3.90\cdot10^{1}$	$5.3\cdot10^{-2}$	0.45	0.46
Th-229	$4.20\cdot10^{-3}$	$5.00\cdot10^{-3}$	$6.30\cdot10^{-7}$	$3.90\cdot10^{1}$	$3.90\cdot10^{1}$	$5.3\cdot10^{-2}$	0.45	0.46
Th-230	$4.20\cdot10^{-3}$	$5.00\cdot10^{-3}$	$6.30\cdot10^{-7}$	$3.90\cdot10^{1}$	$3.90\cdot10^{1}$	$5.3\cdot10^{-2}$	0.45	0.46
Th-232	$4.20\cdot10^{-3}$	$5.00\cdot10^{-3}$	$6.30\cdot10^{-7}$	$3.90\cdot10^{1}$	$3.90\cdot10^{1}$	$5.3\cdot10^{-2}$	0.45	0.46
U-233	$4.20\cdot10^{-3}$	$5.00\cdot10^{-3}$	$6.30\cdot10^{-7}$	$3.90\cdot10^{1}$	$3.90\cdot10^{1}$	$5.3\cdot10^{-2}$	0.45	0.46
U-234	$4.20\cdot10^{-3}$	$5.00\cdot10^{-3}$	$6.30\cdot10^{-7}$	$3.90\cdot10^{1}$	$3.90\cdot10^{1}$	$5.3\cdot10^{-2}$	0.45	0.46
U-235	$4.20\cdot10^{-3}$	$5.00\cdot10^{-3}$	$6.30\cdot10^{-7}$	$3.90\cdot10^{1}$	$3.90\cdot10^{1}$	$5.3\cdot10^{-2}$	0.45	0.46
U-236	$4.20\cdot10^{-3}$	$5.00\cdot10^{-3}$	$6.30\cdot10^{-7}$	$3.90\cdot10^{1}$	$3.90\cdot10^{1}$	$5.3\cdot10^{-2}$	0.45	0.46
U-238	$4.20\cdot10^{-3}$	$5.00\cdot10^{-3}$	$6.30\cdot10^{-7}$	$3.90\cdot10^{1}$	$3.90\cdot10^{1}$	$5.3\cdot10^{-2}$	0.45	0.46
Zr-93	$4.20\cdot10^{-3}$	$5.00\cdot10^{-3}$	$6.30\cdot10^{-7}$	4.70	4.70	$2.1\cdot10^{-2}$	0.45	0.46

Table 3-4. Median values of solubilities (temperate conditions, see Appendix F), IRF and CRF used in the deterministic near-field and far-field calculations. If IRF+CRF is greater than one CRF is 1-IRF. The solubility, CSOL, $1.00 \cdot 10^{17}$ corresponds to unlimited solubility.

	CSOL (mol/dm^3)	IRF (–)	CRF (–)
Ac-227	$1.00 \cdot 10^{17}$	0.00	0.00
Ag-108m	$1.10 \cdot 10^{-5}$	1.00	0.00
Am-241	$2.50 \cdot 10^{-6}$	0.00	0.00
Am-242m	$2.50 \cdot 10^{-6}$	0.00	0.00
Am-243	$2.50 \cdot 10^{-6}$	0.00	0.00
C-14	$1.00 \cdot 10^{17}$	$9.20 \cdot 10^{-2}$	$6.40 \cdot 10^{-1}$
Cd-113m	$1.00 \cdot 10^{17}$	1.00	0.00
Cl-36	$1.00 \cdot 10^{17}$	$8.60 \cdot 10^{-2}$	$1.50 \cdot 10^{-2}$
Cm-245	$2.60 \cdot 10^{-6}$	0.00	0.00
Cm-246	$2.60 \cdot 10^{-6}$	0.00	0.00
Cs-135	$1.00 \cdot 10^{17}$	$2.90 \cdot 10^{-2}$	0.00
Cs-137	$1.00 \cdot 10^{17}$	$2.90 \cdot 10^{-2}$	0.00
Eu-152	$1.00 \cdot 10^{17}$	0.00	0.00
H-3	$1.00 \cdot 10^{17}$	1.00	0.00
Ho-166m	$4.10 \cdot 10^{-6}$	0.00	0.00
I-129	$1.00 \cdot 10^{17}$	$2.90 \cdot 10^{-2}$	0.00
Mo-93	$1.00 \cdot 10^{17}$	$1.20 \cdot 10^{-2}$	$8.10 \cdot 10^{-1}$
Nb-93m	$4.90 \cdot 10^{-5}$	$1.70 \cdot 10^{-2}$	1.00
Nb-94	$4.90 \cdot 10^{-5}$	$1.80 \cdot 10^{-2}$	1.00
Ni-59	$3.00 \cdot 10^{-4}$	$1.20 \cdot 10^{-2}$	$9.60 \cdot 10^{-1}$
Ni-63	$3.00 \cdot 10^{-4}$	$1.20 \cdot 10^{-2}$	$9.70 \cdot 10^{-1}$
Np-237	$1.00 \cdot 10^{-9}$	0.00	0.00
Pa-231	$3.30 \cdot 10^{-7}$	0.00	0.00
Pb-210	$1.70 \cdot 10^{-6}$	0.00	0.00
Pd-107	$3.90 \cdot 10^{-6}$	$2.00 \cdot 10^{-3}$	0.00
Pu-238	$4.80 \cdot 10^{-6}$	0.00	0.00
Pu-239	$4.80 \cdot 10^{-6}$	0.00	0.00
Pu-240	$4.80 \cdot 10^{-6}$	0.00	0.00
Pu-242	$4.80 \cdot 10^{-6}$	0.00	0.00
Ra-226	$9.10 \cdot 10^{-7}$	0.00	0.00
Se-79	$6.70 \cdot 10^{-9}$	$4.20 \cdot 10^{-3}$	$1.30 \cdot 10^{-4}$
Sm-151	$1.10 \cdot 10^{-7}$	0.00	0.00
Sn-121m	$9.00 \cdot 10^{-8}$	$1.90 \cdot 10^{-4}$	$5.20 \cdot 10^{-1}$
Sn-126	$9.00 \cdot 10^{-8}$	$3.00 \cdot 10^{-4}$	0.00
Sr-90	$3.70 \cdot 10^{-3}$	$2.50 \cdot 10^{-3}$	0.00
Tc-99	$3.80 \cdot 10^{-9}$	$2.00 \cdot 10^{-3}$	$6.10 \cdot 10^{-5}$
Th-229	$2.60 \cdot 10^{-9}$	0.00	0.00
Th-230	$2.60 \cdot 10^{-9}$	0.00	0.00
Th-232	$2.60 \cdot 10^{-9}$	0.00	0.00
U-233	$9.50 \cdot 10^{-10}$	0.00	$2.50 \cdot 10^{-1}$
U-234	$9.50 \cdot 10^{-10}$	0.00	0.00
U-235	$9.50 \cdot 10^{-10}$	0.00	0.00
U-236	$9.50 \cdot 10^{-10}$	0.00	0.00
U-238	$9.50 \cdot 10^{-10}$	0.00	0.00
Zr-93	$1.80 \cdot 10^{-8}$	$9.20 \cdot 10^{-6}$	$1.30 \cdot 10^{-1}$

Table 3-5. Median values of transport parameters used as input data in the deterministic near-field calculations.

	Isostatic load, pinhole base case and no spalling	Pinhole Crown space	Pinhole no EDZ	Pinhole max EDZ 6	Pinhole max EDZ 7
U0_1 (m/yr)	$7.00\cdot10^{-6}$	$6.7\cdot10^{-6}$	$5.00\cdot10^{-6}$	$6.90\cdot10^{-6}$	$6.50\cdot10^{-6}$
QEQ_1 (m^3/yr)	$4.20\cdot10^{-6}$	$4.2\cdot10^{-6}$	$4.50\cdot10^{-6}$	$4.30\cdot10^{-6}$	$4.20\cdot10^{-6}$
FLEN (m)	6.00	6.20	$1.60\cdot10^{1}$	5.90	6.00
TW_1 (yr)	$2.10\cdot10^{2}$	$1.20\ \cdot10^{2}$	$4.70\cdot10^{2}$	$1.30\cdot10^{2}$	$1.60\cdot10^{2}$
F_1 (yr/m)	$5.50\cdot10^{6}$	$3.20\cdot10^{6}$	$4.90\cdot10^{7}$	$2.60\cdot10^{6}$	$3.80\cdot10^{6}$
QEQ_2 (m^3/yr)	$9.30\cdot10^{-5}$	$9.50\cdot10^{-5}$	0.00	$6.00\cdot10^{-4}$	$2.20\cdot10^{-4}$
TW_2 (yr)	$1.90\cdot10^{2}$	$9.50\cdot10^{1}$	0.00	$1.10\cdot10^{2}$	$1.40\cdot10^{2}$
F_2 (yr/m)	$3.50\cdot10^{6}$	$1.2\cdot10^{6}$	0.00	$9.20\cdot10^{5}$	$1.60\cdot10^{6}$
QEQR_3 (m^3/yr)	$1.20\cdot10^{-4}$	$2.70\cdot10^{-4}$	$2.00\cdot10^{-5}$	$8.40\cdot10^{-4}$	$3.30\cdot10^{-4}$
TW_3 (yr)	$1.70\cdot10^{2}$	$8.00\cdot10^{1}$	$2.90\cdot10^{2}$	$1.10\cdot10^{2}$	$1.40\cdot10^{2}$
F_3 (yr/m)	$2.40\cdot10^{6}$	$6.00\cdot10^{5}$	$1.10\cdot10^{7}$	$6.30\cdot10^{5}$	$1.30\cdot10^{6}$
TRAPP_3 (m)	$4.50\cdot10^{-1}$	1.00	$4.50\cdot10^{-1}$	$4.50\cdot10^{-1}$	$4.50\cdot10^{-1}$
LR_TUN_3 (m)	5.10	118	$1.80\cdot10^{1}$	5.00	5.30
TR_TUN_3 (yr)	$2.00\cdot10^{5}$	890	$1.20\cdot10^{6}$	$2.60\cdot10^{5}$	$2.40\cdot10^{5}$

Table 3-6. Median values of transport parameters used as input data in the deterministic far-field calculations.

	Isostatic load, pinhole base case and no spalling	Pinhole Crown space	Pinhole no EDZ	Pinhole max EDZ 6	Pinhole max EDZ 7
TW_1 (yr)	$1.80\cdot10^{2}$	$9.20\cdot10^{1}$	$2.10\cdot10^{2}$	$1.06\cdot10^{2}$	$1.35\cdot10^{2}$
F_1 (yr/m)	$4.00\cdot10^{6}$	$2.20\cdot10^{6}$	$1.20\cdot10^{7}$	$1.68\cdot10^{6}$	$2.57\cdot10^{6}$
TW_2 (yr)	$1.60\cdot10^{2}$	$7.90\cdot10^{1}$	$1.00\cdot10^{-21}$	$9.70\cdot10^{1}$	$1.27\cdot10^{2}$
F_2 (yr/m)	$2.30\cdot10^{6}$	$7.50\cdot10^{5}$	$1.00\cdot10^{-21}$	$6.19\cdot10^{5}$	$1.12\cdot10^{6}$
TW_3 (yr)	$1.50\cdot10^{2}$	$6.30\cdot10^{1}$	$2.00\cdot10^{2}$	$9.60\cdot10^{1}$	$1.26\cdot10^{2}$
F_3 (yr/m)	$1.90\cdot10^{6}$	$3.20\cdot10^{5}$	$5.10\cdot10^{6}$	$5.08\cdot10^{5}$	$1.01\cdot10^{6}$

Table 3-7. Basic Landscape Dose Factors (Sv/yr per Bq/yr), Dose Conversion Factors for pulse releases and distributed Dose Conversion Factors /Avila et al. 2010/.

Radionuclide	Basic LDF (Sv/yr per Bq/yr)	LDF pulse (Sv/yr per Bq/yr)	Distributed LDF (Sv/yr per Bq/yr)
Ag-108m	$7.05\cdot10^{-13}$	$5.08\cdot10^{-16}$	$7.99\cdot10^{-14}$
Ac-227	$1.30\cdot10^{-11}$		
Am-241	$1.46\cdot10^{-12}$		$7.34\cdot10^{-13}$
Am-243	$1.53\cdot10^{-12}$		$7.57\cdot10^{-13}$
C-14	$5.44\cdot10^{-12}$		$9.48\cdot10^{-13}$
Cl-36	$5.84\cdot10^{-13}$	$4.29\cdot10^{-15}$	$1.86\cdot10^{-13}$
Cm-244	$8.74\cdot10^{-13}$		$4.41\cdot10^{-13}$
Cm-245	$1.58\cdot10^{-12}$		$7.78\cdot10^{-13}$
Cm-246	$1.55\cdot10^{-12}$		$7.75\cdot10^{-13}$
Cs-135	$3.96\cdot10^{-14}$	$1.84\cdot10^{-16}$	$1.16\cdot10^{-14}$
Cs-137	$1.20\cdot10^{-13}$		$6.03\cdot10^{-14}$
Ho-166m	$5.90\cdot10^{-14}$		$1.15\cdot10^{-14}$
I-129	$6.46\cdot10^{-10}$	$5.56\cdot10^{-14}$	$5.96\cdot10^{-11}$
Nb-94	$4.00\cdot10^{-12}$	$3.18\cdot10^{-16}$	$2.29\cdot10^{-13}$
Ni-59	$7.39\cdot10^{-14}$	$9.67\cdot10^{-18}$	$6.57\cdot10^{-15}$
Ni-63	$1.21\cdot10^{-15}$		$5.88\cdot10^{-16}$
Np-237	$4.83\cdot10^{-11}$		$2.48\cdot10^{-11}$
Pa-231	$8.10\cdot10^{-12}$		$2.94\cdot10^{-12}$
Pb-210	$5.07\cdot10^{-12}$		$2.56\cdot10^{-12}$
Pd-107	$6.73\cdot10^{-15}$		$2.00\cdot10^{-15}$
Po-210	$8.86\cdot10^{-12}$		$4.47\cdot10^{-12}$
Pu-239	$1.94\cdot10^{-12}$		$1.00\cdot10^{-12}$
Pu-240	$1.88\cdot10^{-12}$		$9.54\cdot10^{-13}$
Pu-242	$1.89\cdot10^{-12}$		$1.03\cdot10^{-12}$
Ra-226	$3.75\cdot10^{-12}$		$1.40\cdot10^{-12}$
Se-79	$1.21\cdot10^{-9}$	9.70^{-14}	$1.50\cdot10^{-10}$
Sm-151	$7.16\cdot10^{-16}$		$3.61\cdot10^{-16}$
Sn-126	$2.47\cdot10^{-11}$	2.31^{-15}	$2.58\cdot10^{-12}$
Sr-90	$2.19\cdot10^{-13}$		$1.10\cdot10^{-13}$
Tc-99	$8.98\cdot10^{-13}$	2.81^{-15}	$2.03\cdot10^{-13}$
Th-229	$3.61\cdot10^{-12}$		$1.80\cdot10^{-12}$
Th-230	$1.31\cdot10^{-11}$		$3.48\cdot10^{-12}$
Th-232	$1.72\cdot10^{-12}$		$8.51\cdot10^{-13}$
U-233	$2.50\cdot10^{-12}$		$4.24\cdot10^{-13}$
U-234	$3.62\cdot10^{-12}$		$5.19\cdot10^{-13}$
U-235	$2.76\cdot10^{-12}$		$4.41\cdot10^{-13}$
U-236	$1.85\cdot10^{-12}$		$3.37\cdot10^{-13}$
U-238	$1.85\cdot10^{-12}$		$3.30\cdot10^{-13}$
Zr-93	$2.77\cdot10^{-14}$		$6.35\cdot10^{-15}$

3.7.3 QA-related issues

Used scripts, input data and main results are archived at SKB, see Table 3-8.

During the work and final control of data according to the SR-Site quality assurance plan described in Section 2.9 of the **SR-Site Main report**, some data have been changed or were identified as being erroneous. The treatment of such data is as follows:

- The correlation groups for K_d in rock were changed at a late stage of the SR-Site project, when most of the cases had been calculated. The effects of the change were investigated in an alternative calculation case of the central corrosion case, see Section 4.5.5. The conclusion is that the correlation groups have negligible influence on the results. Hence, no other cases were recalculated.
- The radionuclide inventory for nuclides present in PWR control rods was changed when most of the cases had been calculated. The changes in inventory were negligible for all nuclides except Ag-108m. In calculation cases where Ag-108m contributes to the total dose, the results were updated by scaling the old results to appropriately account for the corrected input. This is further described in Appendix E. The solubility for Ag-108m has not been changed in the calculations due to the changes in the inventory. This is a pessimistic approach.
- Minor changes of the probabilistic distributions for the porosity of the buffer bentonite in the **Data report**. The **Data report** recommends a double triangular distribution (0.124, 0.174, 0.241) for anions, while the calculations in this report use a triangular distribution (0.13, 0.18, 0.24). For cations the **Data report** recommends a triangular distribution (0.41, 0.435, 0.46), while the calculations in this report use a triangular distribution (0.43, 0.44, 0.47). Since these changes are minor and since the results are not sensitive to uncertainties in buffer porosity, it is concluded that the changes in input data would result in insignificant changes of the results if they were to be implemented. No recalculations were, therefore, performed.
- Some erroneous correlations between input data were identified when carrying out the sensitivity analysis.
  - One of these was a strong, positive correlation between the fuel dissolution rate and the corrosion release rate, i.e. of two input data sets that are not correlated. The calculations for the central corrosion case and the shear load case with failure during the period 1,000 years to one million years were, therefore, recalculated, with the recalculated result being used in this report. The effect on the mean effective dose was negligible and hence no other cases were recalculated.
  - There are also erroneous input data correlations between K_d for buffer and K_d for backfill, De for buffer and De for backfill and porosity for buffer and porosity for backfill. These correlations are only present in the hypothetical residual scenarios and hence no effort was made to investigate the effect of these unwanted correlations. Based on the low sensitivity of the result on these input data uncertainties, these errors are, however, assessed to have a minor, if any, impact on the resulting mean doses.
- The solubility limits for plutonium are too high because of an incorrect value for the associated error in an equilibrium constant used in the calculations. Figures in Appendix F have been corrected but incorrect solubility limits for plutonium have been used in all calculation cases. No recalculations were made since the fault was found at a very late stage of the SR-Site project, during the review of this report. Further, the approach used is pessimistic and does not affect the total releases. Solubility limits are not included in the calculation cases where the canister fails due to corrosion, except for the variant that includes solubility limits. The contribution from plutonium is already low in this variant. In the cases where the canister fails due to shear load, isostatic load or have a growing pinhole, solubility limits have been included in the calculations but the contribution from plutonium is already several hundred times lower than the total release.

Table 3-8. List of scripts, input data and main results are archived at SKB (access might be given on request).

SKBdoc id, version	Title	Issuer, year
1256019 ver 1.0	Hydrogeological model data and results – Forsmark	SKB, 2010
1260107 ver 1.0	Supporting calculations related to radionuclide tramsport	SKB, 2010
1260295 ver 1.0	Results from radionuclide transport calculations with COMP23 and FARF31	SKB, 2010
1260297 ver 1.0	Scripts and input data used for radionuclide transport calculations with COMP23	SKB, 2010
1265612 ver 1.0	Scripts and data used for Analytical erosion corrosion calculations	SKB, 2010
1266150 ver 1.0	Radionuclide transport calculations with MARFA	SKB, 2010

4 Canister failure due to corrosion

4.1 Introduction

In the ‘canister failure due to corrosion’ scenario (called briefly the corrosion scenario below) canisters fail as a result of enhanced corrosion due to advective conditions in the deposition hole following the loss of buffer through erosion.

For this failure mode, both the canister and the buffer are bypassed, and the rock retention is small since substantial copper corrosion after buffer erosion only occurs in deposition holes with high flow rates, which in general are associated with flow paths to the surface of low geosphere retention.

4.1.1 Evolution of the canister after canister failure

According to the analysis of copper corrosion for advective conditions, a band, 0.35 m high and covering half the circumference of the canister, is assumed to be evenly corroded /SKB 2010/. This means that when penetration occurs, a large amount of damage must be assumed in the copper shell.

The time required to penetrate the cast iron insert is pessimistically neglected since it is difficult to estimate a reasonable development for this process for this failure mode. Also, because penetration of the copper shell in general occurs after several hundred thousand years for the few canisters exposed to the highest corrosion rates, the additional time to penetrate the cast iron insert is of less importance.

Once the copper canister and the cast iron insert have failed, the void in the insert is assumed to be rapidly filled with water due to the high flow rate and the lack of transport resistances in the absence of the buffer and with a large amount of damage also to the cast iron insert.

4.1.2 Radionuclide release

Advective conditions in the buffer must be assumed also for the consequence calculations for the corrosion scenario. There is no buffer hindering the outward transport of radionuclides meaning that this is controlled by the flow rate through the deposition hole, q (m^3/yr). The following three contributions to the outward transport can be distinguished.

- The instantaneously accessible fraction of radionuclides, IRF, that is assumed to rapidly dissolve in the water in the void volume and be subsequently flushed from the canister. This gives rise to a pulse of uncertain duration, the uncertainty stemming from e.g. uncertainties in the detailed development of the canister failure through which the IRF is made accessible. The treatment of the IRF pulse is further described below.
- A contribution from the corrosion of metal parts in the fuel assemblies and the congruent release of radionuclides embedded in the metal parts. These inventories are collectively called the corrosion release fraction, abbreviated CRF.
- A contribution from fuel dissolution and the congruent release of radionuclides embedded in the fuel matrix.

In a case where the buffer is severely eroded, a colloid filter /**Buffer, backfill and closure process report**/ cannot be guaranteed. This means that the use of elemental solubilities as a limit for radionuclide release could be questioned, since it cannot be excluded that the solid particles formed by various radionuclides reaching saturation would leave the canister and migrate further. In this case, however, this is of minor concern, since the flow through the deposition hole is often too high for solid phases to precipitate (with the exception of uranium). This is demonstrated in Section 4.5.2 below by analysing a case where solubility limits are included.

The release into the fracture is thus controlled by the corrosion rate and the fuel dissolution rate, with two exceptions:

1. For uranium, a concentration limit is still an effective constraint on release, due to the large amount of U-238 present in the fuel. This limits the near-field releases of uranium isotopes, but also leads to increased near-field releases of Th-230, Th-229 and Pa-231 generated by the re-precipitated U-234, U-233 and U-235, respectively.
2. It cannot be excluded that co-precipitation processes and sorption/immobilisation in the remaining bentonite in the deposition hole could confine Th-230 to the near field. If this is the case, its daughter nuclide, the considerably more mobile Ra-226, would be released. The so generated Ra-226 is assumed to be released to the flowing groundwater in the fracture intersecting the deposition hole. This causes higher releases of Ra-226, since there is a contribution not only directly from the fuel dissolution, but also from the confined Th-230. Since Ra-226 is often the main contributor to dose, this also causes higher total doses. Sorption of thorium in the near field is thus assumed. The effect of disregarding thorium sorption is analysed as a separate calculation case.

Furthermore, as the flow rate in the intersecting fracture is high, the retention in the rock is in general limited for these deposition holes.

A description of the discretisation and boundary condition used in COMP23 is given in Appendix G, Section G.6.

4.1.3 IRF-pulse

The fraction of the inventory assumed to be instantaneously released from the fuel upon water contact is expected to be released to the geosphere in a matter of years in the corrosion scenario, since the flow rates at the deposition positions with the eroded buffer and failed canister are high, see further Table 4-3 below. Since these nuclides are in general non-sorbing and since the flow related retardation properties in the geosphere are poor for the flow paths associated with the deposition positions in question, they are generally released as pulses of durations of tens of years from the geosphere to the biosphere. In this case, the basic LDF values would yield overly pessimistic estimates of doses. Therefore, the calculations for the IRF are made separately. There are two reasons to calculate them separately; one is the fact that the calculated basic LDF-values are not developed for peak releases as described in Section 3.5 and the other is that it is not meaningful to present many sharp peaks (up to almost 2,000 in one of the probabilistic cases) in a figure.

A number of nuclides with an IRF, and with half-lives up to 10,000 years (e.g. Sr-90, Cs-137, Ag-108m and C-14,), were excluded from the analysis of the corrosion cases since they would decay to insignificance before a failure would occur.

Tc-99

The release of the IRF part of Tc-99 has been calculated in two different ways for the near field and for the far field. For the near field the dose equivalent release is calculated in the same way as for all other IRF nuclides. The far-field pulse release is modelled with the far-field transport model since sorption in the geosphere is considerable for Tc-99. To obtain the far-field annual effective dose the IRF of Tc-99 was included in a separate calculation with COMP23 and transferred to the FARF31 calculations. This means that the far-field annual effective dose of all Tc-99 (the IRF and non IRF parts) is available when the figures for the far-field release are plotted, however the mean annual effective dose is lower than 10^{-3} μSv for all corrosion cases and therefore not visible in the figures.

Deterministic calculations

Deterministic calculations of the IRF-pulse from I-129, Se-79, Cs-135, Ni-59, Cl-36, Sn-126 and Nb-94 are calculated as follows. The total dose associated with a pulse release, $D_{TotPulse}$, is calculated by taking the IRF inventory at 100,000 years multiplied by the pulse LDF-values, given in Table 3-7, to yield a total peak dose from the pulse release for one canister. The IRF inventory could be taken at the actual failure time for the different cases, but this would not affect the result much since these nuclides are long-lived in comparison to the failure times.

Note that it is also pessimistic to apply the pulse LDF approach because the maximum dose for a given mass released to the biosphere is obtained when the entire mass is released at once, noting that the LDF pulse values are by definition taken for the point in time in the landscape development where the consequences are maximal.

Probabilistic calculations

The IRF pulses in the probabilistic cases are shown to give negligible contribution to the mean dose, by applying the treatment for the central corrosion case, see Section 4.4.2. Therefore, the IRF-pulse releases are not reported for the other cases. However, they are considered in the account of risk dilution reported in the **Main report** Section 13.9.

4.2 Summary of calculation cases

There are three hydrogeological models (semi-correlated, uncorrelated and fully correlated), described by /Joyce et al. 2010/ and summarised in the **Data report**, Section 6.7, that form the base for the calculation cases. In Figure 4-1 the hydrogeological models are indicated with blue boxes.

Three erosion cases (orange boxes in Figure 4-1) are included yielding nine corrosion variants to consider in the derivation of calculation cases for radionuclide transport and dose. Of these, the three 'no advection' variants are not further treated as they do not lead to canister failures. A *central corrosion variant* base on the 'SR-Site erosion model' was identified as the one on which assessments of radionuclide transport and dose should primarily be made. In addition the variant with initial advection was studied. The green boxes in Figure 4-1 indicate all the calculation cases for radionuclide transport and dose. The cases are reported in the same order as in the figure.

The *central corrosion case* consists of the semi-correlated hydrogeological DFN-model, the SR-Site erosion model and base case transport assumptions. The following cases of alternative transport conditions are analysed for the central corrosion variant:

- a case disregarding thorium sorption in the near field;
- a case including solubility limits in the near field,
- a case with decreased sorption of lead in the geosphere,
- a case with K_d for U(VI) instead of U(IV) in the geosphere,
- a case assessing the influence of correlation groups for K_d in the geosphere,
- cases with colloid facilitated transport in the geosphere,
- a case with varying climate conditions,
- a case with varying climate conditions and colloid facilitated transport in the geosphere.

The other five relevant corrosion cases are analysed with the base case transport assumption.

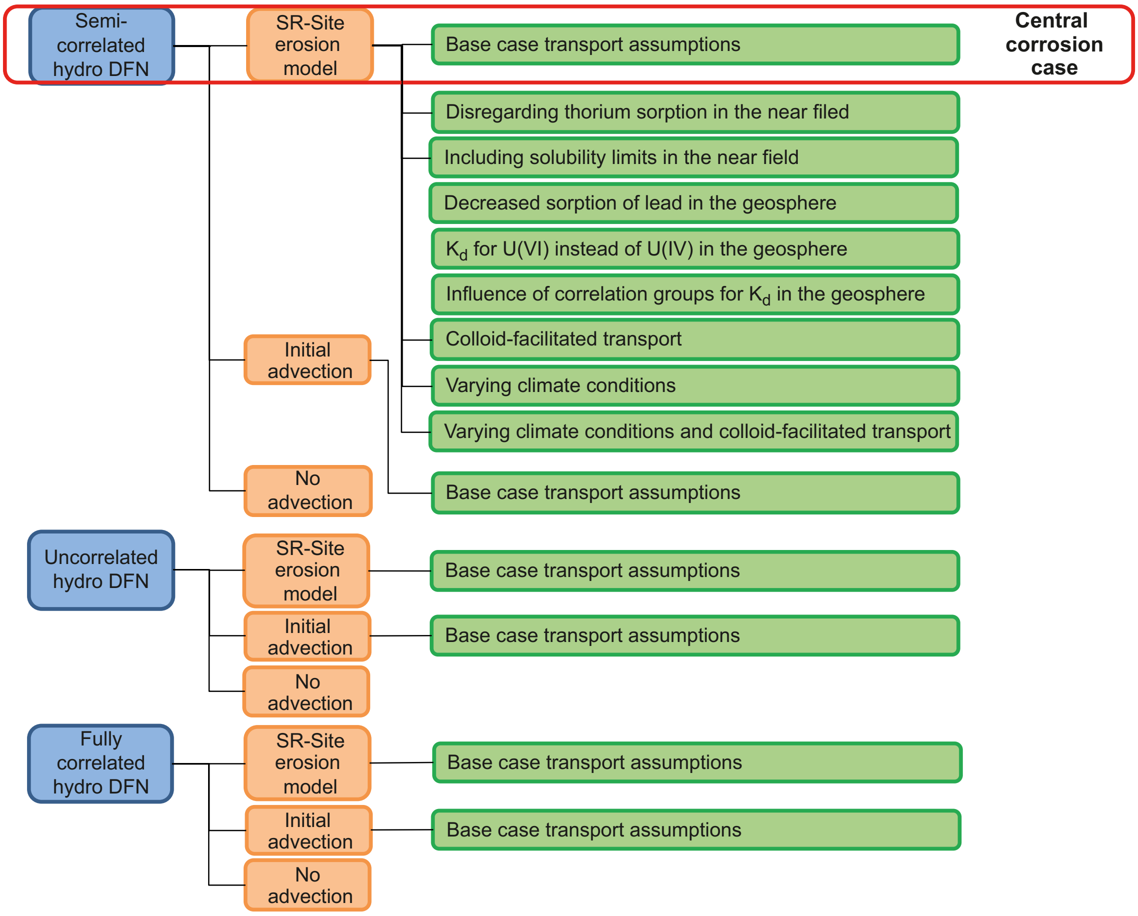

Figure 4-1. *Overview of calculation cases for the corrosion scenario. Blue boxes indicate hydrogeological DFN models, orange boxes indicate erosion/corrosion variants and green boxes indicate the calculation cases for radionuclide transport and dose. The calculation cases are presented in the same order as in this figure.*

4.3 Input data specific for the corrosion scenario

Most of the input data used in the corrosion scenario are given in Section 3.7 that summarises data for all scenarios. In this section more details regarding the used hydrogeological calculations and failure times are given.

The failure times are obtained as output from the erosion/corrosion calculations reported in /SKB 2010/ and the results are available in SKBdoc, see Table 3-8. The input to those calculations is qualified in the SR-Site **Data report**.

Several realisations of each of the three variants of the hydrogeological DFN model are propagated to the corrosion scenario, see Table 4-1. In all calculations for this scenario, deposition positions are rejected according to the EFPC criterion (canister positions intersected by fractures that also intersect the entire tunnel perimeter have been discarded) in the output from the hydrogeological modelling. In the central corrosion case, data from the 10 realisations of the semi-correlated DFN model are used.

Table 4-1. Hydrogeological realisations used in the corrosion scenario /Joyce et al. 2010/.

Hydrogeological DFN model	Realisations
Semi-correlated model	Base case and 10 additional realisations
Uncorrelated model	Base case and 5 additional realisations
Fully correlated model	Base case and 5 additional realisations

The corrosion case is based on data for only the few deposition holes that experience canister failure due to corrosion. This means that all deposition holes of relevance experience a high flow rate and in general also a low flow-related rock transport resistance, since these properties are strongly correlated. It is noted that the calculated hydraulic and transport properties of these deposition holes are from the extreme tails of distributions derived from a complex hydrogeological model with stochastic components (the generated fracture network). For the deterministic calculations of the corrosion scenario the parameters used are those connected to the earliest failure time; these parameters are summarised in Table 4-2. For probabilistic calculations, the ten realisations of the semi-correlated model variant are used in order to obtain more reliable representations of these tails, see Table 4-3. For the uncorrelated and fully correlated DFN model variants, for which consequences are analysed in Section 4.6 and 4.7, the five available realisations are used.

Table 4-2. Data for the deposition holes where the first canister fails, used in deterministic calculations.

Hydrogeological model/ Erosion model	Time of failure (yr)	Rock transport resistance, F (yr/m)	Advective travel time, t_w (yr)	Advective flow through deposition hole, q (m^3/yr)
Semi-correlated/SR-Site	114,485	53,660	6	0.733
Uncorrelated/SR-Site	97,815	5,757,000	292	0.641
Fully correlated/SR-Site	99,700	45,600	12	0.626
Semi-correlated/Initial advection	44,049	53,660	6	0.733
Uncorrelated/Initial advection	47,107	5,757,000	292	0.641
Fully correlated/Initial advection	47,657	45,600	12	0.626

Table 4-3. Data for the deposition holes where canisters fail due to corrosion for the ten realisations of the semi-correlated DFN model. Sorted by ascending time of failure.

Time of failure (yr)	Rock transport resistance, F (yr/m)	Advective travel time, t_w (yr)	Advective flow through deposition hole, q (m^3/yr)
114,485	53,660	6	0.733
122,557	564,900	61	0.557
132,155	14,510	23	0.267
157,452	26,260	7	0.358
157,805	642,100	78	0.316
179,621	87,820	14	0.251
201,037	89,910	17	0.144
230,828	818,600	38	0.148
305,884	33,970	16	0.082
313,807	33,140,000	2,501	0.079
361,884	2,184,000	124	0.083
377,494	38,170	14	0.095
391,981	24,220,000	2,021	0.060
402,471	157,900	19	0.086
442,257	155,100	19	0.075
471,801	163,400	29	0.067
480,309	25,290,000	2,070	0.047
504,166	53,660	6	0.733
521,967	24,830,000	1,994	0.042
526,759	116,600	241	0.050
531,274	53,660	6	0.733
569,225	53,660	6	0.733
569,701	564,900	61	0.557
595,478	53,660	6	0.733
600,806	564,900	61	0.557
612,248	471,800	31	0.048
612,252	53,660	6	0.733
644,354	564,900	61	0.557
652,328	211,100	20	0.044
674,477	564,900	61	0.557
693,725	564,900	61	0.557
705,692	1,710,000	99	0.033
714,768	26,260	7	0.358
750,814	642,100	78	0.316
753,537	26,260	7	0.358
777,848	14,510	23	0.267
792,067	642,100	78	0.316
803,247	11,330	20	0.035
807,815	26,260	7	0.358
822,765	14,510	23	0.267
845,022	87,820	14	0.251
845,360	26,260	7	0.358
849,820	642,100	78	0.316
869,351	26,260	7	0.358
885,650	14,510	23	0.267
889,770	642,100	78	0.316
891,310	87,820	14	0.251
893,681	53,660	6	0.733
901,874	9,083,000	601	0.026
915,297	642,100	78	0.316
918,487	2,008,000	135	0.024
929,149	14,510	23	0.267
941,008	61,400	18	0.032
956,114	87,820	14	0.251
956,944	14,510	23	0.267
978,463	3,845,000	91	0.033

4.4 Central corrosion case

4.4.1 Deterministic calculations

Hydrogeological case:	Semi-correlated, ten realisations
Erosion/corrosion model:	SR-Site model
Failure time:	114,485 years
Number of failed canisters:	1
Solubility limits:	No
Thorium sorption in near field:	Yes (modelled as low solubility limit)
Number of realisations:	1
Number of nuclides:	37

A deterministic calculation of the central corrosion case is performed for a canister taken from the realisation with the earliest failure time of the analysed realisations (114,485 years after deposition) with corresponding geosphere transport data, i.e. data used to calculate the corrosion time are from the same hydrogeological calculation as the geosphere transport data. Advection occurs in the buffer void and the dose equivalent releases are primarily determined by the fuel dissolution rate set to 10^{-7}/yr. The contributions from the instantly released fraction of nuclides, IRF, are calculated separately.

Table 4-4 shows peak annual doses from the pulse releases from the instantly released fraction, IRF. The IRF inventory at 100,000 years has been multiplied by the pulse LDF-values given in Table 3-7.

Figure 4-2 shows the near-field releases converted to doses through multiplying the release rate by the LDF-value. As mentioned in Section 3.5, the conversion to dose is done to obtain a convenient metric of release consequence that can also be summed to obtain a metric that considers all nuclides.

The dose equivalent releases from the geosphere are shown in Figure 4-3.

The dose equivalent release from the near field is dominated by Tc-99 (as IRF-pulse), Nb-94 and Ni-59. The peak contributions from Nb-94 and Ni-59 are due to the relatively fast release of the part of these nuclides embedded in the metal in the fuel assemblies. The time for metal corrosion is short (log-triangular 10^2, 10^3, 10^4 yr) compared to the time scale for the release. The doses caused by releases from the far field are dominated by I-129 (as IRF-pulse), Ra-226 and Se-79 (as IRF pulse). The far-field pulse release for Tc-99 is modelled with the far-field transport model since sorption in the geosphere is considerable for Tc-99. The pulse release of Tc-99 is thus included in the results shown in Figure 4-3.

Table 4-4. Peak annual dose from the pulse releases from the instantly released fraction, IRF, for a deterministic calculation of the central corrosion case. The dose is calculated at 100,000 years.

Nuclide	Peak annual dose (μSv)
I-129	3.82
Se-79	1.72
Cs-135	0.21
Cl-36	0.12
Nb-94	0.026
Sn-126	0.019
Ni-59	0.012
Tc-99	6.81[a)]

[a)] The peak annual dose for Tc-99 is only valid for the near field.

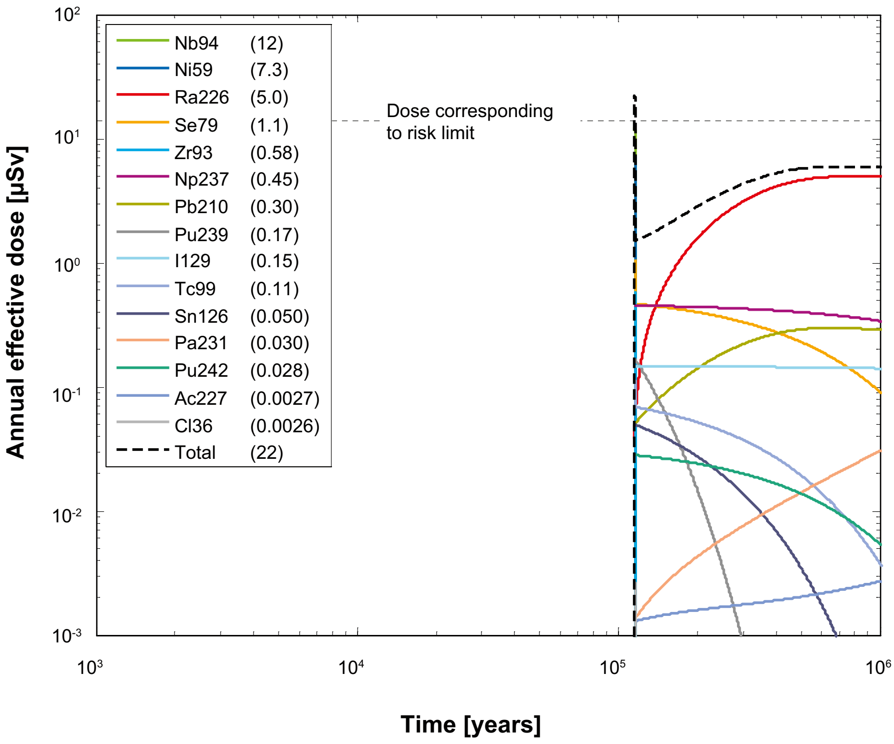

Figure 4-2. *Near-field dose equivalent release for a deterministic calculation of the central corrosion case. The legend is sorted by peak (in the one-million year period) of the annual effective dose. The values in brackets are peak dose in units of µSv. The curves for Nb-94 and Ni-59 are hidden under the curve showing the total dose equivalent release.*

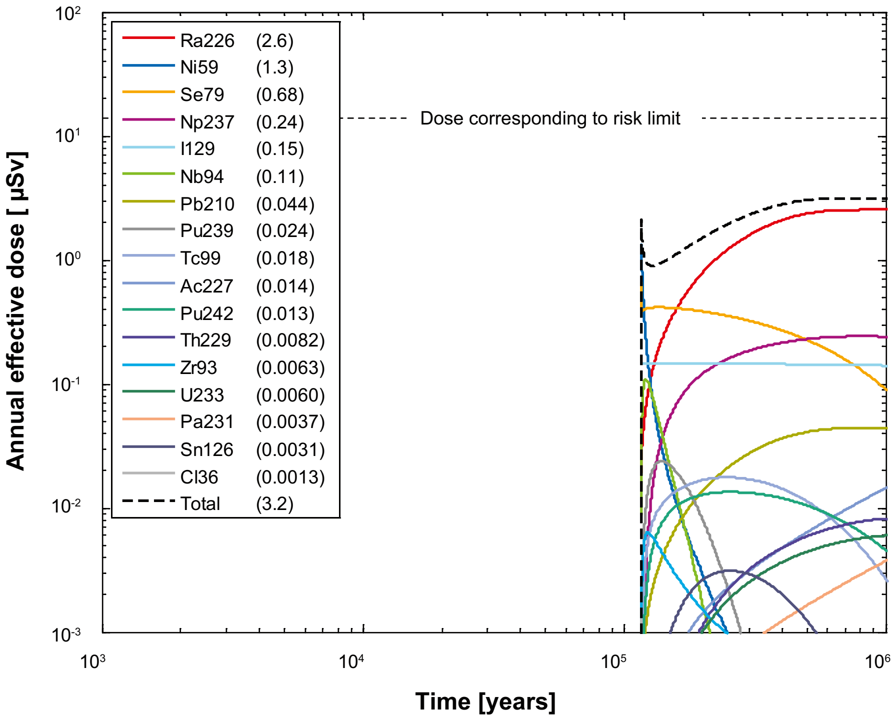

Figure 4-3. *Far-field annual effective dose for a deterministic calculation of the central corrosion case. The legend is sorted by peak (in the one-million year period) of the annual effective dose. The values in brackets are peak dose in units of µSv.*

4.4.2 Probabilistic calculations

Hydrogeological case:	Semi-correlated, ten realisations
Erosion/corrosion model:	SR-Site model
Failure time:	56 times according to Table 4-3
Average number of failed canisters:	0.12
Solubility limits:	No
Thorium sorption in near field:	Yes (modelled as low solubility limit)
Number of realisations:	50 per canister failure time
Number of nuclides:	37

A probabilistic calculation of the central corrosion case is performed with failure times and geosphere transport data from the ten realisations of the semi-correlated DFN model, see Table 4-3. The mean number of failed canisters, 0.12, is an outcome of the corrosion calculations /SKB 2010/. The contributions from the instantly released fraction of nuclides, IRF, are calculated separately.

The contribution from the IRF pulse in the probabilistically calculated mean dose is treated as follows. The probability of canister failure, p_{Fail}, is determined for each 100,000 year interval from the calculated distribution of canister failure times for the central corrosion case. The total probability until one million years is the sum of all p_{Fail}, i.e. 0.12 for the central corrosion case. The width of the dose curves in the biosphere is typically 1,000 years. The likelihood that an exposure due to a pulse release, p_{Expo}, is present at a given point in time during the 100,000 year interval is thus $10^{-2} \cdot p_{Fail}$. (The likelihood of overlaps between pulses is very small due to the low probabilities.) The total dose associated with a pulse release $D_{TotPulse}$ is determined at the start of each 100,000 year interval (in the same way as described for the deteministic case). The probabilistically calculated mean dose is then obtained as the probability of exposure multiplied with the total dose associated with the pulse release ($p_{Expo} \cdot D_{TotPuls}$). The result of this procedure for the central corrosion case is shown in Table 4-5. As seen in the table, the highest mean dose is around $1 \cdot 10^{-3}$ μSv, i.e. more than four orders of magnitude below the dose corresponding to the risk limit. The pulse releases thus give negligible contributions to the probabilistically calculated mean dose. It is also noted that this treatment assumes that temperate conditions are prevailing. Including probabilities of periglacial and glacial climate conditions would reduce the mean dose further. The IRF pulse of Tc-99 is modelled with the far-field transport model since sorption in the geosphere is considerable for Tc-99. The pulse release of Tc-99 is thus included in the results shown in Figure 4-5.

Figure 4-4 shows near-field dose equivalent releases and Figure 4-5 shows the corresponding far-field dose equivalent releases. The failure times are reflected as distinct features in the release curves, in particular for the near field. The pulse like features are due to release controlled by corrosion of the metal parts of the fuel assemblies (e.g. Ni-59). The metal corrosion times (ranging between 100 and 10,000 years) are such that the releases appear as pulses on the time scale of the dose curves. The first releases occur after around 110,000 years when the first canister fails.

Table 4-5. Calculation of the total mean dose from release of the instant release fraction, IRF, in the central corrosion case.

Time interval [yr]	p_{Fail}	p_{Expo}	$D_{TotPulse}$ [μSv]	Mean dose [μSv]
0–100,000	0	0	0	0
100,000–200,000	$1.25 \cdot 10^{-2}$	$1.25 \cdot 10^{-4}$	5.92	$7.4 \cdot 10^{-4}$
200,000–300,000	$4.17 \cdot 10^{-3}$	$4.17 \cdot 10^{-5}$	5.54	$2.3 \cdot 10^{-4}$
300,000–400,000	$1.04 \cdot 10^{-2}$	$1.04 \cdot 10^{-4}$	5.25	$5.5 \cdot 10^{-4}$
400,000–500,000	$8.33 \cdot 10^{-3}$	$8.33 \cdot 10^{-5}$	5.01	$4.2 \cdot 10^{-4}$
500,000–600,000	$1.46 \cdot 10^{-2}$	$1.46 \cdot 10^{-4}$	4.81	$7.0 \cdot 10^{-4}$
600,000–700,000	$1.46 \cdot 10^{-2}$	$1.46 \cdot 10^{-4}$	4.64	$6.8 \cdot 10^{-4}$
700,000–800,000	$1.25 \cdot 10^{-2}$	$1.25 \cdot 10^{-4}$	4.49	$5.6 \cdot 10^{-4}$
800,000–900,000	$2.29 \cdot 10^{-2}$	$2.29 \cdot 10^{-4}$	4.37	$1.0 \cdot 10^{-3}$
900,000–1,000,000	$1.67 \cdot 10^{-2}$	$1.67 \cdot 10^{-4}$	4.26	$7.1 \cdot 10^{-4}$

The doses caused by releases from the near field are dominated by Ra-226. Much of the Ra-226 released from the near field is transmitted through the geosphere since the failed canisters are located in deposition holes intersected by large, highly transmissive fractures with low retention. The release of Ra-226 from the geosphere is almost exclusively due to Ra released from the near field and not to in-growth in the geosphere. This, in turn, is related to the fact that the parent nuclide Th-230 is assumed to be confined to the near field. Despite the fast release in the far field the dose from Pb-210 decrease significantly due to its short half-life (22 years). The far field also significantly influences nuclides controlled by corrosion with pulse like releases in the near field, for example Ni-59. For Tc-99 the geosphere retention is significant and the dose is below 10^{-3} µSv/yr

Some statistics for the far-field release are shown in Figure 4-6. Note that these are derived only for the realisations of the failure times where failures actually occur in the corrosion calculations. Since the mean number of failed canisters is about 0.12, the most likely outcome of the corrosion calculations is zero failures. This is not reflected in the percentiles in Figure 4-6, other than for the mean value. Taking this into account would bring the 99th and 95th percentiles closer to the mean.

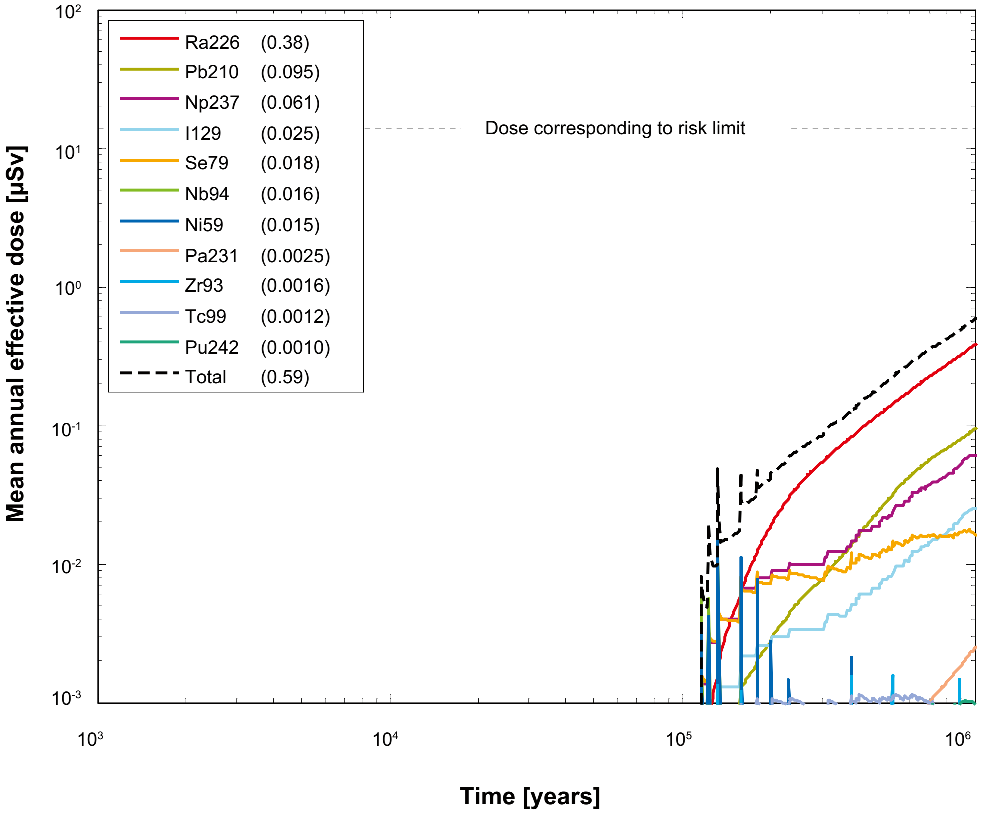

Figure 4-4. *Near-field dose equivalent release for a probabilistic calculation of the central corrosion case. The average number of failed canisters is 0.12. The legend is sorted by peak (in the one-million year period) of the mean annual effective dose. The values in brackets are peak dose in units of µSv.*

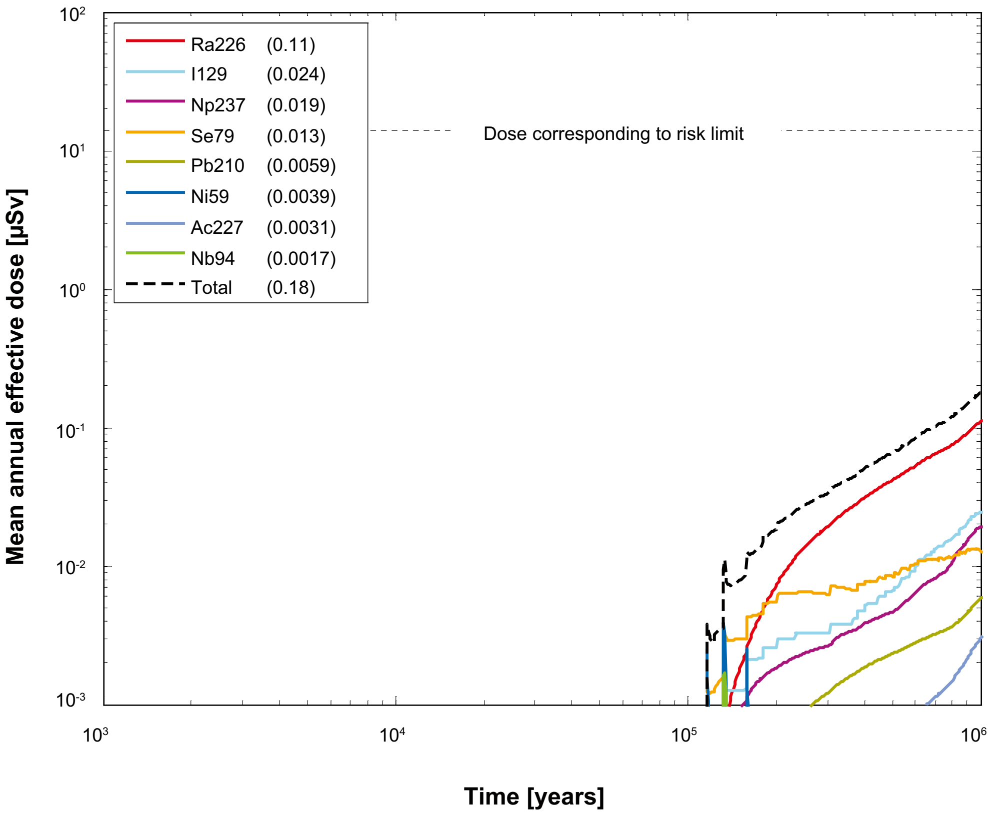

Figure 4-5. *Far-field mean annual effective dose for a probabilistic calculation of the central corrosion case. The legend is sorted by peak (in the one-million year period) of the mean annual effective dose. The values in brackets are peak dose in units of µSv.*

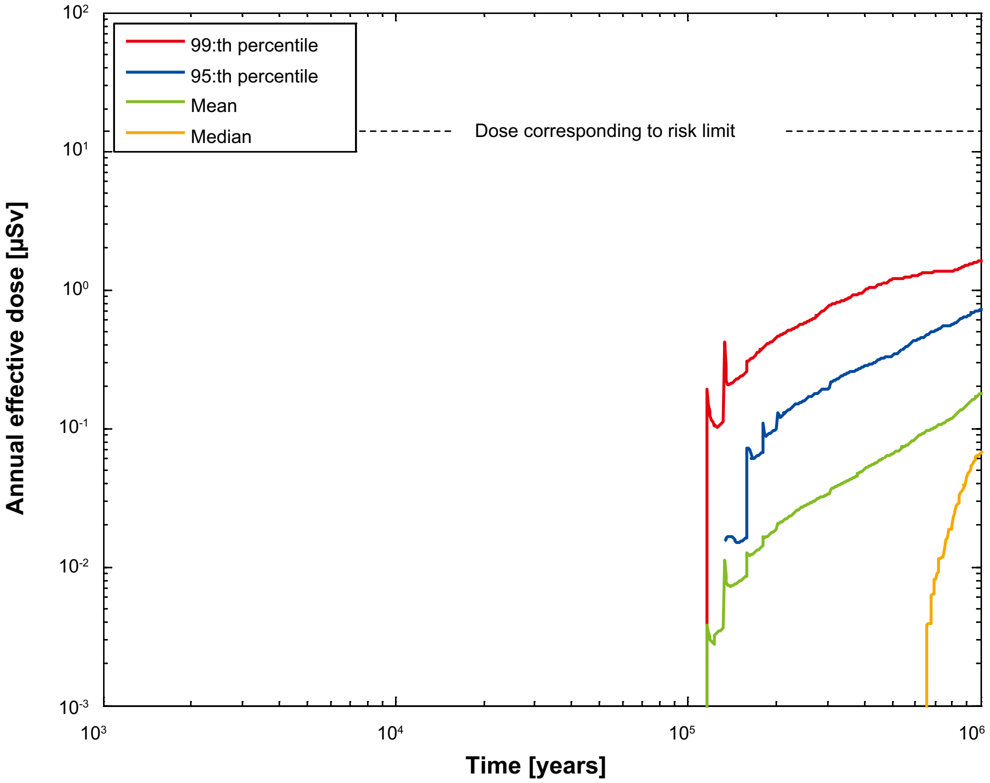

Figure 4-6. *Far-field annual effective dose (mean, median, 95th and 99th percentiles) for the probabilistic calculation of the central corrosion case.*

4.4.3 Sensitivity analysis

Introduction

This section presents results of sensitivity analyses of the results of the dose calculations, i.e. the sensitivity of the uncertainty in calculated dose to uncertainties in the input parameters is analysed. All analyses concern the probabilistic calculation of the central corrosion case.

It is of interest to determine i) the variables that correlate with the dose over the entire dose range and ii) the parameter values that are related to high and low doses. Ra-226 dominates the dose in most of the realisations in the central corrosion case and it is thus of particular interest to clarify sensitivities of the Ra-226 dose to input parameters.

Global sensitivity analysis

The first purpose is thus to perform a so-called global sensitivity analysis, i.e. to identify the input parameters that have the greatest influence on the spread of the results. The contribution to output spread depends on both the spread of the input parameter and the model's sensitivity to variations in that particular input parameter. A range of methods for this type of sensitivity analysis exists /Saltelli et al. 2000/. Several studies and reviews have demonstrated that standardised rank regression is a suitable method for sensitivity analysis of non-linear systems where the calculation end point is a monotonic function of the input variables /Saltelli et al. 1993, Helton 1993, Hamby 1994, Iman and Conover 1979/. This applies to the present non-linear and monotonic system /Hedin 2003/, and the standardised rank regression coefficient (SRRC) is, therefore, used for identifying the most important variables contributing to dose uncertainty.

A standardised rank regression analysis of the total dose at 10^6 years on the input variables yields, in descending order, the fuel dissolution rate D_{Fuel}, the flow-related transport resistance along the geosphere flow path, F, and the failure time $t_{Failure}$ as the input parameters most affecting dose results, see Figure 4-7. Regressing on Ra-226 dose at 10^6 years yields a similar result due to the dominance of Ra-226. The ranking of the two most important variables is switched in this case. This switching of the ranking is consistent with the fact that the fuel dissolution rate, D_{Fuel}, affects all nuclides whereas the F parameter only affects sorbing nuclides. Thus F is relatively more important for the Ra-226 dose than for the total dose, which is in some of the realisations dominated by the non-sorbing I-129. It is

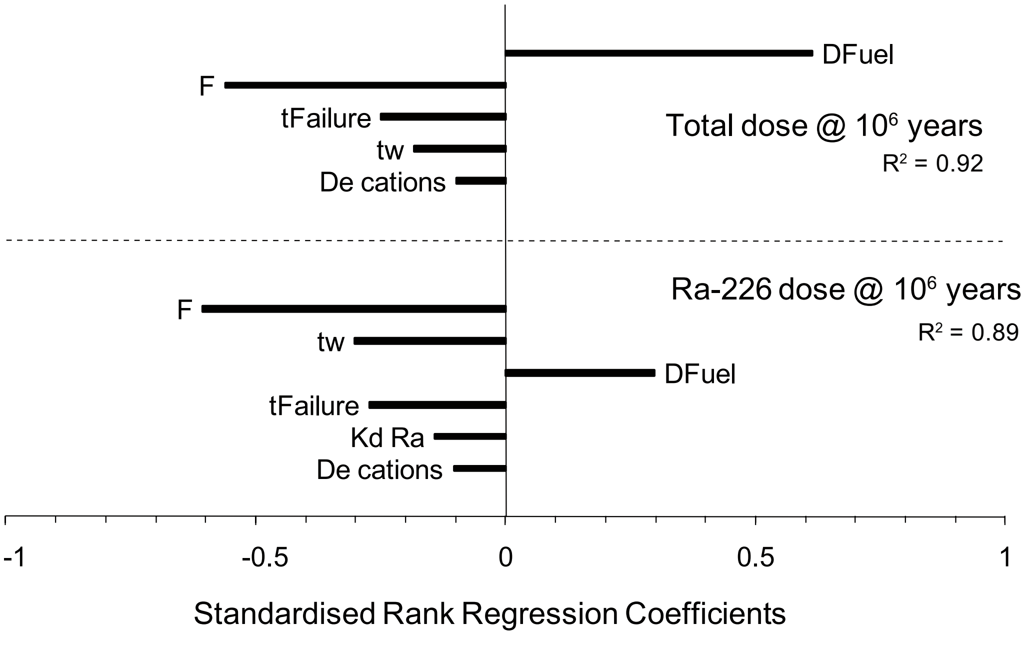

Figure 4-7. *Results of standardised rank regression for the central corrosion case. Regressing on total dose at 10^6 years and on Ra-226 dose at 10^6 years yields similar results due to the dominance of Ra-226.*

also noted that the three variables *F*, t_w (advective travel time) and $t_{Failure}$ are correlated, meaning that their significance is not necessarily as high as indicated by the SRRC method. This is further investigated with a tailored regression model, as descibed below. Standardised rank regression analysis on maximum of total dose over time yields an almost identical result as regressing on total dose at one million years (not shown in the figure). However, regressing on e.g. peak Ni-59 equivalent dose from the near field (not shown in the figure) identifies also the corrosion release rate, *CRR*, as a sensitive input variable. This sensitivity to *CRR* is consistent with the fact that in some realisations of the central corrosion case, the peak dose due to Ni-59 occurs shortly after canister failure and is then caused by the releases congruent with the corrosion of the metal parts of the fuel assemblies.

Main risk contributors

The standardised rank regression analysis identifies the variables that co-vary with the dependent variable, the total dose, over the entire dose range. To determine the variables that are related to the highest doses, a conditional mean value analysis /Hedin 2002a/ was carried out. Here, the subsets of input parameter values related to the top percentile of the dose are selected. For each such subset, the mean value of the logarithmically transformed data was determined for each parameter and compared to the corresponding mean value of the entire input distribution. A dimensionless, normalised measure, α99, is obtained by dividing the difference between the two mean values by the standard deviation of the entire distribution.

The so determined conditional mean value identifies variables that take on significantly different values in the top percentile realisations compared to the entire dose distribution. In descending order, the $t_{Failure}$, D_{Fuel}, *F* and t_w parameters were identified as most significant, see Figure 4-8. Similarly, α1-values, relating to the lowest percentile of the dose distribution were determined. Also α99 − α1 values were determined to distinguish extreme outcomes from others. The highest ranking variables were, in descending order, D_{Fuel}, *F*, t_w (t_w is strongly correlated to *F*) and $t_{Failure}$.

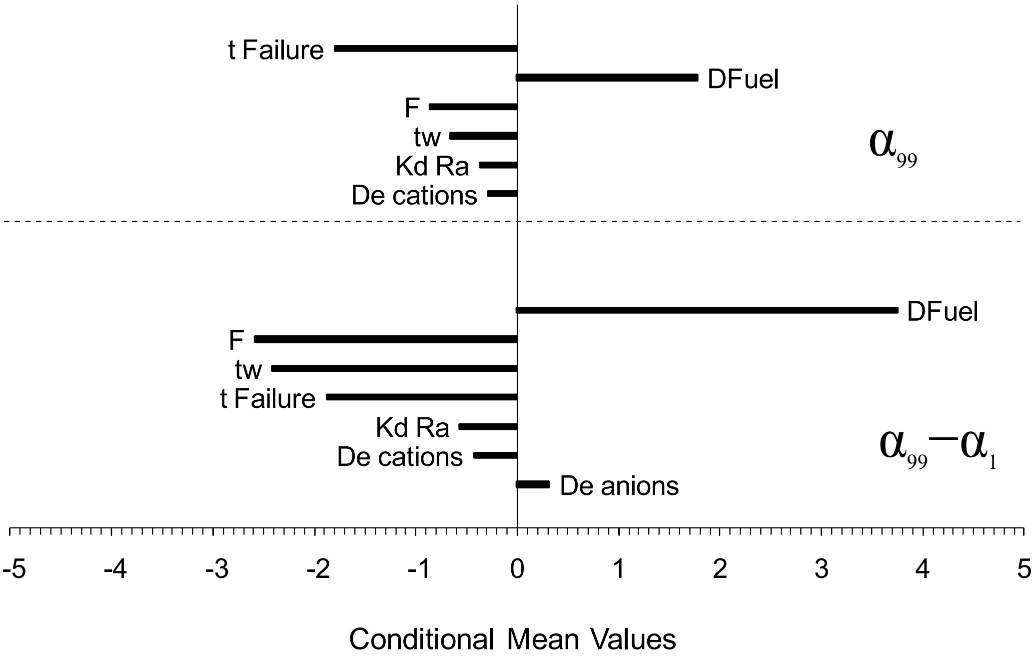

Figure 4-8. Conditional mean values for the central corrosion case.

Tailored regression model

The understanding and mathematical formulation of the transport models used in the dose calculations can be utilised to further explain the results. The release rate of Ra-226 is determined by the amount of its parent nuclide, Th-230, liberated from the fuel matrix and subsequently assumed to sorb in the near field. This amount is proportional to the product of the fuel dissolution rate, D_{Fuel}, and the time, t, elapsed between the canister failure and the point in time for which the dose is calculated, i.e. it is proportional to $D_{Fuel} \cdot t$. In the studied case $t = 10^6 - t_{Failure}$. It can further be shown that the released Ra-226 is transported through the geosphere with a certain transmission efficiency, θ, that in its full expression depends in a complex way on all the uncertain parameters relating to geosphere transport, see e.g. /Hedin 2002b/. However, it can also be demonstrated that most of the variability of θ is captured by the simpler expression /Hedin 2003/:

$$\theta \propto \exp\left(-cF^{0.5}\left(K_dD_e\right)^{0.25}\right) \tag{4-1}$$

where c is a positive constant determined by well known properties like the density of the rock and the half-life of Ra-226. This suggests that the Ra-226 dose varies according to:

$$\log\left(DoseRa226\right) = Constant + \log\left(D_{Fuel}t\right) - cF^{0.5}\left(K_dD_e\right)^{0.25} \tag{4-2}$$

and that a tailored regression model according to the above expression could be successful in explaining the calculated results. Figure 4-9 shows how such a regression model is able to predict the calculated results when successively more terms are included in the model. As seen in the figure, the agreement when all terms are included is good, with an R^2-value of 0.99.

These expressions also reveal combinations of input variables of importance. Obviously, combinations of high D_{Fuel} and t values and combinations of low values of the three factors occurring in the exponent of the first expression favour high doses. This result also illustrates that the variable t_w, identified as important for the Ra-226 dose by the SRRC method above is not needed to explain the Ra-226 dose. It is concluded that t_w is identified in the SRRC method only since it is correlated to the F parameter. (This can be further analysed through use of partial rank correlations in the SRRC method.)

A *partition plot*, Figure 4-10, showing how high and low dose results relate to the variable groups $D_{Fuel} \cdot t$ and $F^{0.5}(K_d \cdot D_e)^{0.25}$ confirms the explanatory power of these variable groups.

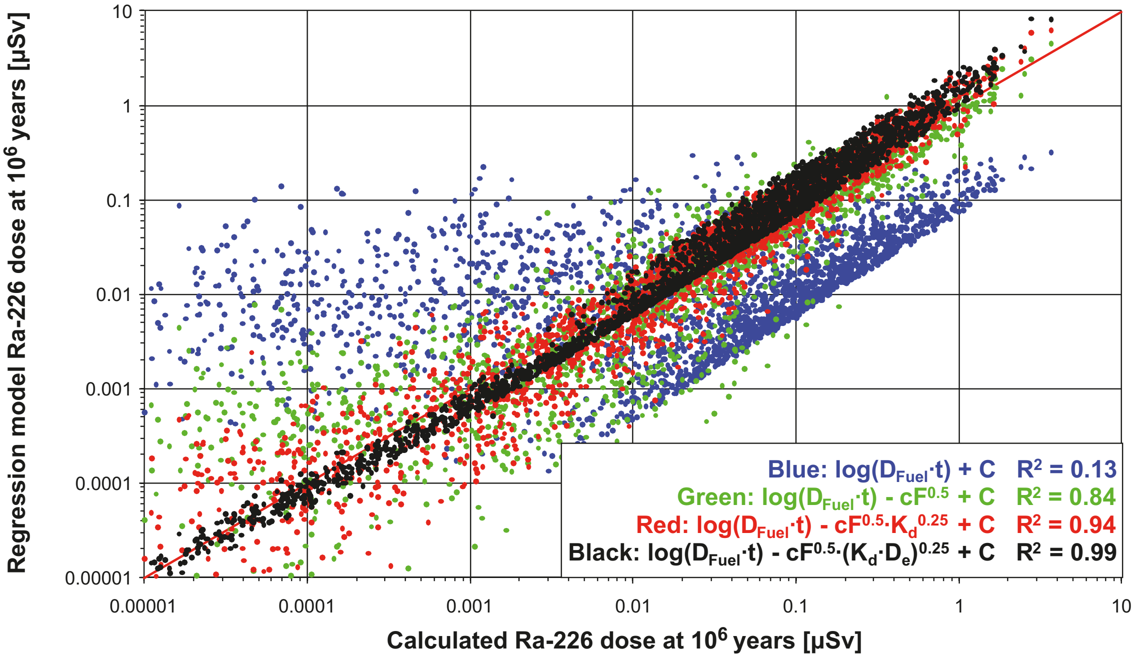

Figure 4-9. *Four tailored regression models, including successively more variables, for the Ra-226 dose at one million years for the central corrosion case.*

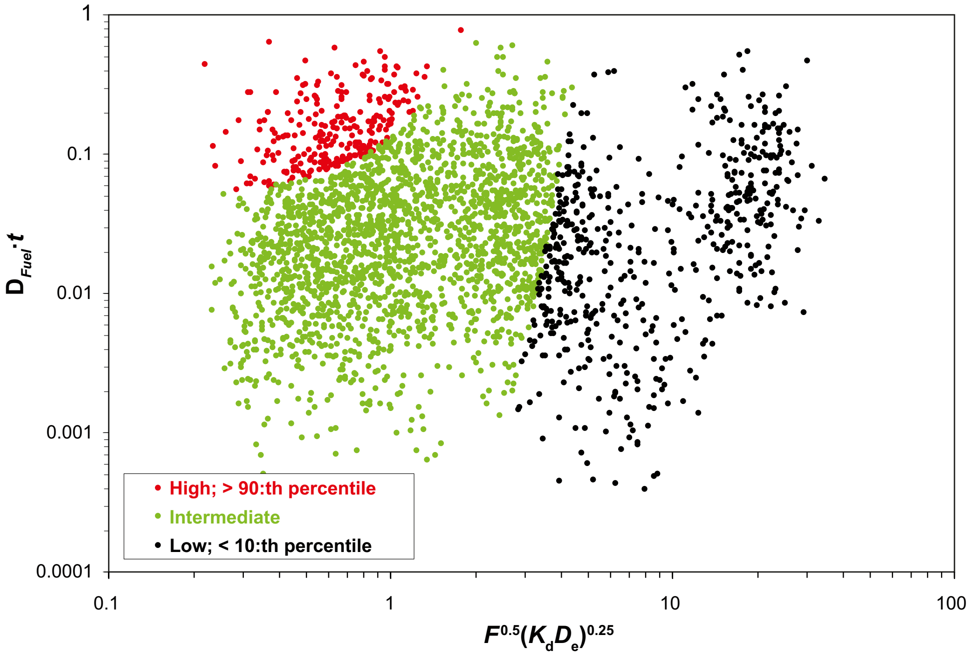

Figure 4-10. *Partition plot demonstrating how the two groups of variables on the axes relate to high and low dose results for Ra-226 for the central corrosion case.*

Conclusions

The above analyses show that relatively simple methods can identify the uncertain input parameters to which the probabilistic result is most sensitive. That sensitivities can be identified with relatively simple methods is in part due to the nature of the conceptualisation of the calculation cases in the corrosion scenario, where the buffer is omitted and the near-field release is essentially controlled only by the fuel dissolution rate.

The fuel dissolution rate, D_{Fuel}, and the geosphere flow-related transport resistance, F, emerge generally as the uncertain input parameters to which the result is most sensitive. The uncertainty in corrosion release rate, *CRR*, has a significant impact on the result of near-field releases immediately after failure for nuclides that are released congruently with metal corrosion.

It is also noted that a number of different assumptions regarding transport conditions are analysed in Section 4.5, where it is found that the sensitivity to these assumptions is low, see Figure 4-58 and Figure 4-59. Similar results are expected for all corrosion variants since they differ from the central corrosion case only through somewhat altered input distributions for the failure times and the hydrogeological transport parameters.

4.4.4 Issues related to the probabilistic nature of the calculations

Convergence

The number of canister failure times varies significantly in the different corrosion cases (from 56 in the central corrosion case to 1,964 in a case that does not use best available technique BAT). Data in the **Data report** have distributions and these have been used to make input files to COMP23 and FARF31 for probabilistic calculations, see Section 3.7.1. To assure a correct use of the probabilistic data, each canister failure time needs to be run several times with different sets of input (realisations). In Figure 4-11 the near-field and far-field releases of Ni-59, in the central corrosion case, are shown for different numbers of realisations per canister failure time. Both curves converge rapidly; 50 realisations were judged to be adequate and this value was used for all the corrosion cases. The choice of 50 realisations provides sufficient accuracy in the statistics without excessive total calculation times.

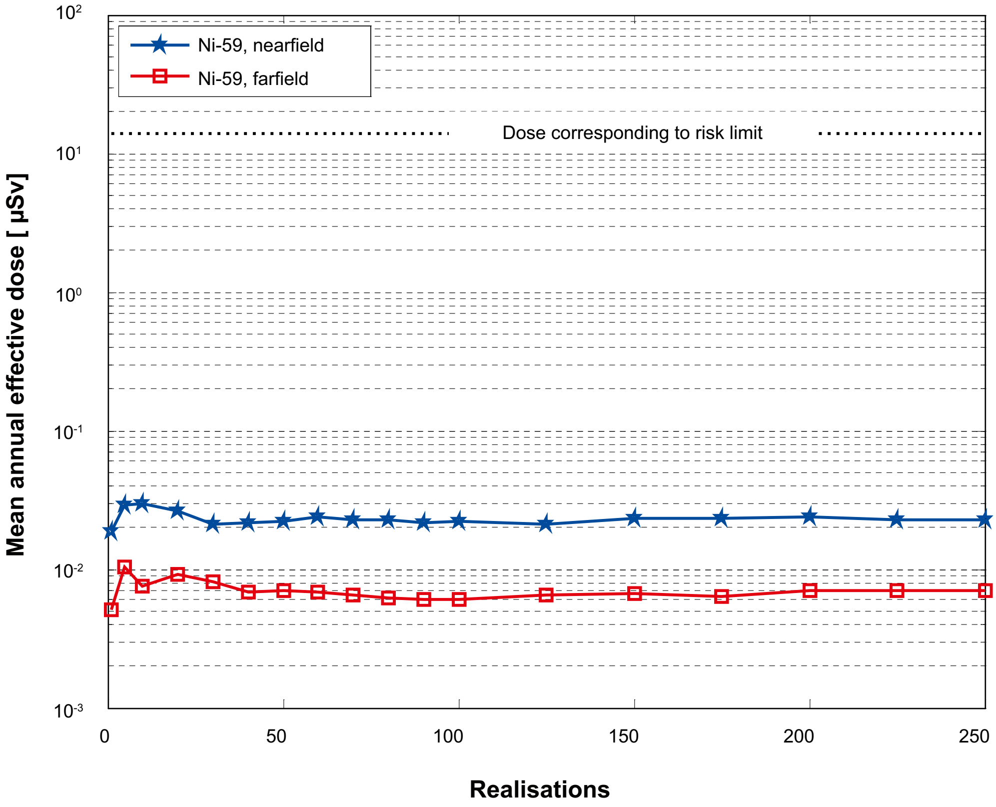

***Figure 4-11.** Mean annual effective dose for Ni-59 as a function of the number of realisations in the central corrosion case.*

Risk dilution

The issue of risk dilution is discussed in the methodology Section 2.6.2 in the **Main report** and needs to be addressed for the corrosion scenario. Doses are accounted for as a continuous contribution and as a relatively short pulse contribution.

In all probabilistic cases of the corrosion scenario, a fixed number of canisters, depending on the case studied, were assumed to fail at a set of fixed times. Thus, this factor cannot give rise to risk dilution. Regarding the pulse releases, these are given as peak doses for an assumed, single release of the entire IRF inventory and can thus not give rise to risk dilution.

The continuous contributions have, for a fixed failure time, an initial peak of limited duration followed by an increasing dose that generally grows beyond the value of the initial peak. Because this means that the maximum dose occurs at the end of the one million year assessment time, risk dilution is not an issue for the continuous contributions; the maximum risk is experienced by the same hypothetical generation living at the end of the assessment period irrespective of failure time. This is verified by comparing the peak-of-the-mean value (0.177 µSv/yr) to the mean-of-the-peaks value (0.179 µSv/yr) for the central corrosion case.

Risk dilution, including a treatment of the pulse releases, is further discussed in Section 13.9 in the **Main report**.

4.5 Alternative cases based on the semi-correlated hydrogeological DFN model

In order to assess the sensitivity of the results to various assumptions, a set of alternative cases based on the semi-correlated hydrogeological DFN model have been undertaken.

4.5.1 Disregarding thorium sorption in the near field

Deterministic calculations

Hydrogeological case:	Semi-correlated, ten realisations
Erosion/corrosion model:	SR-Site model
Failure time:	114,485 years
Number of failed canisters:	1
Solubility limits:	No
Thorium sorption in near field:	**No**
Number of realisations:	1
Number of nuclides:	37

A deterministic calculation of the central corrosion case disregarding thorium sorption in the near field is performed to assess the sensitivity of the release of primarily Ra-226 due to alternative transport conditions for thorium.

The calculation of the IRF-pulses for the deterministic central corrosion case is also valid for the case disregarding thorium sorption in the near field. Hence, Table 4-4 shows the peak annual doses from the pulse releases from the instantly released fraction, IRF.

Figure 4-12 and Figure 4-13 show the deterministic near-field and far-field dose equivalent releases, respectively, for the central corrosion case when disregarding thorium sorption in the near field. The dose from thorium is obviously higher in this case compared to the central corrosion case. The dose caused by the release of the dose-dominating Ra-226 is lower in this case compared to the central corrosion case, showing that the assumption of thorium sorption in the near field made in the central corrosion case is pessimistic.

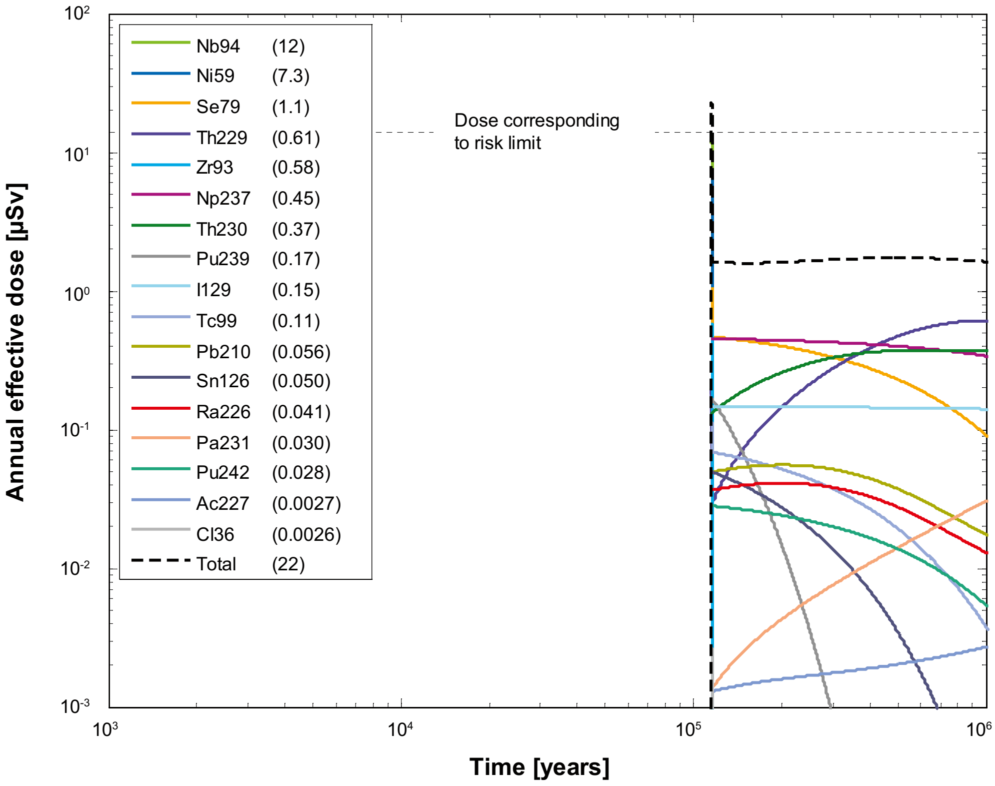

Figure 4-12. *Near-field dose equivalent release for a deterministic calculation of the central corrosion case, disregarding thorium sorption in the near field. The legend is sorted by peak (in the one-million year period) of the annual effective dose. The values in brackets are peak dose in units of µSv.*

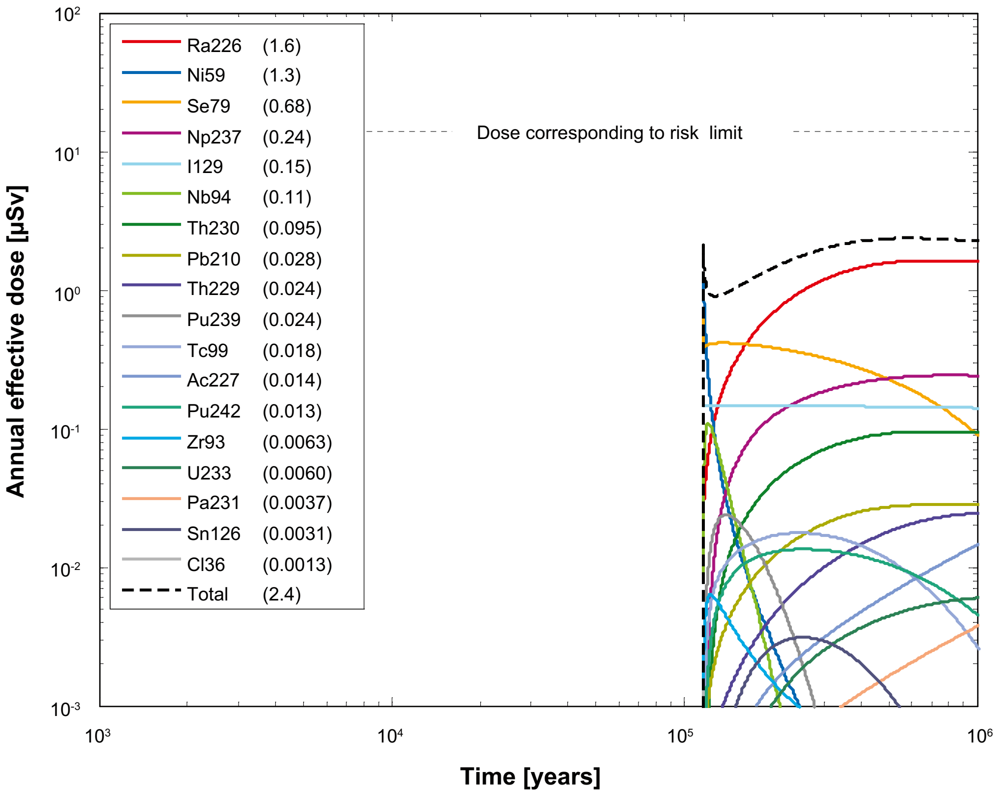

Figure 4-13. *Far-field annual effective dose for a deterministic calculation of the central corrosion case, disregarding thorium sorption in the near field. The legend is sorted by peak (in the one-million year period) of the annual effective dose. The values in brackets are peak dose in units of µSv.*

Probabilistic calculations

Hydrogeological case:	Semi-correlated, ten realisations
Erosion/corrosion model:	SR-Site model
Failure time:	56 times according to Table 4-3
Average number of failed canisters:	0.12
Solubility limits:	No
Thorium sorption in near field:	**No**
Number of realisations:	50 per canister failure time
Number of nuclides:	37

The contributions from the instantly released fraction of nuclides, IRF, are not included in the calculations except for Tc-99 that is included in the far-field calculations. The results for the IRF presented for the central corrosion case is judged to be enough to conclude that their contribution is negligible also in this case, see Section 4.4.2.

Figure 4-14 and Figure 4-15 show near-field and far-field dose equivalent releases, respectively, for the central corrosion case when disregarding thorium sorption in the near field. Doses caused by release of Ra-226 and the total dose are both lower than in the central case, showing that the assumption of thorium sorption in the near field made in the central corrosion case is pessimistic.

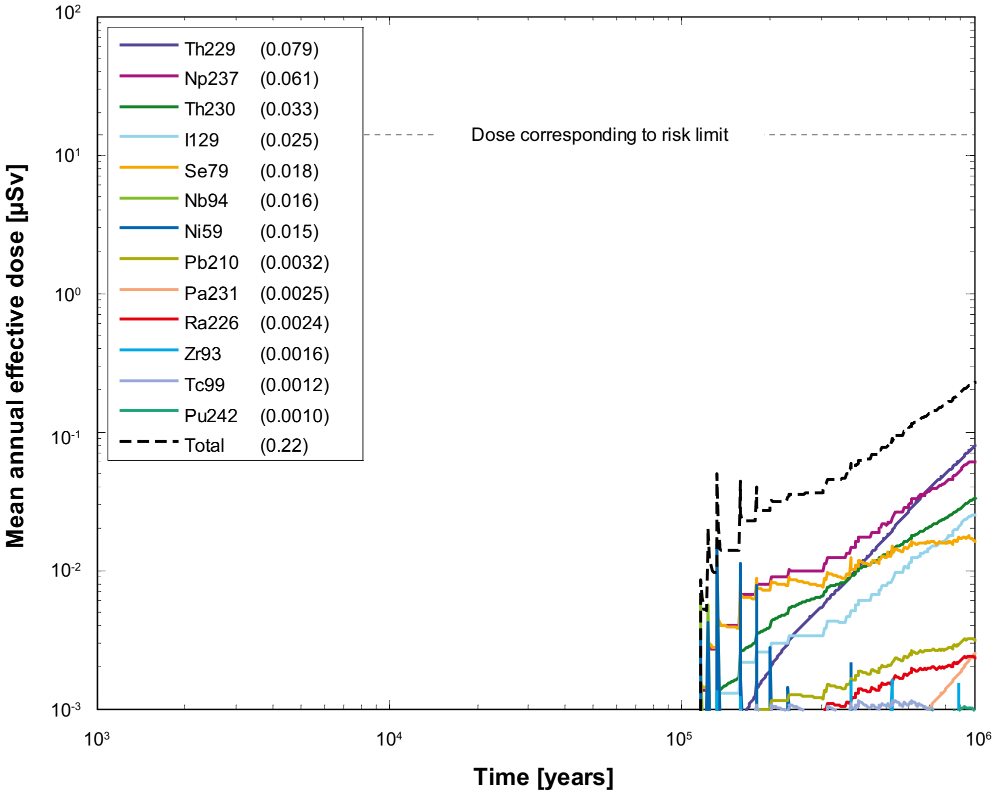

Figure 4-14. *Near-field dose equivalent release for the probabilistic central corrosion case, disregarding thorium sorption in the near field. The legend is sorted by peak (in the one-million year period) of the mean annual effective dose. The values in brackets are peak dose in units of µSv.*

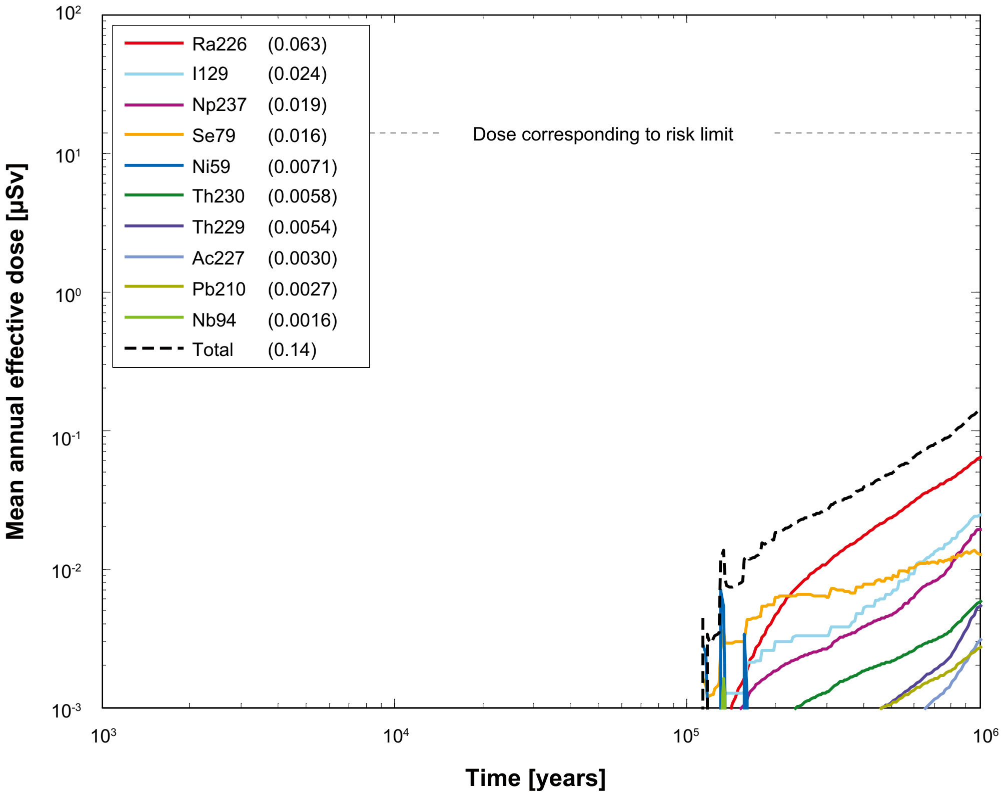

Figure 4-15. *Far-field mean annual effective dose for the probabilistic central corrosion case, disregarding thorium sorption in the near field. The legend is sorted by peak (in the one-million year period) of the mean annual effective dose. The values in brackets are peak dose in units of µSv.*

4.5.2 Including solubility limits in the near field

Deterministic calculations

Hydrogeological case:	Semi-correlated, ten realisations
Erosion/corrosion model:	SR-Site model
Failure time:	114,485 years
Number of failed canisters:	1
Solubility limits:	**Yes**
Thorium sorption in near field:	Yes (modelled as low solubility limit)
Number of realisations:	1
Number of nuclides:	37

The calculation of the IRF-pulses for the deterministic central corrosion case is also valid when including solubility limits in the near field. Hence, Table 4-4 shows the peak annual doses from the pulse releases from the instantly released fraction, IRF.

Figure 4-16 and Figure 4-17 show the deterministic near-field and far-field dose equivalent releases, respectively, for the central corrosion case when including solubility limits in the near field. The constant level of the doses caused by release of Np-237 and Zr-93 in Figure 4-16 indicate that they reach their solubility limits and hence the doses from these two nuclides are lower than in the central corrosion case. The total dose is the same as in the deterministic calculation of the central corrosion case.

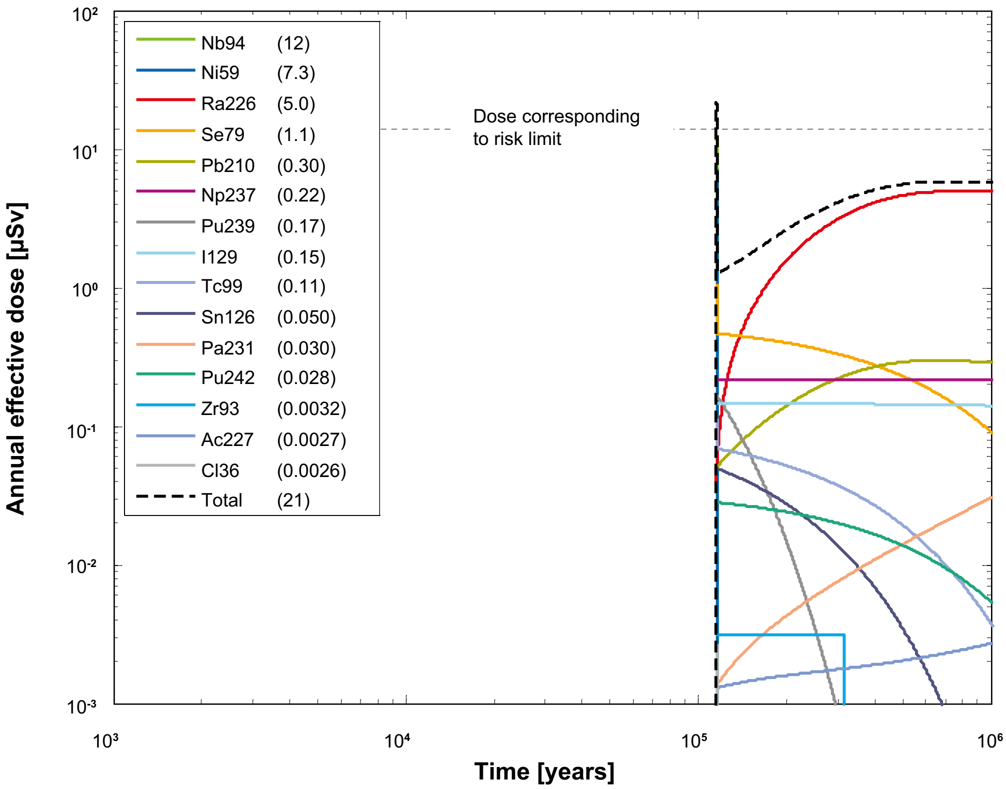

Figure 4-16. *Near-field dose equivalent release for a deterministic calculation of the central corrosion case, including solubility limits in the near field. The legend is sorted by peak (in the one-million year period) of the annual effective dose. The values in brackets are peak dose in units of µSv.*

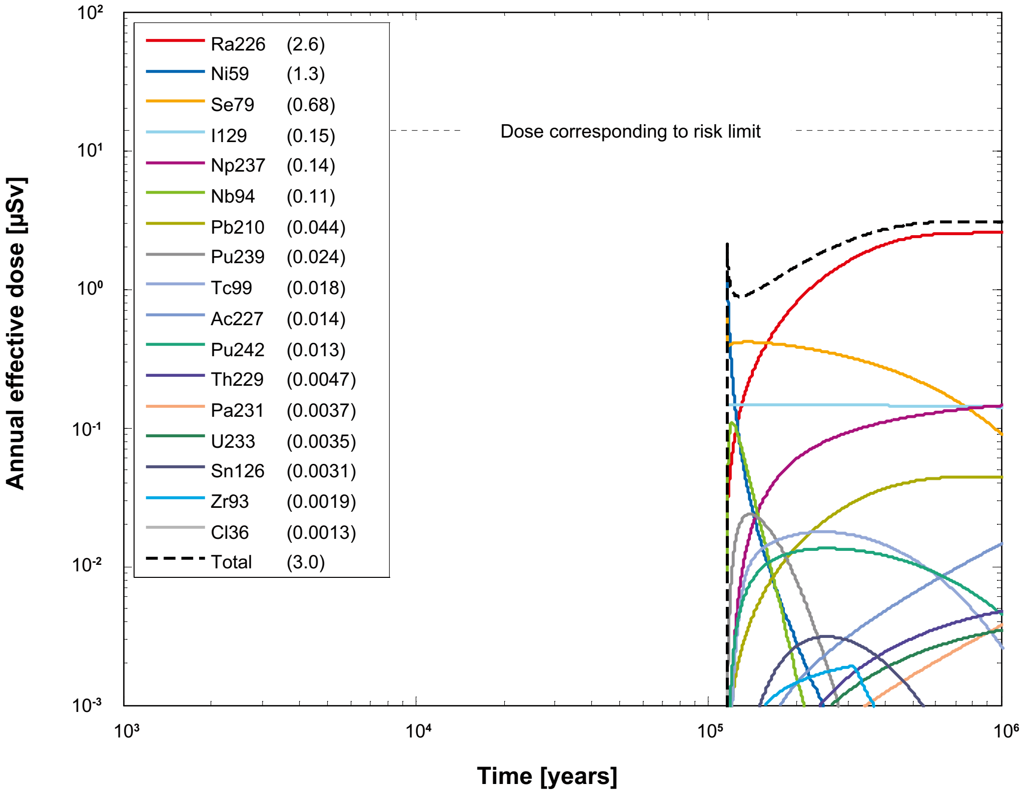

Figure 4-17. *Far-field annual effective dose for a deterministic calculation of the central corrosion case, including solubility limits in the near field. The legend is sorted by peak (in the one-million year period) of the annual effective dose. The values in brackets are peak dose in units of µSv.*

Probabilistic calculations

Hydrogeological case:	Semi-correlated, ten realisations
Erosion/corrosion model:	SR-Site model
Failure time:	56 times according to Table 4-3
Average number of failed canisters:	0.12
Solubility limits:	**Yes**
Thorium sorption in near field:	Yes (modelled as low solubility limit)
Number of realisations:	50 per canister failure time
Number of nuclides:	37

The contributions from the instantly released fraction of nuclides, IRF, are not included in the calculations except for Tc-99 that is included in the far-field calculations. The results for the IRF presented for the central corrosion case are judged to be sufficient to conclude that their contribution is negligible also in this case, see Section 4.4.2.

Figure 4-18 and Figure 4-19 show near-field and far-field dose equivalent releases, respectively, for the central corrosion case when including solubility limits in the near field. The near-field dose caused by release of Pb-210 is considerably higher than for the central corrosion case. This is due to Ra-226 reaching the solubility limit in some realisations and when Ra-226 is confined to the canister interior it generates Pb-210. The far-field doses are, however, similar to those of the central corrosion case. Pb-210 decays considerably in the geosphere because of its short half-life.

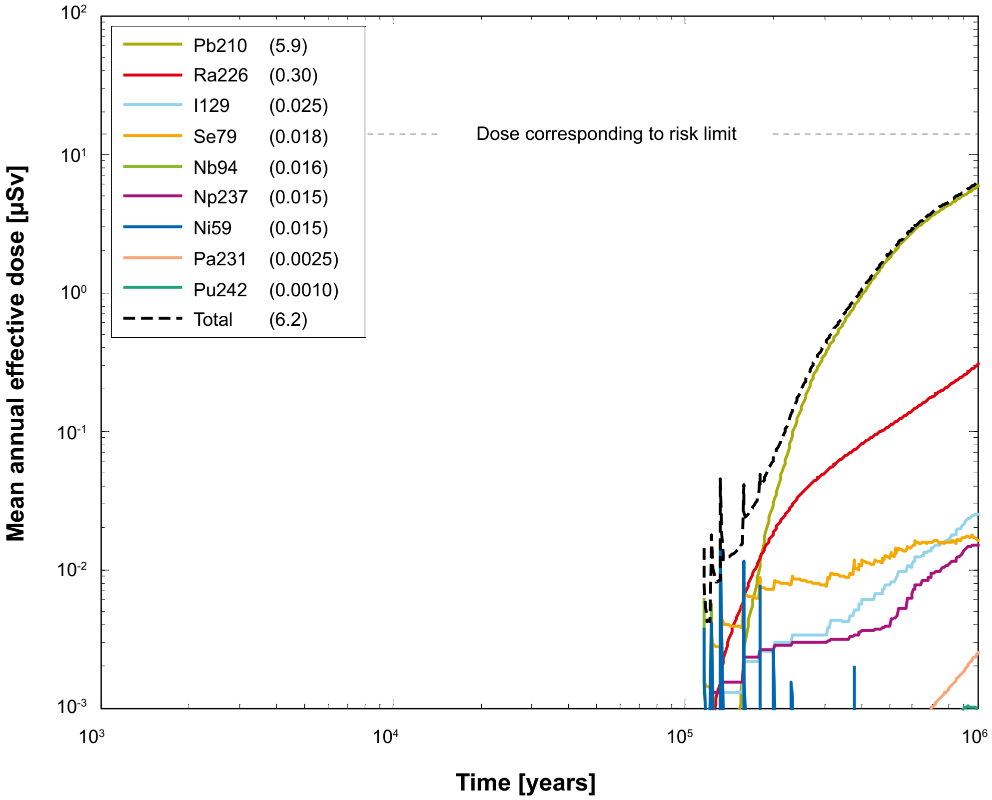

Figure 4-18. *Near-field dose equivalent release for the probabilistic central corrosion case, including solubility limits in the near field. The legend is sorted by peak (in the one-million year period) of the mean annual effective dose. The values in brackets are peak dose in units of µSv.*

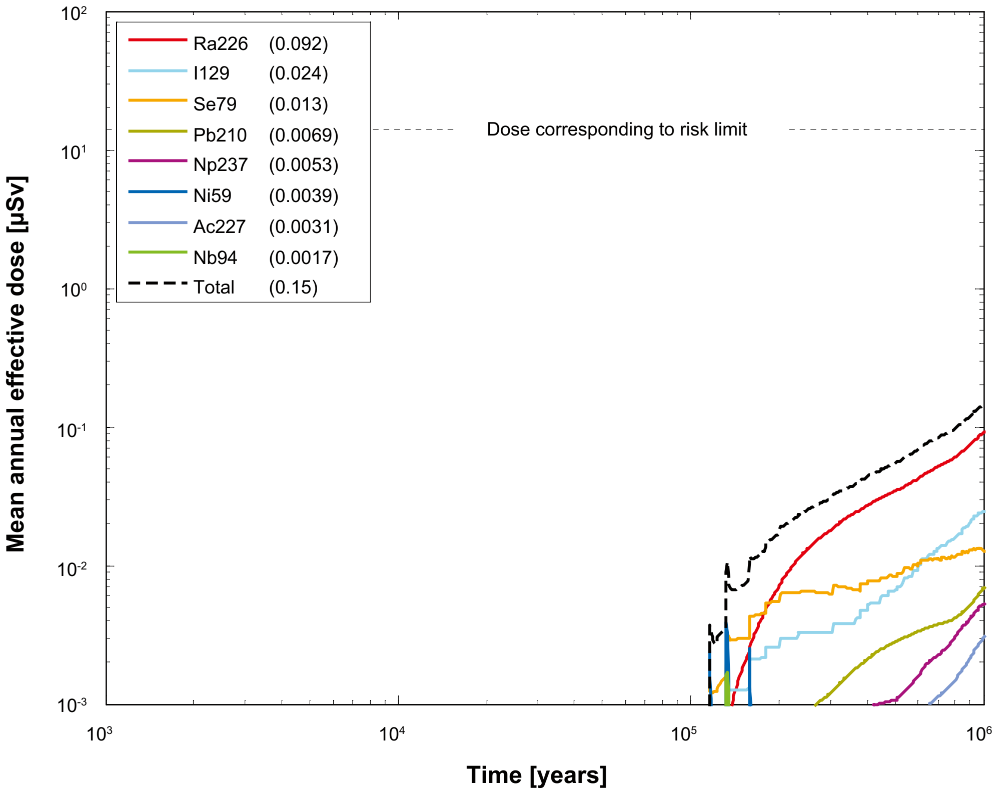

Figure 4-19. *Far-field mean annual effective dose for the probabilistic central corrosion case, including solubility limits in the near field. The legend is sorted by peak (in the one-million year period) of the mean annual effective dose. The values in brackets are peak dose in units of µSv.*

4.5.3 Decreased sorption of lead in the geosphere

In the SR-Site Bedrock K_d data report /Crawford 2010, Section 5.2.6/ it is stated: "Due to the uncertainties outlined above, a case could be made for the use of the geochemical analogue Ni(II) as a sensitivity case study in place of the data ranges given for Pb(II). It is possible, however, that the use of the Ni(II) analogue is overly pessimistic since Ni sorption appears to be more strongly influenced by ionic strength. This may be attributable to the larger first hydrolysis constant for Pb(II) which also implies stronger binding for inner sphere surface complexation. In this regard, the K_d for Pb(II) sorption is expected on theoretical grounds to be larger than that for Ni(II)." This consideration of decreased sorption of Pb(II) has been addressed in a deterministic calculation and is presented in Figure 4-20.

In comparison with the results from the deterministic calculation for the central corrosion case, Figure 4-3, the increase in the effective dose from Pb-210 is almost 20 times. However, the increase in the total dose is only 20%.

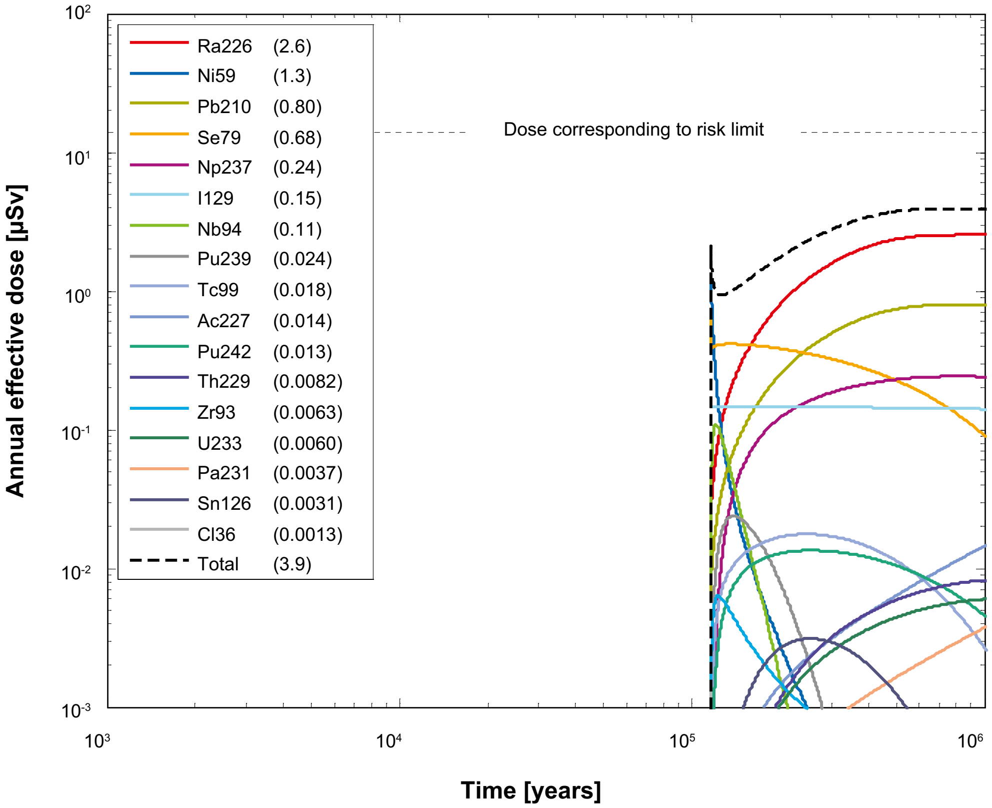

Figure 4-20. *Far-field annual effective dose for a deterministic calculation of the central corrosion case with decreased K_d for lead in the geosphere. The legend is sorted by peak (in the one-million year period) of the annual effective dose. The values in brackets are peak dose in units of µSv.*

4.5.4 K_d for U(VI) instead of U(IV) in the geosphere

All far-field calculations in SR-Site are done with K_d values for U(IV). According to /Crawford 2010/ and also described in Section 2.4.4, it cannot always be guaranteed that U(IV) is the dominant redox species in the repository volume. Therefore, the **Data report** recommends calculations with both U(IV) and U(VI). This statement only influences the K_d values in the rock.

Figure 4-21shows the far-field effective dose for a probabilistic calculation of the central corrosion case with K_d values for U(VI). Compared to the central corrosion case with K_d values for U(IV), Figure 4-5, the doses from the uranium isotopes are increased but no other nuclides are affected. The increase in release of the uranium isotopes is not high enough to affect the total dose. U-233, which increases almost 9 times to 0.0022 µSv, is the only uranium isotope that becomes high enough to be seen in the main part of the figures in this report as they have a limit down to 0.001 µSv.

Figure 4-22 shows a detailed comparison between far-field effective doses from the uranium isotopes for the central corrosion case calculated with K_d values for U(IV) and U(VI). Due to the very low releases of uranium, the limits on the y-axis have been changed in this figure.

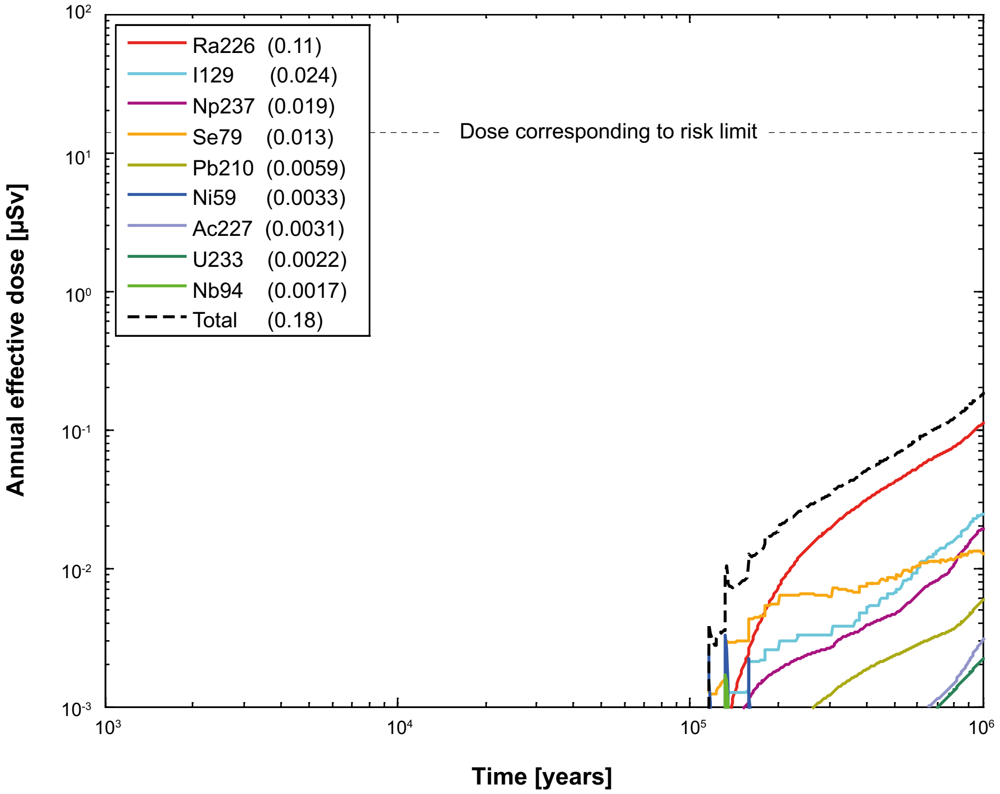

Figure 4-21. *Far-field annual effective dose for a probabilistic calculation of the central corrosion case with K_d values for U(VI). The legend is sorted by peak (in the one-million year period) of the mean annual effective dose. The values in brackets are peak dose in units of µSv.*

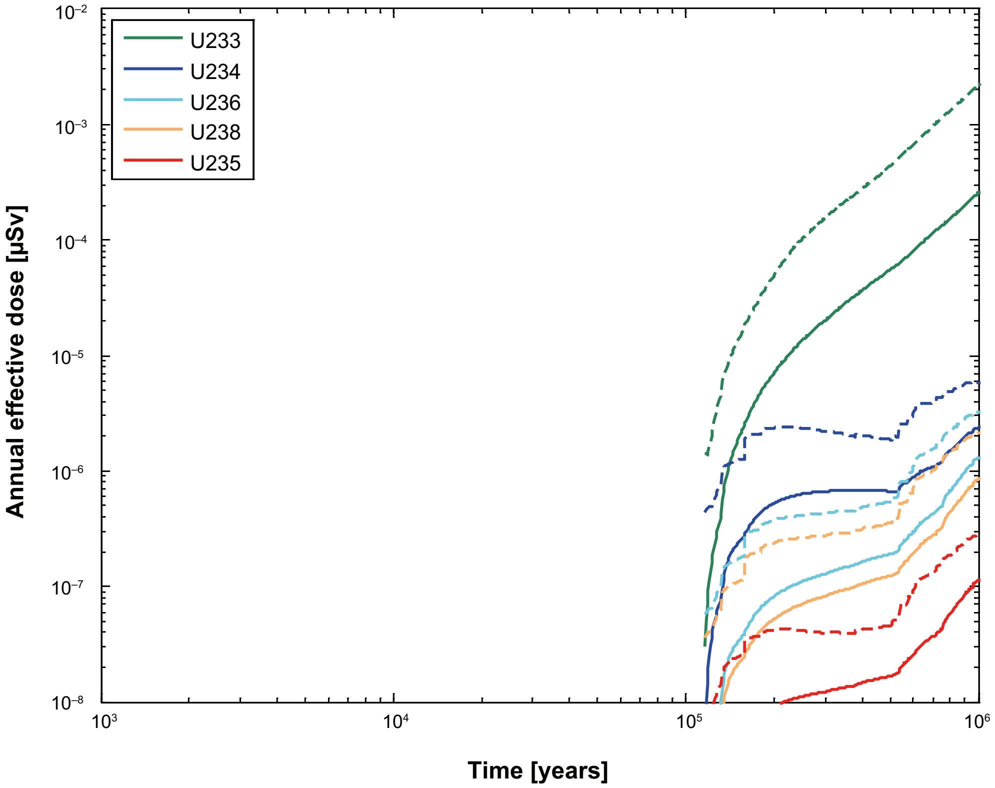

***Figure 4-22.** Comparison between far-field annual effective doses from the uranium isotopes for probabilistic calculations of the central corrosion case with K_d values for U(IV) (solid lines) and U(VI) (dotted lines). Observe the change in y-axis limits.*

4.5.5 Influence of correlation groups for K_d in the geospehere

All calculations in the SR-Site are done with five correlation groups for K_d in rock, according to the data report for the SR-Can assessment /SKB 2006b/. Late in the SR-Site process, when most of the calculations were done, the correlation groups were changed from five to two. The purpose of the calculations presented in this section is to investigate whether the change has any considerable influence on the releases from the far field.

Four cases are used to investigate the influence of correlation groups for K_d in rock. In all cases in this investigation the same releases from the near field, the probabilistic calculation of the central corrosion case, is used as input to the FARF31 calculation. The other input parameter that may influence the far-field releases is D_e for rock. D_e is always fully correlated in SR-Site and in all calculation cases in this comparison except for the case with no correlations, where D_e also is uncorrelated. The following four cases are calculated:

- without any correlation groups,
- fully correlated case, i.e. one correlation group,
- two correlation groups, (according to the **Data report**)
- five correlation groups (according to the data report for SR-Can /SKB 2006b/.

It is not possible to see any differences between the four cases, see Figure 4-23. The conclusion is that the correlation groups have negligible influence on the results. Hence, no corrections have been done to the calculations due to the change in correlation groups for K_d. In addition it is concluded that the influence of correlations for D_e is negligible.

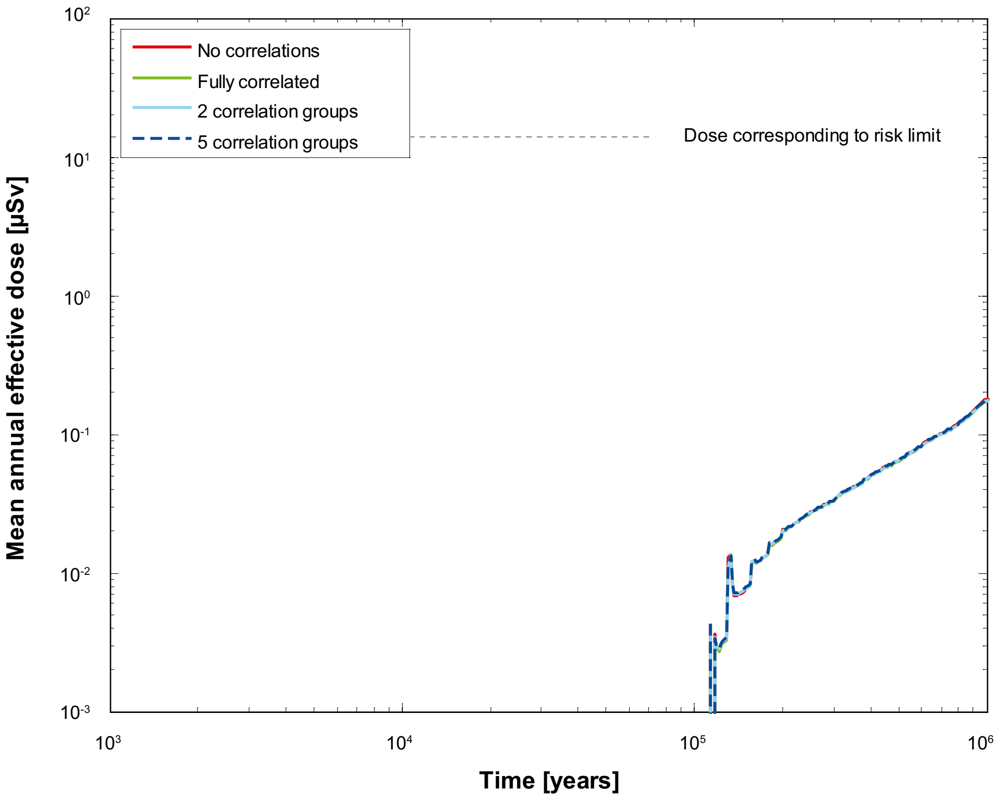

Figure 4-23. *Far-field mean annual effective dose for probabilistic calculations of the central corrosion case with different correlations for* K_d *and* D_e *for rock.*

4.5.6 Colloid-facilitated transport

The presence of bentonite material in tunnel backfill and borehole buffer is expected to result in bentonite colloids in the groundwater near deposition holes and along the geosphere transport pathways. Radionuclides that have a strong affinity for bentonite will sorb onto bentonite colloids and may be transported through the geosphere with reduced interaction with the rock matrix, i.e., with a reduced retention. Colloid facilitated transport involves a complicated combination of processes, many of which can mitigate the transport. Mitigating processes include colloid retardation in fractures, physical filtration (straining) of colloids in fractures, colloid flocculation and sedimentation, saturation of sorption sites on colloids, and competition for sites on colloids. These processes are uncertain or involve uncertain parameters that are difficult to quantify in short duration experiments. Rather than attempting to develop detailed process models for colloid-facilitated transport, potential mitigating processes are ignored so as to place an upper bound on the possible effect. Ignoring these potential mitigating processes and taking into consideration that sorption of radionuclides onto bentonite is understood to be a reversible process on the time scale of geosphere transport /**Buffer, backfill and closure process report**/, the effect of colloids in facilitating transport may be modelled through the introduction of effective transport parameters as described in Appendix I. The effective parameters depend on the colloid concentration and on the equilibrium partitioning coefficient for sorption onto colloids.

Colloid concentrations that can be stably supported are highly sensitive to groundwater chemistry. It has been determined /Wold 2010/ that 10 mg/l is a reasonably pessimistic value for colloid concentrations for typical groundwater chemistries. However, this value may be higher during brief periods when dilute glacial melt water enters the geosphere. A value of 10 g/l has been determined to be a pessimistic value for colloid concentrations in very dilute waters /**Buffer, backfill and closure process report**/.

The partitioning coefficient for sorption onto bentonite colloids K_c may be related to the same parameter for sorption onto bentonite buffer material K_d as $K_c = \gamma K_d$ where γ is a ratio of specific surface areas for colloidal and bulk bentonite. Given that bentonite is a fine-grained material and that equilibrium partitioning coefficients for bentonite are typically measured using colloidal suspensions with particle sizes less than 1 µm, $\gamma \approx 1$ is a reasonable assumption. Thus, K_c distributions were taken from the **Data report** Section 5.3.

Using the MARFA transport code and the effective parameters derived in Appendix I, the effects of colloids are demonstrated in Figure 4-24. Except for the effects of colloids, this modelling case is identical to the central corrosion base case in Section 4.4.2. The dark blue curve is near-field mean-annual release expressed as an effective dose, the black curve is the far-field mean-annual effective dose without colloids. The green and pink curves are the far-field doses with colloid concentrations of 10 mg/l and 10 g/l, respectively.

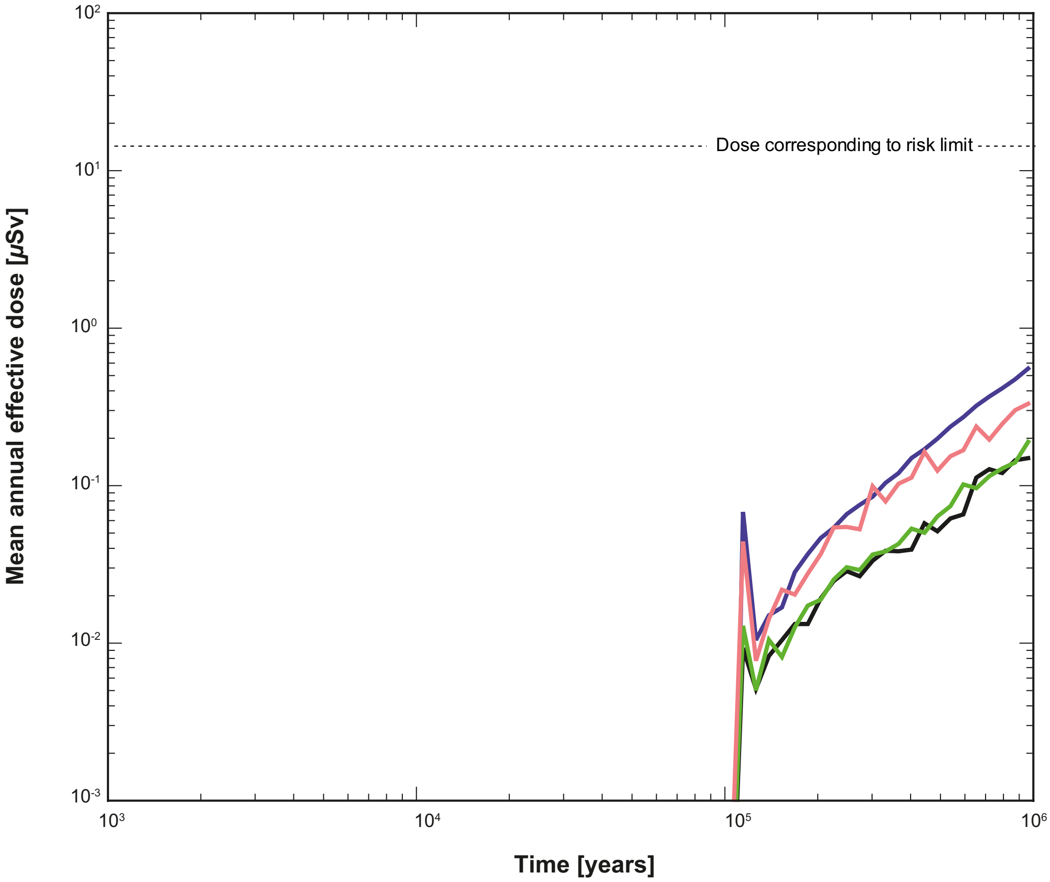

Figure 4-24. *Mean annual effective dose for the probabilistic central corrosion case, with and without the effects of bentonite colloids in facilitating transport. The black, green, and pink curves are far-field dose with colloid concentrations of 0 mg/l, 10 mg/l, and 10 g/l, respectively. The dark blue curve is the near-field dose equivalent release.*

4.5.7 Varying climate conditions

MARFA simulations are undertaken to address the corrosion scenario for a case with unsteady flow caused by climate evolution.

The transport simulations are identical to the central corrosion case described in Section 4.4.2 except for the use of the flow scaling factors shown in Figure 2-3 and the use of sorption K_d-values for oxidising conditions for the redox sensitive elements during ice front passages (i.e., during the time periods when flow scaling factors are 20 and 50, respectively). In addition, different dose conversion factors (LDFs) are applied for different periods in the glacial cycle. The near-field release calculations used as input to the MARFA simulations do not take into consideration the changes in flow. This simplification is based on the fact that releases of radioelements that are not solubility limited will be limited by the rate of waste-form dissolution, which is independent of flow rate.

Mean annual effective dose versus time for this case is show in Figure 4-25. Also shown is the case without flow changes, i.e., with temperate flow throughout the assessment period. The results are based on 2,800 realisations where both near-field and far-field parameters follow distributions, as described in Section 3.7.1.

The results in Figure 4-25 indicate that the flow, K_d and LDF changes collectively cause a slight increase in peak dose. However, the main effect is the sharp downward spikes in dose during the time of glacial approach and retreat. Although the radionuclide discharge to the biosphere is increased sharply during these periods due to changes in flow and, more importantly, changes in K_d for redox-sensitive radionuclides, this increase is more than compensated by the greatly reduced LDF factors during these periods.

The results without flow changes can also be compared to the corresponding case calculated using FARF31, see Section 4.4.2, showing very similar total dose results.

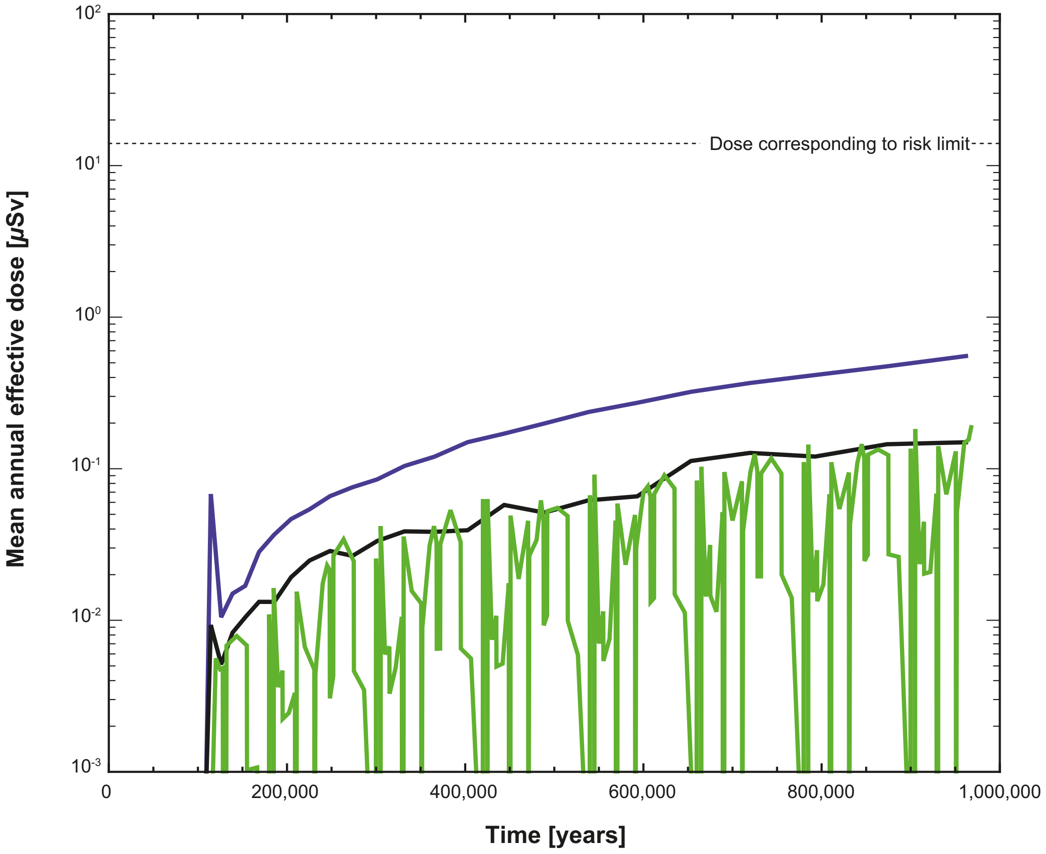

Figure 4-25. *Far-field annual effective dose (green curve) for a probabilistic calculation of the central corrosion case with varying climate conditions. For comparison the near-field dose equivalent release (blue curve) and also the far-field dose (black curve) without flow changes are given.*

4.5.8 Varying climate conditions and colloid-facilitated transport

MARFA calculations are undertaken to evaluate the simultaneous effects of varying climate conditions and colloid-facilitated transport. The simulations are identical to those in Section 4.5.7 except for that the colloid facilitated transport model of Section 4.5.6 is used. As has been noted, 10 mg/l has been determined to be a reasonable value for colloid concentration except during periods where dilute groundwater is expected to contact clay minerals in buffer and backfill. During the periods of dilute groundwater 10 g/l is used for the colloid concentration.

Results for a case with colloid concentration held constant at a high value of 10 g/l is shown in Figure 4-26. By comparing with Figure 4-25 it can be seen that colloids enhance transport over the colloid-free case and that the far-field dose approaches the near-field dose during the temperate period. Mean annual dose is not significant increased in the other periods because the LDF factors are lower then.

Results for a case with varying colloid concentration is shown in Figure 4-27. In this case, the colloid concentration is 10 g/l during periods of dilute groundwater and 10 mg/l otherwise. Dilute groundwaters are assumed to exist during the brief periods of glacial retreat/advance and also during the second halves of the glacial maximum and temperate periods /**Climate report**/. Results are similar to those of Figure 4-26 except that the period of colloid-enhanced dose is limited to the second half of the temperate period.

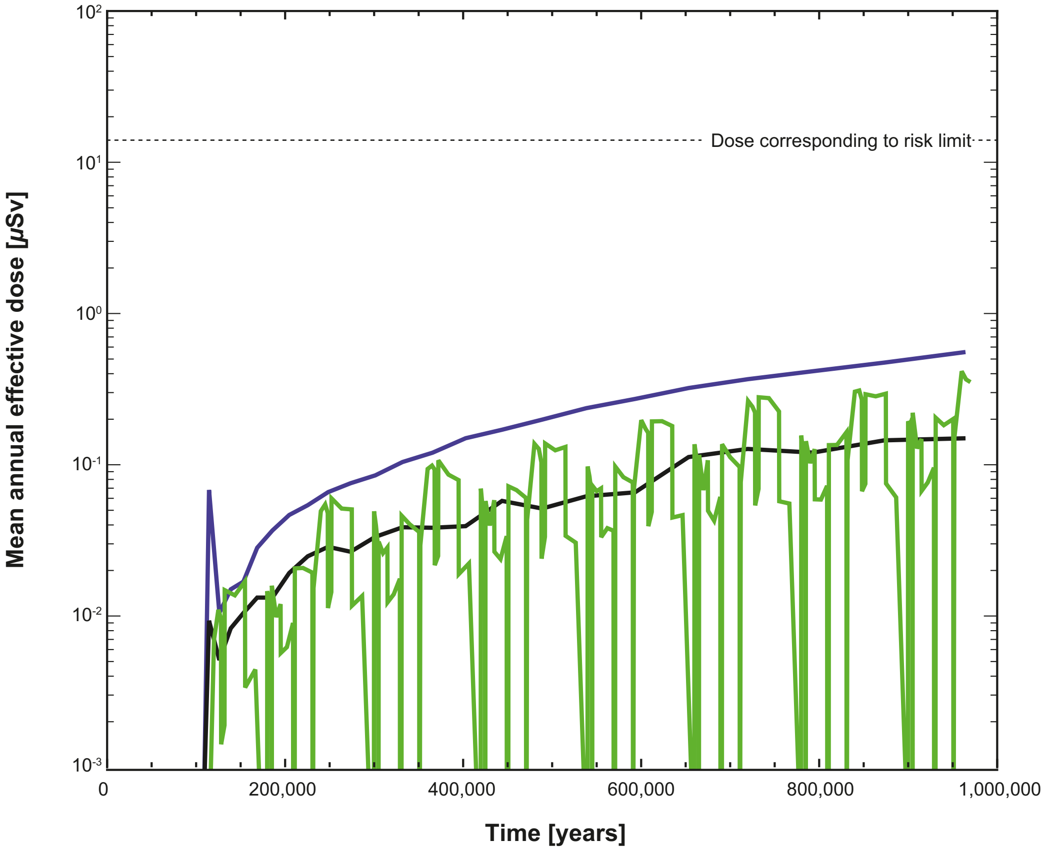

Figure 4-26. *Far-field annual effective dose (green curve) for a probabilistic calculation of the central corrosion case with varying climate conditions and colloid-facilitated transport of actinides and transition metals. For comparison the near-field dose (blue curve) is given. The colloid concentration is constant in this case and has a value of 10 g/l.*

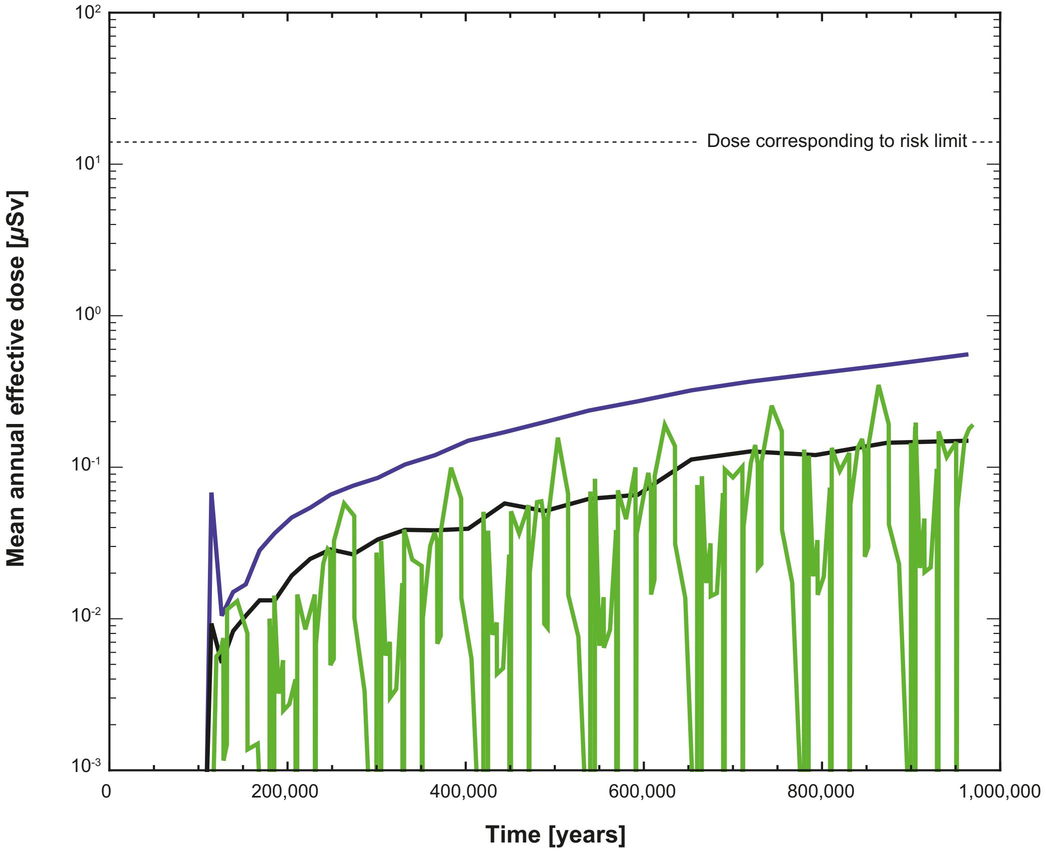

Figure 4-27. *Far-field annual effective dose (green curve) for a probabilistic calculation of the central corrosion case with varying climate conditions and colloid-facilitated transport of actinides and transition metals. For comparison the near-field dose (blue curve) is given.*

4.5.9 Initial advection

Deterministic calculations

Hydrogeological case:	Semi-correlated, ten realisations
Erosion/corrosion model:	Initial advection
Failure time:	44,049 years, according to Table 4-2
Number of failed canisters:	1
Solubility limits:	No
Thorium sorption in near field:	Yes (modelled as low solubility limit)
Number of realisations:	1
Number of nuclides:	37

A deterministic calculation of the semi-correlated case with initial advection is performed for a canister taken from the realisation with the earliest failure time of the analysed realisations, (44,049 years after deposition) with corresponding geosphere transport data, i.e. data used to calculate the corrosion time are from the same hydrogeological calculation as the geosphere transport data. Advection occurs in the buffer void and the dose equivalent releases are primarily determined by the fuel dissolution rate set to 10^{-7}/yr. Table 4-4 shows the peak annual doses from the pulse releases from the instantly released fraction, IRF.

Figure 4-28 and Figure 4-29 show the deterministic near-field and far-field dose equivalent releases, respectively, for the semi-correlated case with initial advection. Note that the peak in Figure 4-28 reaches outside the figure (doses larger than 100 µSv) but the real maximum doses are given in brackets in the figure legend. Doses from the near field are dominated by releases of Nb-94 and Ni-59 shortly after canister failure and by Ra-226 in the longer term. Doses from the far field are dominated by releases of Ra-226.

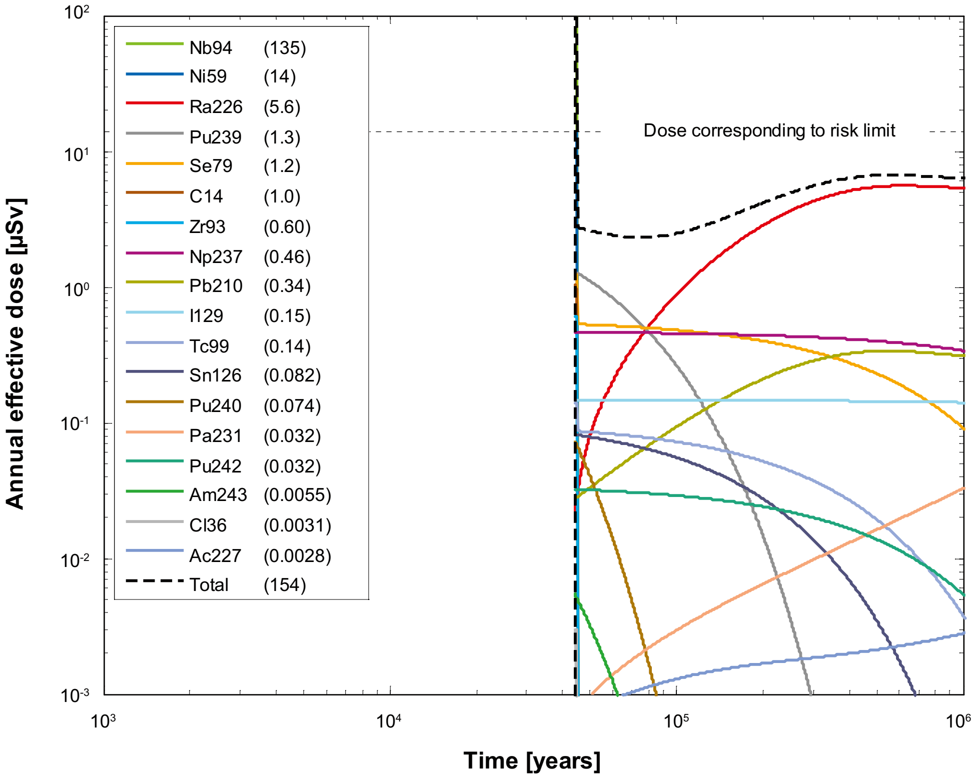

Figure 4-28. *Near-field dose equivalent release for a deterministic calculation of the central corrosion case, with initial advection in the erosion/corrosion model. The legend is sorted by peak (in the one-million year period) of the annual effective dose. The values in brackets are peak dose in units of µSv. Note that the dose equivalent release for Nb-94 is 135 µSv/year, i.e. above the limit of the y-axis.*

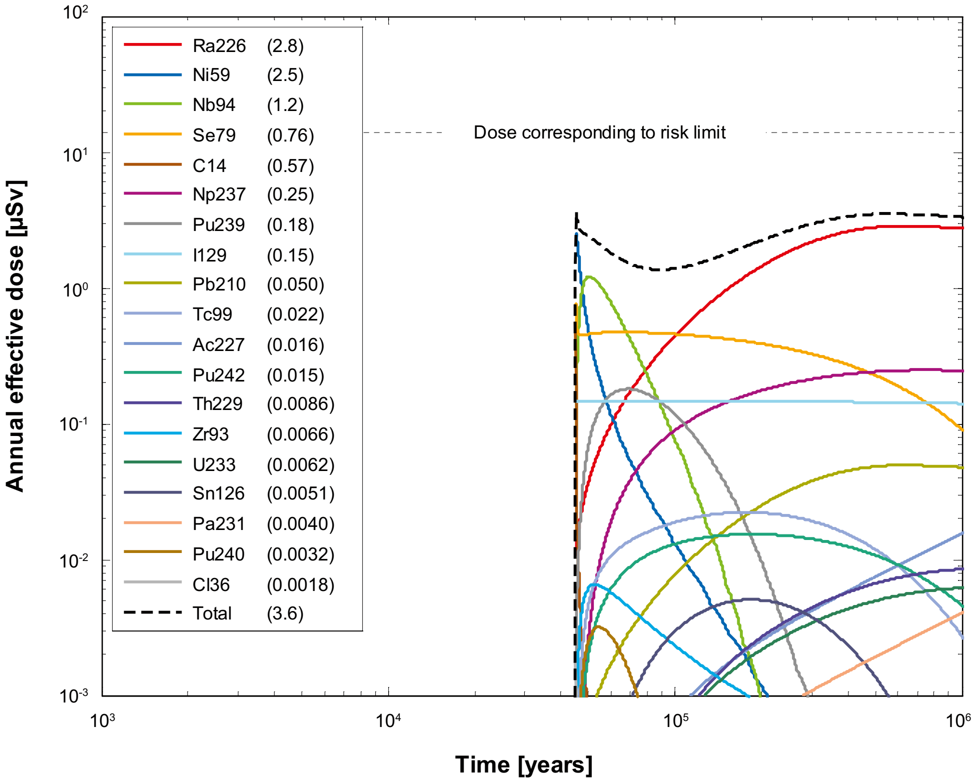

Figure 4-29. *Far-field annual effective dose for a deterministic calculation of the central corrosion case, with initial advection in the erosion/corrosion model. The legend is sorted by peak (in the one-million year period) of the annual effective dose. The values in brackets are peak dose in units of µSv.*

Probabilistic calculations

Hydrogeological case:	**Semi-correlated, ten realisations**
Erosion/corrosion model:	**Initial advection**
Failure time:	**84 times according to the erosion/corrosion calculations**
Average number of failed canisters:	**0.17**
Solubility limits:	No
Thorium sorption in near field:	Yes (modelled as low solubility limit)
Number of realisations:	50 per canister failure time
Number of nuclides:	37

A probabilistic calculation of the semi-correlated case with initial advection is performed with failure times and geosphere transport data from the ten realisations of the semi-correlated DFN model and failure times from the corrosion calculations with initial advection. The contributions from the instantly released fraction of nuclides, IRF, are not included in the calculations except for Tc-99 that is included in the far-field calculations. The results for the IRF presented for the central corrosion case are judged to be sufficient to conclude that their contribution is negligible also in this case, see Section 4.4.2.

Figure 4-30 and Figure 4-31 show the near-field and far-field dose equivalent releases, respectively, for the semi-correlated case with initial advection. The total dose in the longer term is about 1.5 times higher than in the central corrosion case and is dominating by Ra-226.

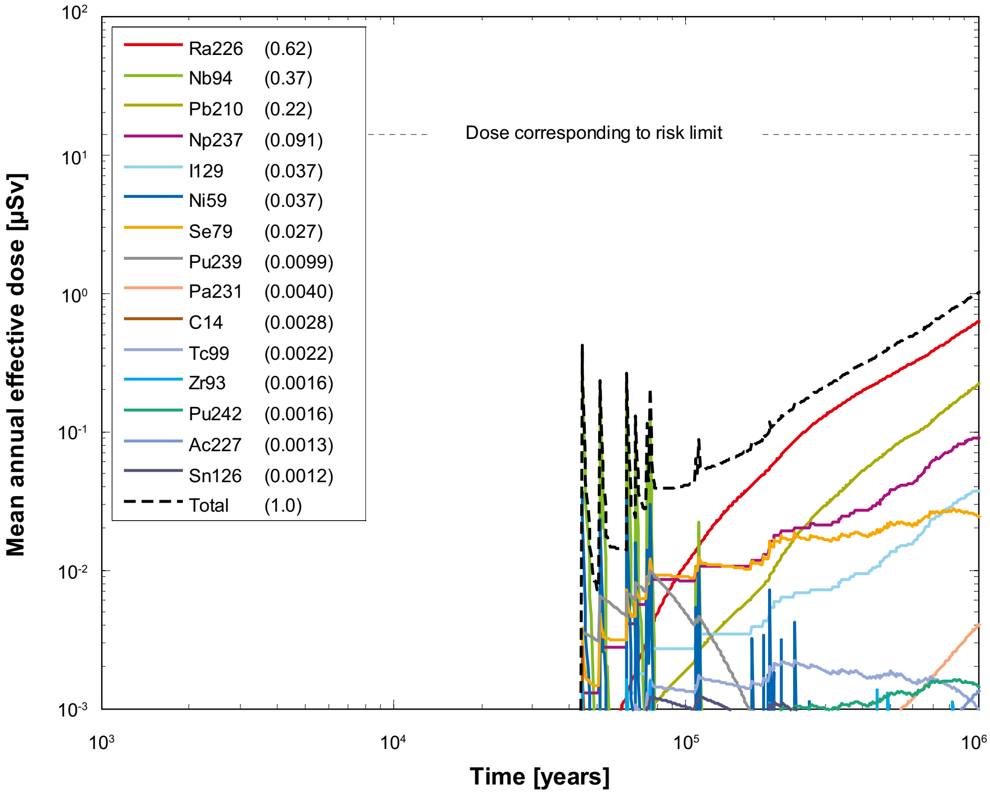

Figure 4-30. *Near-field dose equivalent release for a probabilistic calculation of the central corrosion case, with initial advection in the erosion/corrosion model. The legend is sorted by peak (in the one-million year period) of the mean annual effective dose. The values in brackets are peak dose in units of µSv.*

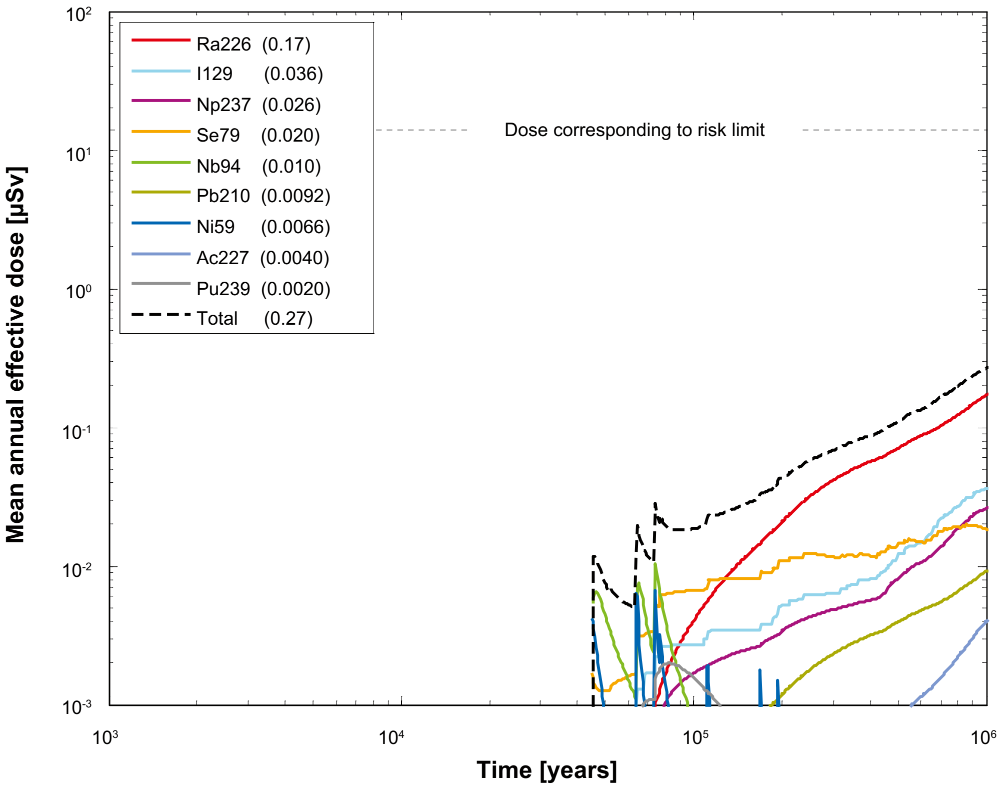

Figure 4-31. *Far-field mean annual effective dose for a probabilistic calculation of the central corrosion case, with initial advection in the erosion/corrosion model. The legend is sorted by peak (in the one-million year period) of the mean annual effective dose. The values in brackets are peak dose in units of µSv.*

4.6 Uncorrelated hydrogeological DFN model

4.6.1 Base case transport assumptions

Deterministic calculations

Hydrogeological case:	**Uncorrelated, five realisations**
Erosion/corrosion model:	SR-Site model
Failure time:	**97,815 years, according to Table 4-2**
Number of failed canisters:	**1**
Solubility limits:	No
Thorium sorption in near field:	Yes (modelled as low solubility limit)
Number of realisations:	1
Number of nuclides:	37

A deterministic calculation of the central corrosion case is performed for a canister taken from the realisations with the earliest failure time of the analysed realisation (97,815 years after deposition) with corresponding geosphere transport data, i.e. data used to calculate the corrosion time are from the same hydrogeological calculation as the geosphere transport data. Advection occurs in the buffer void and the dose equivalent releases are primarily determined by the fuel dissolution rate set to 10^{-7}/yr. Table 4-4 shows the peak annual doses from the pulse releases from the instantly released fraction, IRF.

Figure 4-32 and Figure 4-33 show the deterministic near-field and far-field dose equivalent releases, respectively, for the uncorrelated case. Doses caused by Nb-94 and Ni-59 are dominating the releases from the near field and I-129 is dominating the far-field releases. The low releases of Ra-226 from the far field is an effect of the high F-factor, see Table 4-2.

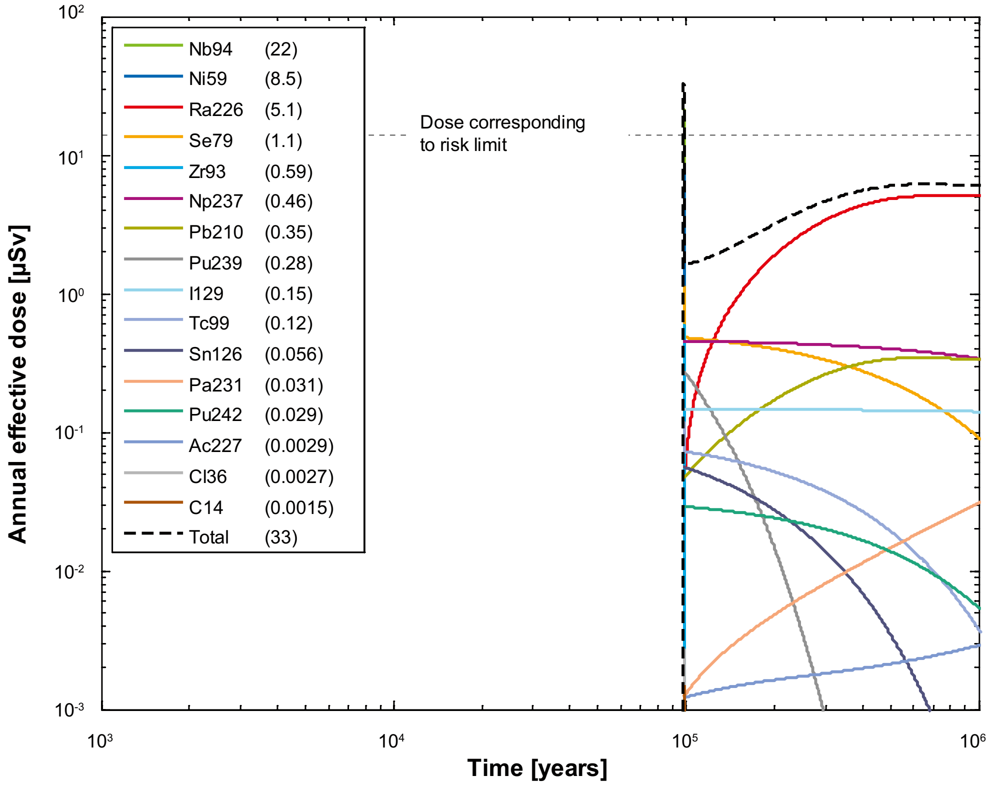

Figure 4-32. *Near-field dose equivalent release for a deterministic calculation of the corrosion scenario, with hydrogeological data from the uncorrelated model. The legend is sorted by peak (in the one-million year period) of the annual effective dose. The values in brackets are peak dose in units of µSv.*

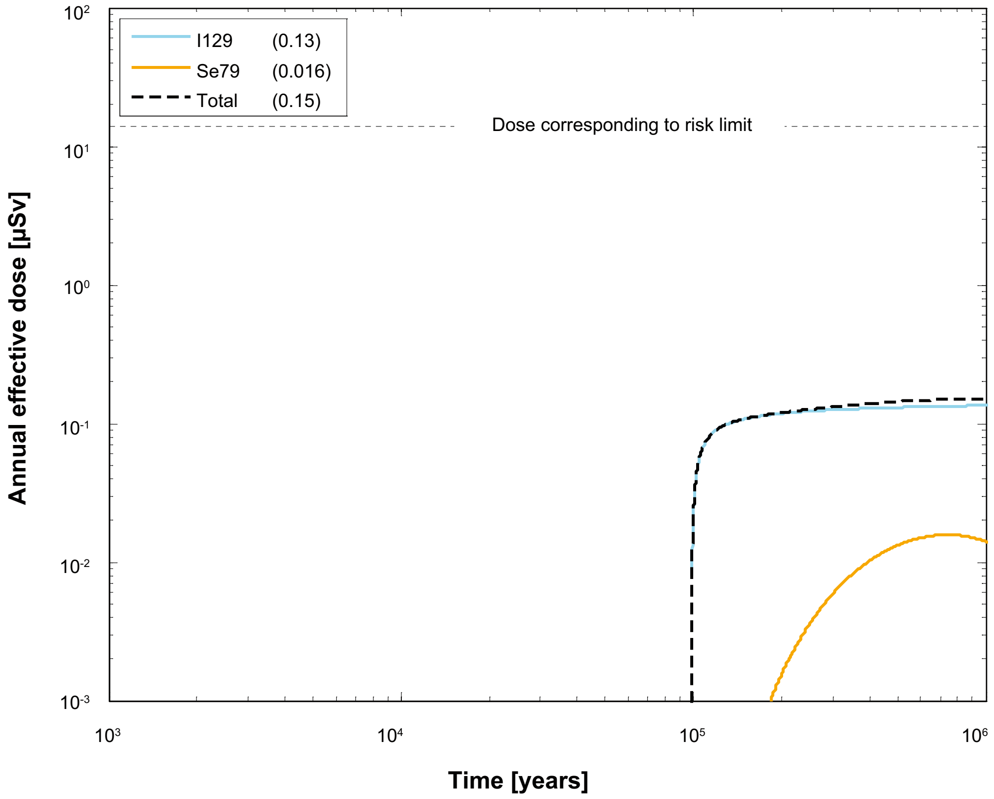

Figure 4-33. *Far-field annual effective dose for a deterministic calculation of the corrosion scenario, with hydrogeological data from the uncorrelated model. The legend is sorted by peak (in the one-million year period) of the annual effective dose. The values in brackets are peak dose in units of µSv.*

Probabilistic calculations

Hydrogeological case:	**Uncorrelated, five realisations**
Erosion/corrosion model:	SR-Site model
Failure time:	**154 times according to the erosion/corrosion calculations**
Average number of failed canisters:	**0.65**
Solubility limits:	No
Thorium sorption in near field:	Yes (modelled as low solubility limit)
Number of realisations:	50 per canister failure time
Number of nuclides:	37

A probabilistic calculation of the central corrosion case is performed with failure times and geosphere transport data from the five realisations of the uncorrelated DFN model. The contributions from the instantly released fraction of nuclides, IRF, are not included in the calculations except for Tc-99 that is included in the far-field calculations. The results for the IRF presented for the central corrosion case are judged to be sufficient to conclude that their contribution is negligible also in this case, see Section 4.4.2.

Figure 4-34 and Figure 4-35 show the near-field and far-field dose equivalent releases, respectively, for the uncorrelated case. The total doses from the near field and far field are about 5 times higher and 2.5 times higher, respectively, compared to the central corrosion case, and are dominated by the Ra-226 release.

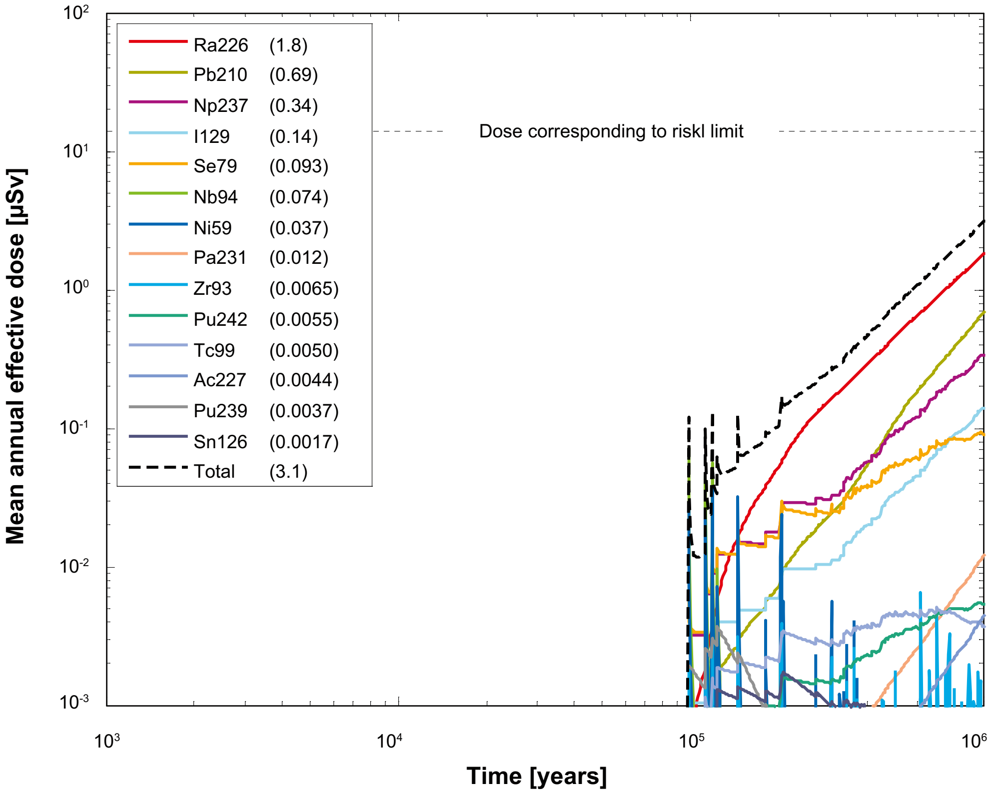

Figure 4-34. *Near-field dose equivalent release for the probabilistic calculation of the corrosion scenario, with hydrogeological data from the uncorrelated model. The legend is sorted by peak (in the one-million year period) of the mean annual effective dose. The values in brackets are peak dose in units of µSv.*

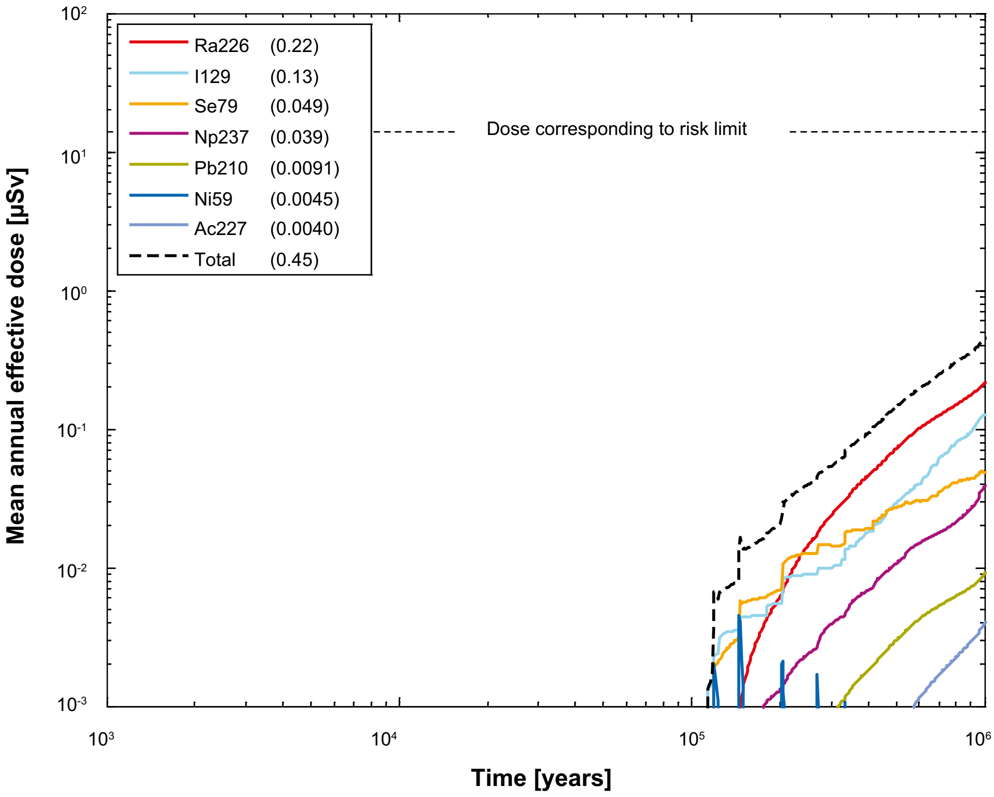

Figure 4-35. *Far-field mean annual effective dose for the probabilistic calculation of the corrosion scenario, with hydrogeological data from the uncorrelated model. The legend is sorted by peak (in the one-million year period) of the mean annual effective dose. The values in brackets are peak dose in units of µSv.*

4.6.2 Initial advection

Deterministic calculations

Hydrogeological case:	**Uncorrelated, five realisations**
Erosion/corrosion model:	**Initial advection**
Failure time:	**47,107 years, according to Table 4-2**
Number of failed canisters:	1
Solubility limits:	No
Thorium sorption in near field:	Yes (modelled as low solubility limit)
Number of realisations:	1
Number of nuclides:	37

A deterministic calculation of the uncorrelated case with initial advection is performed for a canister taken from the realisation with the earliest failure time of the analysed realisations (47,107 years after deposition) with corresponding geosphere transport data, i.e. data used to calculate the corrosion time are from the same hydrogeological calculation as the geosphere transport data. Advection occurs in the buffer void and the dose equivalent releases are primarily determined by the fuel dissolution rate set to 10^{-7}/yr. Table 4-4 shows the peak annual doses from the pulse releases from the instantly released fraction, IRF.

Figure 4-36 and Figure 4-37 show the deterministic near-field and far-field dose equivalent releases, respectively, for the uncorrelated case with initial advection. Note that the peak in Figure 4-36 reaches outside the figure (doses larger than 100 µSv) but the real maximum doses are given in brackets in the figure legend. Doses from the near field are dominated by releases of Nb-94 and Ni-59 shortly after canister failure and by Ra-226 in the longer term. Releases of I-129 are dominating the doses from the far field. The high F-factor, see Table 4-2, implies that the far-field releases of Ra-226 are low.

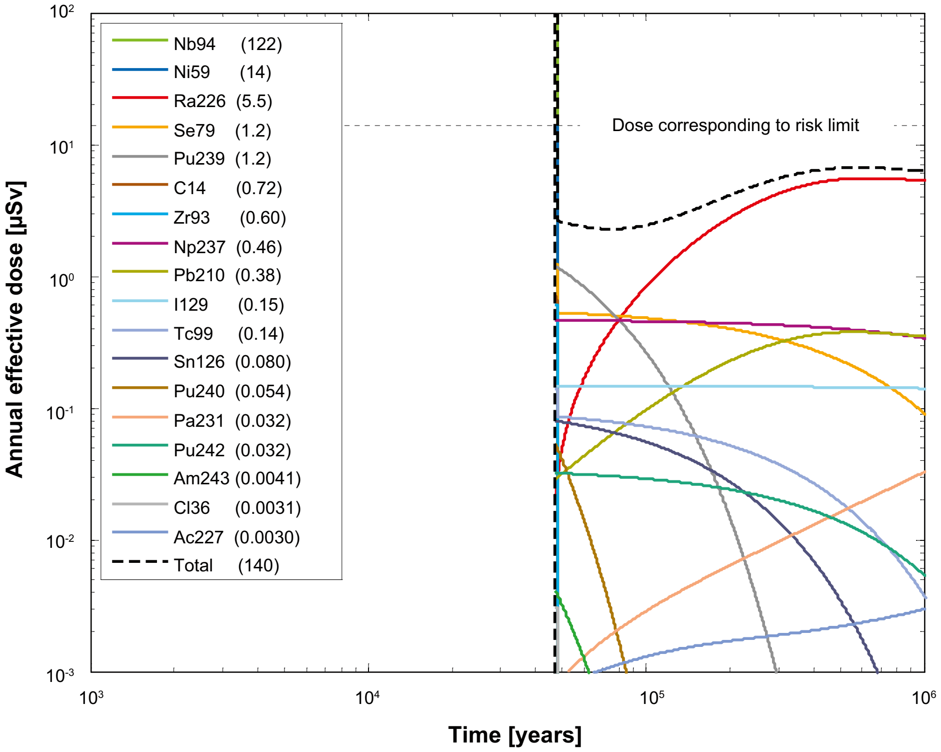

Figure 4-36. *Near-field dose equivalent release for a deterministic calculation of the corrosion scenario, with hydrogeological data from the uncorrelated model and initial advection in the erosion/corrosion model. The legend is sorted by peak (in the one-million year period) of the annual effective dose. The values in brackets are peak dose in units of µSv. Note that the dose equivalent release for Nb-94 is 122 µSv/year, i.e. above the end of the y-axis.*

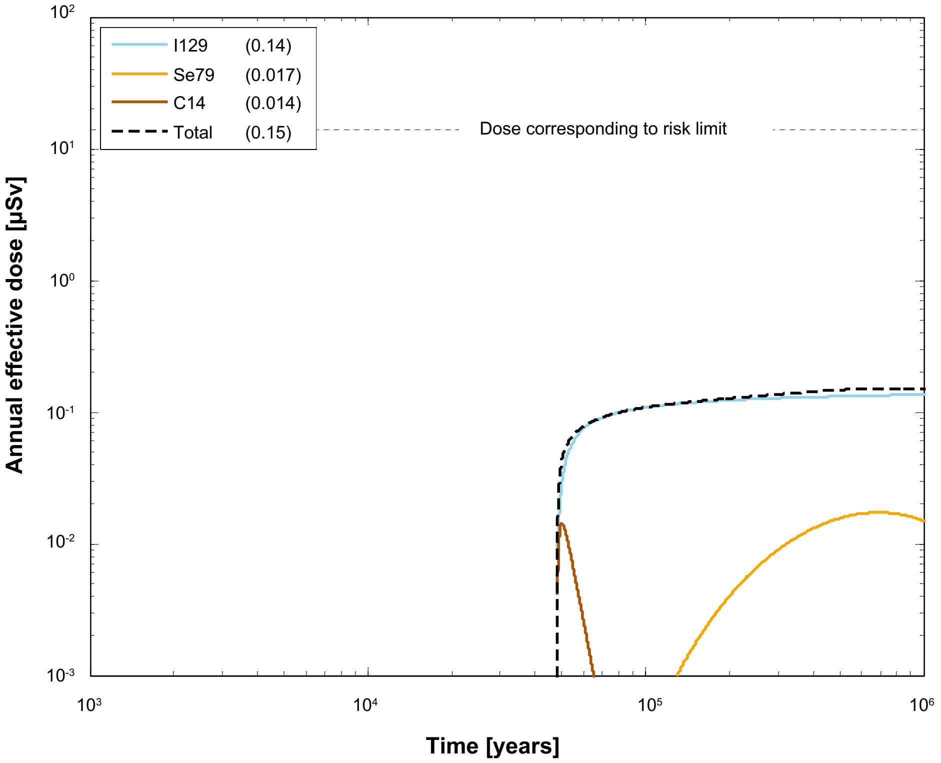

Figure 4-37. *Far-field annual effective dose for a deterministic calculation of the corrosion scenario, with hydrogeological data from the uncorrelated model and initial advection in the erosion/corrosion model. The legend is sorted by peak (in the one-million year period) of the annual effective dose. The values in brackets are peak dose in units of µSv.*

Probabilistic calculations

Hydrogeological case: **Uncorrelated, five realisations**
Erosion/corrosion model: **Initial advection**
Failure time: **289 times according to the erosion/corrosion calculations**
Average number of failed canisters: **1.22**
Solubility limits: No
Thorium sorption in near field: Yes (modelled as low solubility limit)
Number of realisations: 50 per canister failure time
Number of nuclides: 37

A probabilistic calculation of the uncorrelated case with initial advection is performed with failure times and geosphere transport data from the five realisations of the uncorrelated DFN model. The average number of failed canisters is 1.22. The contributions from the instantly released fraction of nuclides, IRF, are not included in the calculations except for Tc-99 that is included in the far-field calculations. The results for the IRF presented for the central corrosion case is judged to be enough to conclude that their contribution is negligible also in this case, see Section 4.4.2.

Figure 4-38 and Figure 4-39 show the near-field and far-field dose equivalent releases, respectively, for the uncorrelated case with initial advection. Doses from the near field are dominated by releases of Ra-226 and Pb-210 and from the far field by Ra-226 and I-129. The total doses from the near-field and the far-field are about 12 times higher and 5 times higher, respectively, compared to the central corrosion case.

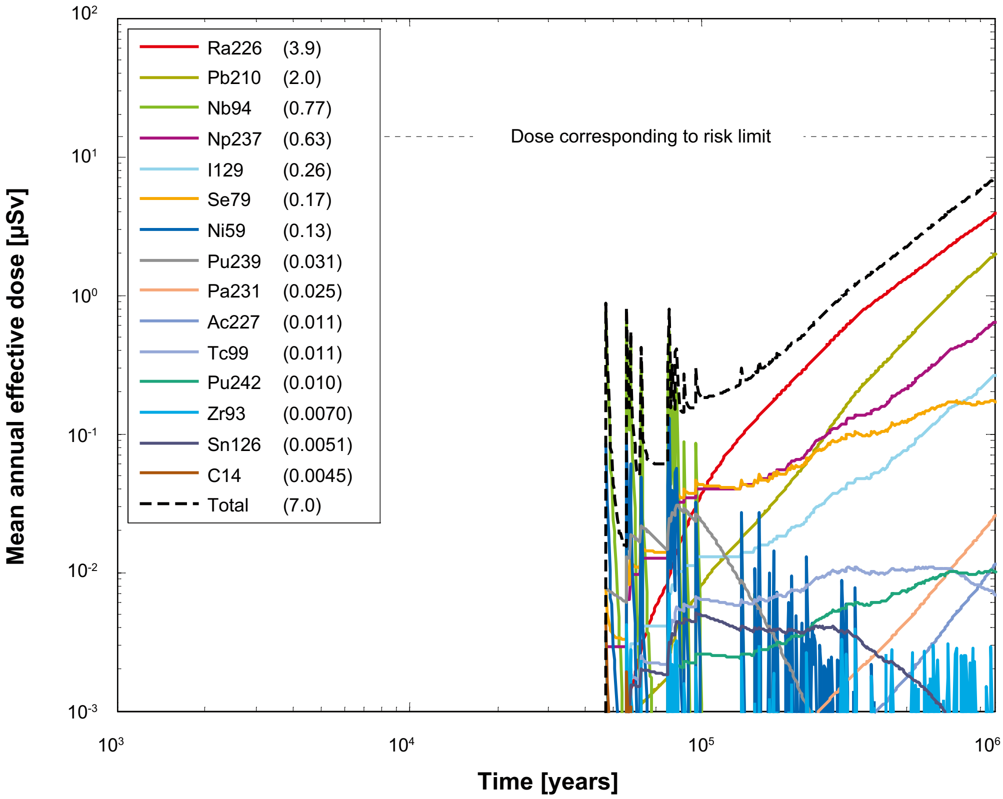

Figure 4-38. *Near-field dose equivalent release for the probabilistic calculation of the corrosion scenario, with hydrogeological data from the uncorrelated model and initial advection in the erosion/corrosion model. The legend is sorted by peak (in the one-million year period) of the mean annual effective dose. The values in brackets are peak dose in units of µSv.*

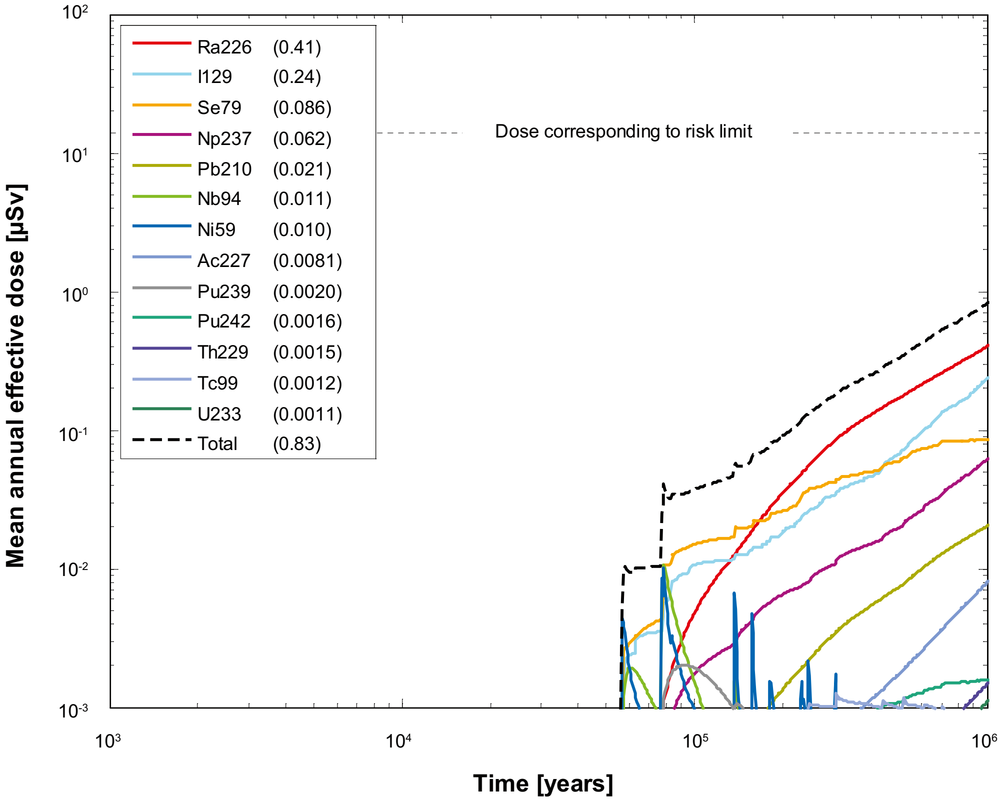

Figure 4-39. *Far-field mean annual effective dose for the probabilistic calculation of the corrosion scenario, with hydrogeological data from the uncorrelated model and initial advection in the erosion/corrosion model. The legend is sorted by peak (in the one-million year period) of the mean annual effective dose. The values in brackets are peak dose in units of µSv.*

4.7 Fully correlated hydrogeological DFN model

4.7.1 Base case transport assumptions

Deterministic calculations

Hydrogeological case:	**Fully correlated, five realisations**
Erosion/corrosion model:	SR-Site model
Failure time:	**99,700 years, according to Table 4-2**
Number of failed canisters:	**1**
Solubility limits:	No
Thorium sorption in near field:	Yes (modelled as low solubility limit)
Number of realisations:	1
Number of nuclides:	37

A deterministic calculation of the fully correlated case is performed for a canister taken from the realisation with the earliest failure time of the analysed realisations (99,700 years after deposition) with corresponding geosphere transport data, i.e. data used to calculate the corrosion time are from the same hydrogeological calculation as the geosphere transport data. Advection occurs in the buffer void and the dose equivalent releases are primarily determined by the fuel dissolution rate set to 10^{-7}/yr. Table 4-4 shows the peak annual doses from the pulse releases from the instantly released fraction, IRF.

Figure 4-40 and Figure 4-41 show the deterministic near-field and far-field dose equivalent releases, respectively, for the fully correlated case. Doses caused by Nb-94 and Ni-59 are dominating the releases from the near field shortly after canister failure and releases of Ra-226 are dominating in the longer term in the near filed as well as in the far field.

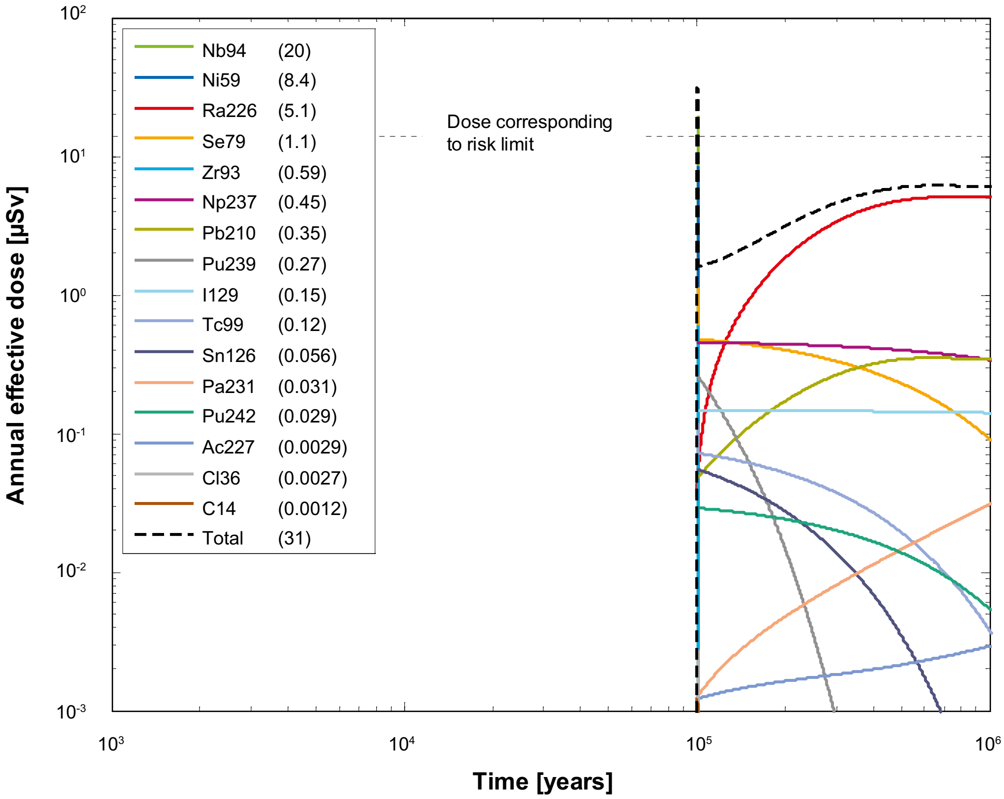

Figure 4-40. *Near-field dose equivalent release for a deterministic calculation of the corrosion scenario, with hydrogeological data from the fully correlated model. The legend is sorted by peak (in the one-million year period) of the annual effective dose. The values in brackets are peak dose in units of µSv.*

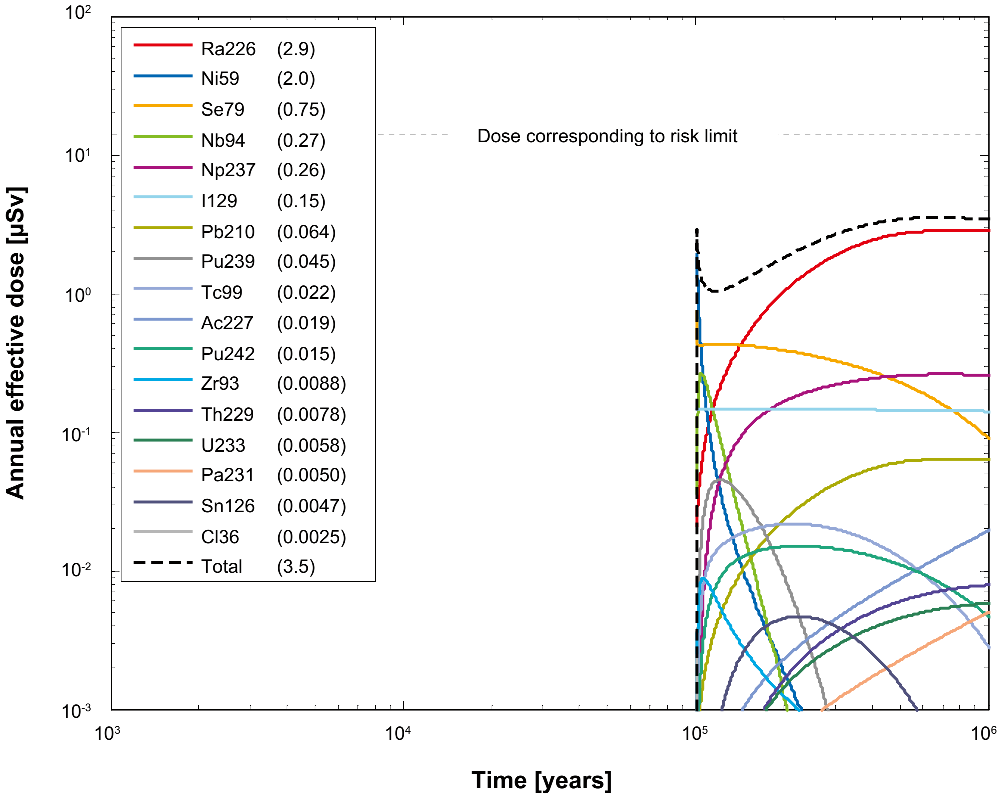

Figure 4-41. *Far-field annual effective dose for a deterministic calculation of the corrosion scenario, with hydrogeological data from the fully correlated model. The legend is sorted by peak (in the one-million year period) of the annual effective dose. The values in brackets are peak dose in units of µSv.*

Probabilistic calculations

Hydrogeological case:	**Fully correlated, five realisations**
Erosion/corrosion model:	SR-Site model
Failure time:	**132 times according to the erosion/corrosion calculations**
Average number of failed canisters:	**0.57**
Solubility limits:	No
Thorium sorption in near field:	Yes (modelled as low solubility limit)
Number of realisations:	50 per canister failure time
Number of nuclides:	37

A probabilistic calculation of the fully correlated case was performed with failure times and geosphere transport data from the five realisations of the uncorrelated DFN model and the erosion/corrosion calculations in SKBdoc, see Table 3-8. The average number of failed canisters is 0.57. The contributions from the instantly released fraction of nuclides, IRF, are not included in the calculations except for Tc-99 that is included in the far-field calculations. The results for the IRF presented for the central corrosion case are judged to be sufficient to conclude that their contribution is negligible also in this case, see Section 4.4.2.

Figure 4-42 and Figure 4-43 show the near-field and far-field dose equivalent releases, respectively, for the fully correlated case. The near-field doses are dominated by Ra-226 and are about 5 times higher than in the central corrosion case. The far-field doses are dominated by Ra-226 and I-129 and are about 3.5 times higher than in the central corrosion case.

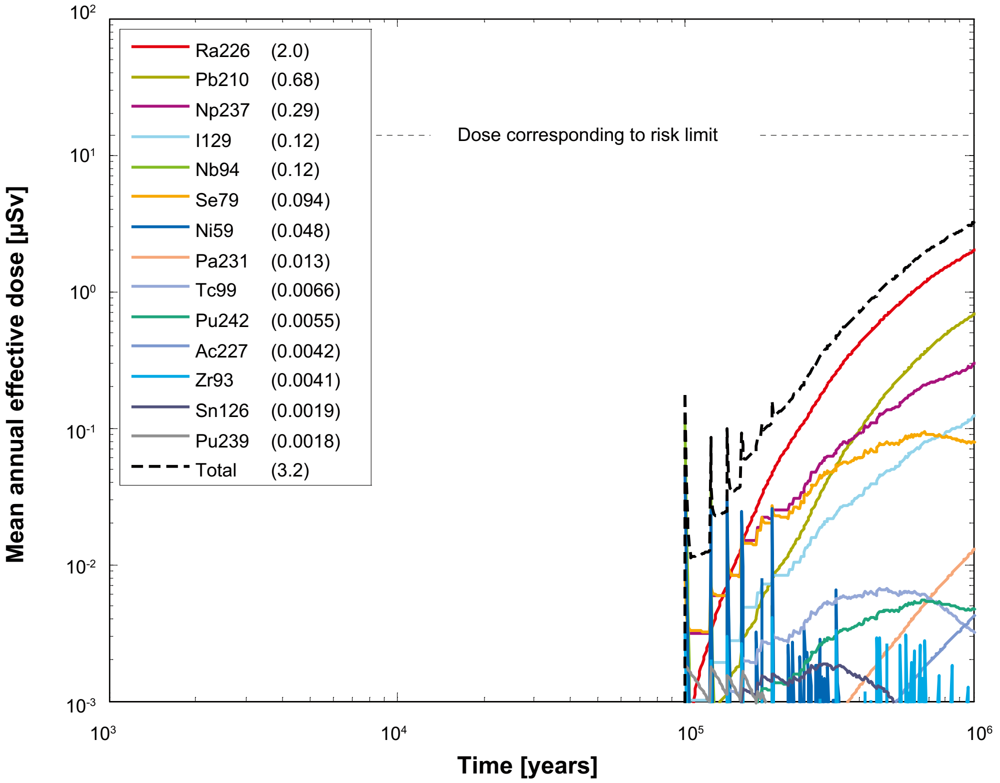

Figure 4-42. *Near-field dose equivalent release for the probabilistic calculation of the corrosion scenario, with hydrogeological data from the fully correlated model. The legend is sorted by peak (in the one-million year period) of the mean annual effective dose. The values in brackets are peak dose in units of µSv.*

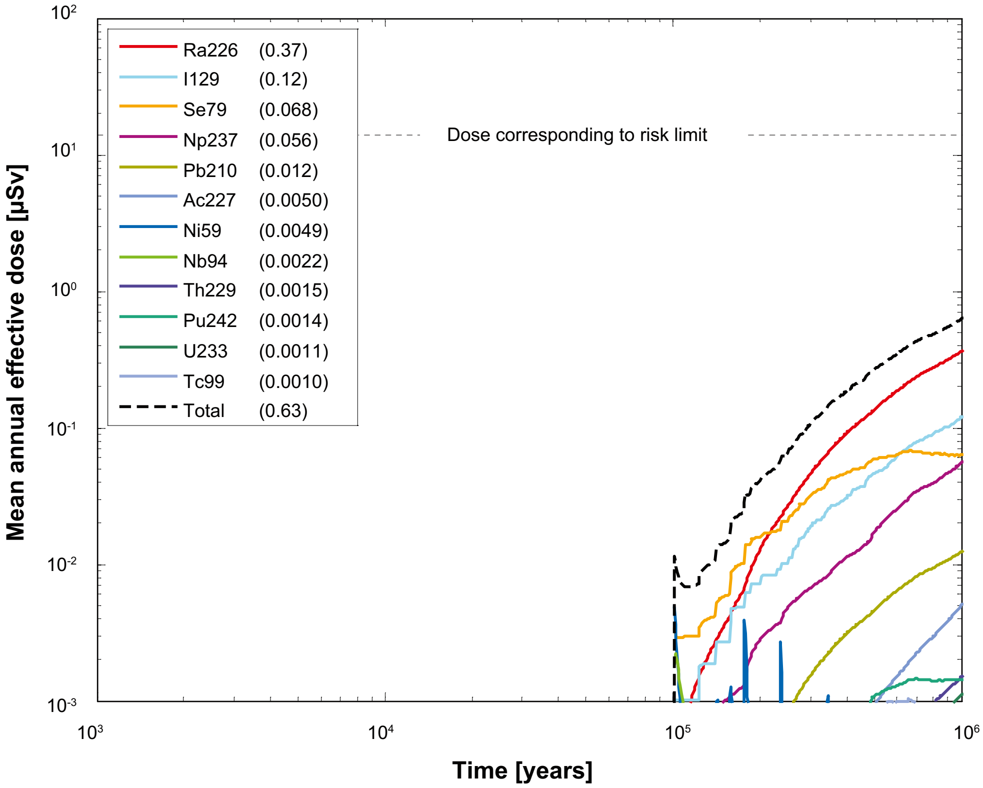

Figure 4-43. *Far-field mean annual effective dose for the probabilistic calculation of the corrosion scenario, with hydrogeological data from the fully correlated model. The legend is sorted by peak (in the one-million year period) of the mean annual effective dose. The values in brackets are peak dose in units of µSv.*

4.7.2 Initial advection

Deterministic calculations

Hydrogeological case:	**Fully correlated, five realisations**
Erosion/corrosion model:	**Initial advection**
Failure time:	**47,657 years, according to Table 4-2**
Number of failed canisters:	1
Solubility limits:	No
Thorium sorption in near field:	Yes (modelled as low solubility limit)
Number of realisations:	1
Number of nuclides:	37

A deterministic calculation of the fully correlated case with initial advection is performed for a canister taken from the realisation with the earliest failure time of the analysed realisations (47,657 years after deposition) with corresponding geosphere transport data, i.e. data used to calculate the corrosion time are from the same hydrogeological calculation as the geosphere transport data. Advection occurs in the buffer void and the dose equivalent releases are primarily determined by the fuel dissolution rate set to 10^{-7}/yr. Table 4-4 shows the peak annual doses from the pulse releases from the instantly released fraction, IRF.

Figure 4-44 and Figure 4-45 show the deterministic near-field and far-field dose equivalent releases, respectively, for the fully correlated case with initial advection. Note that the peak in Figure 4-44 reaches outside the figure (doses larger than 100 µSv) but the real maximum doses are given in brackets in the figure legend. Doses from the near field are dominated by releases of Nb-94 and Ni-59 shortly after canister failure and by Ra-226 in the longer term. The same nuclides are dominating the doses from the far field.

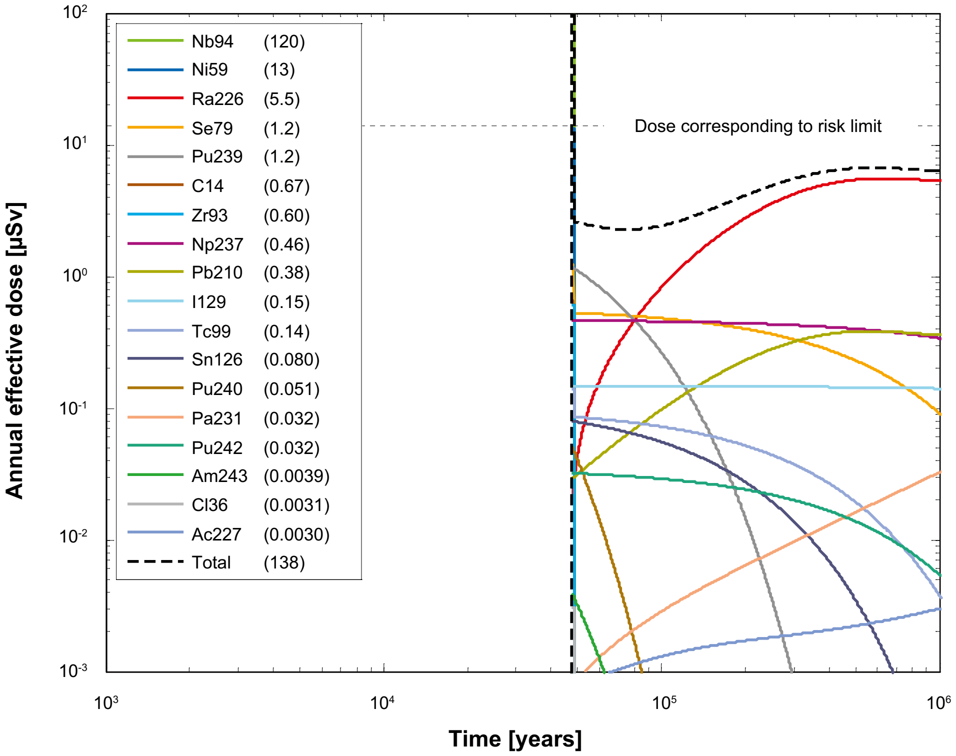

Figure 4‑44. *Near-field dose equivalent release for a deterministic calculation of the corrosion scenario, with hydrogeological data from the fully correlated model and initial advection in the erosion/corrosion model. The legend is sorted by peak (in the one-million year period) of the annual effective dose. The values in brackets are peak dose in units of µSv. Note that the dose equivalent release forNb-94 is 120 µSv/year, i.e. above the limit of the y-axis.*

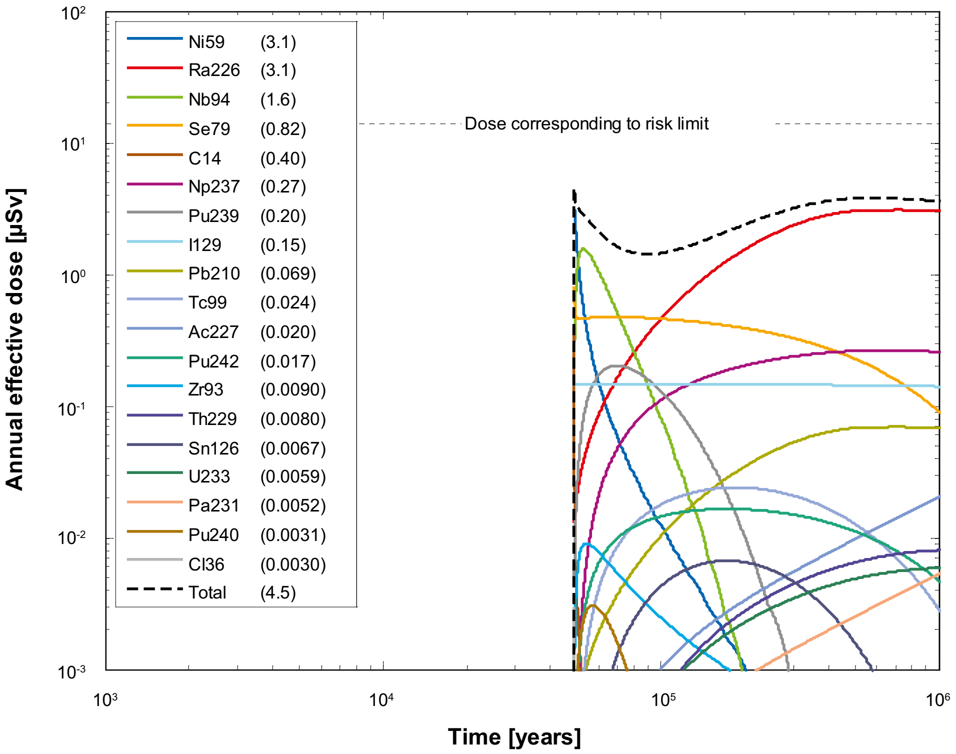

Figure 4‑45. *Far-field annual effective dose for a deterministic calculation of the corrosion scenario, with hydrogeological data from the fully correlated model and initial advection in the erosion/corrosion model. The legend is sorted by peak (in the one-million year period) of the annual effective dose. The values in brackets are peak dose in units of µSv.*

Probabilistic calculations

Hydrogeological case:	**Fully correlated, five realisations**
Erosion/corrosion model:	**Initial advection**
Failure time:	**200 times according to the erosion/corrosion calculations**
Average number of failed canisters:	**0.86**
Solubility limits:	No
Thorium sorption in near field:	Yes (modelled as low solubility limit)
Number of realisations:	50 per canister failure time
Number of nuclides:	37

A probabilistic calculation of the fully correlated case with initial advection was performed with failure times and geosphere transport data from the five realisations of the uncorrelated DFN model and the erosion/corrosion calculations in SKBdoc, see Table 3-8. The average number of failed canisters is 0.86. The contributions from the instantly released fraction of nuclides, IRF, are not included in the calculations except for Tc-99 that is included in the far-field calculations. The results for the IRF presented for the central corrosion case are judged to be sufficient to conclude that their contribution is negligible also in this case, see Section 4.4.2.

Figure 4-46 and Figure 4-47 show the near-field and far-field dose equivalent releases, respectively, for the fully correlated case with initial advection. Both near-and far-field doses are dominated by releases of Ra-226 and the total doses are about 10 times higher and 5 times higher, respectively, compared to the central corrosion case.

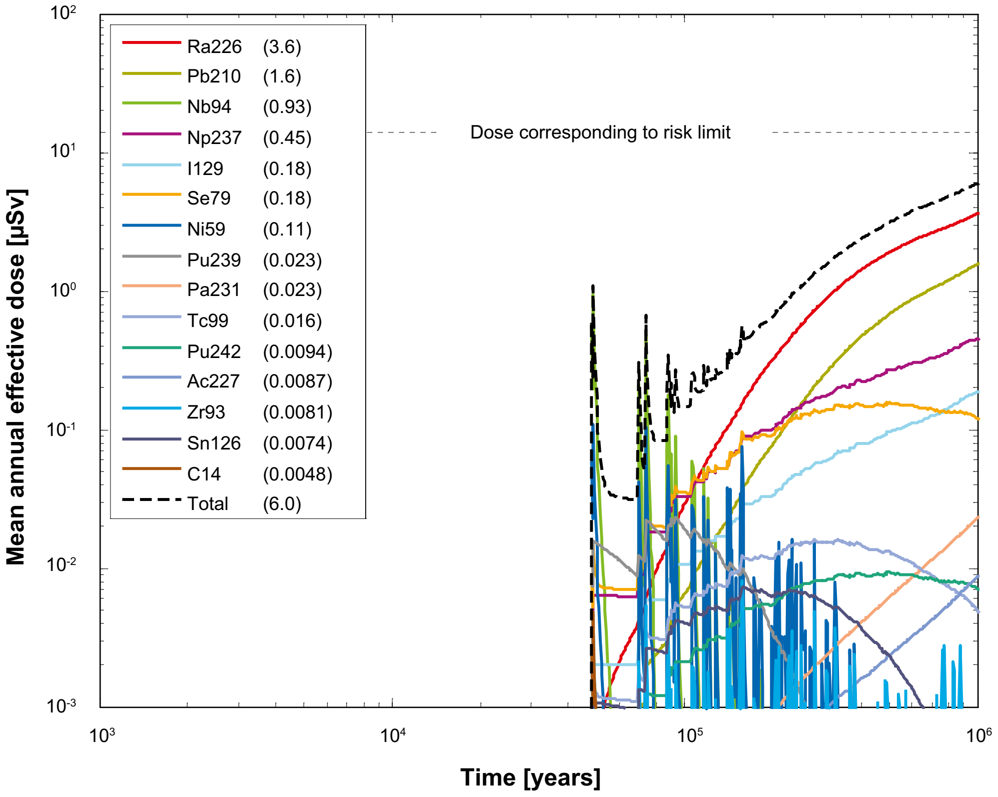

Figure 4-46. *Near-field dose equivalent release for the probabilistic calculation of the corrosion scenario, with hydrogeological data from the fully correlated model and initial advection in the erosion/corrosion model. The legend is sorted by peak (in the one-million year period) of the mean annual effective dose. The values in brackets are peak dose in units of µSv.*

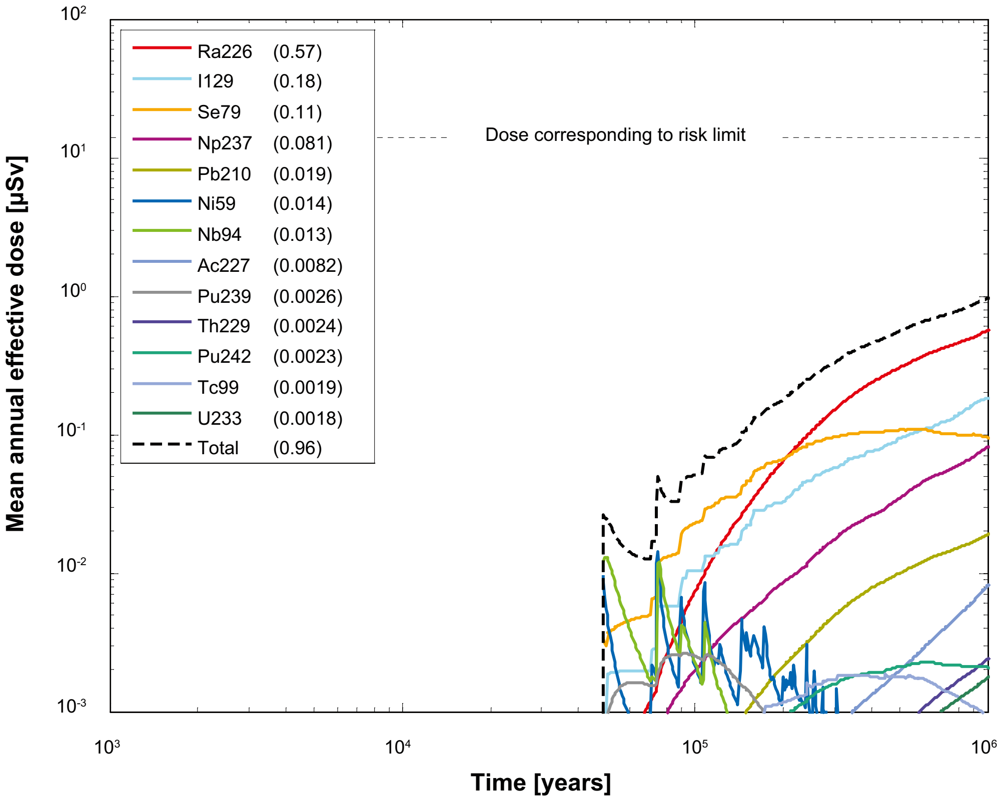

Figure 4-47. *Far-field mean annual effective dose for the probabilistic calculation of the corrosion scenario, with hydrogeological data from the fully correlated model and initial advection in the corrosion model. The legend is sorted by peak (in the one-million year period) of the mean annual effective dose. The values in brackets are peak dose in units of µSv.*

4.8 Cases addressing best available technique (BAT)

According to Swedish legislation, a licence application for a final repository needs to address the issues of best available technique (BAT). Factors considered in this section are:

- Alternative copper shell thickness, 25 mm and 100 mm, respectively.
- Alternative deposition hole rejection criteria

These factors are implemented in the corrosion calculations and analysed as BAT-cases. The BAT cases are variant cases that do not use best available technique.

Alternative copper shell thickness

Hydrogeological case:	Semi-correlated, ten realisations
Erosion/corrosion models:	SR-Site model
Failure time:	107 times (25 mm) 21 times (100 mm)
Average number of failed canisters:	0.22 (25 mm) 0.044 (100mm)
Solubility limits:	No
Thorium sorption in near field:	Yes (modelled as low solubility limit)
Number of realisations:	50 per canister failure time
Number of nuclides:	37

Two probabilistic calculations of the corrosion case were performed with transport data from the ten realisations of the semi-correlated DFN model and corrosion model for copper thicknesses of 25 mm and 100 mm. In the reference design is the copper thickness 50 mm. The average number of failed canisters is 0.22 and 0.044 for copper thickness of 25 mm and 100 mm, respectively. The contributions from the instantly released fraction of nuclides, IRF, are not included in the calculations.

Figure 4-48 and Figure 4-49 show the near- and far-field total dose equivalent releases, respectively, for corrosion cases with copper thicknesses of 25 mm, 50 mm (central corrosion case) and 100 mm. Doses both from the near-field and the far-field become about two times lower if the thickness of the copper shell is doubled.

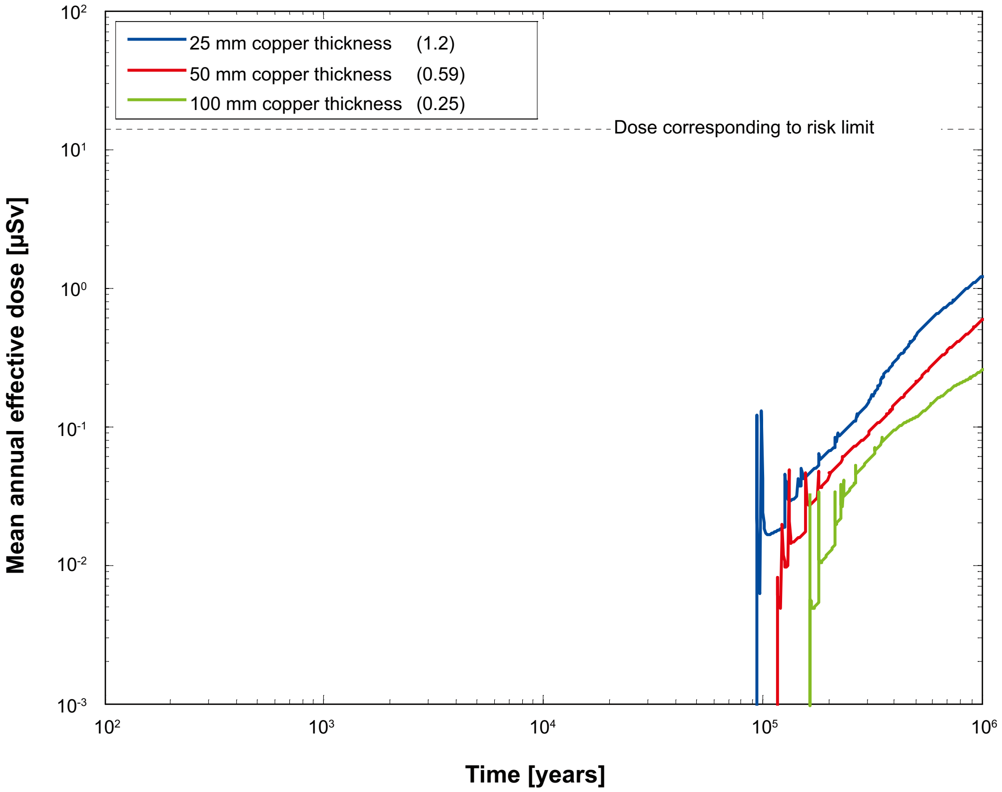

Figure 4-48. *Near-field dose equivalent releases for probabilistic calculations of the cases with a copper thickness of 25 mm, 50 mm (central corrosion case) and 100 mm. The legend is sorted by peak (in the one-million year period) of the mean annual effective dose. The values in brackets are peak dose in units of µSv.*

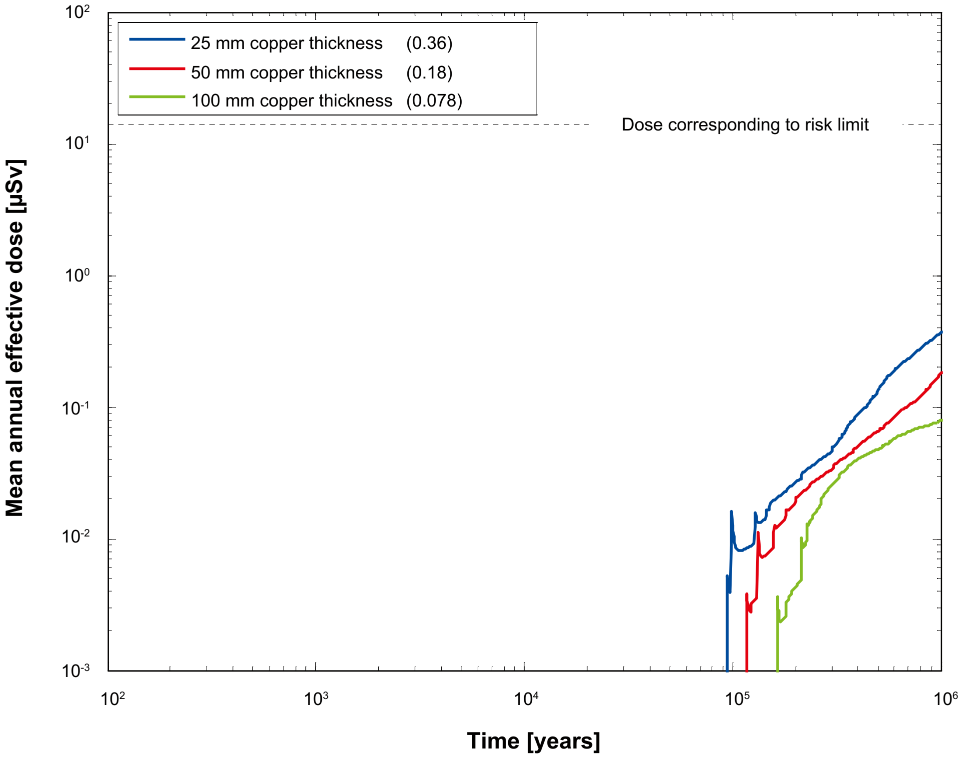

Figure 4-49. *Far-field mean annual effective dose for the probabilistic calculations of the cases with a copper thickness of 25 mm, 50 mm (central corrosion case) and 100 mm. The legend is sorted by peak (in the one-million year period) of the mean annual effective dose. The values in brackets are peak dose in units of µSv.*

Alternative deposition hole rejection criteria

Hydrogeological case:	Semi-correlated, ten realisations
Erosion/corrosion models:	SR-Site model
Failure time:	126 times (no T/L-filtering) 1,964 times (neither T/L- nor EFPC-filtering)
Average number of failed canisters:	0.26 (no T/L-filtering) 3.7 (neither T/L- nor EFPC-filtering)
Solubility limits:	No
Thorium sorption in near field:	Yes (modelled as low solubility limit)
Number of realisations:	50 per canister failure time
Number of nuclides:	37

The groundwater flow around and through deposition holes have a large impact on both the loss of bentonite which may potentially lead to advective conditions and on the rate of corrosion by sulphide in the groundwater. Applying the EFPC criterion means to avoid deposition holes with high groundwater flow and it has been applied to all calculations. Furthermore, an additional deposition hole rejection criterion related to the combination of a high transmissivity and length of the intersecting fracture (T/L-filtering) was assumed in all the calculations.

Two probabilistic calculations of the corrosion case were performed with transport data from the ten realisations of the semi-correlated DFN model, without T/L-filtering and without both T/L-filtering and EFPC-filtering. The average number of failed canisters is 0.26 and 3.7 for no T/L-filtering and neither T/L- nor EFPC-filtering, respectively. The contributions from the instantly released fraction of nuclides, IRF, are not included in the calculations.

Figure 4-50 and Figure 4-51 show the near- and far-field total dose equivalent releases, respectively, for corrosion cases with no T/L-filtering, neither T/L- nor EFPC-filtering and the central corrosion case (T/L- and EFPC-filtering). Dose from the far field increases 67 times for the case without T/L- nor EFPC-filtering compared to the central corrosion case.

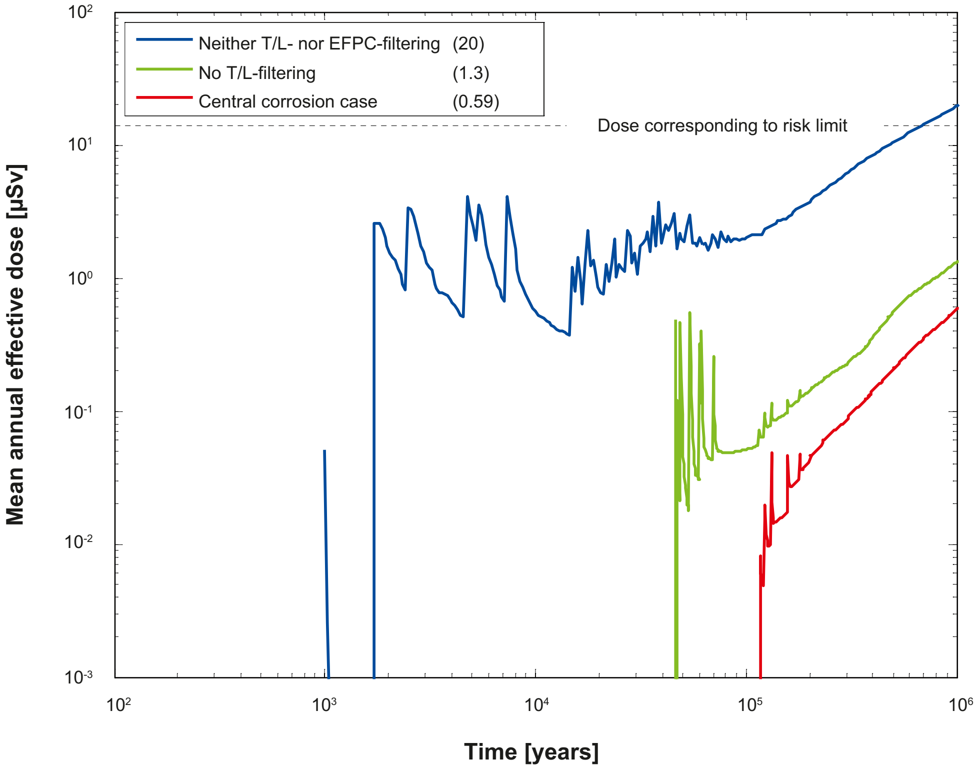

Figure 4-50. *Near-field dose equivalent release for the probabilistic calculations of the cases with no T/L-filtering, neither T/L- nor EFPC-filtering and the central corrosion case (T/L- and EFPC-filtering). The legend is sorted by peak (in the one-million year period) of the mean annual effective dose. The values in brackets are peak dose in units of μSv.*

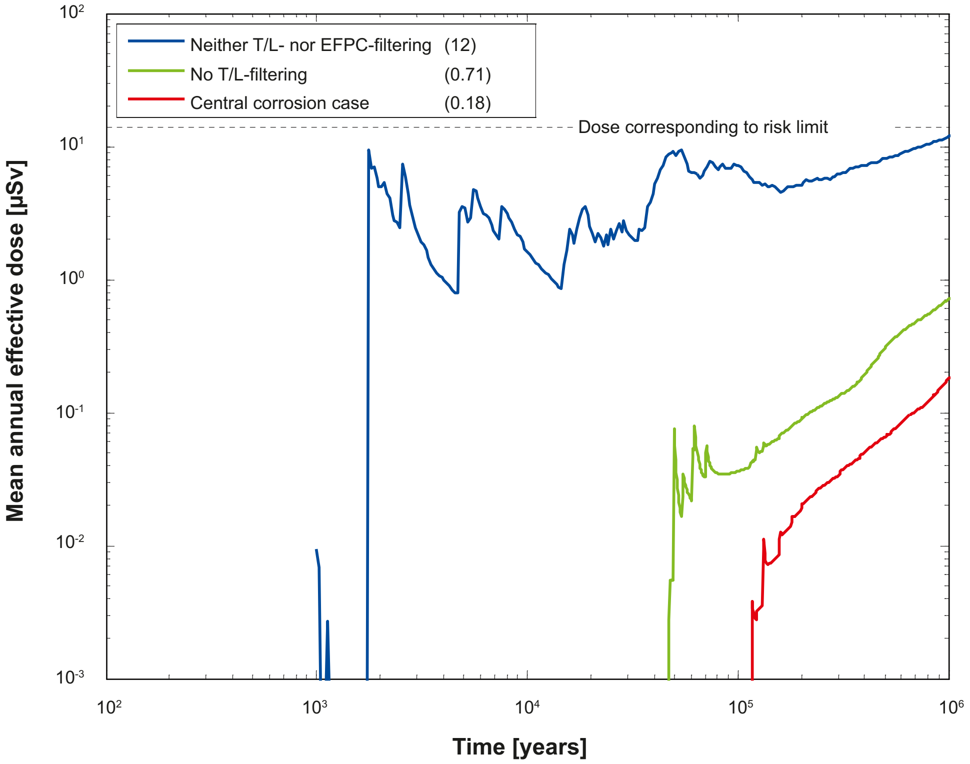

Figure 4-51. *Far-field mean annual effective dose for the probabilistic calculations of the cases with no T/L-filtering, neither T/L- nor EFPC-filtering and the central corrosion case (T/L- and EFPC-filtering). The legend is sorted by peak (in the one-million year period) of the mean annual effective dose. The values in brackets are peak dose in units of μSv.*

4.9 Alternative safety indicators for the central corrosion case

Four alternative indicators to risk are used in SR-Site: release of activity from the geosphere, radiotoxicity flux from the geosphere, concentrations of radionuclides in ecosystems and natural geosphere fluxes of radionuclides. The following reference values are used when evaluating these indicators.

- The Finnish activity release constraints. These constraints are strictly applicable only in the Finnish regulatory context, but are nevertheless deemed useful as reference values for SR-Site.
- The reference value for radiotoxicity flux from the geosphere suggested by the EU SPIN project.
- Measured concentrations of naturally occurring radionuclides in ecosystems at the Forsmark site or other, comparable sites. Not further described here, see **Main report** Section 13.5.8.
- Naturally occurring fluxes of radionuclides at the site.

4.9.1 Finnish activity release constraints

The Finnish Radiation and Nuclear Safety Authority STUK has issued activity release constraints to the environment /STUK 2001/.

These nuclide specific constraints are defined for long-lived radionuclides only. The effects of their short-lived progeny have been taken into consideration in the constraints defined for the long-lived parents. The nuclide-specific release rate constraints are:

- 0.03 GBq/yr for the long-lived α-emitting isotopes of Ra, Th, Pa, Pu, Am and Cm,
- 0.1 GBq/yr for Se-79, I-129, and Np-237,
- 0.3 GBq/yr for C-14, Cl-36, Cs-135, and the long-lived isotopes of U,
- 1 GBq/yr for Nb-94 and Sn-126,
- 3 GBq/yr for Tc-99,
- 10 GBq/yr for Zr-93,
- 30 GBq/yr for Ni-59,
- 100 GBq/yr for Pd-107 and Sm-151.

The constraints apply to activity releases that arise from the expected evolution scenarios and that may enter the environment after several thousands of years, whereas dose rate constraints are applied in the shorter term. In applying the above constraints, the activity releases can be averaged over 1,000 years at the most. The sum of the ratios between the nuclide-specific activity releases and the respective constraints shall be less than one. It should be noted that the Finnish regulator has derived these constraints partly based on a set of reference biospheres considered possible in the future at the planned disposal site, Olkiluoto at the coast of the Baltic Sea, and partly on natural fluxes of radionuclides established for similar environments. The reference values of the Finnish regulatory guide are thus not directly applicable for other disposal concepts and sites /EU 2002/. However, both the disposal concept and the sites considered in Sweden are similar to those for which the Finnish activity release constraints have been developed.

Figure 4-52 shows the result of applying this activity constraint to releases calculated for the central corrosion case. The releases from the geosphere are around two orders of magnitude lower than the STUK constraint.

The pulses from IRF are not included in these calculations. But applying that the activity releases can be averaged over 1,000 years, implies that the release of the IRF give a negligible contribution to the calculated total activity release.

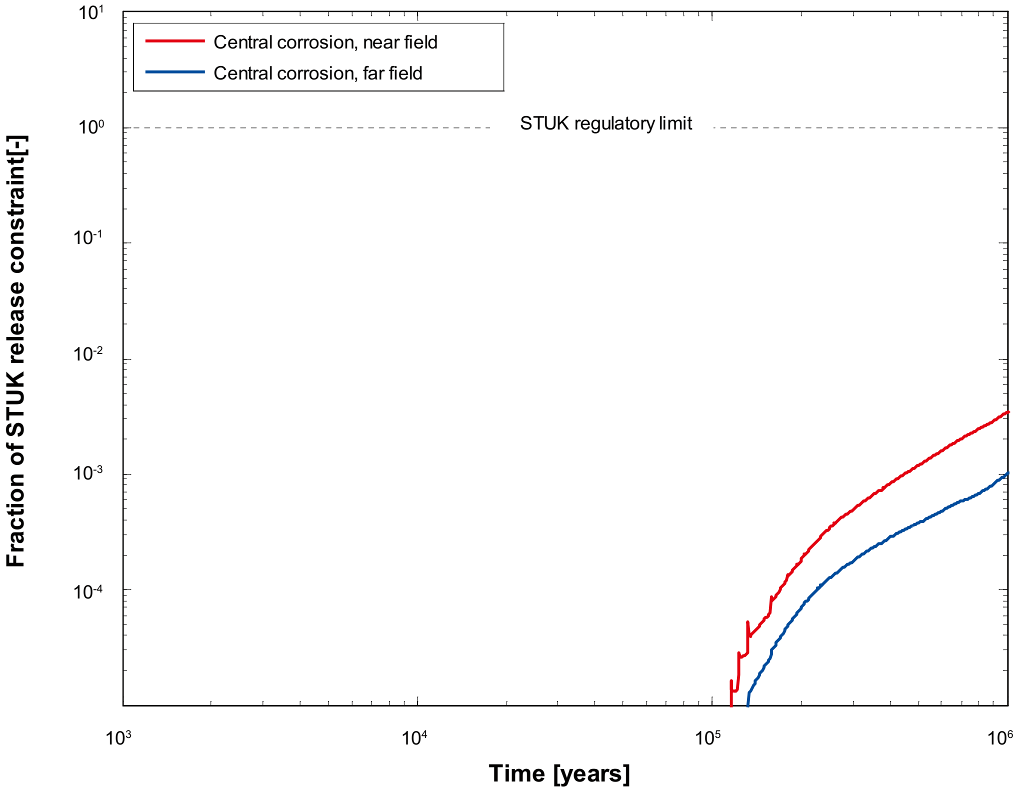

***Figure 4-52.** Releases as a fraction of the activity release constraint index adopted by the Finnish regulator.*

4.9.2 Radiotoxicity flux from the geosphere – EU SPIN Project

An EU project /EU 2002/ concludes that two alternative indicators could preferably be used to complement the dose indicator. These are:

- Radiotoxicity concentration in biosphere water: preference for medium time frames, i.e. several thousand to several tens of thousands of years.
- Radiotoxicity flux from the geosphere: preference for later time frames.

The project also reports on reference values that could tentatively be used for comparisons to calculated concentrations and fluxes of radionuclides from the repository. Regarding radiotoxicity flux from the geosphere, an indicative reference value of 60 Sv/yr for a typical area of 200 km^2 was suggested. The SPIN reference value was calculated from natural activity flux (Bq/year) converting to radiotoxicity flux by using ingestion dose coefficients from ICRP72 /ICRP 1996/. It was assumed that each daughter is in secular equilibrium with its parent, i.e. the dose coefficients of the daughter nuclides (half-life >1 day) are added to the studied nuclide. For further details see the SPIN project report /EU 2002/.

The same approach was used on the central corrosion case. The release rate (Bq/yr) is converted to a radiotoxicity flux (Sv/yr) using the ICRP72 ingestion dose coefficients (Sv/Bq) /ICRP 1996/ (the same values as reported by EU /EU 1996/ and also by IAEA /IAEA 1996/). Table 4-6 show the nuclides that have daughters that are in secular equilibrium, i.e. the dose coefficients of the daughter nuclides (half-life >1 day) are added to the studied parent nuclide. Note that shorter-lived progany have small ingestion dose coefficients and their in-growth following ingestion of their parents is explicitly addressed in the ICRP biokenetic and dosimetric models.

Figure 4-53 shows the results for the central corrosion case. The releases from the geosphere, 0.011 Sv/year, are around four orders of magnitude lower than the SPIN reference value.

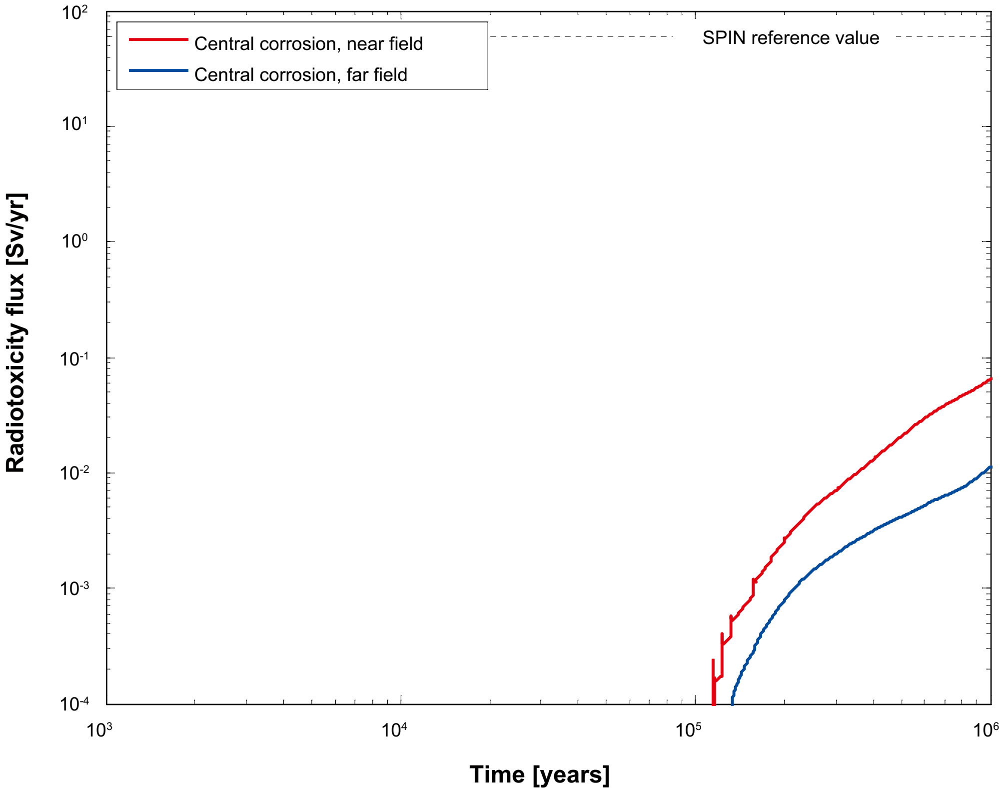

***Figure 4-53.** Radiotoxicity flux in the central corrosion case compared to the SPIN reference value.*

Table 4-6. Parent nuclides and nuclides assumed to be in secular equilibrium.

Parent nuclide	Daughter in secular equilibrium (half-life >1 day)
Th-232	+ Ra-228 + Th-228 + Ra-224
Cm-245	+ Pu-241
Np-237	+ Pa-233
Th-229	+ Ra-225 + Ac-225
U-238	+ Th-234
Pb-210	+ Bi-210 + Po-210
Am-242m	+ Cm-242
Am-243	+ Np-239
Ac-227	+ Th-227 + Ra-223

4.9.3 Naturally occurring fluxes of radionuclides at the site

The last alternative indicator to risk used in SR-Site is naturally occurring fluxes of radionuclides at the site. The naturally occurring fluxes of U-238, U-234 and Ra-226, are estimated based on measured activities during the site investigations, see Section 2.3. Figure 4-54 shows the far-field release rates of U-238, U-234 and Ra-226 in the central corrosion case compared to the naturally occurring fluxes at Forsmark. The naturally occurring fluxes of U-238, U-234 and Ra-226 have also been converted to effective dose by using the basic LDF values, the obtained dose is shown in Figure 4-55 together with the far-field annual effective dose in the central corrosion case and the case with K_d for U(VI) in the rock . It is noted that the releases from the repository could be concentrated to one or a few of the landscape objects in the release area. There are about ten objects in the area used in the derivation of the naturally occurring fluxes, suggesting that the natural fluxes would exceed those from the repository even if all the release from the repository were to occur to a single landscape object.

The repository-derived flux of Ra-226 is about two orders of magnitude below the naturally occurring flux of Ra-226. For the U isotopes, the fluxes from the repository are about six orders of magnitude below the natural fluxes, irrespective of whether rock K_d-distributions for U(IV) or U(VI) are used.

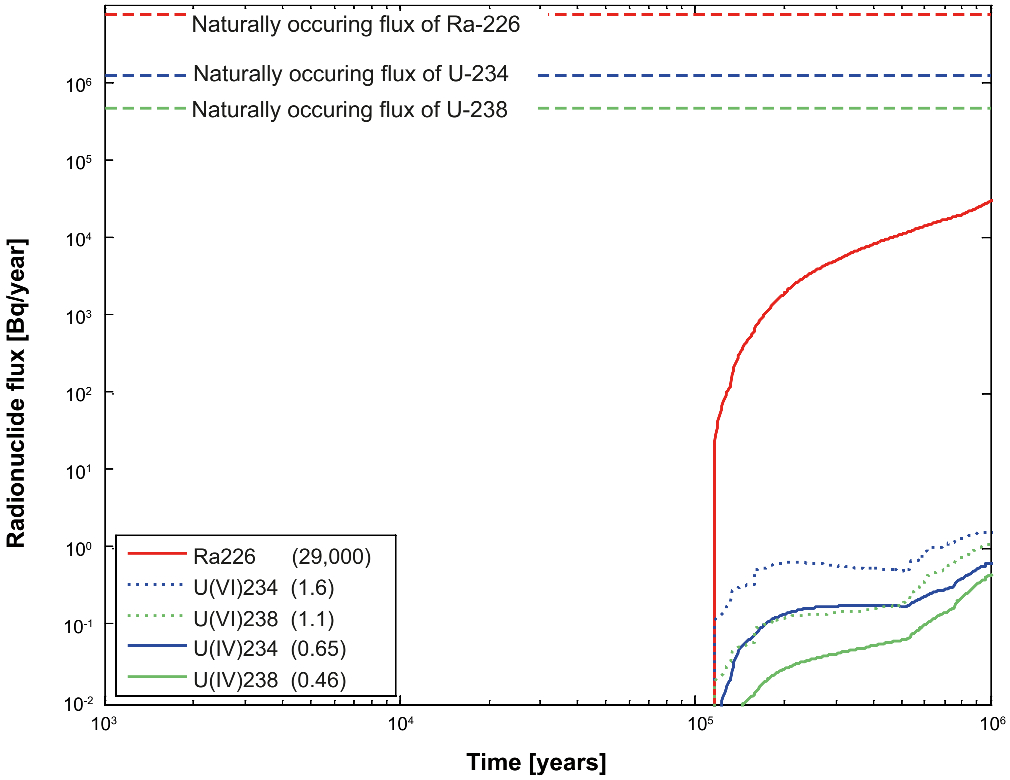

Figure 4-54. *Far-field release rates (Bq/year) of U-238, U-234 and Ra-226 in the central corrosion case compared to the naturally occurring fluxes at Forsmark.*

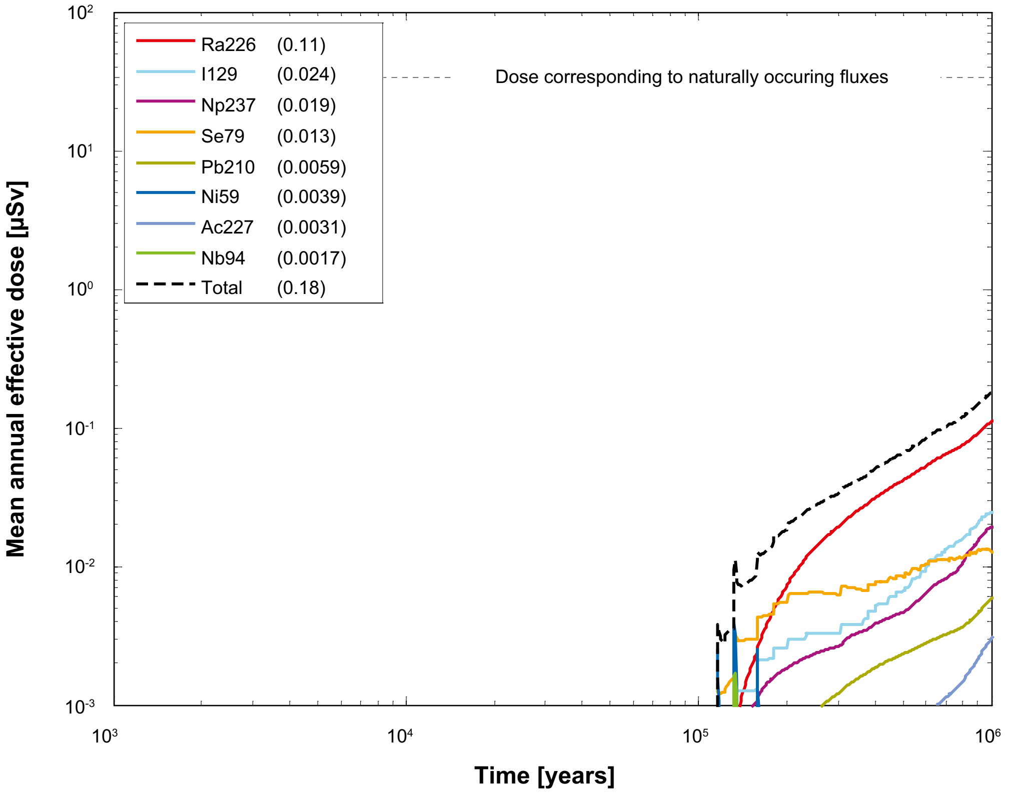

Figure 4-55. *Far-field annual effective dose in the central corrosion case compared to the naturally occurring fluxes of U-238, U-234 and Ra-226 at Forsmark converted to dose using the basic LDF values. The legend is sorted by peak (in the one-million year period) of the mean annual effective dose. The values in brackets are peak dose in units of µSv.*

4.10 Calculation with analytical models

As mentioned in Section 3.6.5, simplified, analytical models are available for the modelling of radionuclide transport in the near field and the far field. The models are documented in /Hedin 2002b/. The analytical models are applied to the six corrosion variants of the corrosion scenario.

Regarding the application of the models to the corrosion scenario, the following, further simplifying conditions are noted. The near-field release is determined by the rate of radionuclide release to water in the void space because the flow rate in the Q1 fracture is not a limitation (canister failures due to corrosion only occur in the deposition holes with the highest flow rates). Therefore, the release rate from the near field is simply modelled as the dissolution rate of the fuel, alternatively the corrosion rate of the metal parts, in both cases multiplied by the inventory. As in the numerical models, the IRF is not included but handled separately.

The release rate from the far field is in most cases calculated as the release rate from the near field times a geosphere transmission factor /Hedin 2002b/. This yields a good approximation in cases of a continuous release over long times.

However, in some cases of relatively short-duration releases caused by corrosion of the metal parts of the fuel, the treatment is overly pessimistic. In such cases the release of the entire inventory in the metal parts, M_0, as a pulse to the geosphere is also considered. This yields a peak release rate from the geosphere of M_0/τ where τ is obtained from /SKB 2006a, Appendix B/.

Hydrodynamic and molecular dispersion in the flowing fracture are pessimistically neglected when this expression is used. Also, radioactive decay is neglected in the expression since no appreciable decay will take place during the short transients of concern here.

Since both the above approaches overestimate the release rate from the far field, the smaller of the two is chosen in each realisation.

It is also noted that chain decay in the geosphere is not accounted for when applying the transmission factors for geosphere retention. The theory for a full, analytical treatment of chain decay in transmission factors has been developed, but is not yet implemented in the analytical model. Using the numerical models, it has been demonstrated that chain decay of parent nuclides of Ra-226 in the far field has a negligible impact on the releases of Ra-226 in the corrosion scenario.

The result of the analytical modelling of the probabilistic central corrosion case is shown in Figure 4-56. As seen by comparing the results in Figure 4-56 with those of the corresponding numerical case in Figure 4-5, the agreement of the peak doses is very good for nuclides emerging from the fuel matrix, whereas doses from nuclides embedded in metal parts (Ni-59 and Nb-94) are somewhat overestimated with the analytical model. This is due to the pessimistic modelling of nuclides released from corrosion of metal parts discussed above.

The modelling results of the six corrosion variants are shown in Figure 4-57. Each case was modelled with 20,000 realisations using Latin Hypercube Sampling. As seen by comparing the results in Figure 4-57 with those in Figure 4-59, which shows far-field annual effective dose for all corrosion cases calculated with FARF31, the agreement between results obtained with the two sets of models is good. All peak doses over one million years are the same to within less than a factor of 1.5.

That the numerical calculations are in good agreement with the analytical calculations significantly enhances confidence in the dose equivalent releases provided here and in the **Main report** for two reasons. First, the comparison provides an important quality assurance check on the numerical modelling of dose equivalent releases. This check applies not only to the numerical calculations but also to the data/parameter transfers, as the data for the analytical calculations were taken directly from the **Data repor**t independently of the numerical calculations. Second, it demonstrates that dose equivalent releases for the corrosion cases are controlled by relatively simple processes that are straightforward to understand.

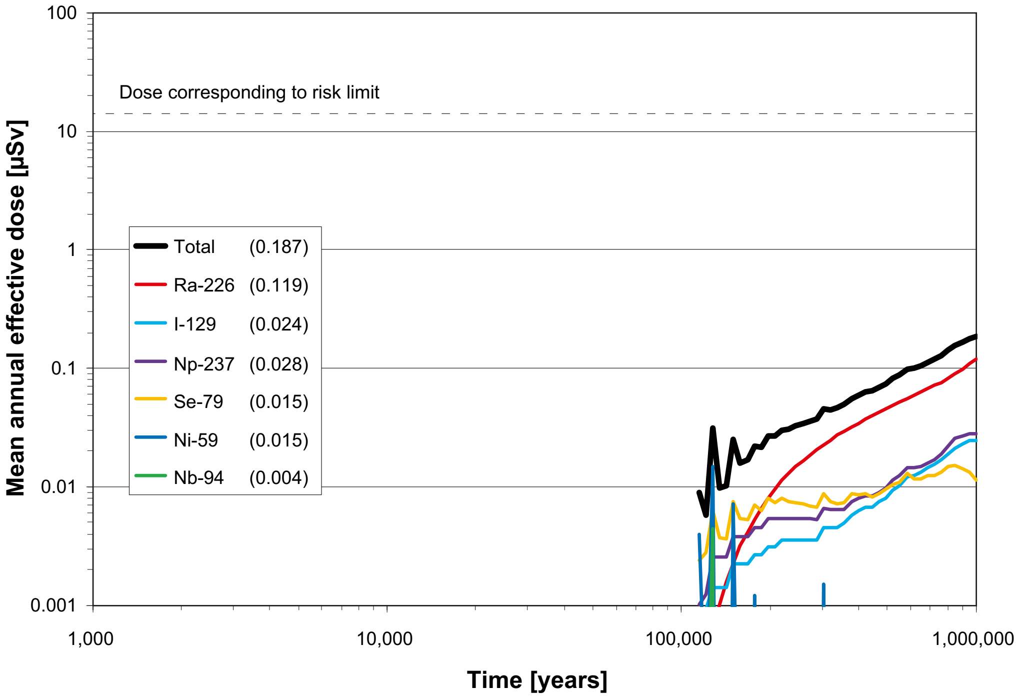

Figure 4-56. *Far-field mean annual effective dose for the central corrosion case, obtained with analytical models. The legend is sorted by peak (in the one-million year period) of the mean annual effective dose. The values in brackets are peak dose in units of µSv.*

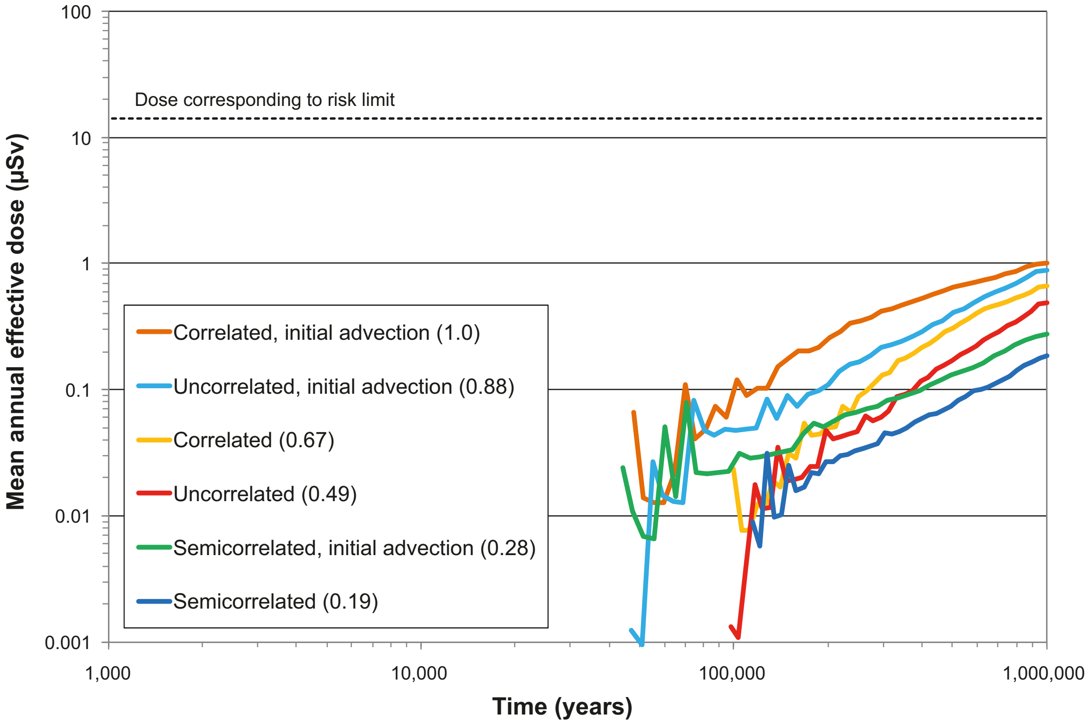

Figure 4-57. *Summary of far-field mean annual effective dose for analytical, probabilistic calculations of the six corrosion variants of the corrosion scenario. These results can be compared to the corresponding results obtained with numerical models in Figure 4-59.*

4.11 Summary and conclusions for the corrosion scenario

Figure 4-58 shows the total dose equivalent releases for cases calculated probabilistically with COMP23 in Chapter 4. All other things being equal, the correlated and the uncorrelated cases produce larger dose equivalent releases from the near field as compared with the semi-correlated cases. Cases with initial advection produce earlier and larger releases than the cases without. Disregarding thorium sorption in the near field in the semi-correlated case results in significantly lower dose equivalent releases. Thus the assumption of thorium sorption in the near field made in all other corrosion cases should be pessimistic.

Figure 4-59 shows the far-field total effective dose calculated with FARF31 for the same cases as in Figure 4-58. The modelling cases that have larger near-field dose equivalent releases experience more attenuation in the far field, thereby reducing the variation among the cases. Significantly, the far-field total effective doses are all at least an order of magnitude smaller than the dose corresponding to the risk limit. Moreover, peaks of the far-field total effective doses span a range of less than one order of magnitude. This relatively tight clustering of results suggests relative insensitivity to the modelling assumptions.

Peak total effective dose for the corrosion cases that relied on COMP23 and MARFA are summarised in Table 4-7. All of these cases used the semi-correlated DFN model. For comparison the peak of the mean annual dose equivalent near-field release is 0.59 μSv (see Figure 4-4).

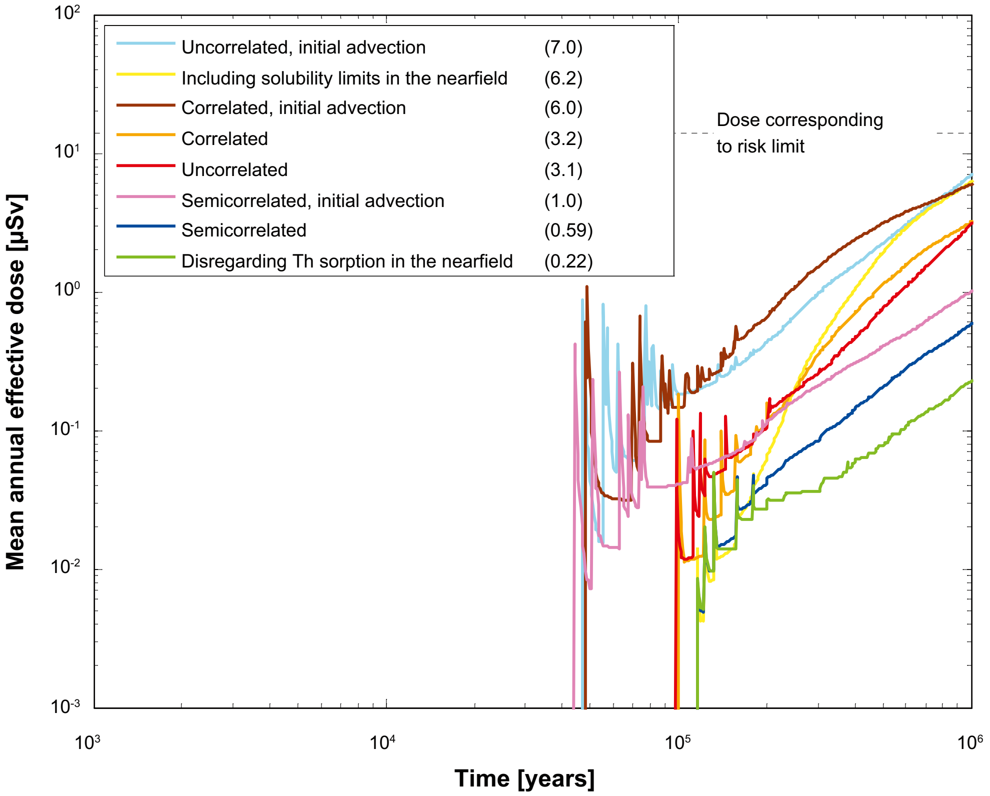

Figure 4-58. *Near-field dose equivalent release for probabilistic corrosion cases. The legend is sorted by peak (in the one-million year period) of the mean annual effective dose. The values in brackets are peak dose in units of μSv.*

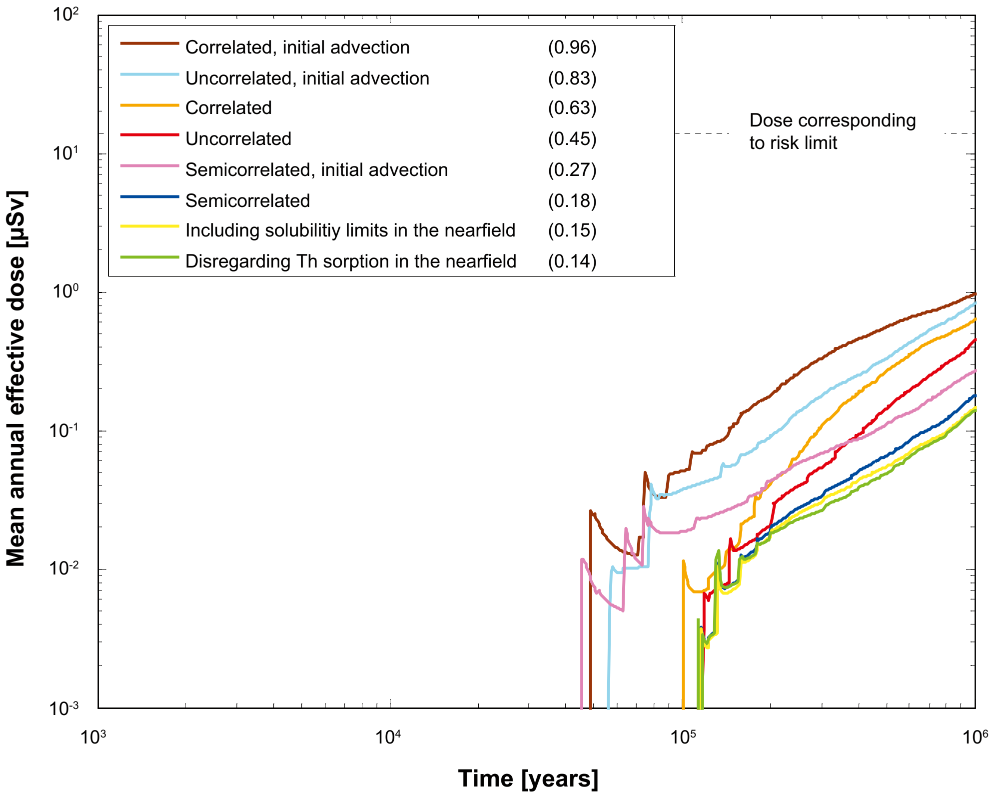

Figure 4-59. *Far-field annual effective dose for probabilistic corrosion cases calculated with FARF31. The legend is sorted by peak (in the one-million year period) of the mean annual effective dose. The values in brackets are peak dose in units of µSv.*

Table 4-7. Far-field peak of the mean annual effective dose for corrosion cases modelled with COMP23 and MARFA.

Calculation case	Far-field peak annual effective dose (µSv)
Steady conditions, no colloids	0.15
Steady conditions, 10 mg/l colloids	0.19
Steady conditions, 10 g/l colloids	0.33
Varying climate, no colloids	0.19
Varying climate, steady colloid concentration of 10 g/l	0.41
Varying climate, unsteady colloid concentrations	0.35

5 Canister failure due to shear load

5.1 Introduction

In the ‘canister failure due to shear load’ scenario (called briefly the shear load scenario below), a canister fails as a result of secondary rock movements induced by a large earthquake. It was demonstrated in the **Main report** to have a low probability in the reference evolution. Pessimistic estimates of the extent of this failure mode indicate that the probability that one out of the 6,000 canisters has failed at the end of the one million year assessment period is 0.079 /Main report Section 10.4.5/. A failure frequency as a function of time is also provided in the Main report Section 10.4.5 and this is used in the probabilistic assessment of the shear load scenario. For this failure mode, the canister is bypassed, the thickness of the buffer is reduced and the rock retention is insignificant, since a shearing fracture must have a considerable size with properties difficult to assess.

5.2 Calculation of doses for the shear load scenario

An earthquake can cause canister failure at any time after closure of the repository. The likelihood is varying during different time periods. Three different cases of failure times have been considered in the calculations: a postulated failure of one canister at 100,000 years, failure during the period 1,000 years to one million years and early failure. The following data and assumptions are used in the calculation cases:

- In the affected deposition holes the faulting is supposed to be so large that it causes massive failure of the canister, i.e. there will be no delay between failure and the onset of radionuclide transport and no credit from limited transport resistance in the canister.
- The shear movement will not affect the buffer to the extent that its protection against advective flow will be impaired, but effective amount of buffer between the canister and the shearing fracture is assumed to be reduced from 35 cm to 25 cm.
- The canister failure location is assumed to fully coincide with the location of the shearing fracture. Furthermore, the shear is assumed to increase the fracture transmissivity significantly. The Q_{eq} value for the intersecting fracture is, therefore, assumed to be sufficiently high (1 m^3/yr) that it does not contribute to the transport resistance in the near field.
- The shearing fracture is likely to be among the larger in the modelled fracture network and its properties after shearing are difficult to assess. Therefore, no credit for radionuclide retention in the geosphere is taken.
- Solubility limits are included in the calculations, since, contrary to cases in the corrosion scenario, the buffer is in place in the shear load scenario.
- The contributions from the instantly released fraction of nuclides, IRF, are included in the case with early release but not in the other cases. The contribution from the IRF is judged to be negligible based on the low probability for this scenario and the low contribution shown in the central corrosion case in Section 4.4.2.

A detailed description of the discretisation, diffusion resistances and boundary conditions used in COMP23 is given in Appendix G, section Canister failure due to shear load.

5.2.1 Postulated failure of one canister at 100,000 years

Deterministic calculations

Hydrogeological case:	Semi-correlated, base realisation
Failure time:	100,000 years
Number of failed canisters:	1
Solubility limits:	Yes
Number of realisations:	1
Number of nuclides:	45

A deterministic calculation of the shear load case is performed for a postulated failure of one canister at 100,000 years. No retention in the geosphere occurs and hence the release calculated for the near field is also valid for the far field. The contributions from the instantly released fraction of nuclides, IRF, are not included in the calculations. Table 4-4 shows the peak annual doses from pulse releases of the instantly released fraction, IRF.

Figure 5-1 show the deterministic near-field and far-field dose equivalent releases, for the shear load case with a postulated failure of one canister at 100,000 years. Shortly after the canister failure the dose is dominated by releases of Ni-59 and in the longer term the dose is dominated by Ra-226.

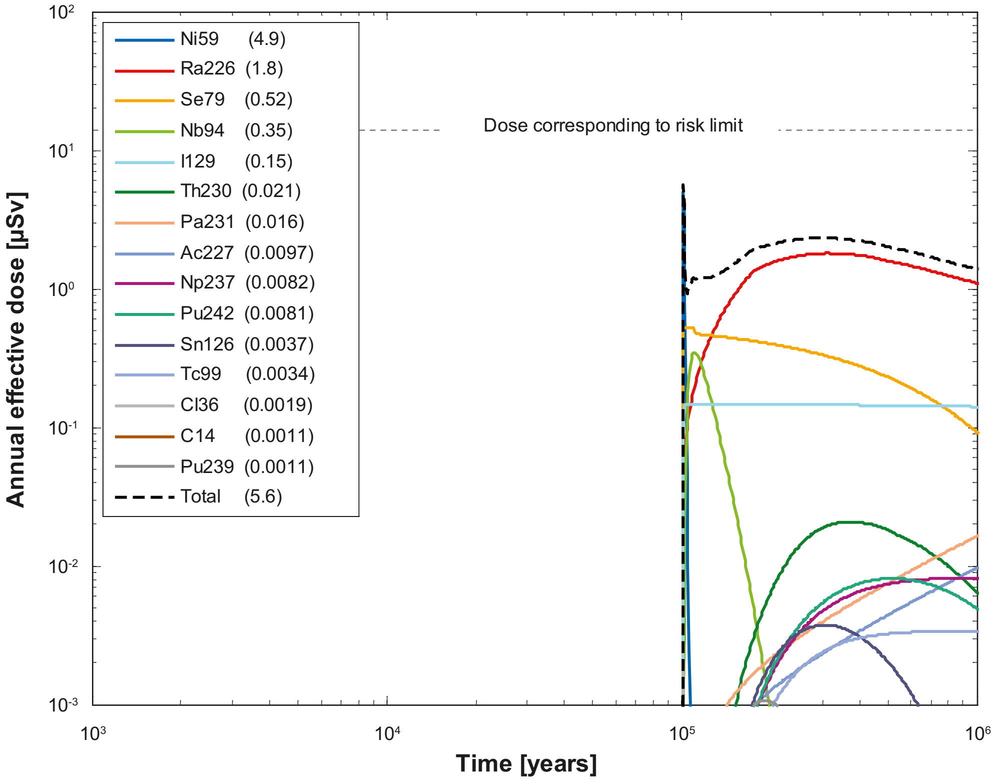

Figure 5-1. *Near-field and far-field annual effective dose for a deterministic calculation of the shear load scenario, with a postulated failure of one canister at 100,000 years. The legend is sorted by peak (in the one-million year period) of the annual effective dose. The values in brackets are peak dose in units of µSv.*

Probabilistic calculations

Hydrogeological case:	Semi-correlated, base realisation
Failure time:	100,000 years
Number of failed canisters:	1 (postulated)
Solubility limits:	Yes
Number of realisations:	1,000
Number of nuclides:	37

A probabilistic calculation of the shear load case is performed for a postulated failure time at 100,000 years and geosphere transport data from the base realisation of the semi-correlated DFN model. The postulated number of failed canisters is 1. The contributions from the instantly released fraction of nuclides, IRF, are not included in the calculations. Table 4-4 shows the peak annual doses from the pulse releases from the instantly released fraction, IRF. No retention in the geosphere occurs and hence the release calculated for the near field is also valid for the far field.

Figure 5-2 show the near-field and far-field dose equivalent releases for the shear load case with a postulated failure of one canister at 100,000 years. Shortly after the canister failure the dose is dominated by releases of Ni-59 and in the longer term the dose is dominated by releases of Ra-226.

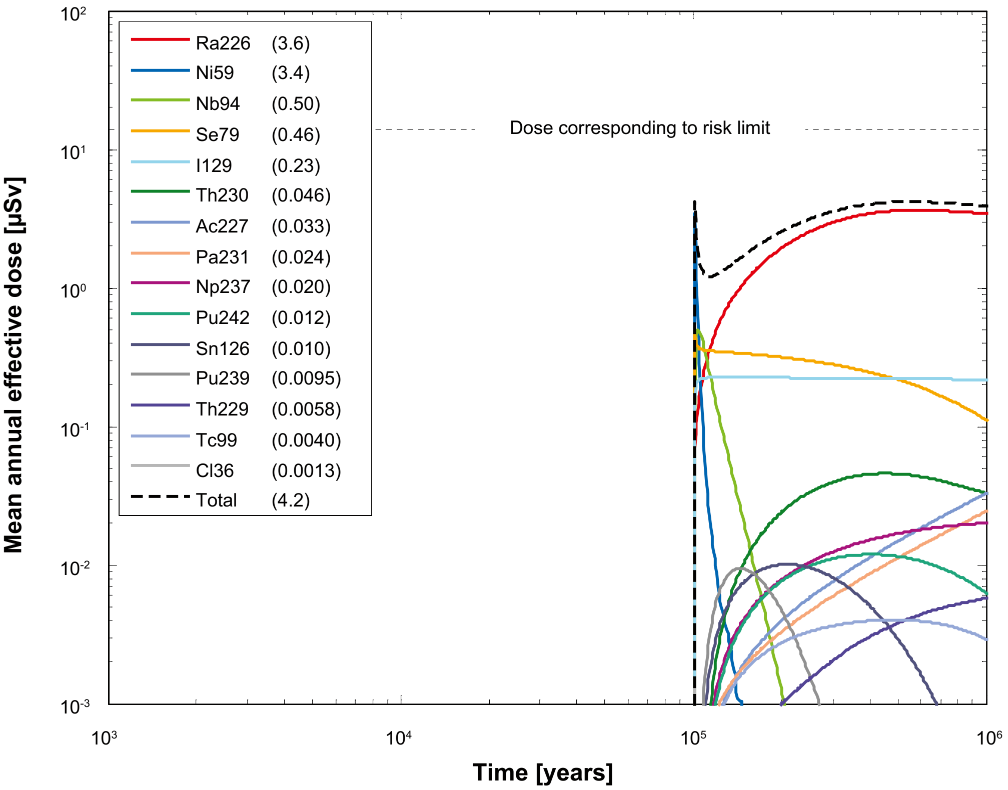

Figure 5-2. *Near-field and far-field mean annual effective dose for the probabilistic calculation of the shear load scenario, with a postulated failure of one canister at 100,000 years. The legend is sorted by peak (in the one-million year period) of the mean annual effective dose. The values in brackets are peak dose in units of µSv.*

5.2.2 Failure during the period 1,000 years to one million years

Probabilistic calculations

Hydrogeological case:	Semi-correlated, base realisation
Failure time:	1,000 to one million years
Average number of failed canisters:	0.079
Solubility limits:	Yes
Number of realisations:	6,916
Number of nuclides:	37

A probabilistic calculation of the shear load case is performed with failure during the period 1,000 years to one million years and geosphere transport data from the base realisation of the semi-correlated DFN model. The average number of failed canisters is 0.079. The contributions from the instantly released fraction of nuclides, IRF, are not included in the calculations, except for Tc-99, which is included. The contribution from the IRF is judged to be negligible based on the low probability for this scenario and the low contribution shown in the central corrosion case in Section 4.4.2. The influence is also shown to be small at early failure times, see 5.2.3. No retention in the geosphere occurs and hence the release calculated for the near field is also valid for the far field.

Figure 5-3 show the near-field and far-field dose equivalent releases for the shear load case with failure during the period 1,000 years to one million years. For an early failure time, the dose is dominated by release of C-14, thereafter by Nb-94 and in the longer term the dose is dominated by Ra-226. The dose at one million years in the present case is about 28 times lower than in the case where one canister fails at 100,000 years, but in the former case the average number of failed canisters is 0.079 compared to one in the latter.

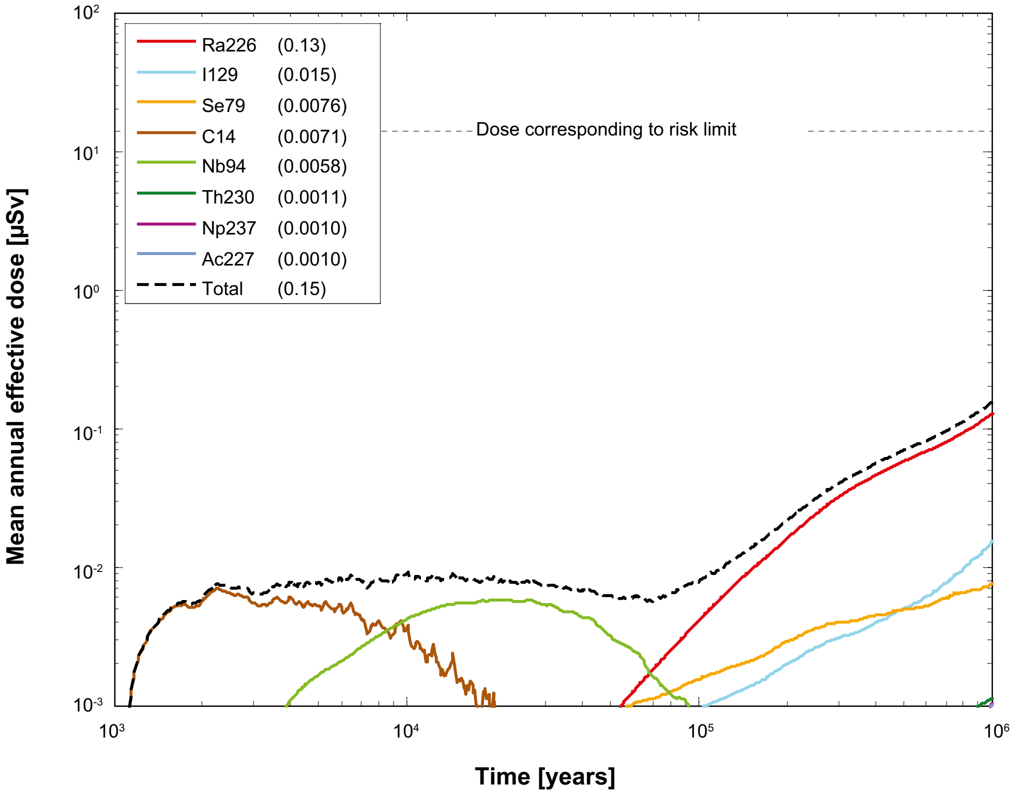

Figure 5-3. *Near-field and far-field mean annual effective dose for the probabilistic calculation of the shear load scenario, with failure during the period 1,000 years to one million years. The legend is sorted by peak (in the one-million year period) of the mean annual effective dose. The values in brackets are peak dose in units of µSv.*

Global sensitivity analysis

A global sensitivity analysis on the results of the probabilistic shear load case using the SRRC method as for the central corrosion case yields results according to Figure 5-4.

Regressing the total dose at 10^6 years on the input variables yields, in descending order, the fuel dissolution rate D_{Fuel}, the solubilities of radium and thorium, and the failure time $t_{Failure}$ as the input parameters most affecting dose results. Regressing on Ra-226 dose at 10^6 years yields a similar result due to the dominance of Ra-226. The significance of the solubility of thorium is due to decay of Th-230 to Ra-226 in the buffer, where the release of Th-230 to the buffer is controlled by the solubility of thorium. A further scrutiny of individual realisations reveals that the significance of the limited solubility overall is due to a relatively limited number of realisations with low solubilities, whereas the total dose is dominated by the larger number of realisations that have solubilities that are sufficiently high so as to not limit the release. Solubilities of neither Th nor Ra (taking into account co-precipitation with Ba) significantly limit the mean release rate of Ra-226. This conclusion is corroborated by the fact that the case with the omitted buffer (Section 5.2.4), where neither sorption in the buffer nor solubility limits are included, increases Ra-226 mean dose by only a factor of 2.

Regressing instead on the maximum of total dose over time yields the failure time and the corrosion release rate, *CRR*, as significant variables. This is consistent with the fact that for early failures, the highest doses occur due to release of e.g. C-14 and Nb-94 congruently with the corrosion of structural parts of the fuel elements.

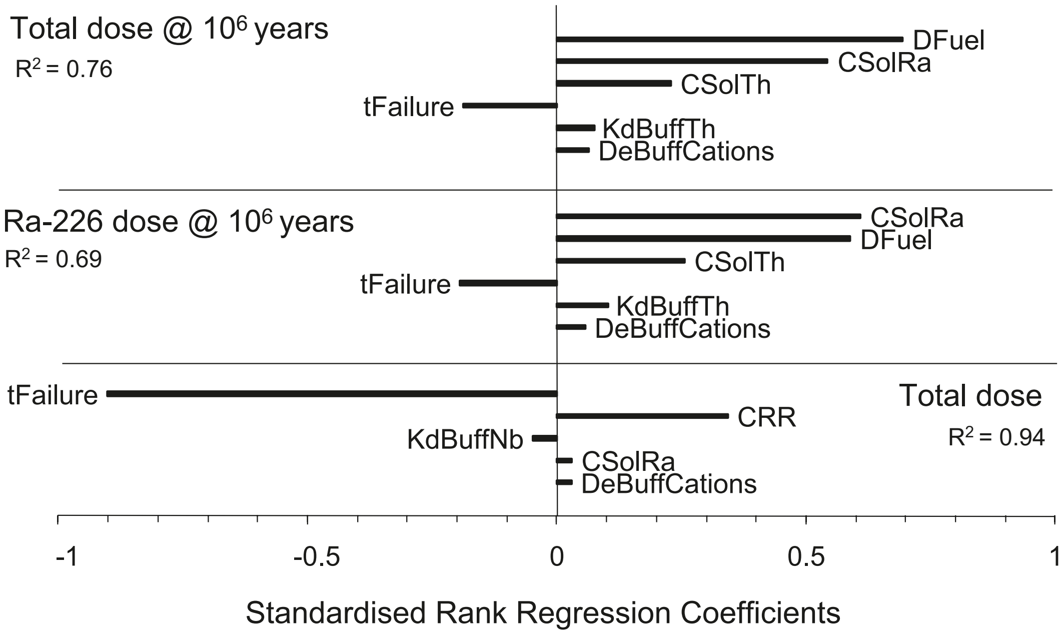

Figure 5-4. *Results of standardised rank regression for the probabilistic calculation of the shear load scenario, with failure during the period 1,000 to one million years. Regressing on total dose at 10^6 years and on Ra-226 dose at 10^6 years yields similar results due to the dominance of Ra-226. Regression on the maximum of total dose over time identifies CRR as an additional sensitive input.*

Risk dilution

Risk dilution for the shear load scenario needs to be considered, because canisters fail at probabilistically determined times.

An illustration is obtained by comparing the results in Figure 5-2 (postulated, deterministic failure time) with those in Figure 5-3 (distribution of failure times). If the result in Figure 5-2 is multiplied by the overall probability of the event occurring during the assessment period, i.e. 0.079, then the dose at one million years (0.28 μSv) is relatively close to that obtained at one million years in Figure 5-3 (0.15 μSv). This small difference is because the consequences are determined i) by in-growth of Ra-226 and ii) by the build-up of Th-230 released from the fuel and precipitated in the canister interior or sorbed in the buffer, which in general occur long after the failure time. The in-growth of Ra-226 is essentially controlled by the build-up of its parent nuclide Th-230, which occurs on a time scale comparable to the half-life of Th-230 (approximately 75,000 years). The build-up of Th-230 occurs on time scales determined by the fuel dissolution rate, which are of the order of one million years.

Risk dilution, including a treatment of the pulse releases, is further discussed in Section 13.9 in the **Main report**.

Probabilistic calculations, disregarding co-precipitation of radium and barium

Hydrogeological case:	Semi-correlated, base realisation
Failure time:	1,000 to one million years
Average number of failed canisters:	0.079
Solubility limits:	Yes, disregarding co-precipitation of radium and barium
Number of realisations:	6,916
Number of nuclides:	37

Due to the assumed high equivalent flow rate in the Q1 buffer/rock interface, the release rate of radionuclides from the near field is in general sufficiently high in comparison to the fuel dissolution rate to render solubility limits inside the canister ineffective. As an illustration, a probabilistic case where no credit was taken for co-precipitation of Ra/Ba was calculated, i.e. where the solubility of Ra was increased by a factor of 1,000. Figure 5-5 show the near-field and far-field dose equivalent releases for the shear load case with failure during the period 1,000 years to one million years and disregarding co-precipitation of Ra/Ba. This assumption led to an increase of the release rate of Ra by only a factor of about 1.5.

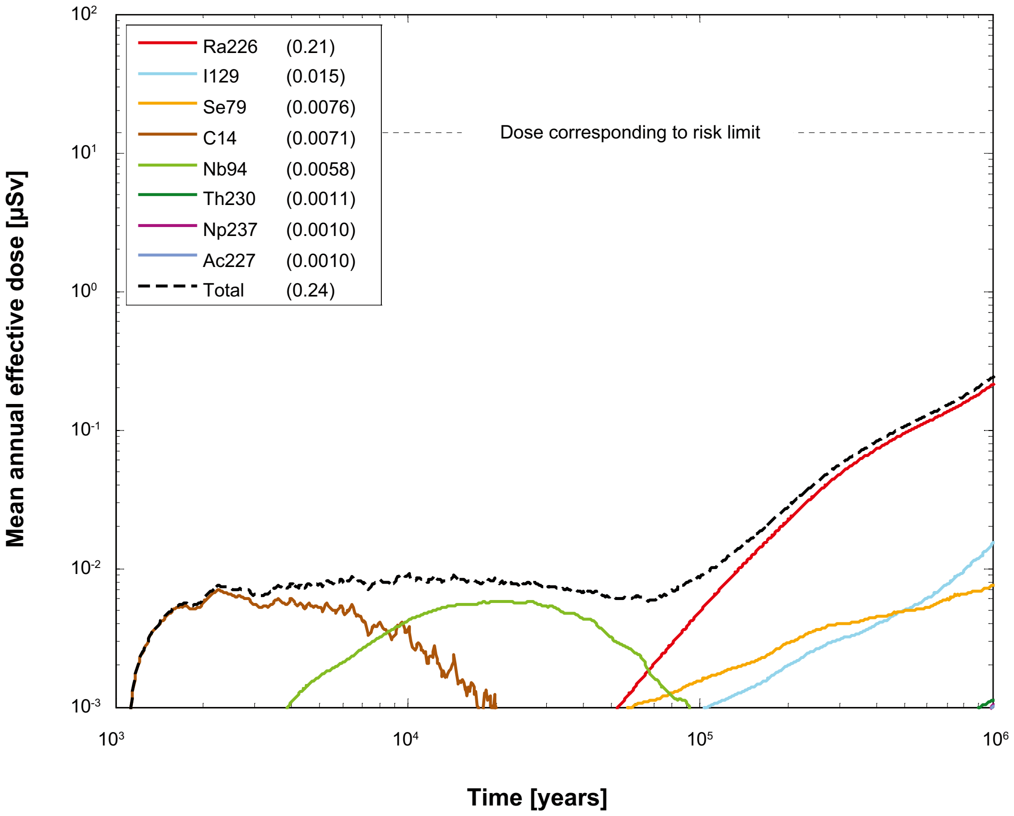

Figure 5-5. *Near-field and far-field mean annual effective dose for the probabilistic calculation of the shear load scenario, with failure during the period 1,000 years to one million years, disregarding co-precipitation of radium and barium. The legend is sorted by peak (in the one-million year period) of the mean annual effective dose. The values in brackets are peak dose in units of µSv.*

5.2.3 Early failure

Probabilistic calculations

Hydrogeological case:	Semi-correlated, base realisation
Failure time:	0–10,000 years
Average number of failed canisters:	$2.4 \cdot 10^{-8}$/year
Solubility limits:	Yes
Number of realisations:	6,916
Number of nuclides:	45

For times up to 1,000 years after closure, the frequency of earthquakes is assessed to be lower, with a probability of failure of one of the 6,000 canisters by the end of the initial 1,000 year period being $2.4 \cdot 10^{-5}$ or $2.4 \cdot 10^{-8}$/year /**Main report** Section 10.4.5/. Also, the use of basic LDF-values overestimates the doses in this time interval for two reasons. First, the basic LDF is a pessimistic upper bound for releases occurring continuously over an entire interglacial period taking into account accumulation because a large part of the interglacial period has elapsed without any releases when the repository is sealed. Second, it is not meaningful to use the LDF concept for a radionuclide that decays to insignificance over an interglacial period because the concept is based on a continuous uniform release over the period.

A more detailed calculation of the shear load scenario for the initial 10,000 years was done to facilitate comparison with the results for the one million year time frame presented above. In this calculation, releases from the near field were determined as for all other cases; the IRF:s were also included. Because no credit is taken for geosphere retention in the shear scenario, the near-field releases are used as direct input to the biosphere modelling. In addition, because it is not possible to determine a location of the releases among the identified potential landscape objects, the release is fed to each object and the time dependent development of radionuclide transport and dose in the landscape is calculated for each object. The object giving the highest dose is then determined for each point in time and for each radionuclide. This entity is pessimistically defined as the calculated dose consequence for the case of a shear failure during the initial 10,000 years. A well is included in each landscape object in the same way as for the LDF calculations.

The result of this calculation is that the peak dose is almost four orders of magnitude lower than that corresponding to the regulatory risk limit, see Figure 5-6. (Note the extended dose scale compared to most other figures). Releases of Cs-137 and Sr-90 dominate in the beginning and thereafter C-14, I-129, Ag-108m and Nb-94 dominate.

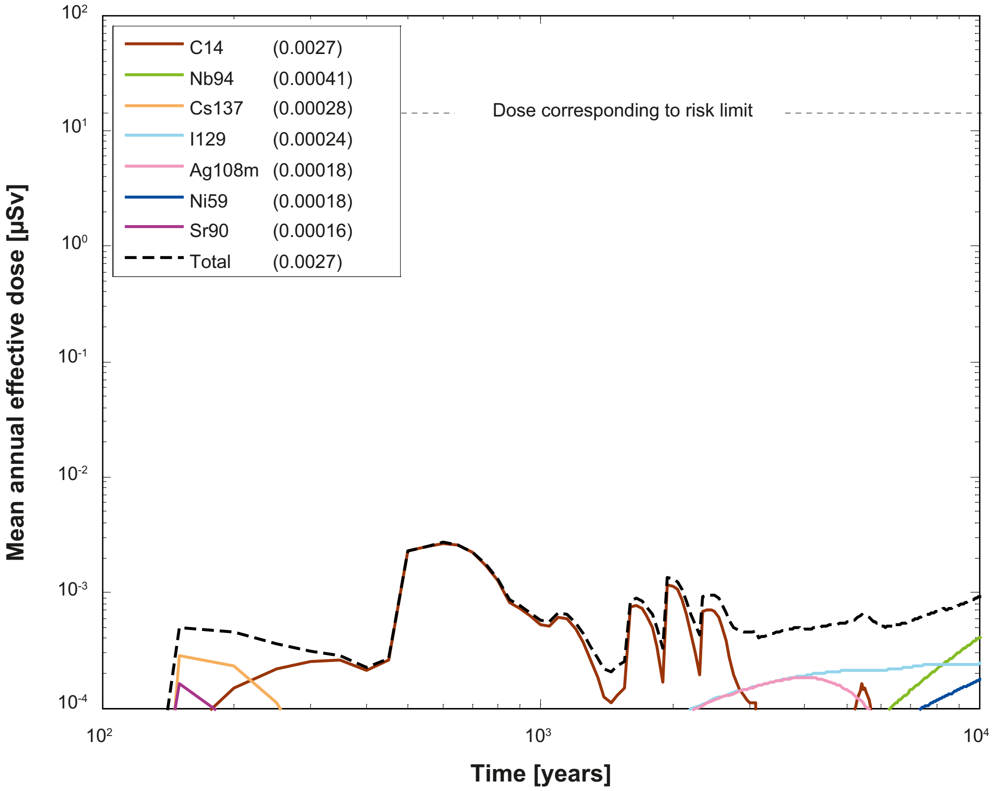

__Figure 5-6.__ Near-field and far-field mean annual effective dose for the probabilistic calculation of the shear load scenario, with failure during the period up to 10,000 years. The legend is sorted by peak (in the one-million year period) of the mean annual effective dose. The values in brackets are peak dose in units of µSv.

5.2.4 Combination of shear load and buffer advection

Probabilistic calculations

Hydrogeological case:	Semi-correlated, base realisation
Failure time:	1,000 to one million years
Average number of failed canisters:	0.079
Solubility limits:	No
Thorium sorption in near field:	Yes (modelled as low solubility limit)
Number of realisations:	6,916
Number of nuclides:	37

In this case the combination of the shear load and the buffer advection scenarios /**Main report** Section 12.9.3/ is addressed and the consequences of a shear failure followed by buffer erosion is considered, since it is reasonable to assume that the groundwater flow in a fracture that has undergone a major secondary shear movement could be high. Buffer erosion could then ultimately lead to loss of the buffer and its retardation function in the deposition hole with the canister failed due to shearing. A similar situation could arise if the buffer material is transformed through interaction with iron ions from the failed canister, as discussed in the **Main report** in the buffer transformation scenario /**Main report** Section 12.4/.

The case with shear failures distributed between 1,000 and one million years was therefore calculated also for near-field conditions with a missing buffer. The conceptualisation of the near field is thus the same as in the corrosion scenario, but near-field flow data are stylised and geosphere retention is disregarded as in other consequence calculations for the shear load scenario. The results are shown in Figure 5-7.

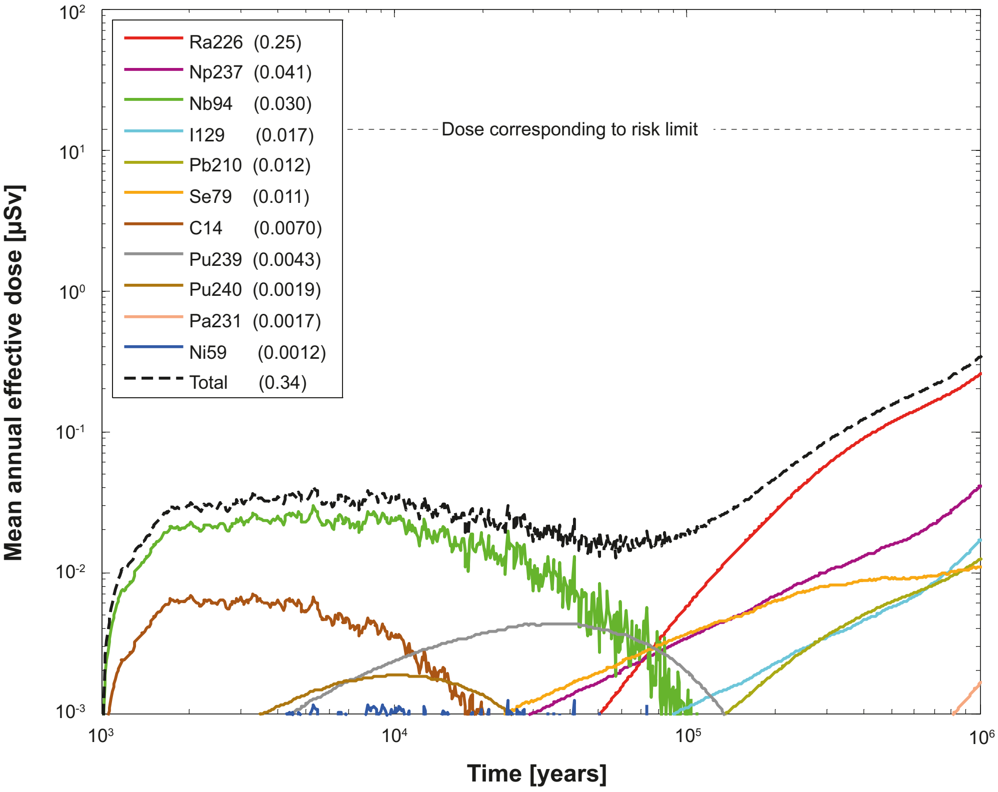

Figure 5-7. *Near-field and far-field mean annual effective dose for a probabilistic calculation of the shear load scenario, with advective conditions in the deposition hole, failure during the period between 1,000 years and one million years. The legend is sorted by peak (in the one-million year period) of the mean annual effective dose. The values in brackets are peak dose in units of µSv.*

The result is similar to the situation where the buffer is present in Figure 5-3 especially beyond 100,000 years. The peak annual effective dose from Ra-226 increases by about a factor of 2 from 0.13 μSv/yr to 0.25 μSv/yr. The retardation in the buffer and the limited solubility of the dose driving Ra-226, both of which contribute to retardation only when the buffer is present, are thus of minor importance in the shear load scenario.

The main difference for the radionuclides contributing most to dose is for Nb-94, as this radionuclide is significantly retained in the buffer when it is present. However, Nb-94 contributes to dose mainly before 100,000 years. The above case is only relevant after the buffer has been eroded. Since the near-field hydrogeological conditions are stylised with respect to radionuclide transport in the above case, they are not necessarily relevant for estimating the time taken for buffer erosion to cause advective conditions in the deposition hole. The first advective positions occur after several tens of thousands of years in the buffer advection scenario. However, considering the unknown nature of the hydraulic conditions in the deposition hole after a shear failure, the results in Figure 5-7 are seen as cautiously representative of a combined scenario for times beyond 10,000 years.

5.3 Alternative safety indicators for shear load case 1,000 years to one million years

Four alternative indicators to risk are used in SR-Site: release of activity from the geosphere, radiotoxicity flux from the geosphere, concentrations of radionuclides in ecosystems and natural geosphere fluxes of radionuclides. The following reference values are used when evaluating these indicators.

- The Finnish activity release constraints. These constraints are strictly applicable only in the Finnish regulatory context, but are nevertheless deemed useful as reference values for SR-Site.
- The reference value for radiotoxicity flux from the geosphere suggested by the EU SPIN project.
- Measured concentrations of naturally occurring radionuclides in ecosystems at the Forsmark site or other, comparable sites. Not further described here, see **Main report** Section 13.5.8.
- Naturally occurring fluxes of radionuclides at the site.

For further descriptions of the indicators, see Alternative safety indicators for the central corrosion case in Section 4.9.

5.3.1 Finnish activity release constraints

The activity release constraints issued by STUK, see Section 4.9.1, have been applied to releases calculated for the shear load scenario, with failure during the period 1,000 years to one million years. The releases are around three orders of magnitude lower than the STUK constraint, see Figure 5-8.

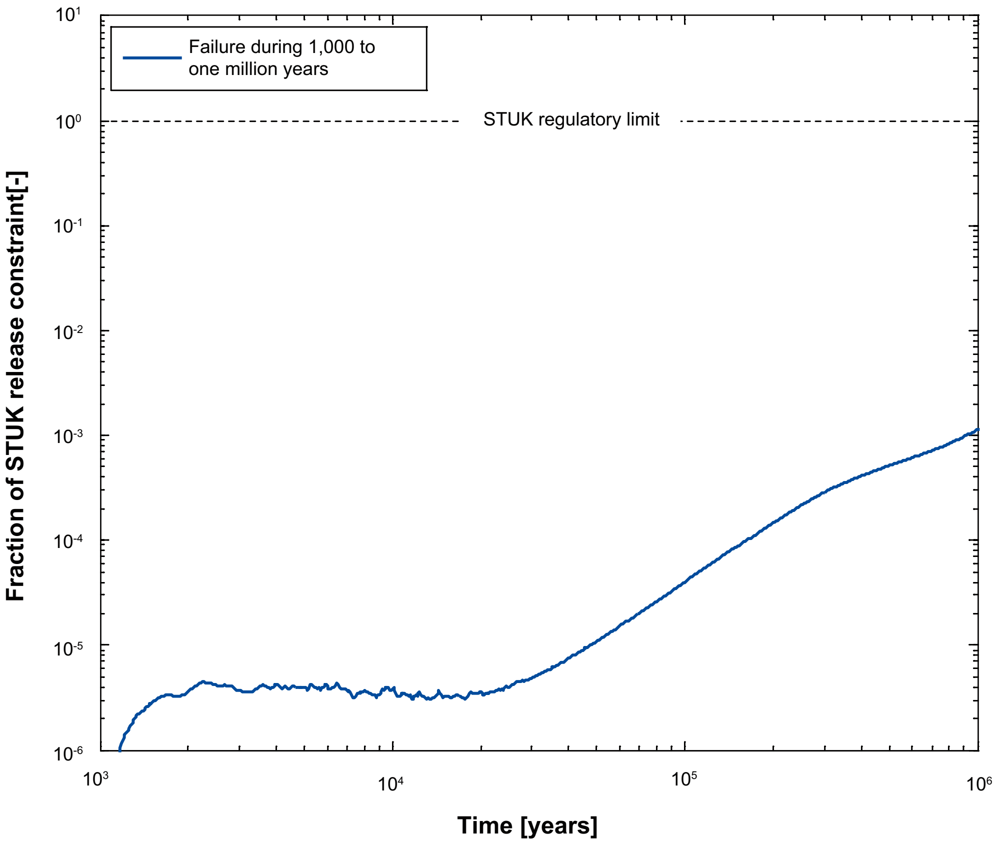

Figure 5-8. *Releases as a fraction of the activity release constraint index adopted by the Finnish regulator for the shear load case with failure during the period 1,000 years to one million years.*

5.3.2 Radiotoxicity flux from the geosphere – EU SPIN Project

The EU SPIN project, see Section 4.9.2, approach was used on the releases calculated for the shear load scenario, with failure during the period 1,000 years to one million years. The releases, 0.0096 Sv/year, are around four orders of magnitude lower than the SPIN reference value, 60 Sv/year, see Figure 5-9.

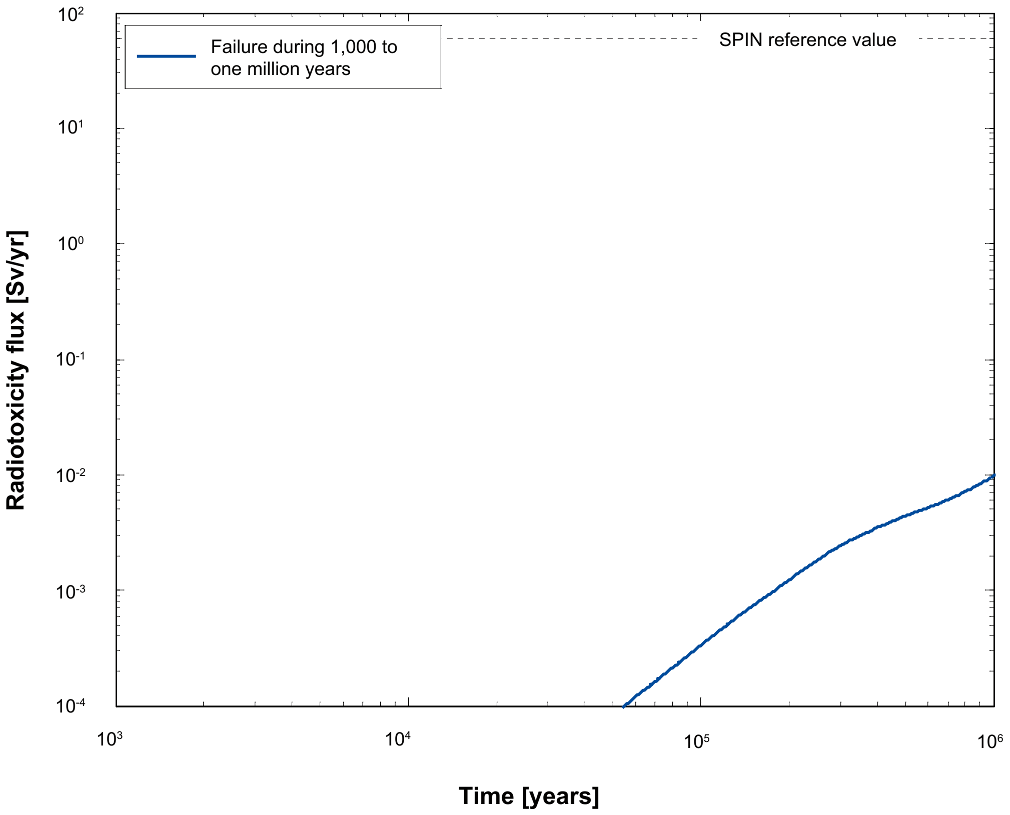

Figure 5-9. *Radiotoxicity flux in the shear load case with failure during the period 1,000 years to one million years compared to the SPIN reference value.*

5.3.3 Naturally occurring fluxes of radionuclides at the site

The last alternative indicator to risk used in SR-Site is naturally occurring fluxes of radionuclides at the site. The naturally occurring fluxes of U-238, U-234 and Ra-226, are estimated based on measured activities during the site investigations, see Section 2.3. Figure 5-10 shows the release rates of U-238, U-234 and Ra-226 for the shear load scenario, with failure during the period 1,000 years to one million years, compared to the naturally occurring fluxes at Forsmark. The naturally occurring fluxes of U-238, U-234 and Ra-226 have been converted to effective dose by using the basic LDF values, the obtained dose is shown together with the far-field annual effective dose in the shear load case 1,000 years to one million years in Figure 5-11.

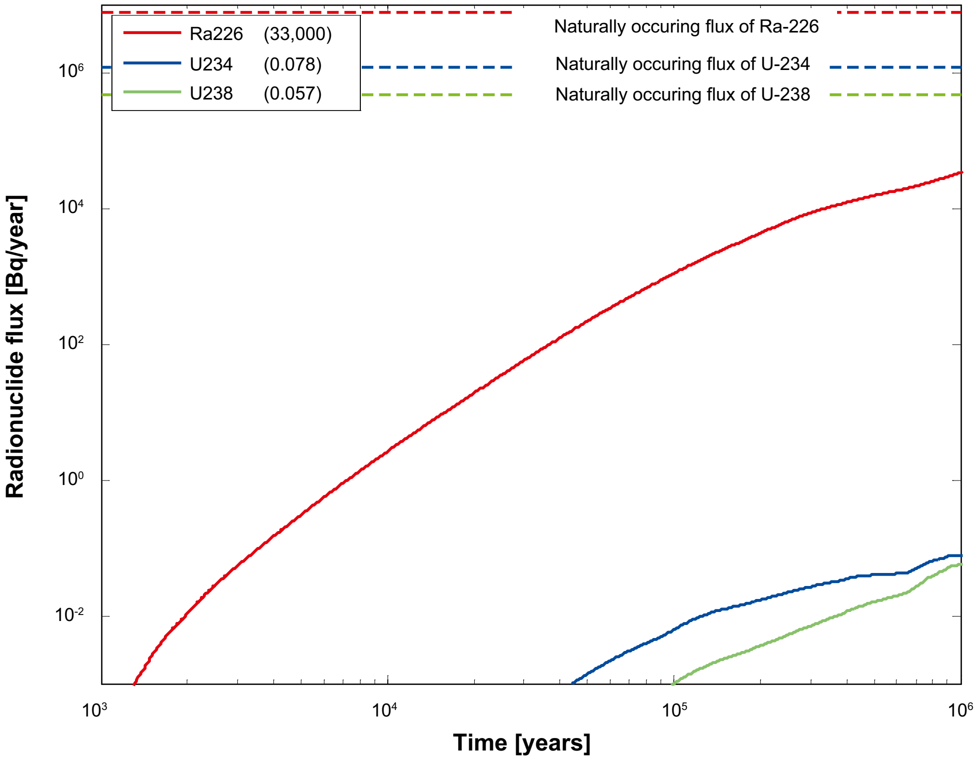

Figure 5-10. *Far-field release rates (Bq/year) of U-238, U-234 and Ra-226 in the shear load case 1,000 years to one million years compared to the naturally occurring fluxes at Forsmark. The legend is sorted by peak (in the one-million year period) of the mean annual radionuclide flux. The values in brackets are peak radionuclide fluxes in units of Bq/yr.*

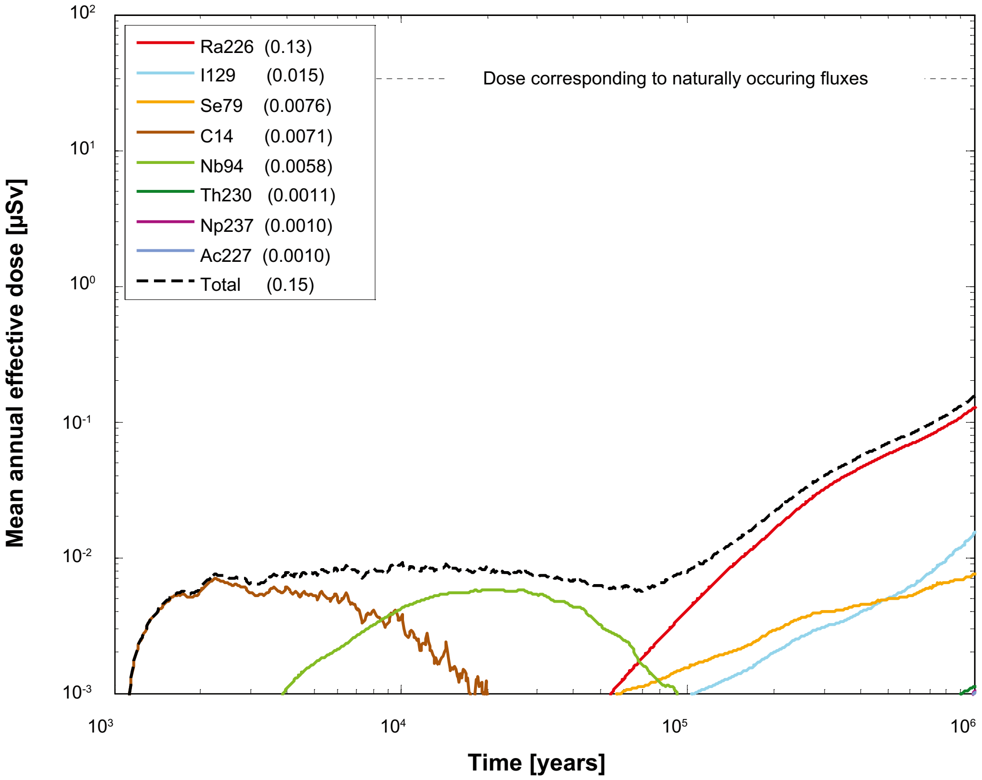

Figure 5-11. *Far-field annual effective dose in the shear load case 1,000 years to one million years compared to the naturally occurring fluxes of U-238, U-234 and Ra-226 at Forsmark converted to dose using the basic LDF values. The legend is sorted by peak (in the one-million year period) of the mean annual effective dose. The values in brackets are peak dose in units of µSv.*

5.4 Calculation with analytical models

For the shear load scenario, analytical models were applied to the variant with the combination of shear load and buffer advection with failure during the period 1,000 years to one million years.

The result of the analytical modelling of the probabilistic shear load and buffer advection case is shown in Figure 5-12. As seen by comparing the results in Figure 5-12 with those of the corresponding numerical case in Figure 5-7, the maximum total doses are almost identical. Together with the good agreement obtained also for the corrosion scenario, Section 4.10, the analytical calculations significantly enhances confidence in the dose equivalent releases provided here and in the **Main report.**

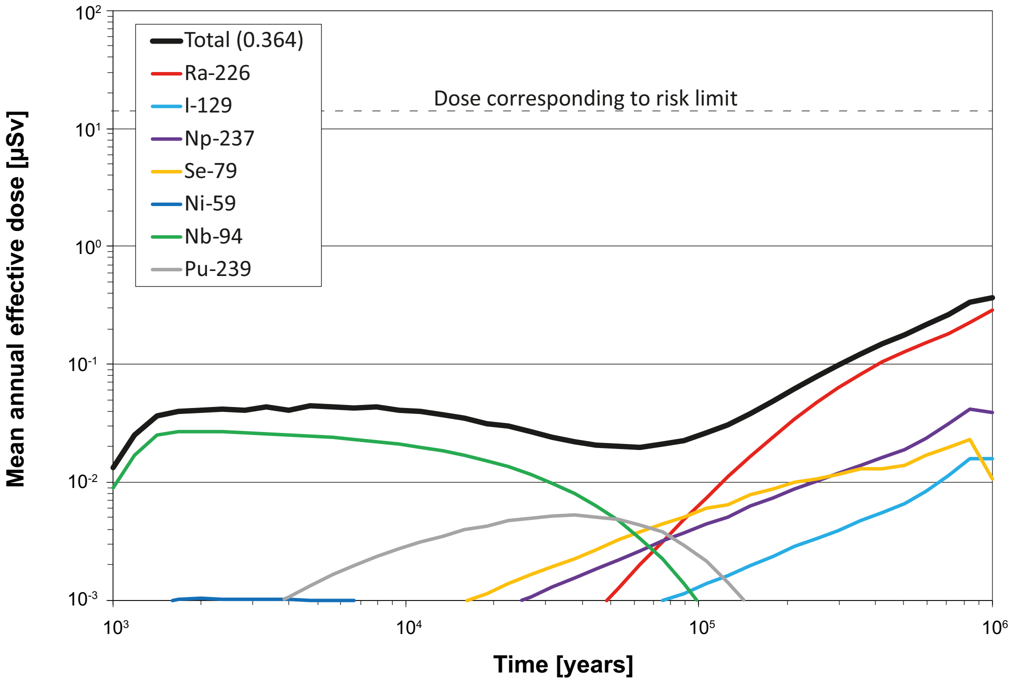

Figure 5-12. Near-field and far-field mean annual effective dose for the probabilistic calculation of the combined shear load and buffer advection scenario, obtained with analytical models, with failure during 1,000 years to one million years.

5.5 Summary and conclusions for the shear load scenario

Figure 5-13 shows the total effective dose for early failure and for failure during the time period 1,000 years to one million years. No retention in the geosphere occurs and hence the release calculated for the near field is also valid for the far field. Note that the two cases have different probability of failure and that a more detailed calculation was performed for early failure (red curve) where the COMP23 results were used as input to the biosphere modelling while for later failure (blue curve) the COMP23 results were treated as in all other cases with basic LDF values.

It is seen that the early failure peak dose has it maximum of 0.0027 µSv after about 600 years. For later failure the peak dose of 0.15 µSv occurs at one million years and is about two orders of magnitude below the dose corresponding to the regulatory risk limit, 14 µSv.

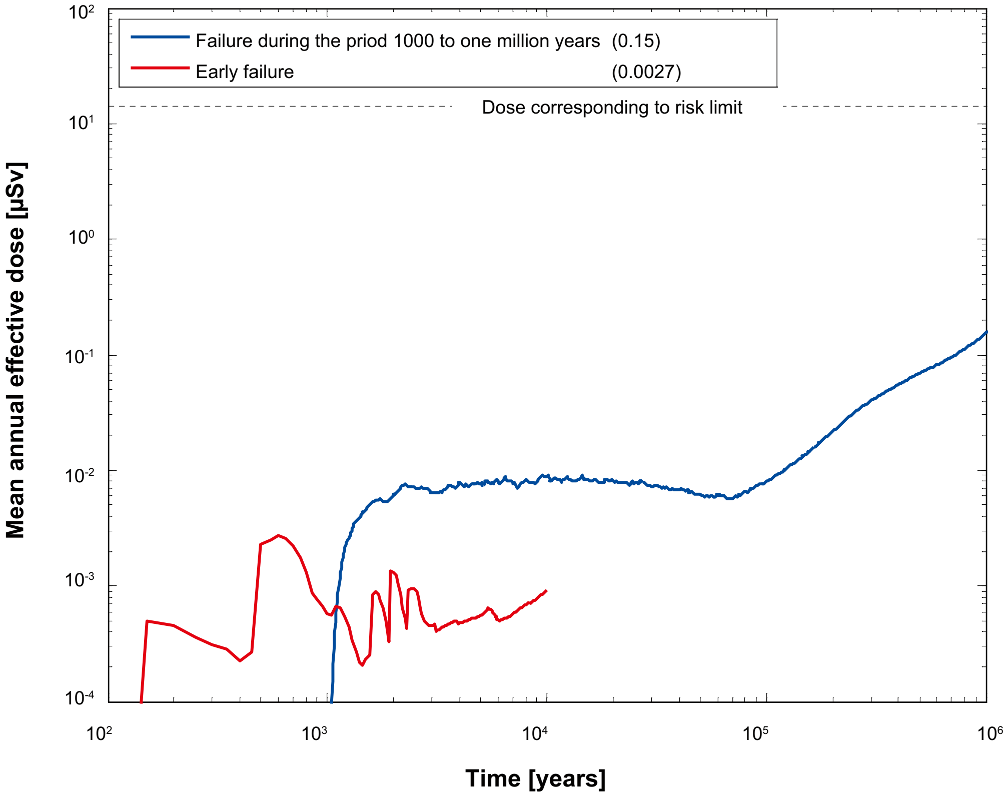

Figure 5-13. *Far-field annual effective dose for the shear load scenario. Note that the case for 1,000 to one million years are calculated with basic LDF values, while the curve for early failure is calculated with time a dependent biosphere model. The legend is sorted by peak (in the one-million year period) of the mean annual effective dose. The values in brackets are peak dose in units of µSv.*

6 Hypothetical residual scenarios to illustrate barrier functions

6.1 Introduction

In this section, hypothetical, residual scenarios to illustrate barrier functions are analysed. They encompass *a*) the scenario 'canister failure due to isostatic load', considered as residual according to the analysis in **Main report** Section 12.8, *b*) a failure mode where a hypothetical initial defect in the form of a penetrating pinhole in the copper shell grows into a larger defect and *c*) a number of additional cases where different barriers are assumed to be completely lost. The canister failure due to isostatic load scenario is analysed in Section 6.2. The pinhole case is analysed in Section 6.3, using the model tools COMP23 and FARF31 and in Section 6.4 using the MARFA code for the far-field transport. Hypothetical cases illustrating consequences of assumed barrier losses in addition to the pinhole case are analysed in Section 6.5.

6.2 Canister failure due to isostatic load

In the 'canister failure to due to isostatic load' scenario (briefly called the isostatic load scenario below) a canister fails due to isostatic collapse. It could occur as a consequence of the increased isostatic pressure due to a glacial overburden. The likelihood for this failure mode is negligible.

For this failure mode the canister is bypassed, whereas the buffer and the geosphere are assumed to have intact retention properties. It thus resembles the final state of the pinhole case, i.e. its state after occurrence of a large failure (Section 6.3).

Three transport paths are modelled:

- Q1, a fracture intersecting the deposition hole at a vertical position of the canister lid. This fracture is placed on the opposite side of the buffer to the canister defect, hence minimising the transport distance and the diffusional transport resistance. Thermally induced spalling is assumed to have occurred in the wall of the deposition hole meaning that the transport resistance at the interface Q1 is decreased.
- Q2, an excavation damage zone, EDZ, in the floor of the deposition tunnel. In the hydrogeological model, EDZ is treated as a thin conductive layer.
- Q3, a fracture intersecting the deposition tunnel. The distance to Q3 is obtained in the hydrogeological model by tracing advectively transported particles released in the deposition tunnel just above the deposition hole. As the distance from the deposition hole to Q3 differs, the longitudinal dimensions of the modelled deposition tunnel are different for different deposition holes.

A detailed description of the discretisation, diffusion resistances and boundary conditions used in COMP23 is given in Appendix G (section Growing pinhole – spalling, large hole).

6.2.1 Postulated failure of one canister at 10,000 years

Deterministic calculations

Hydrogeological case:	Semi-correlated, base realisation
Failure time:	10,000 years
Number of failed canisters:	1
Solubility limits:	Yes
Number of realisations:	1
Number of nuclides:	45

A deterministic calculation of the isostatic load failure was performed with a postulated failure of one canister at 10,000 years.

Figure 6-1 and Figure 6-2 show the deterministic near-field and far-field dose equivalent releases, respectively, for the isostatic load case with a postulated failure of one canister at 10,000 years. The doses from the near field are dominated by releases of I-129 and shortly after canister failure also with contribution of releases of C-14. The doses from the far field are dominated by releases of I-129.

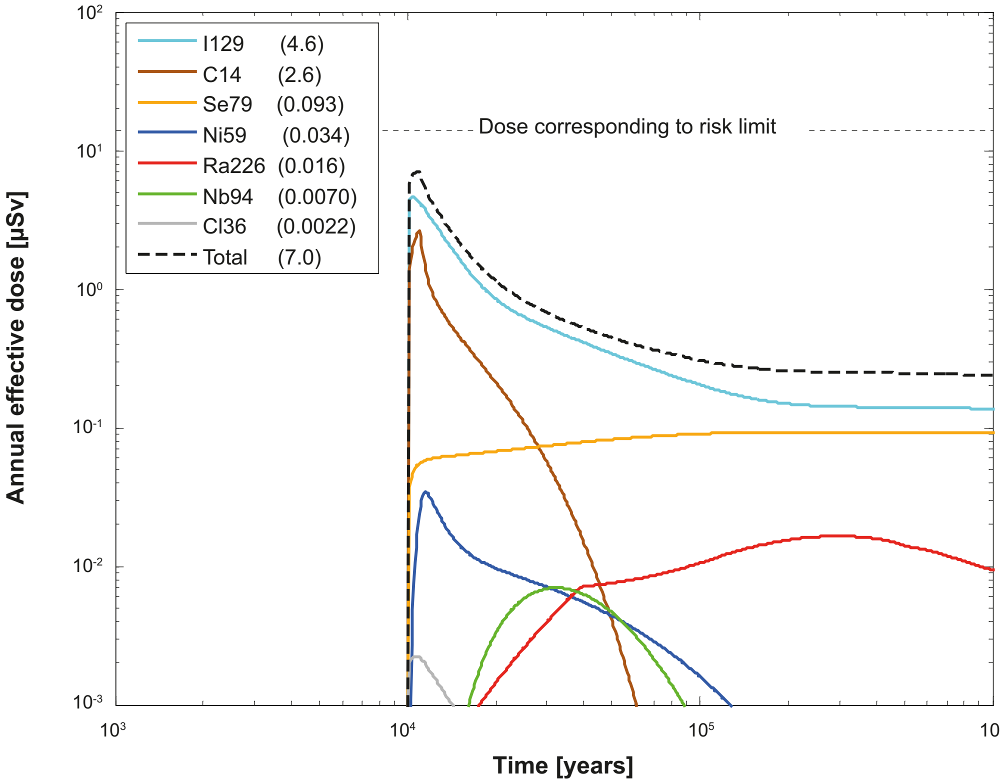

Figure 6-1. *Near-field dose equivalent release for a deterministic calculation of the isostatic load scenario, with a postulated failure of one canister at 10,000 years. The legend is sorted by peak (in the one-million year period) of the annual effective dose. The values in brackets are peak dose in units of µSv.*

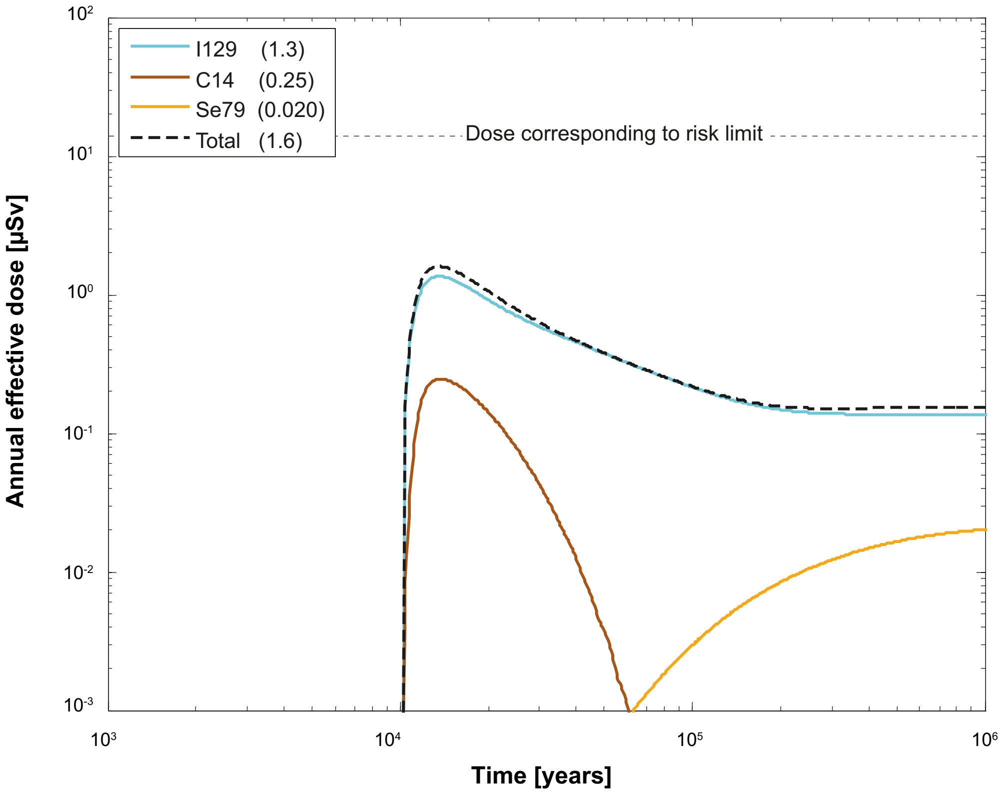

Figure 6-2. *Far-field annual effective dose for a deterministic calculation of the isostatic load scenario, with a postulated failure of one canister at 10,000 years. The legend is sorted by peak (in the one-million year period) of the annual effective dose. The values in brackets are peak dose in units of µSv.*

Probabilistic calculations

Hydrogeological case:	Semi-correlated, base realisation
Failure time:	10,000 years
Number of failed canisters:	1 (postulated)
Solubility limits:	Yes
Number of realisations:	6,916
Number of nuclides:	37

A probabilistic calculation of the isostatic load failure was performed with a postulated failure of one canister at 10,000 years and geosphere transport data from the base realisation of the semi-correlated DFN model.

Figure 6-3 and Figure 6-4 show the near-field and far-field dose equivalent releases, respectively, for the isostatic load failure with a postulated failure of one canister at 10,000 years. Both near-field and far-field doses are dominated by releases of I-129 and shortly after canister failure also with a contribution due to releases of C-14.

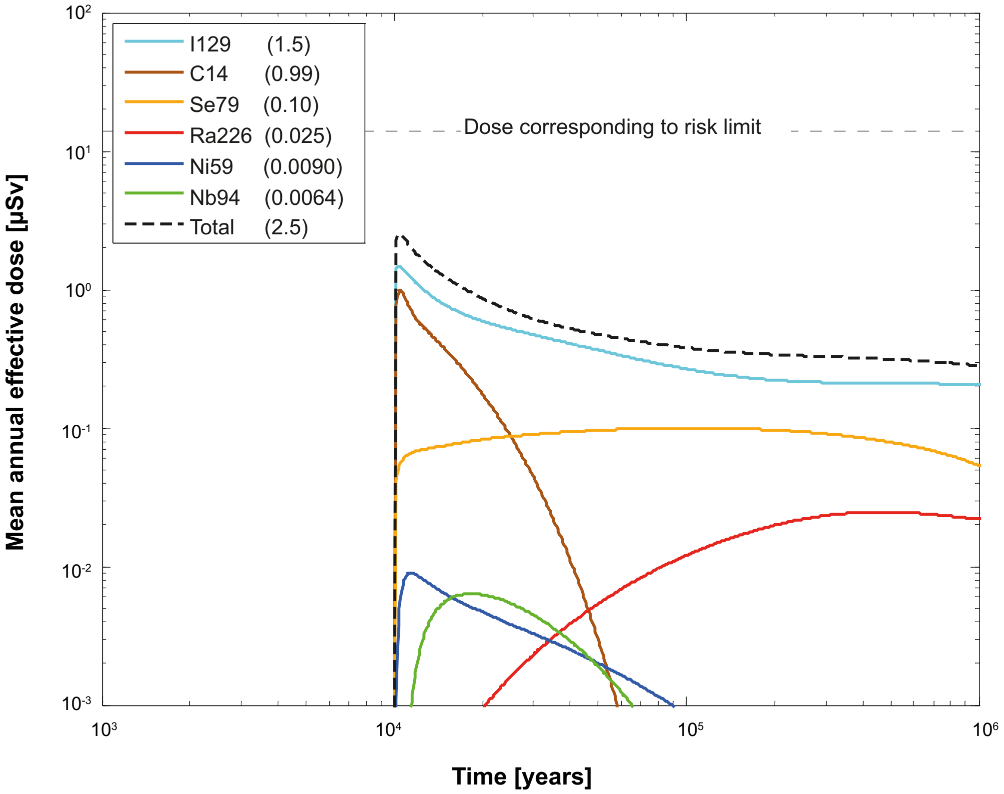

Figure 6-3. *Near-field dose equivalent release for a probabilistic calculation of the isostatic load scenario, with a postulated failure of one canister at 10,000 years. The legend is sorted by peak (in the one-million year period) of the mean annual effective dose. The values in brackets are peak dose in units of µSv.*

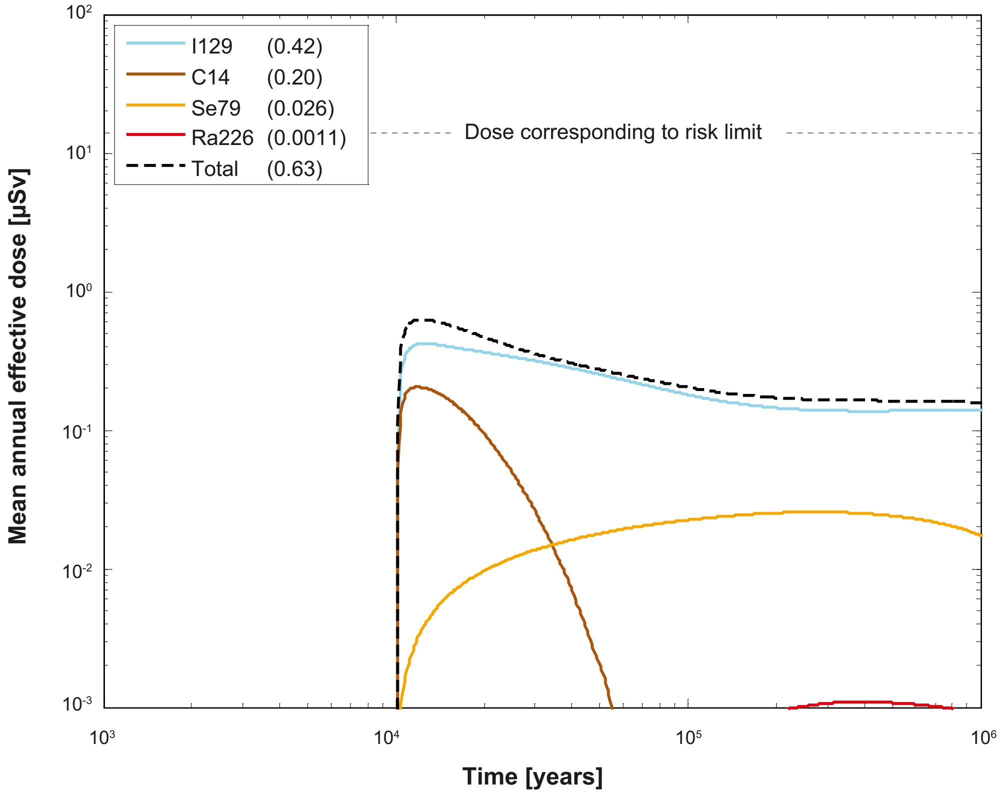

Figure 6-4. *Far-field mean annual effective dose for a probabilistic calculation of the isostatic load scenario, with a postulated failure of one canister at 10,000 years. The legend is sorted by peak (in the one-million year period) of the mean annual effective dose. The values in brackets are peak dose in units of µSv.*

6.2.2 Postulated failure of one canister at 100,000 years

Deterministic calculations

Hydrogeological case:	Semi-correlated, base realisation
Failure time:	100,000 years
Number of failed canisters:	1
Solubility limits:	Yes
Number of realisations:	1
Number of nuclides:	45

A deterministic calculation of the isostatic load failure was performed with a postulated failure of one canister at 100,000 years.

Figure 6-5 and Figure 6-6 show the deterministic near-field and far-field dose equivalent releases, respectively, for the isostatic load case with a postulated failure of one canister at 100,000 years. Both near- and far-field doses are dominated by I-129. Compared to the failure at 10,000 years no peak of C-14 appears shortly after canister failure.

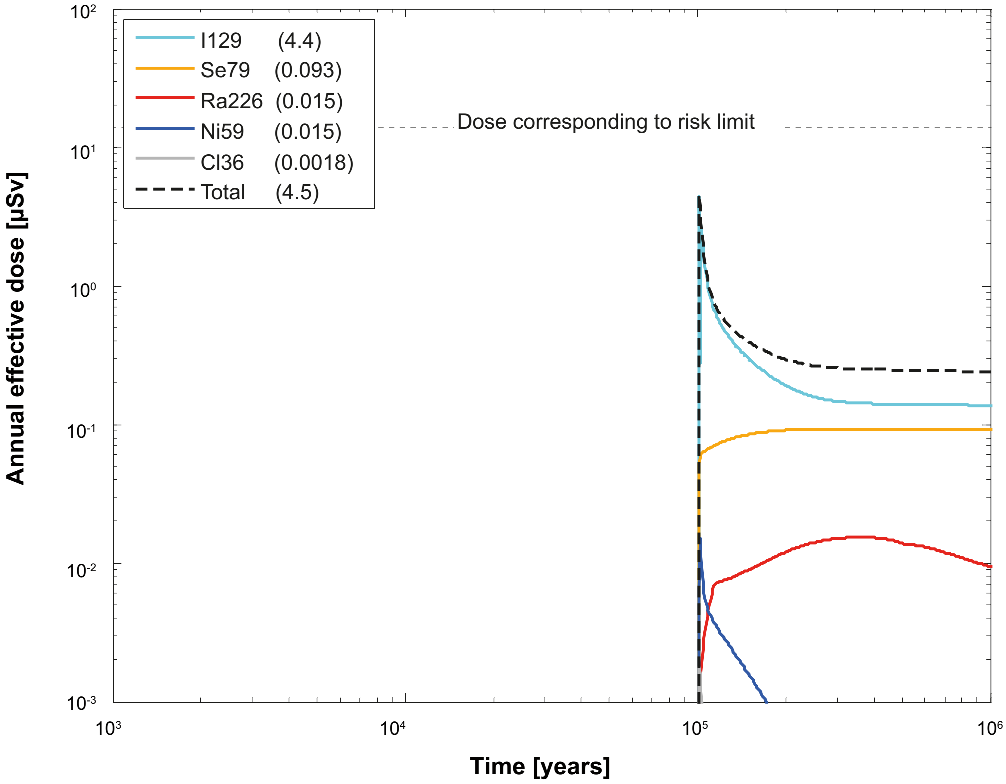

Figure 6-5. *Near-field dose equivalent release for a deterministic calculation of the isostatic load scenario, with a postulated failure of one canister at 100,000 years. The legend is sorted by peak (in the one-million year period) of the annual effective dose. The values in brackets are peak dose in units of µSv.*

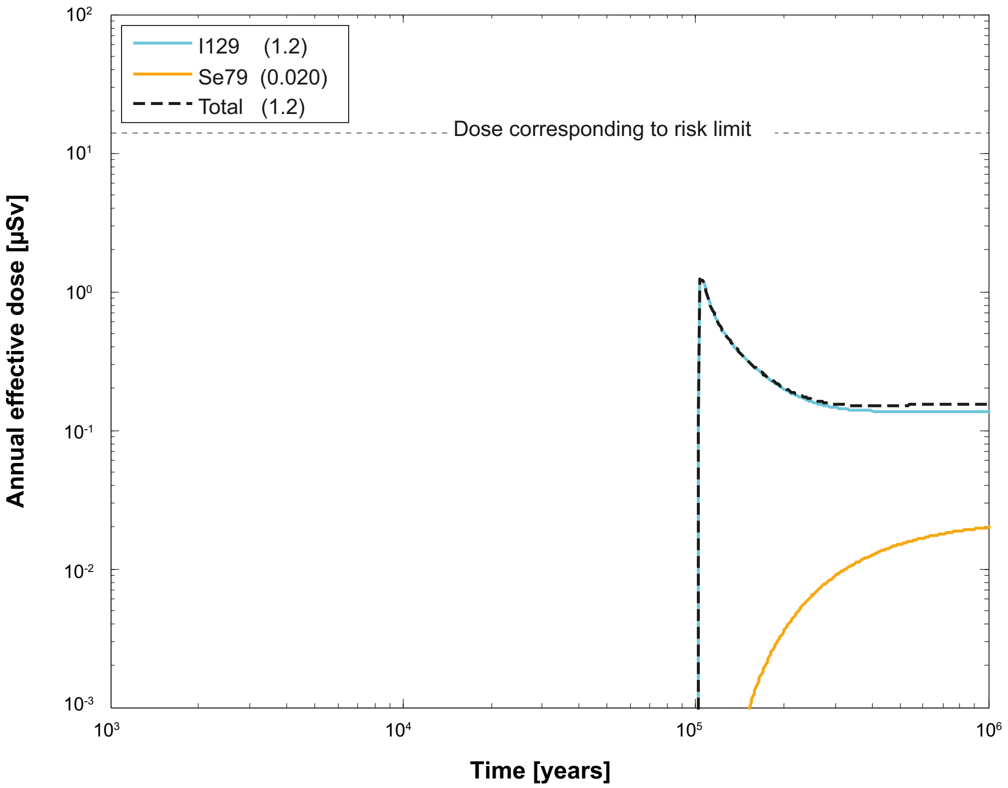

Figure 6-6. *Far-field annual effective dose for a deterministic calculation of the isostatic load scenario, with a postulated failure of one canister at 100,000 years. The legend is sorted by peak (in the one-million year period) of the annual effective dose. The values in brackets are peak dose in units of µSv.*

Probabilistic calculations

Hydrogeological case:	Semi-correlated, base realisation
Failure time:	100,000 years
Number of failed canisters:	1 (postulated)
Solubility limits:	Yes
Number of realisations:	6,916
Number of nuclides:	37

A probabilistic calculation of the isostatic load failure was performed with a postulated failure of one canister at 100,000 years and geosphere transport data from the base realisation of the semi correlated DFN model. The postulated number of failed canisters is 1.

Figure 6-7 and Figure 6-8 show the near-field and far-field dose equivalent releases, respectively, for the isostatic load failure with a postulated failure of one canister at 100,000 years. Both near-field and far-field doses are dominated by releases of I-129. Compared to the case with failure at 10,000 years, the total doses are lower and the contributions to the dose of releases of C-14 are negligible.

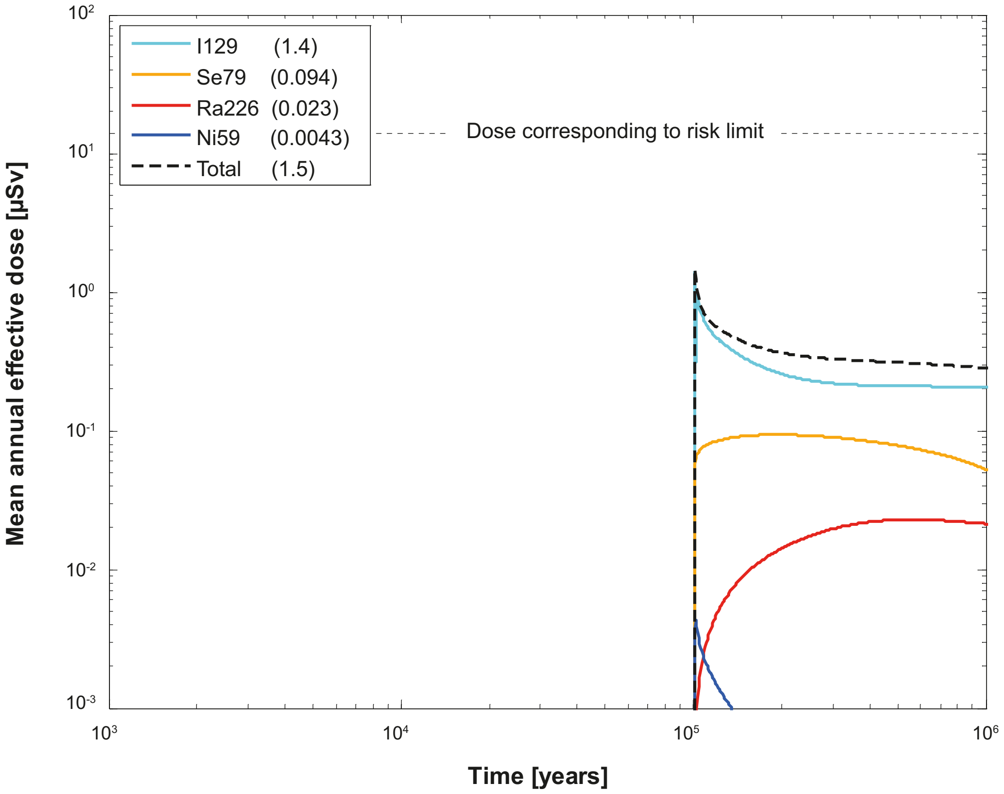

Figure 6-7. *Near-field dose equivalent release for a probabilistic calculation of the isostatic load scenario, with a postulated failure of one canister at 100,000 years. The legend is sorted by peak (in the one-million year period) of the mean annual effective dose. The values in brackets are peak dose in units of µSv.*

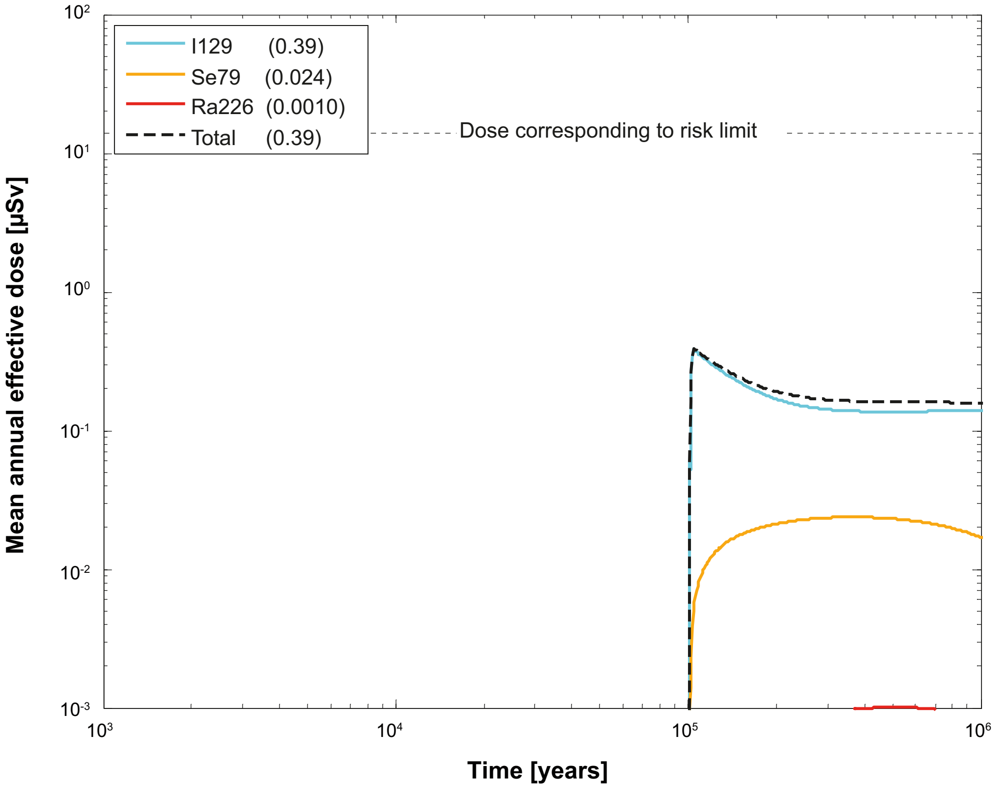

Figure 6-8. *Far-field mean annual effective dose for a probabilistic calculation of the isostatic load scenario, with a postulated failure of one canister at 100,000 years. The legend is sorted by peak (in the one-million year period) of the mean annual effective dose. The values in brackets are peak dose in units of µSv.*

6.2.3 Summary and conclusions for the isostatic load scenario

The consequences of postulated failures of one canister due to isostatic collapse 10,000 years and 100,000 years after repository closure are shown in Figure 6-9 and Figure 6-10 for the near field and far field, respectively. Since both hypothetical global causes (glacial load) and local causes (deficient material properties, higher than intended buffer density) for this scenario can be envisaged, simultaneous failure of more than one canister needs to be considered and would yield consequences in proportion to the number of failed canisters, provided that all releases occur to the same biosphere object. If a large number of canisters fail, it is more appropriate to use the LDF values for a distributed release when converting release to dose (see Table 3-7), since the release can be expected to be distributed over several landscape objects. Illustrations of consequences of extreme cases where all canisters fail at 10,000 and 100,000 years are also shown in Figure 6-9 and Figure 6-10 for the near field and far field, respectively. It is noted that the cases where one canister fails yield lower doses at one million years compared to single failures due both to corrosion where the buffer is eroded away (central corrosion case deterministic calculation, Figure 4-3) and to shear load where geosphere retention is neglected (deterministic calculation with postulated failure at 100,000 years, Figure 5-1).

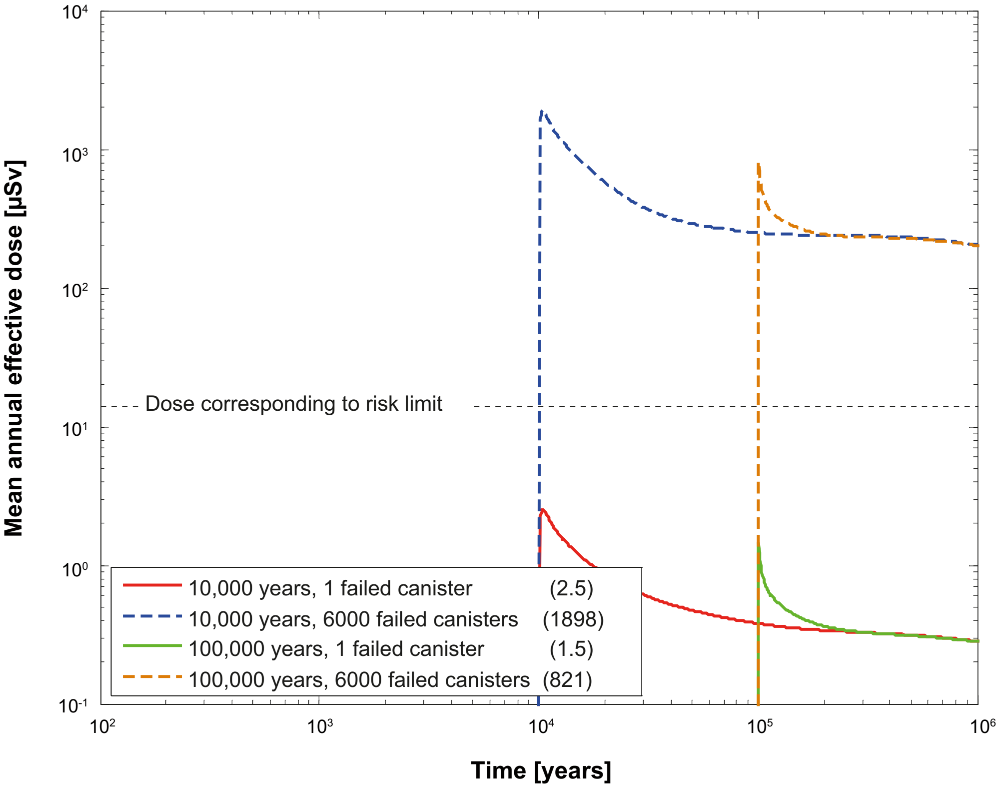

Figure 6-9. *Near-field dose equivalent release, for the isostatic load scenario. One failed canister (basic LDF) and 6,000 failed canisters (distributed LDF) at 10,000 years and 100,000 years. The values in brackets in the legend are peak dose in units of µSv.*

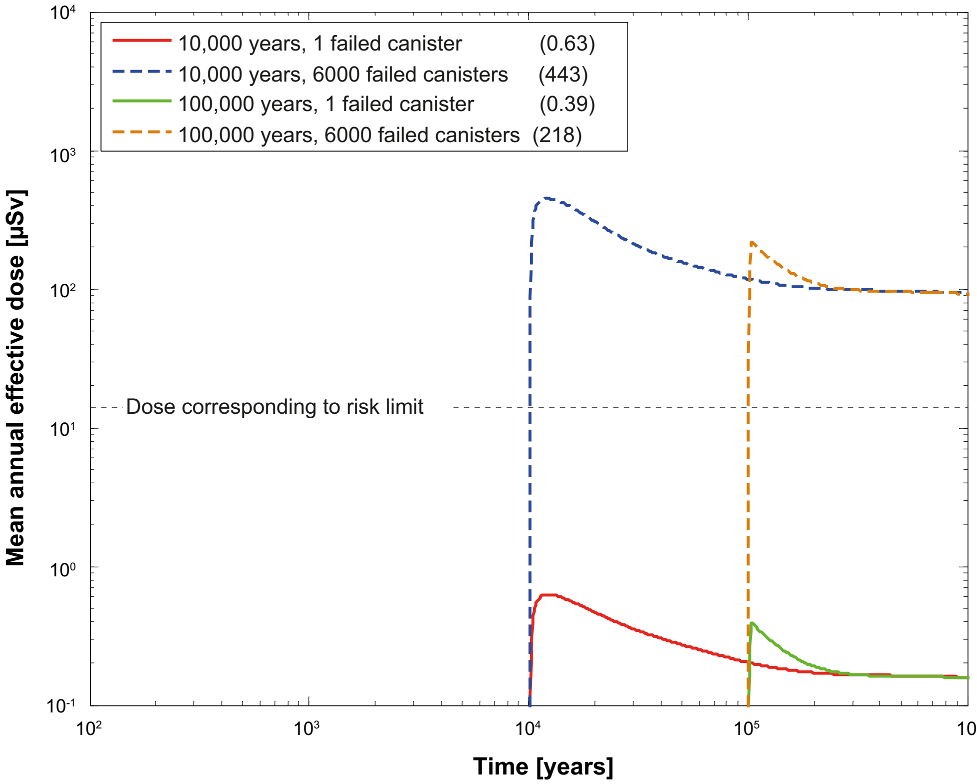

Figure 6-10. *Far-field mean annual effective dose, for the isostatic load scenario. One failed canister (basic LDF) and 6,000 failed canisters (distributed LDF) at 10,000 years and 100,000 years. The values in brackets in the legend are peak dose in units of µSv.*

6.3 The growing pinhole failure

A hypothetical, postulated failure mode where an initial defect in the form of a penetrating pinhole in the copper shell grows over time into a larger defect is analysed. In the pinhole failure mode, a pinhole in the canister wall initially offers considerable transport resistance that is subsequently lost as the defect expands with time, whereas the buffer and the geosphere have intact retention properties. It is, therefore, a convenient case for demonstrating the retarding capacity of the buffer and the geosphere and for exploring uncertainties and sensitivities related to these repository subsystems.

Details of the pinhole scenario are as follows: One canister at an unknown location is assumed to have a small defect. Transport is assumed to start 1,000 years after emplacement. Initially, transport is through a hole with 2-mm radius. At 10,000 years after emplacement, complete loss of transport resistance is assumed for the copper canister. This loss of transport resistance is modelled by allowing the water filled, nuclide containing canister void to directly contact bentonite in a 0.5-m-high region next to the defect. The time-dependent release of radionuclides into the geosphere occurs through the Q1, Q2 and Q3 release path. A more detailed description of the discretisation, diffusion resistances and boundary conditions used in COMP23 is given in Appendix G.

As a base case for the analysis of the pinhole failure mode, the base case of the hydrogeological semi-correlated DFN model was adopted. The EFPC criterion has been applied for the base case, i.e. canister positions intersected by fractures that also intersect the entire tunnel perimeter have been discarded. This means that 612 deposition holes out of 6,916 have been filtered from the results of the hydrogeological calculations. Furthermore, it was assumed that the equivalent flow rates for the path Q1 are affected by spalling.

The following is a brief description of the development of the system, driven by the processes that are quantified in the transport models, as an introduction to the presentation of the results of the calculations.

1. No releases occur from the canister before a continuous water pathway has been formed between the fuel and the exterior of the failed canister, which could take thousands of years. In these calculations the delay time is assigned to be 1,000 years. Radioactive decay reduces the radionuclide content and total radiotoxicity of the fuel.

2. As soon as a continuous water pathway has formed, the instant release fraction of the inventory dissolves in the water in the canister void. If the solubility limit is reached, the concentration of the dissolved nuclide in the water does not increase further. The nuclides dissolved in the water begin to diffuse out of the canister. The release of nuclides embedded in the fuel is determined by the fuel dissolution rate and the release of nuclides in metal parts is determined by the corrosion release rate. Also in this case, the solubilities of the nuclides limit the concentrations that can occur in the water.

3. The nuclides are sorbed with varying efficiency in the buffer and the diffusion and sorption properties determine the time for diffusion through the buffer. If this time is shorter than a few half-lives of the nuclide, it passes out into the rock.

4. In the rock, the nuclide's sorption properties, together with the rock's transport properties, determine the time for transport through the rock to the biosphere. As in the buffer, the half-life of the nuclide determines whether it passes through the geosphere before decaying to a substantial degree.

5. In the biosphere, the nuclide gives rise to a dose that is dependent on its inherent radiotoxicity and its turnover in the biosphere type to which it is released. Both of these factors are included in the LDF value used.

In general, nuclides with a relatively high instant release fraction also tend to be readily soluble and relatively mobile in both buffer and rock. Several percent of the inventory of I-129, for example, is instantly released; iodine has a very high solubility and is not sorbed in either buffer or rock. Plutonium isotopes, on the other hand, lie completely embedded in the fuel matrix, have low solubility and are sorbed strongly in both buffer and rock. Isotopes of uranium, thorium and americium have similar properties to plutonium.

6.3.1 Base case, including the effect of spalling

Deterministic calculations

Hydrogeological case:	Semi-correlated, base case
Failure time:	0 and 10,000 years
Number of failed canisters:	1
Solubility limits:	Yes
Spalling:	Yes
Number of realisations:	1
Number of nuclides:	37

A deterministic calculation of the hypothetical pinhole failure mode including the effect of spalling was performed for a canister with an initial penetrating pinhole that grows to a large hole after 10,000 years. Transport out of the canister is assumed to be established 1,000 years after deposition. Median values of geosphere transport data from the base case of the semi-correlated DFN model are used. The number of failed canisters is 1.

Figure 6-11 shows the deterministic near-field dose equivalent releases for the pinhole case including the effect of spalling. Figure 6-12 shows the same near-field dose equivalent releases decomposed into Q1, Q2 and Q3. Doses from the near field are dominated by C-14 and I-129 and Q1 is the dominating release path. Figure 6-13 shows the far-field dose equivalent releases for the pinhole case including the effect of spalling and Figure 6-14 shows the same releases decomposed into Q1, Q2 and Q3. Also the dose from the far field is dominated by I-129 and Q1 is again the dominating release path.

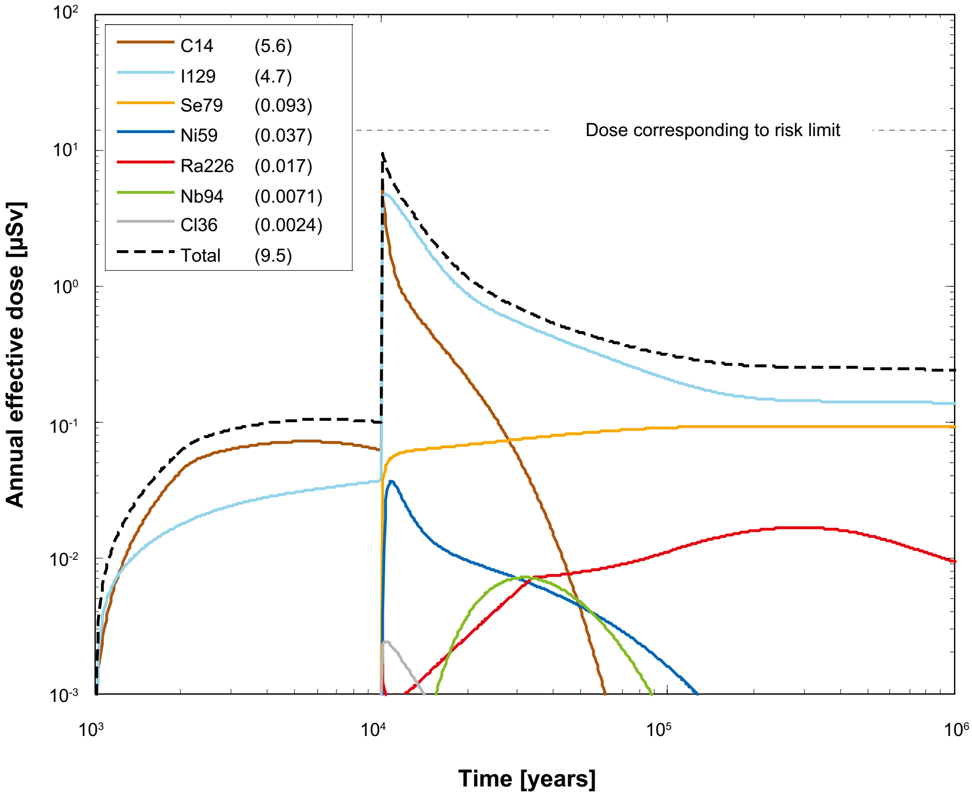

Figure 6-11. *Near-field dose equivalent release for a deterministic calculation of the pinhole case, including the effect of spalling. Summed doses for all release paths (Q1+Q2+Q3). The legend is sorted by peak (in the one-million year period) of the annual effective dose. The values in brackets are peak dose in units of µSv.*

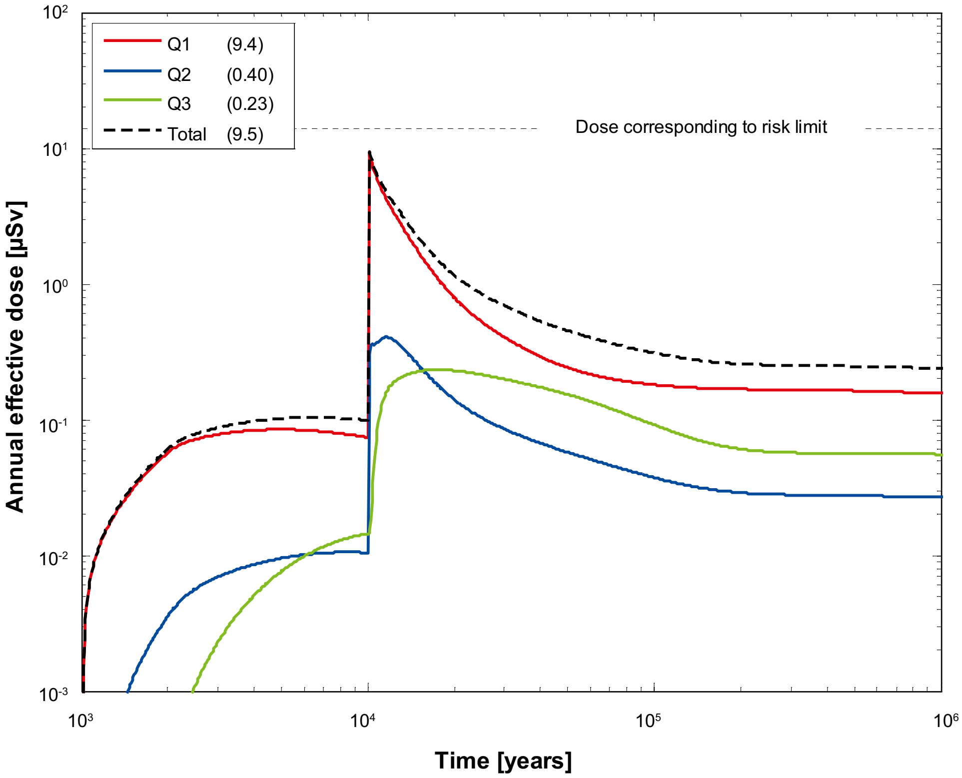

Figure 6-12. *Near-field dose equivalent release for a deterministic calculation of the pinhole case, including the effect of spalling. Doses decomposed into Q1, Q2 and Q3. The legend is sorted by peak (in the one-million year period) of the annual effective dose. The values in brackets are peak dose in units of µSv.*

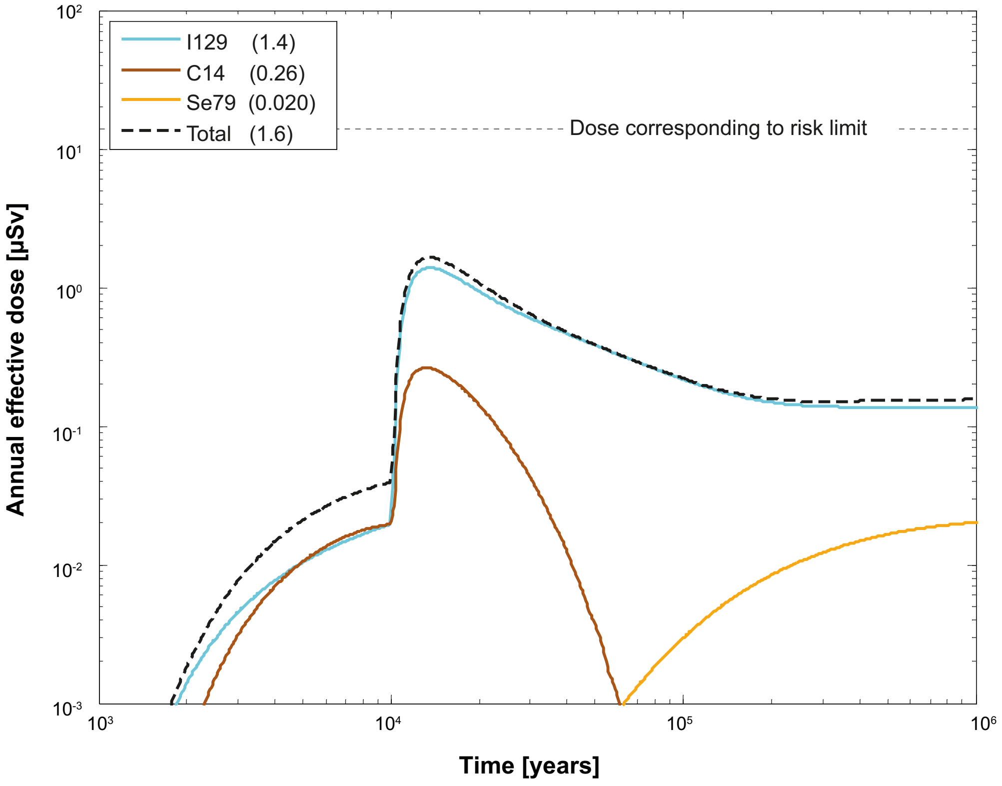

***Figure 6-13.** Far-field annual effective dose for a deterministic calculation of the pinhole case, including the effect of spalling. Summed doses for all release paths (Q1+Q2+Q3). The legend is sorted by peak (in the one-million year period) of the annual effective dose. The values in brackets are peak dose in units of µSv.*

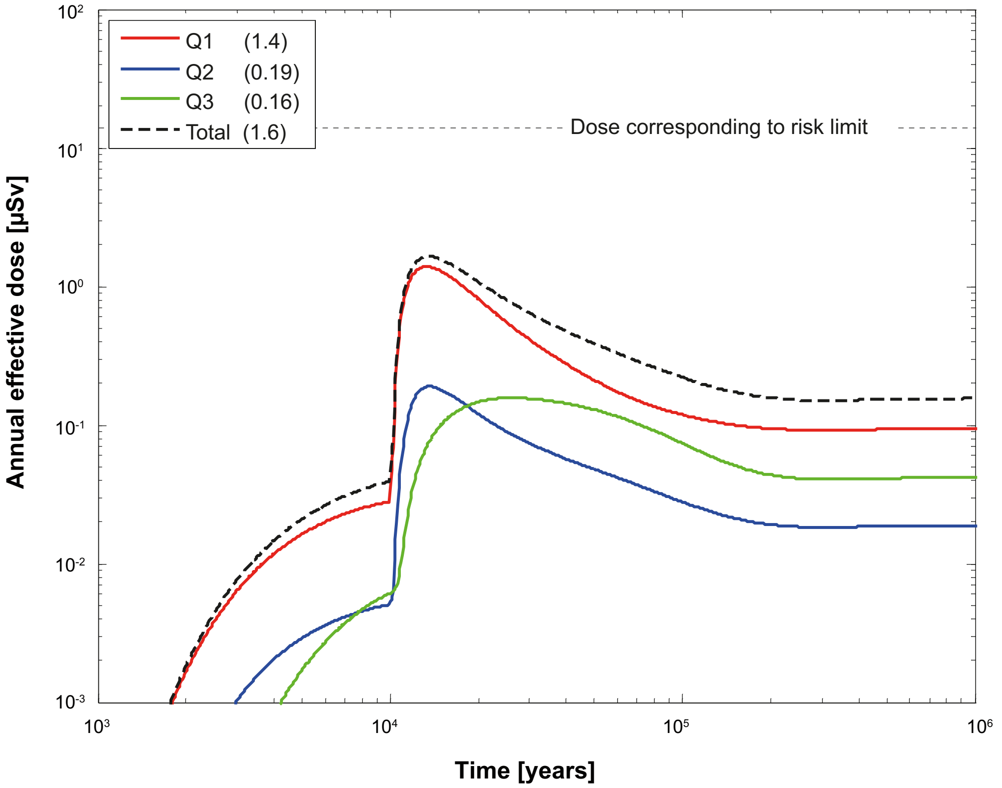

***Figure 6-14.** Far-field annual effective dose for a deterministic calculation of the pinhole case, including the effect of spalling. Doses decomposed into Q1, Q2 and Q3. The legend is sorted by peak (in the one-million year period) of the annual effective dose. The values in brackets are peak dose in units of µSv.*

Probabilistic calculations

Hydrogeological case:	Semi-correlated, base case
Failure time:	0 and 10,000 years
Number of failed canisters:	1
Solubility limits:	Yes
Spalling:	Yes
Number of realisations:	6,916
Number of nuclides:	37

A probabilistic calculation of the hypothetical pinhole failure mode including the effect of spalling was performed for one canister with an initial penetrating pinhole that grows to a large hole after 10,000 years. Transport out of the canister is assumed to be established 1,000 years after deposition. Geosphere transport parameters from the base realisation of the semi correlated DFN model are used. The number of failed canisters is 1. The calculation was run for each of the 6,916 positions and a mean result was calculated over all positions.

Figure 6-15 shows the near-field dose equivalent releases for the pinhole case including the effect of spalling and Figure 6-16 shows the same releases decomposed into Q1, Q2 and Q3. Figure 6-17 shows the corresponding far-field dose equivalent releases and Figure 6-18 shows the same releases decomposed into Q1, Q2 and Q3. Doses from both the near field and the far field are dominated by C-14 and I-129. Q1 is the dominating release path till shortly after the large hole in the canister has developed. In the longer term Q3 becomes the dominating release path.

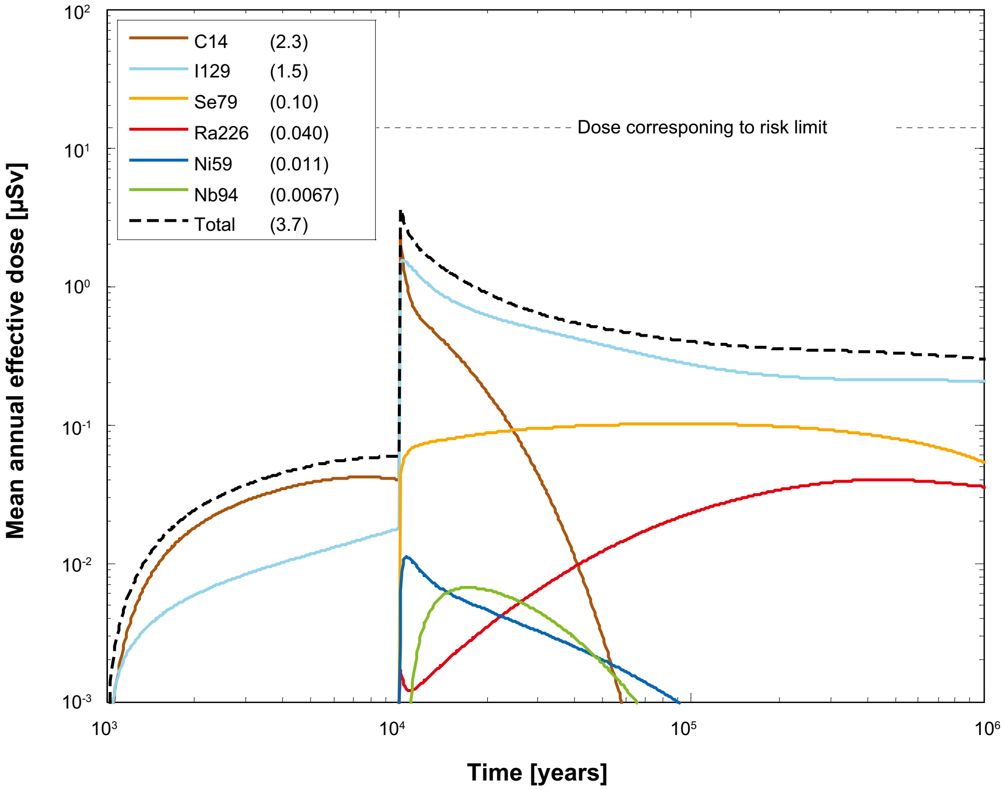

Figure 6-15. *Near-field dose equivalent release for the probabilistic calculation of the pinhole case, including the effect of spalling. Summed doses for all release paths (Q1+Q2+Q3). The legend is sorted by peak (in the one-million year period) of the mean annual effective dose. The values in brackets are peak dose in units of µSv.*

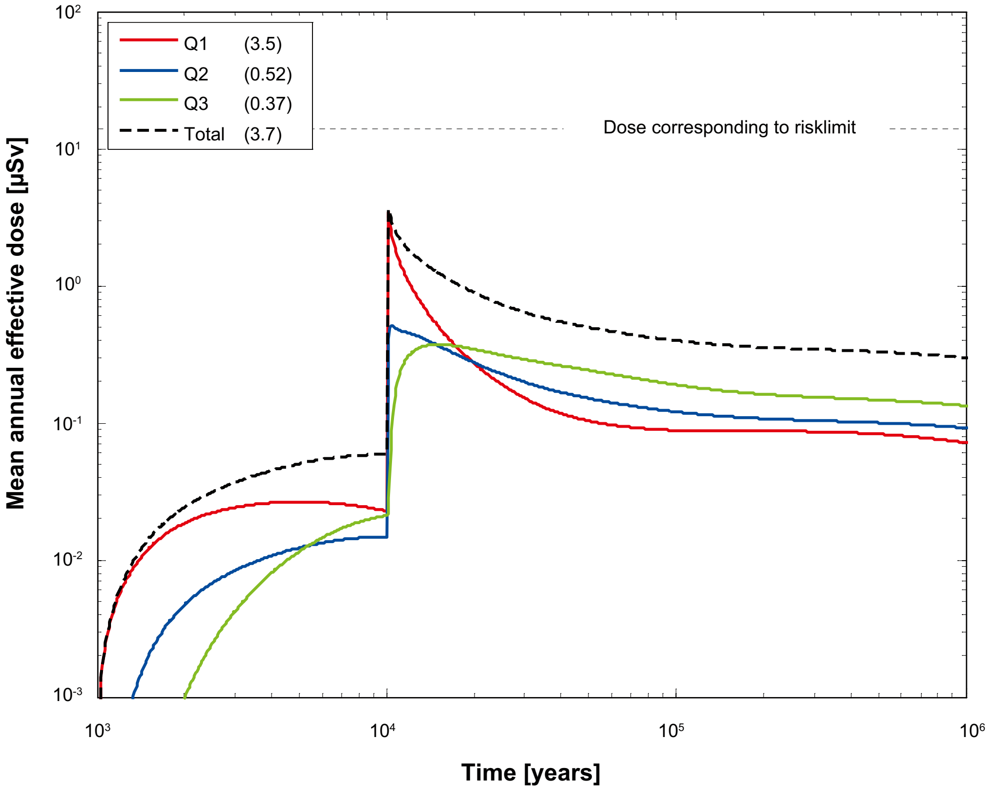

***Figure 6-16.** Near-field dose equivalent release for the probabilistic calculation of the pinhole case, including the effect of spalling. Doses decomposed into Q1, Q2 and Q3. The legend is sorted by peak (in the one-million year period) of the mean annual effective dose. The values in brackets are peak dose in units of µSv.*

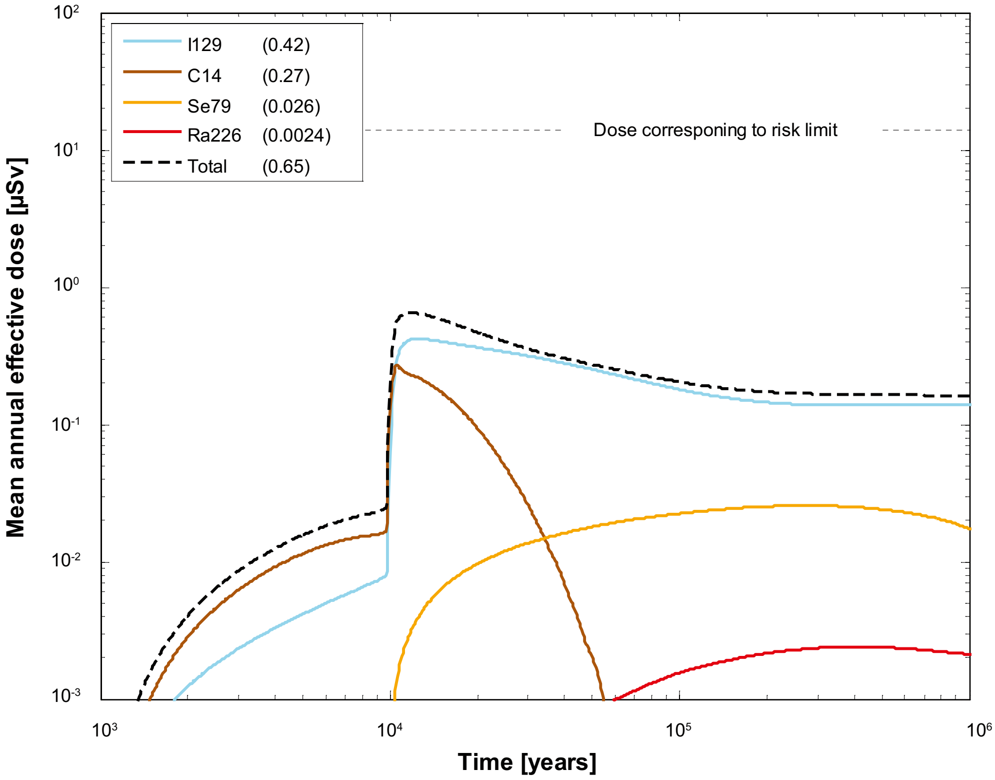

***Figure 6-17.** Far-field mean annual mean effective dose for the probabilistic calculation of the pinhole case, including the effect of spalling. Summed doses for all release paths (Q1+Q2+Q3). The legend is sorted by peak (in the one-million year period) of the mean annual effective dose. The values in brackets are peak dose in units of µSv.*

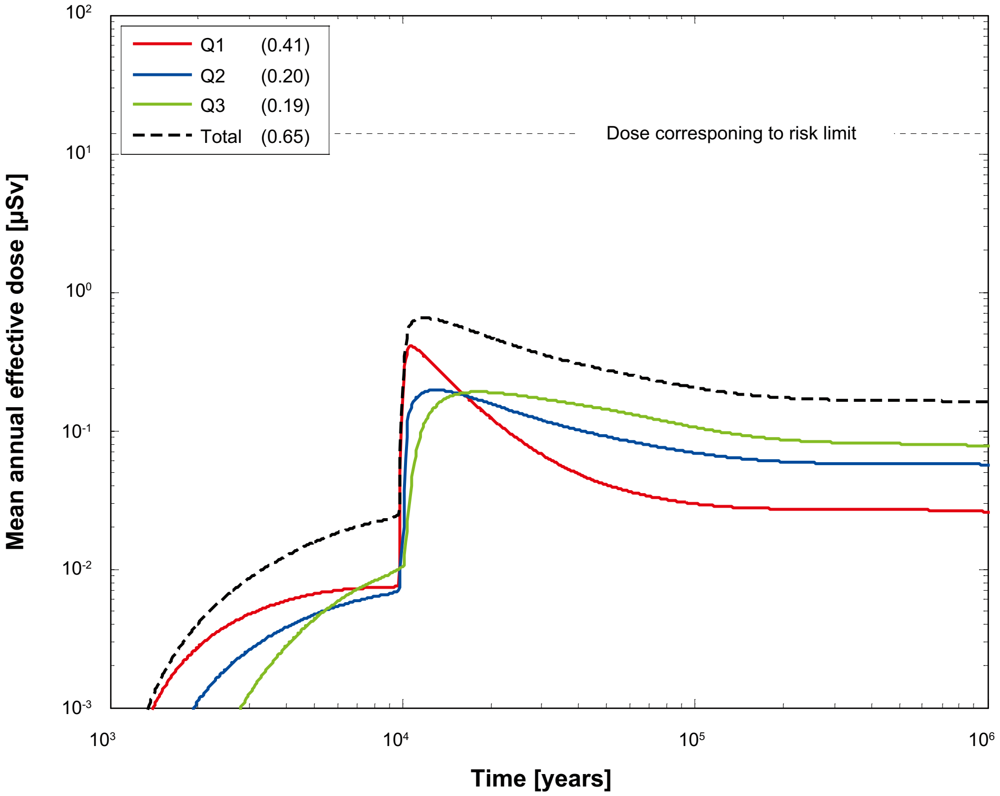

Figure 6-18. *Far-field mean annual effective dose for the probabilistic calculation of the pinhole case, including the effect of spalling. Doses decomposed into Q1, Q2 and Q3. The legend is sorted by peak (in the one-million year period) of the mean annual effective dose. The values in brackets are peak dose in units of µSv.*

6.3.2 Disregarding the effect of spalling

Deterministic calculations

Hydrogeological case:	Semi-correlated, base case
Failure time:	0 and 10,000 years
Number of failed canisters:	1
Solubility limits:	Yes
Spalling:	No
Number of realisations:	1
Number of nuclides:	37

A deterministic calculation of the hypothetical pinhole failure mode disregarding the effect of spalling was performed for a canister with an initial penetrating pinhole that grows to a large hole after 10,000 years. Transport out of the canister is assumed to be established 1,000 years after deposition. Median values of geosphere transport data from the base case of the semi correlated DFN model are used. The number of failed canisters is 1.

Figure 6-19 shows the deterministic near-field dose equivalent releases for the pinhole case disregarding the effect of spalling and Figure 6-20 shows the same near-field dose equivalent releases decomposed into Q1, Q2 and Q3. Disregarding spalling in the near-field results in doses about 13 times lower and release through Q3 are more dominating, compared to the pinhole case including spalling. Figure 6-21 shows the far-field dose equivalent releases for the pinhole case disregarding the effect of spalling and Figure 6-22 shows the same releases decomposed into Q1, Q2 and Q3. Doses from the far field are about 4 times lower and releases through Q3 are dominating.

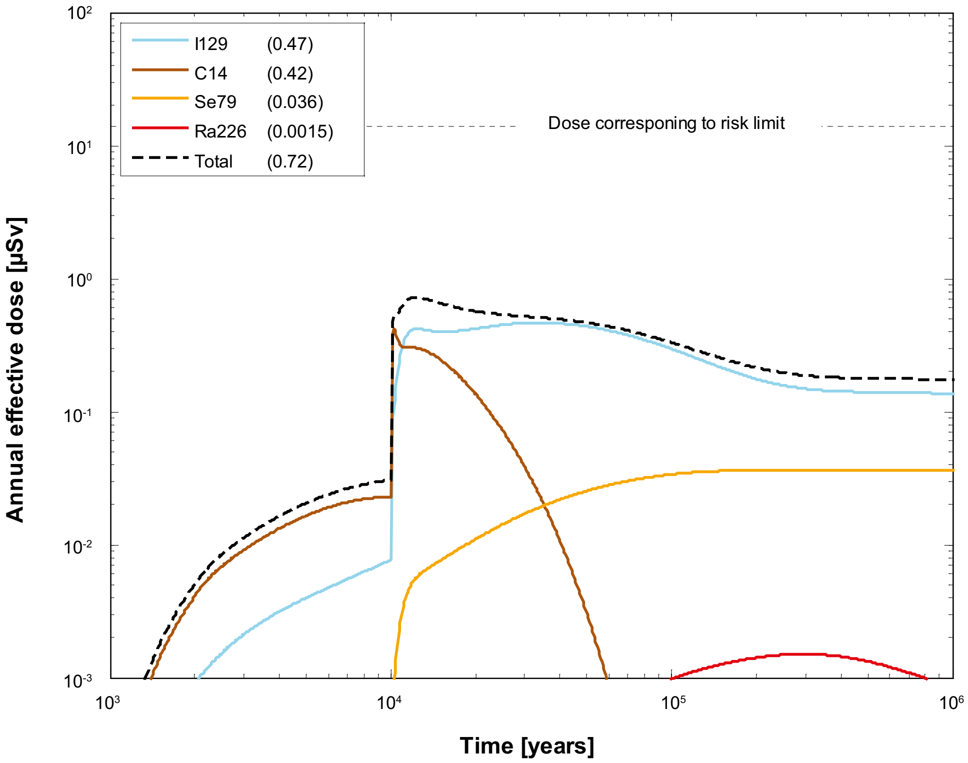

Figure 6-19. *Near-field dose equivalent release for a deterministic calculation of the pinhole case, disregarding the effect of spalling. Summed doses for all release paths (Q1+Q2+Q3). The legend is sorted by peak (in the one-million year period) of the annual effective dose. The values in brackets are peak dose in units of µSv.*

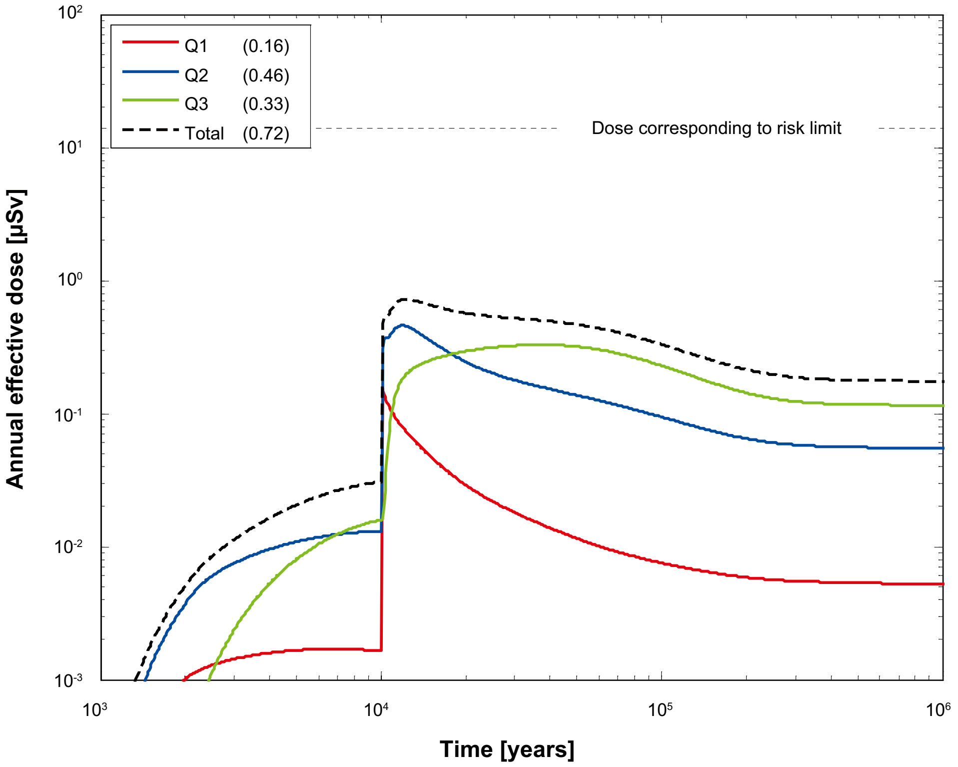

Figure 6-20. *Near-field dose equivalent release for a deterministic calculation of the pinhole case, disregarding the effect of spalling. Doses decomposed into Q1, Q2 and Q3. The legend is sorted by peak (in the one-million year period) of the annual effective dose. The values in brackets are peak dose in units of µSv.*

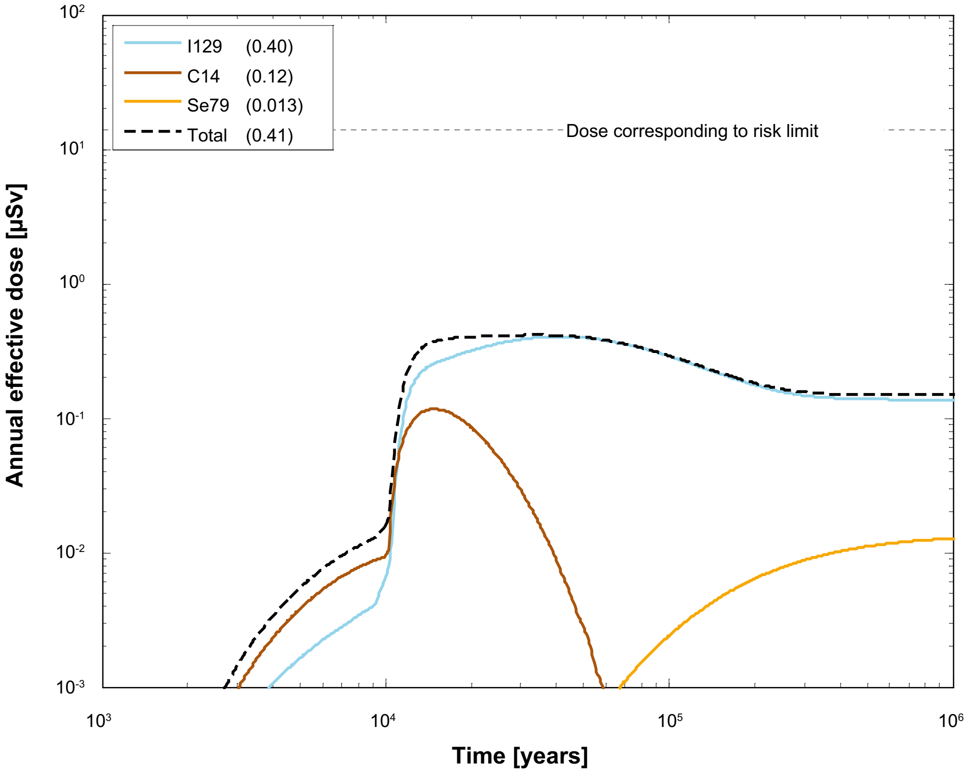

Figure 6-21. *Far-field annual effective dose for a deterministic calculation of the pinhole case, disregarding the effect of spalling. Summed doses for all release paths (Q1+Q2+Q3). The legend is sorted by peak (in the one-million year period) of the annual effective dose. The values in brackets are peak dose in units of µSv.*

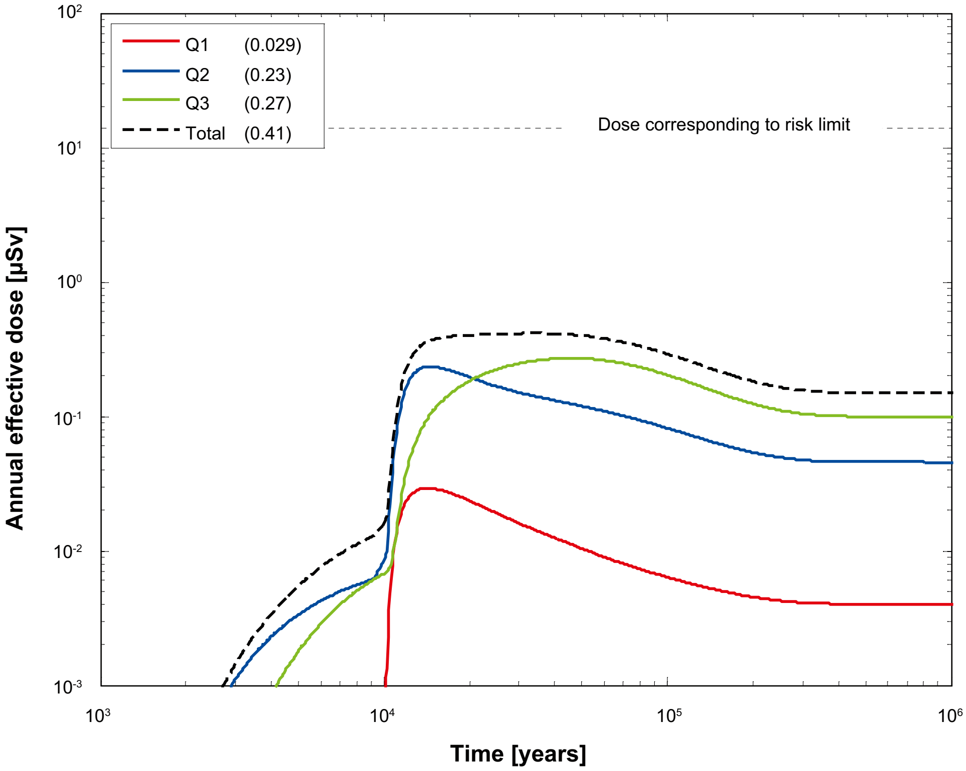

Figure 6-22. *Far-field annual effective dose for a deterministic calculation of the pinhole case, disregarding the effect of spalling. Doses decomposed into Q1, Q2 and Q3. The legend is sorted by peak (in the one-million year period) of the annual effective dose. The values in brackets are peak dose in units of µSv.*

Probabilistic calculations

Hydrogeological case:	Semi-correlated, base case
Failure time:	0 and 10,000 years
Number of failed canisters:	1
Solubility limits:	Yes
Spalling:	No
Number of realisations:	6,916
Number of nuclides:	37

A probabilistic calculation of the hypothetical pinhole failure mode disregarding the effect of spalling was performed for one canister with an initial penetrating pinhole that grows to a large hole after 10,000 years. Transport out of the canister is assumed to be established 1,000 years after deposition. Geosphere transport parameters from the base case of the semi correlated DFN model are used. The number of failed canisters is 1. The calculation was run for each of the 6,916 positions and a mean result was calculated over all positions.

Figure 6-23 shows the near-field dose equivalent releases for the pinhole case disregarding the effect of spalling and Figure 6-24 shows the same releases decomposed into Q1, Q2 and Q3. Disregarding spalling in the near-field results in doses about 4 times lower and release through Q2 and Q3 are completely dominating, compared to the pinhole case including spalling. Figure 6-25 shows the far-field dose equivalent releases for the pinhole case disregarding the effect of spalling and Figure 6-26 shows the same releases decomposed into Q1, Q2 and Q3. Doses from the far field are similar to the doses when the effect of spalling is included, but releases through Q2 and Q3 are completely dominating over Q1.

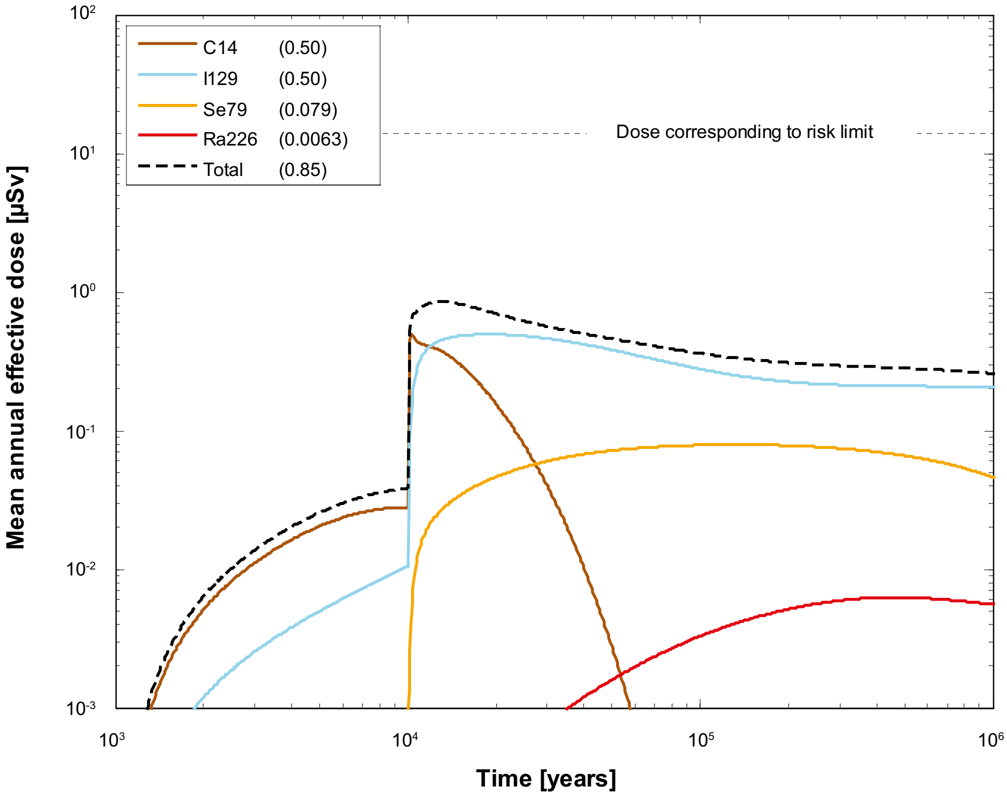

Figure 6-23. *Near-field dose equivalent release for the probabilistic calculation of the pinhole case, disregarding the effect of spalling. Summed doses for all release paths (Q1+Q2+Q3). The legend is sorted by peak (in the one-million year period) of the mean annual effective dose. The values in brackets are peak dose in units of µSv.*

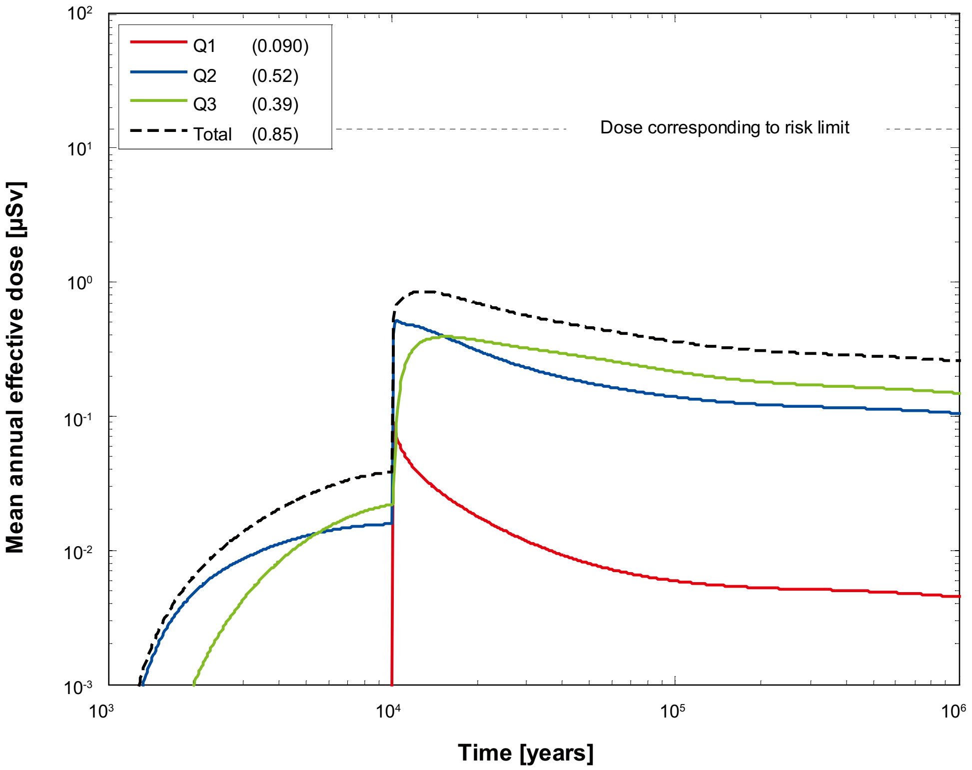

Figure 6-24. *Near-field dose equivalent release for the probabilistic calculation of the pinhole case, disregarding the effect of spalling. Doses decomposed into Q1, Q2 and Q3. The legend is sorted by peak (in the one-million year period) of the mean annual effective dose. The values in brackets are peak dose in units of µSv.*

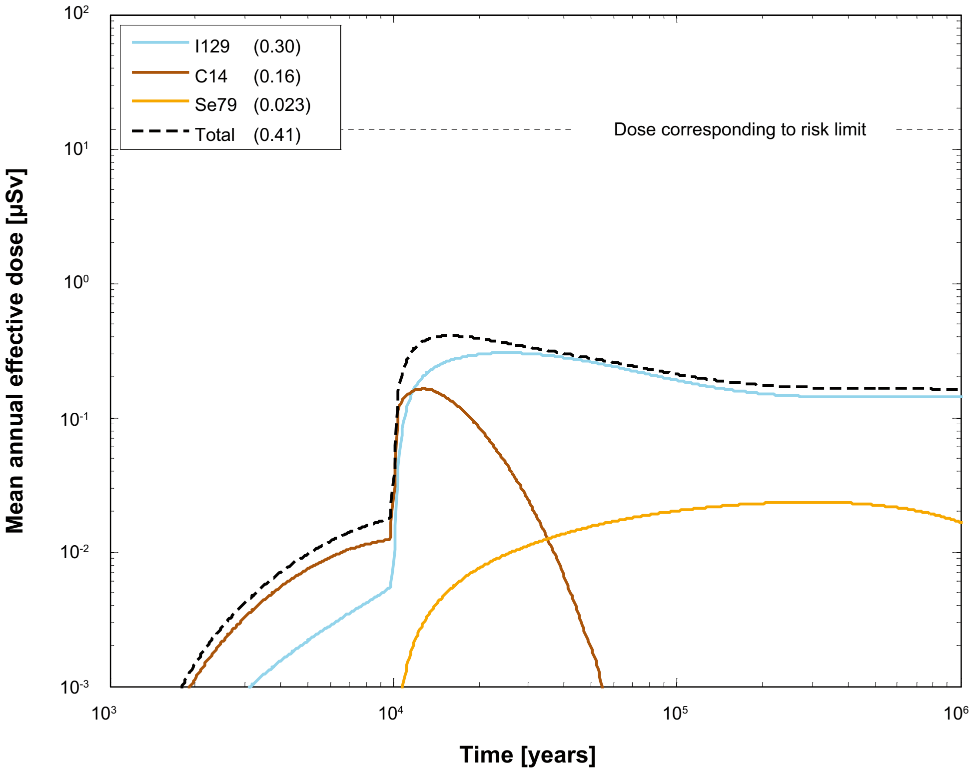

Figure 6-25. *Far-field mean annual mean effective dose for the probabilistic calculation of the pinhole case, disregarding the effect of spalling. Summed doses for all release paths (Q1+Q2+Q3). The legend is sorted by peak (in the one-million year period) of the mean annual effective dose. The values in brackets are peak dose in units of µSv.*

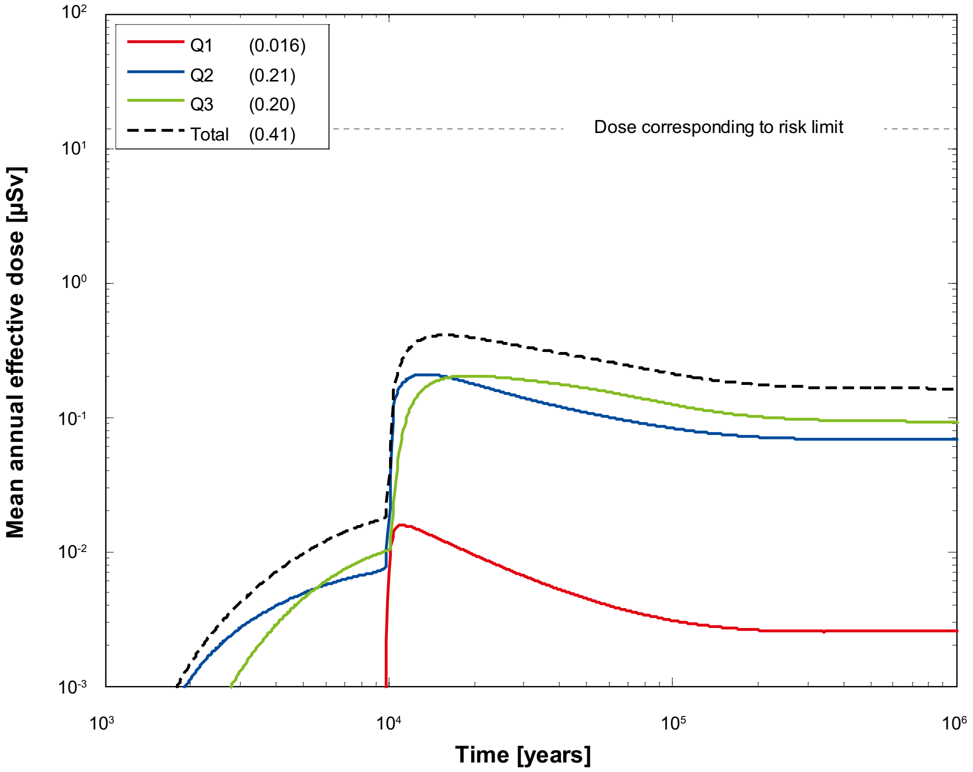

Figure 6-26. *Far-field mean annual effective dose for the probabilistic calculation of the pinhole case, disregarding the effect of spalling. Doses decomposed into Q1, Q2 and Q3. The legend is sorted by peak (in the one-million year period) of the mean annual effective dose. The values in brackets are peak dose in units of µSv.*

6.3.3 Lost swelling pressure in tunnel backfill, "Crown-space"

Deterministic calculations

Hydrogeological case:	Semi-correlated, variant with crown space
Failure time:	0 and 10,000 years
Number of failed canisters:	1
Solubility limits:	Yes
Spalling:	Yes
Number of realisations:	1
Number of nuclides:	37

A deterministic calculation of the hypothetical pinhole failure mode with lost swelling pressure in the tunnel backfill (crown-space) was performed for a canister with an initial penetrating pinhole that grows to a large hole after 10,000 years. Transport out of the canister is assumed to be established 1,000 years after deposition. Median values of geosphere transport data from the variant with crown space of the semi correlated DFN model are used. The number of failed canisters is 1.

Figure 6-27 shows the deterministic near-field dose equivalent releases for the pinhole case with lost swelling pressure in the tunnel backfill and Figure 6-28 shows the same near-field dose equivalent releases decomposed into Q1, Q2 and Q3. The early doses are 1–2 times higher and Q3 is more dominating, as a release path, compared to the pinhole case with an intact tunnel backfill. The doses are at about the same levels after one million years as the pinhole case with intact tunnel backfill (earlier called the pinhole case including the effect of spalling, see Section 6.2.1). Figure 6-29 shows the far-field dose equivalent releases for the pinhole case with lost swelling pressure in the tunnel backfill and Figure 6-30 shows the same releases decomposed into Q1, Q2 and Q3. Early releases of C-14 are considerably higher and contribute more to the total peak dose than in the pinhole case with an intact tunnel backfill.

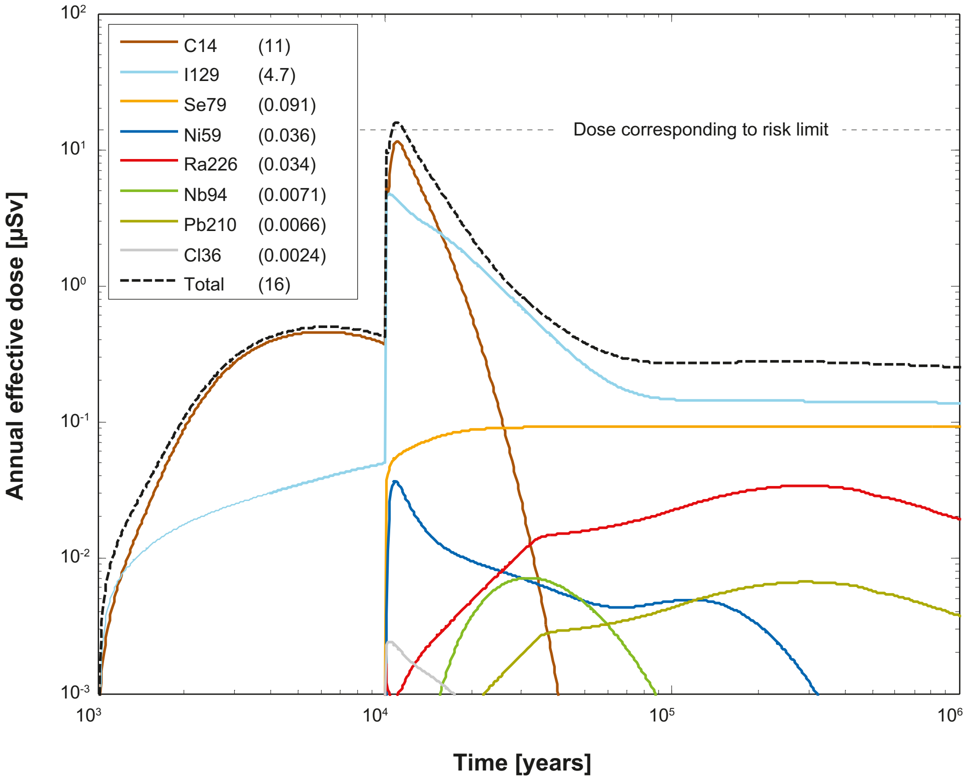

***Figure 6-27.** Near-field dose equivalent release for a deterministic calculation of the pinhole case, with lost swelling pressure in tunnel backfill. Summed doses for all release paths (Q1+Q2+Q3). The legend is sorted by peak (in the one-million year period) of the annual effective dose. The values in brackets are peak dose in units of µSv.*

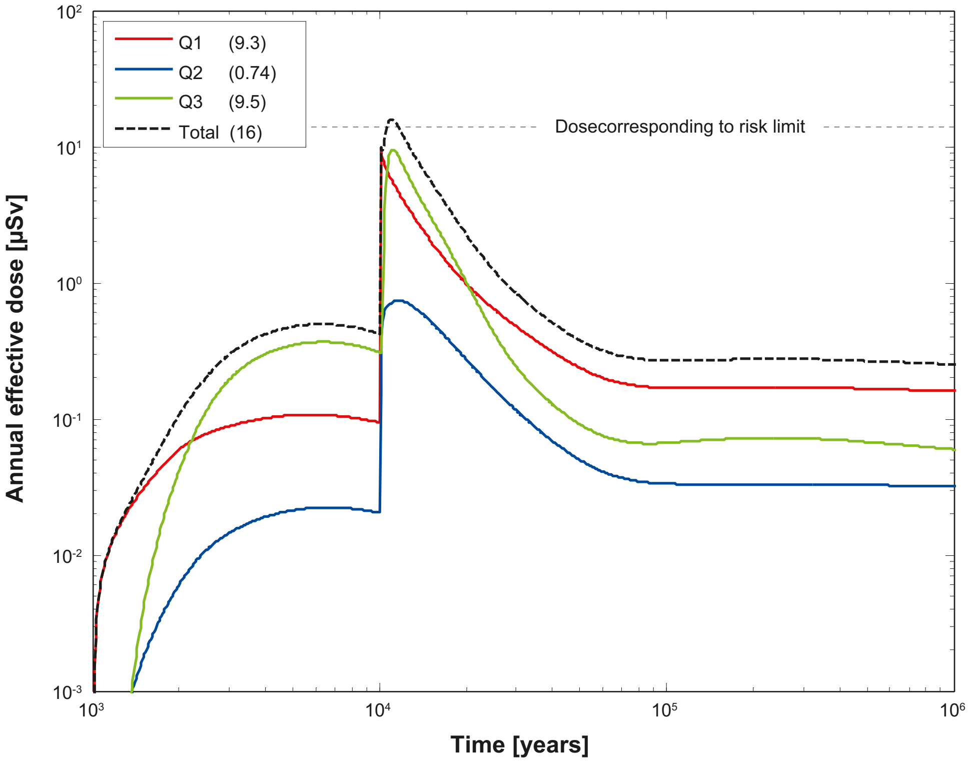

***Figure 6-28.** Near-field dose equivalent release for a deterministic calculation of the pinhole case, with lost swelling pressure in tunnel backfill. Doses decomposed into Q1, Q2 and Q3. The legend is sorted by peak (in the one-million year period) of the annual effective dose. The values in brackets are peak dose in units of µSv.*

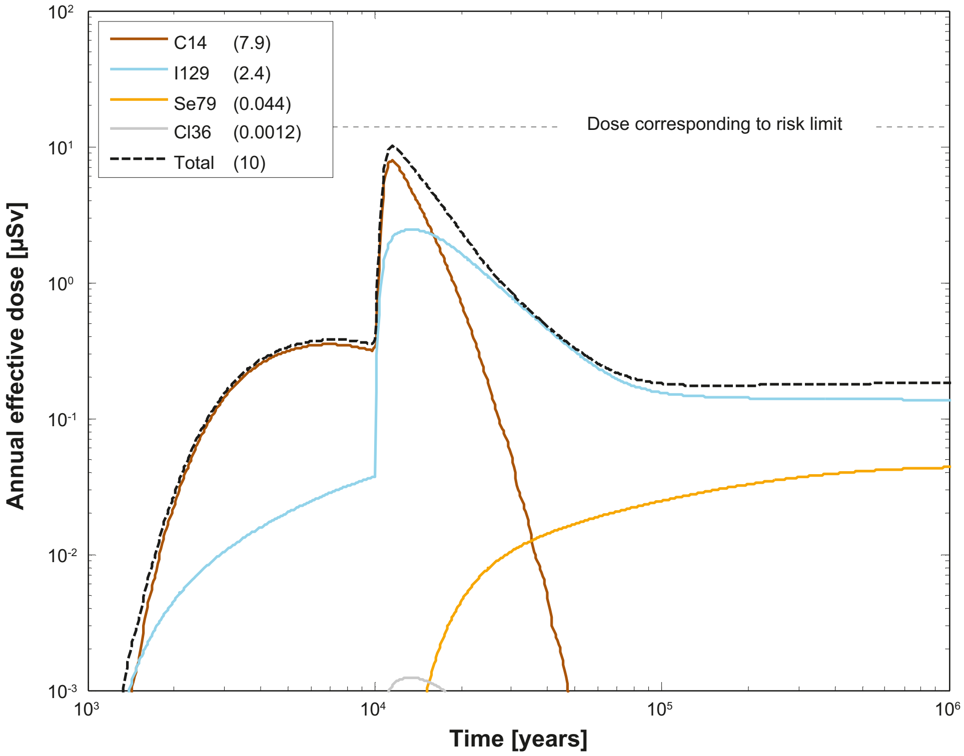

Figure 6-29. *Far-field annual effective dose for a deterministic calculation of the pinhole case, with lost swelling pressure in tunnel backfill. Summed doses for all release paths (Q1+Q2+Q3). The legend is sorted by peak (in the one-million year period) of the annual effective dose. The values in brackets are peak dose in units of µSv.*

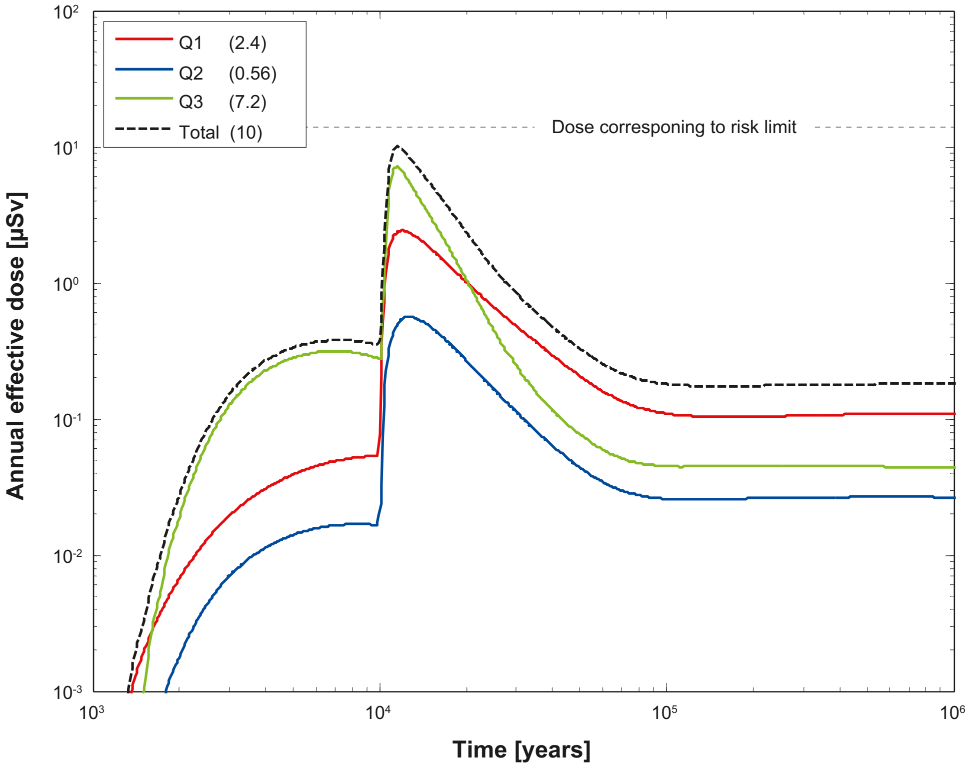

Figure 6-30. *Far-field annual effective dose for a deterministic calculation of the pinhole case, with lost swelling pressure in tunnel backfill. Doses decomposed into Q1, Q2 and Q3. The legend is sorted by peak (in the one-million year period) of the annual effective dose. The values in brackets are peak dose in units of µSv.*

Probabilistic calculations

Hydrogeological case:	Semi-correlated, variant with crown space
Failure time:	0 and 10,000 years
Number of failed canisters:	1
Solubility limits:	Yes
Spalling:	Yes
Number of realisations:	6,916
Number of nuclides:	37

A probabilistic calculation of the hypothetical pinhole failure mode with lost swelling pressure in the tunnel backfill was performed for one canister with an initial penetrating pinhole that grows to a large hole after 10,000 years. Transport out of the canister is assumed to be established 1,000 years after deposition. Geosphere transport parameters from the variant with crown space of the semi correlated DFN model are used. The number of failed canisters is 1. The calculation was run for 6,916 positions and a mean result was calculated over all positions.

Figure 6-31 shows the near-field dose equivalent releases for the pinhole case with lost swelling pressure in the tunnel backfill and Figure 6-32 shows the same near-field dose equivalent releases decomposed into Q1, Q2 and Q3. Peak releases of C-14 are about 3 times higher compared to the pinhole case with an intact tunnel backfill, and Q3 is the dominating release path. In the longer term I-129 and Ra-226 contributes considerably to the total dose. Figure 6-33 shows the far-field dose equivalent releases for the pinhole case with lost swelling pressure in the tunnel backfill and Figure 6-34 shows the same releases decomposed into Q1, Q2 and Q3. Peak releases of C-14 are about 8 times higher compared to the pinhole case with an intact tunnel backfill, and Q3 is the dominating release path. In the longer term, the total dose from the far field is at the same level as in the pinhole case with an intact tunnel backfill.

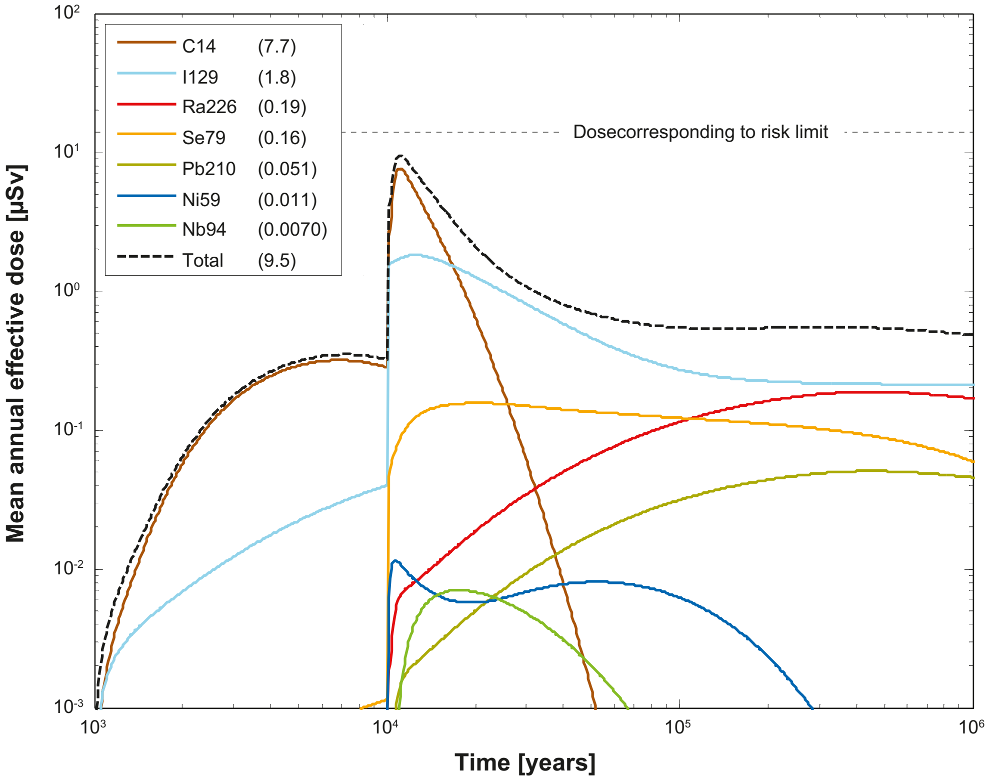

Figure 6-31. *Near-field dose equivalent release for the probabilistic calculation of the pinhole case, with lost swelling pressure in tunnel backfill. Summed doses for all release paths (Q1+Q2+Q3). The legend is sorted by peak (in the one-million year period) of the mean annual effective dose. The values in brackets are peak dose in units of µSv.*

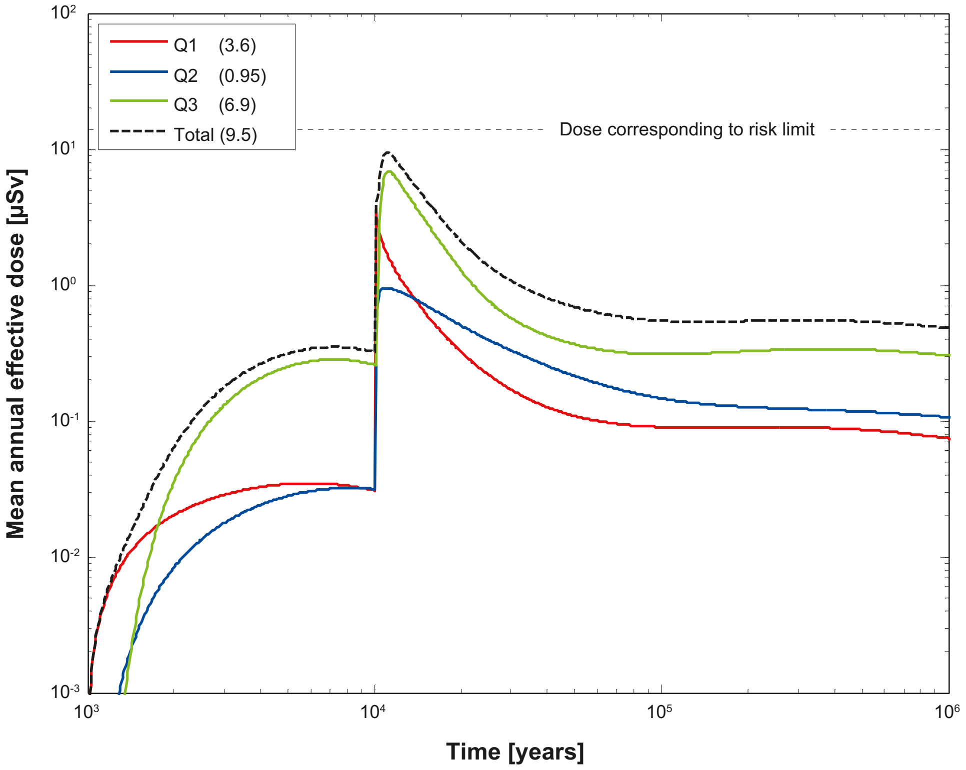

Figure 6-32. *Near-field dose equivalent release for the probabilistic calculation of the pinhole case, with lost swelling pressure in tunnel backfill. Doses decomposed into Q1, Q2 and Q3. The legend is sorted by peak (in the one-million year period) of the mean annual effective dose. The values in brackets are peak dose in units of µSv.*

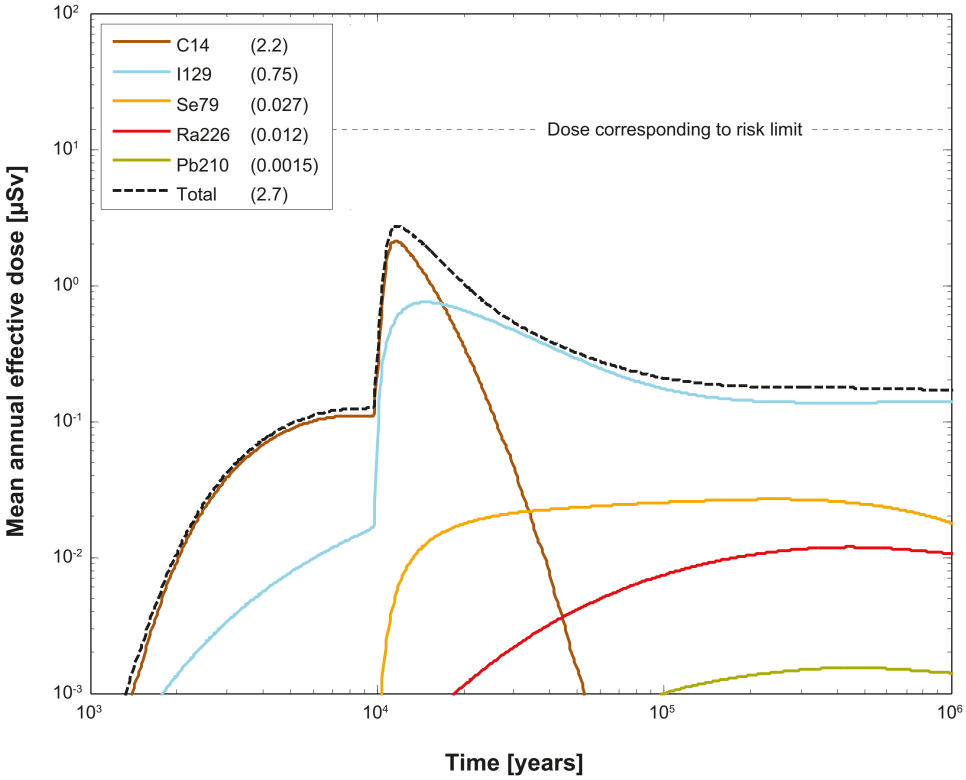

Figure 6-33. *Far-field mean annual mean effective dose for the probabilistic calculation of the pinhole case, with lost swelling pressure in tunnel backfill. Summed doses for all release paths (Q1+Q2+Q3). The legend is sorted by peak (in the one-million year period) of the mean annual effective dose. The values in brackets are peak dose in units of µSv.*

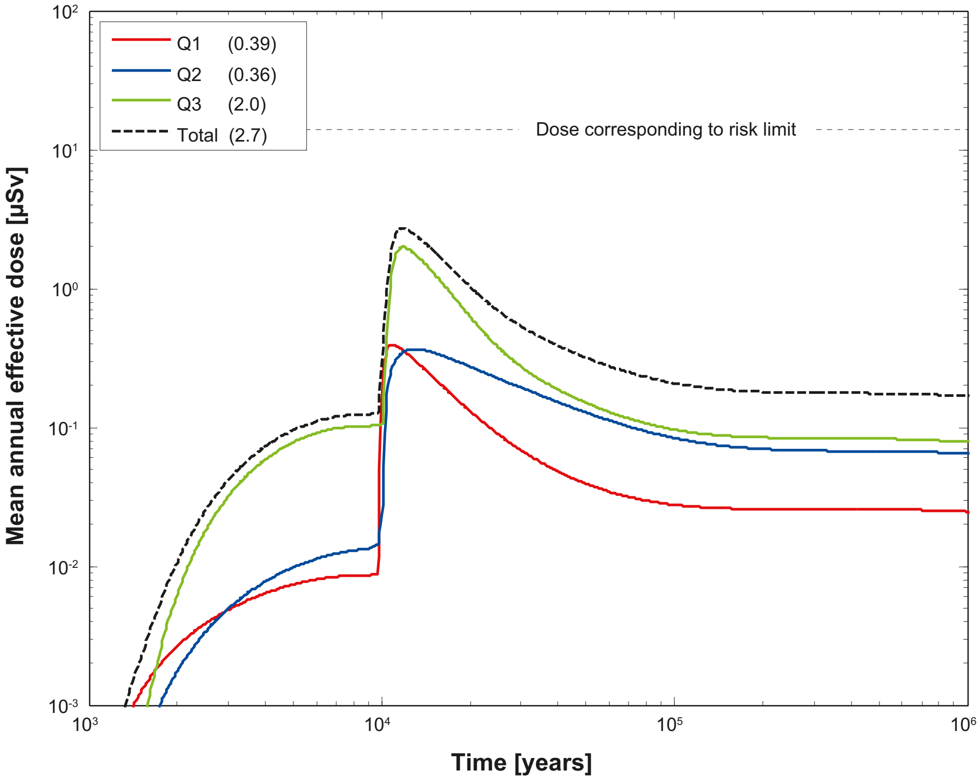

Figure 6-34. *Far-field mean annual effective dose for the probabilistic calculation of the pinhole case, with lost swelling pressure in tunnel backfill. Doses decomposed into Q1, Q2 and Q3. The legend is sorted by peak (in the one-million year period) of the mean annual effective dose. The values in brackets are peak dose in units of µSv.*

6.3.4 Different assumptions regarding EDZ

Hydrogeological case:	Semi-correlated, different variants of EDZ transmissivity
Failure time:	0 and 10,000 years
Number of failed canisters:	1
Solubility limits:	Yes
Spalling:	Yes
Number of realisations:	6,916
Number of nuclides:	37

The excavation damage zone, EDZ, implies a possible release path located in the floor of the deposition tunnel, see Figure 3-1. In the base case (earlier called the pinhole case including the effect of spalling, see Section 6.3.1) is the EDZ transmissivity value 10^{-8} m^{2}/s. The total near-field dose equivalent releases for the pinhole cases with no EDZ, and EDZ transmissivities of 10^{-6} m^{2}/s (EDZ 6), 10^{-7} m^{2}/s (EDZ 7) and 10^{-8} m^{2}/s (based case) are compared in Figure 6-35 and Figure 6-36 shows the same dose equivalent releases decomposed into Q1, Q2 and Q3. Figure 6-37 and Figure 6-38 show the corresponding far-field dose equivalent releases. Eliminating the EDZ decreases the total doses both from near field and far field. The Q2 and Q3 release paths follows the same pattern and the changes are modest. An increase of the EDZ transmissivity above the base case value of 10^{-8} m^{2}/s does not increase the doses from Q1.

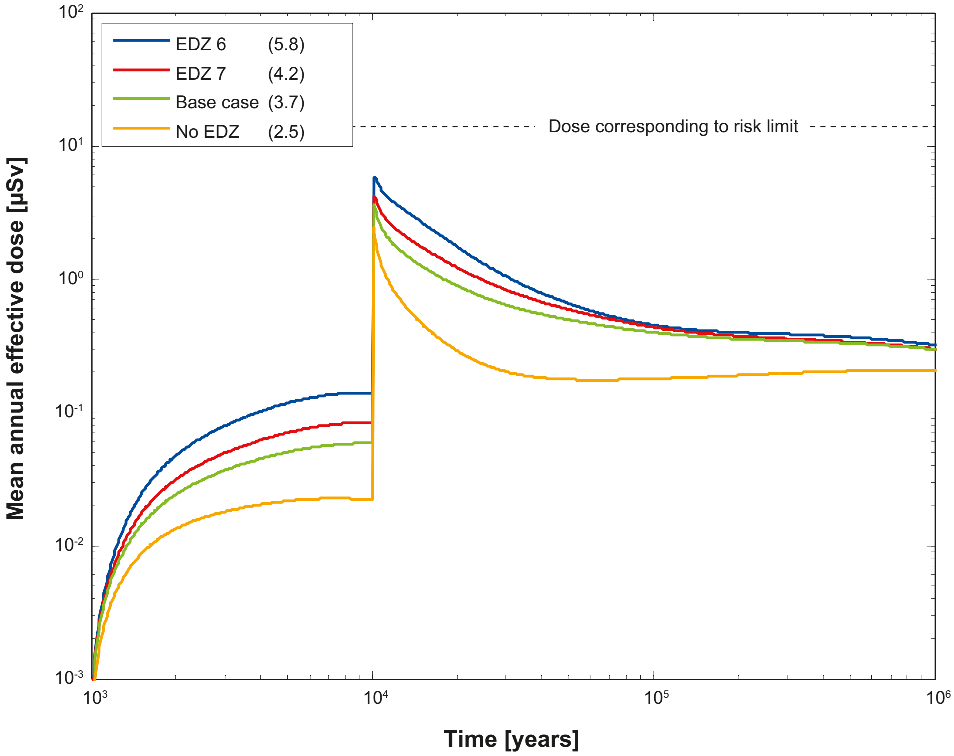

Figure 6-35. *Near-field dose equivalent release for the probabilistic calculation of the pinhole case, comparison between different assumptions regarding EDZ transmissivity (EDZ 6, EDZ 7 and base case correspond to 10^{-6} m^2/s, 10^{-7} m^2/s and 10^{-8} m^2/s, respectively). The legend is sorted by peak (in the one-million year period) of the mean annual effective dose. The values in brackets are peak dose in units of µSv.*

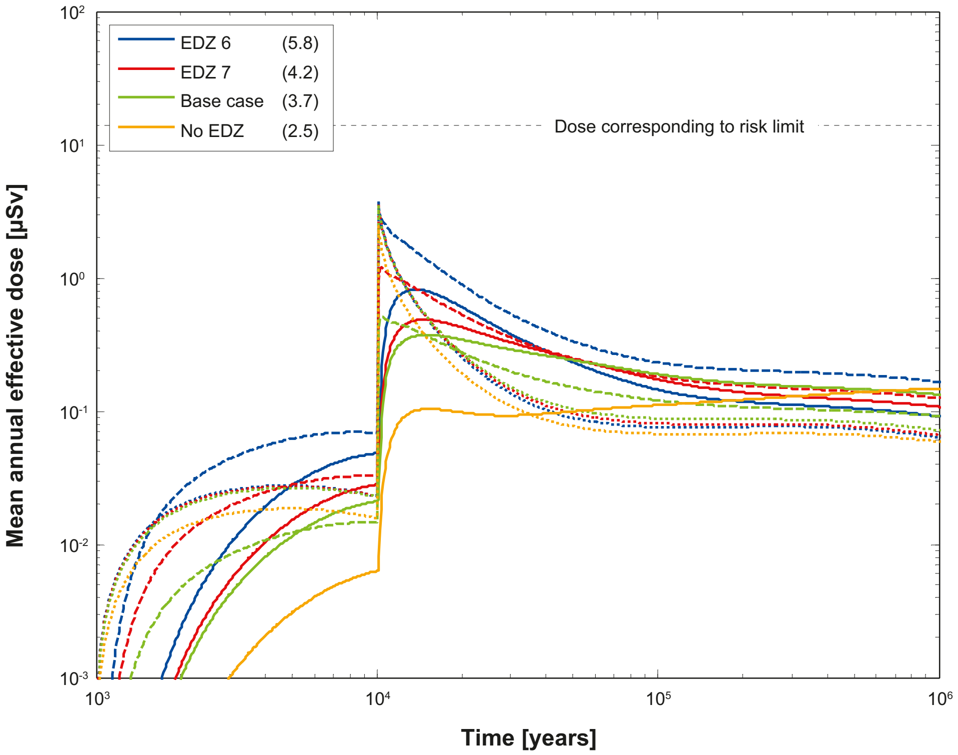

Figure 6-36. *Near-field dose equivalent release for the probabilistic calculation of the pinhole case, comparison between different assumptions regarding EDZ transmissivity (EDZ 6, EDZ 7 and base case correspond to 10^{-6} m^2/s, 10^{-7} m^2/s and 10^{-8} m^2/s, respectively). Doses decomposed into Q1 (dotted lines), Q2 (dashed lines) and Q3 (solid lines). The legend is sorted by peak (in the one-million year period) of the mean annual effective dose. The values in brackets are peak dose in units of µSv.*

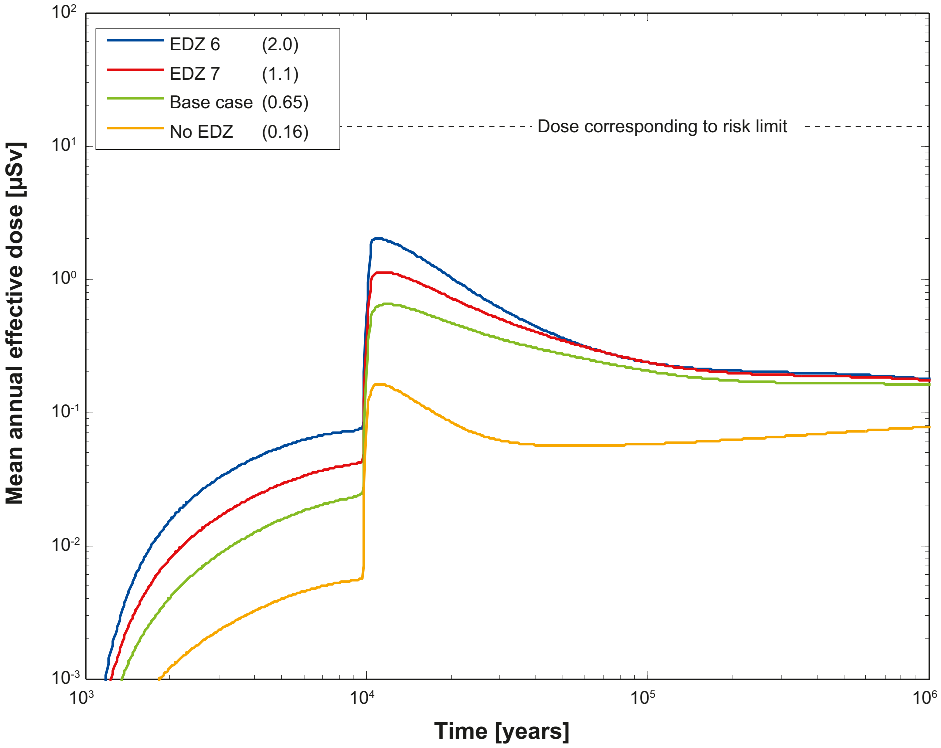

Figure 6-37. *Far-field mean annual effective dose for the probabilistic calculation of the pinhole case, comparison between different assumptions regarding EDZ transmissivity (EDZ 6, EDZ 7 and base case correspond to 10^{-6} m²/s, 10^{-7} m²/s and 10^{-8} m²/s, respectively). The legend is sorted by peak (in the one-million year period) of the mean annual effective dose. The values in brackets are peak dose in units of µSv.*

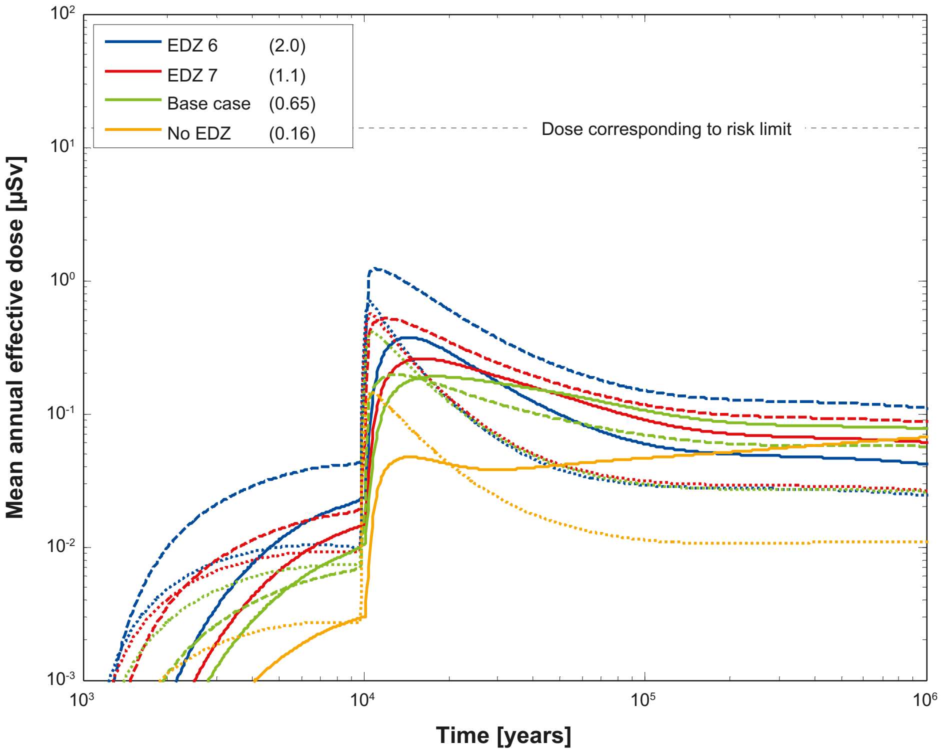

Figure 6-38. *Far-field mean annual effective dose for the probabilistic calculation of the pinhole case, comparison between different assumptions regarding EDZ transmissivity (EDZ 6, EDZ 7 and base case correspond to 10^{-6} m²/s, 10^{-7} m²/s and 10^{-8} m²/s, respectively). Doses decomposed into Q1 (dotted lines), Q2 (dashed lines) and Q3 (solid lines). The legend is sorted by peak (in the one-million year period) of the mean annual effective dose. The values in brackets are peak dose in units of µSv.*

6.3.5 Summary and conclusions for the growing pinhole scenario

Several variants of the growing pinhole scenario have been calculated to examine sensitivities to various transport conditions. The results are summarised in Figure 6-39 and Figure 6-40. The crown space case, in which tunnel backfill has compacted with a resulting gap at the tunnel crown, dominates the releases. Comparing variants with different excavation damage zone (EDZ) transmissivity, shows that the releases decrease with decreasing EDZ transmissivity. Thermally induced spalling is assumed to occur in the walls of the deposition holes and decrease the transport resistance in the interface between the buffer and the rock. The effect of of spalling is assessed by a case that does not include spalling. The maximum dose is about 4 times lower in the case that does not include spalling.

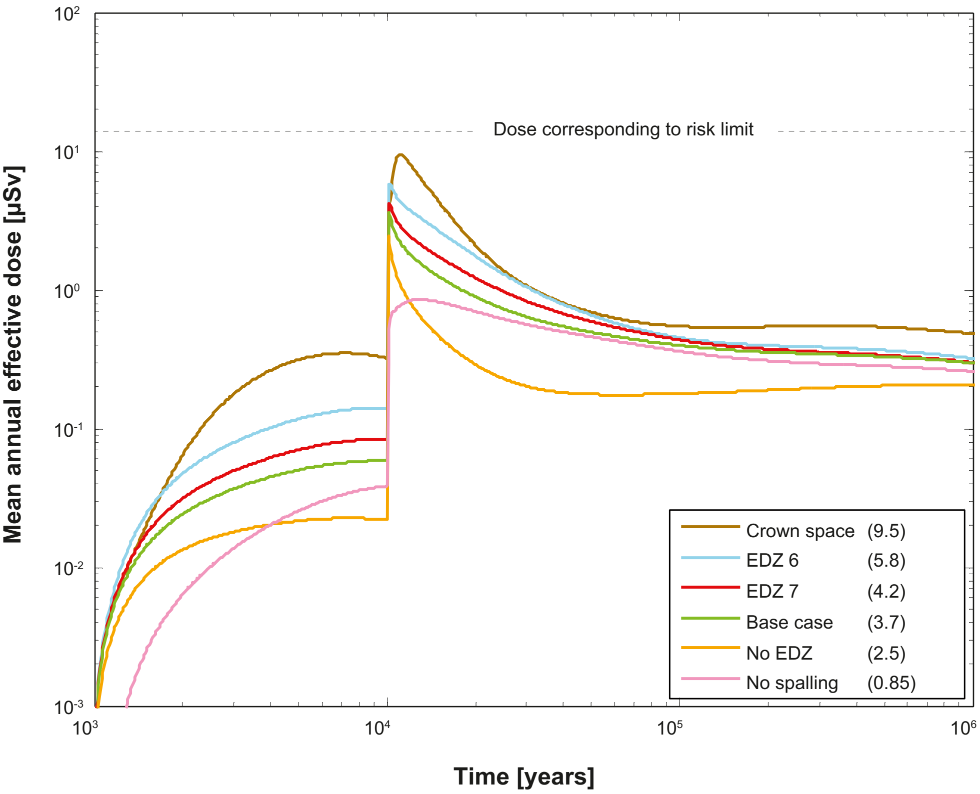

Figure 6-39. *Near-field mean annual effective dose equivalent for the probabilistic calculations of the pinhole base case and cases with no spalling, with different assumptions regarding EDZ and with a crown space in the deposition tunnel. The legend is sorted by peak (in the one-million year period) of the mean annual effective dose. The values in brackets are peak dose in units of µSv. (EDZ 6, EDZ 7 and base case correspond to a transmissivity of* 10^{-6} *m²/s,* 10^{-7} *m²/s and* 10^{-8} *m²/s, respectively).*

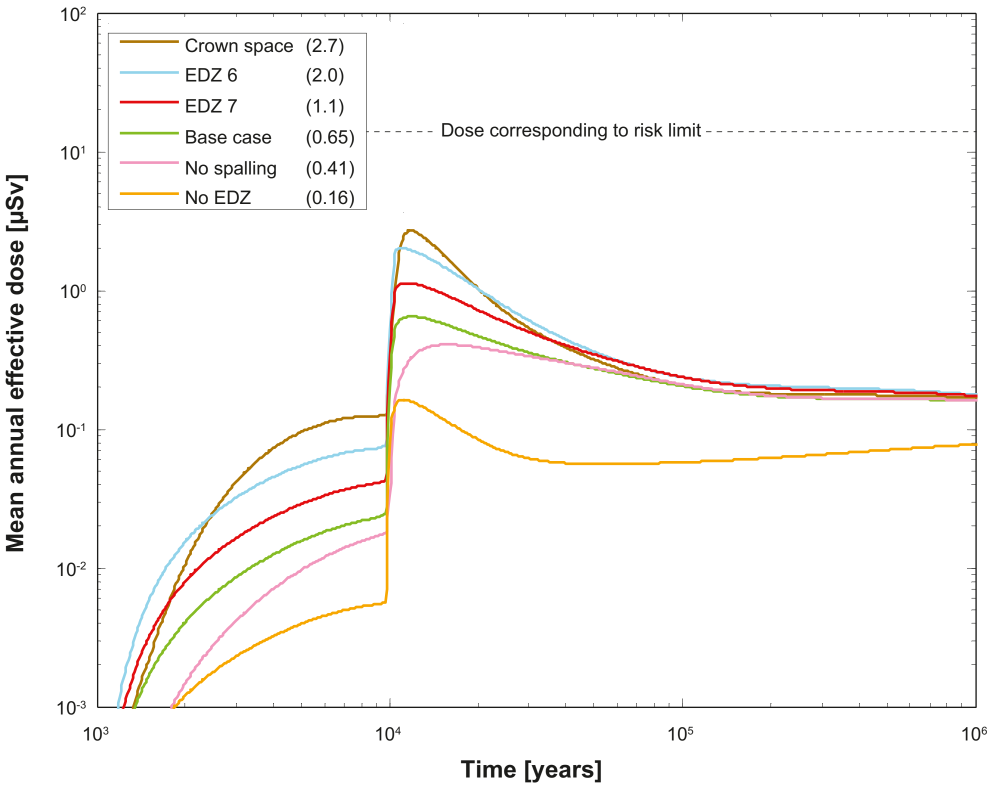

Figure 6-40. *Far-field mean annual effective dose for the probabilistic calculations of the pinhole base case and cases with no spalling, with different assumptions regarding EDZ and with a crown space in the deposition tunnel. The legend is sorted by peak (in the one-million year period) of the mean annual effective dose. The values in brackets are peak dose in units of µSv. (EDZ 6, EDZ 7 and base case correspond to a transmissivity of 10^{-6} m²/s, 10^{-7} m²/s and 10^{-8} m²/s, respectively).*

6.4 Exploration of geosphere barrier performance using the growing pinhole case

The growing pinhole failure case provides a convenient hypothetical scenario to illustrate various sensitivities related to the geosphere barrier. To that end, deterministic values are used for initial radionuclide inventories and for all near-field and far-field parameters not related to flow. However, because the location of the defective canister is not known in this scenario, effective dose results are calculated as mean values over all potential locations of the defective canister. That is, full spatial variability in flow-related parameters is included.

COMP23 and MARFA are used here for the near-field and far-field transport. Recall that MARFA supports spatial variability both along and among transport pathways, thus making it possible to address aspects of geosphere barrier performance that cannot be addressed with FARF31.

Specific sensitivities studied include:

- The role of advective transport in tunnels and soils.
- The role of sorption in tunnels and soils.
- The effect of a crown space formed by compaction of backfill in repository tunnels.
- Sensitivity to assumed fracture transmissivity in excavation damage zones.
- Implications of assuming one or multiple transport pathways per deposition hole.

6.4.1 Input parameters

The sensitivity study described in this section assumes steady groundwater flow corresponding to the temperate period. ConnectFlow ptb- and ptv-files for the reference case flow model and key variants provide the relevant information for use in COMP23 and MARFA, as shown in Table 6-1. The semi-correlated DFN model is used.

Table 6-1. SR-Site temperate period flow fields used in this study. Unless otherwise noted, the ptv-/ptb-files include all deposition holes with one pathway per hole.

ptv/ptb file	Description
fs_Q*m*_2000_pline_merged (with *m* = 1,2,3)	Base cases
fs_crown_Q1_2000_pline_merged	Crown space variant, Q1 release
fs_crown_start_Q3_2000_pline_merged	Crown space variant, Q3 release*
fs_maxedz_7_Q*m*_2000_pline_merged (*m* = 1,2,3)	EDZ transmissivity of 10^{-7} m^2/s
fs_maxedz_6_Q*m*_2000_pline_merged (*m* = 1,2,3)	EDZ transmissivity of 10^{-6} m^2/s
fs_noedz_Q*m*_2000_pline_merged (*m* = 1,3)	No EDZ
fs_newtop25_Q1_2000_pline10_merged	Q1 base case for top† 25% of deposition holes with 10 pathways per hole

* Q3 pathways for the crown space variant were defined by releasing particles into the crown space, to be consistent with COMP23 definition of near-field release for that variant. For all other variants, Q3 pathways were defined by releasing particles in the tunnel 1 m above the deposition hole.

† Based on initial velocity.

The ptv-files provide by ConnectFlow were modified for two combinations of flow variants and transport assumptions. The ConnectFlow ptv-files include pathline segments that pass through tunnels and soils represented as Continuum Porous Medium (CPM) in addition to fractured rock segments. The CPM segments contribute nothing to the flow-related transport resistance, F-factor, but do contribute to the advective travel time t_w. Thus, for variant modelling cases designed to quantify the contribution of tunnels and soils by neglecting travel distances in those regions, CPM segments were removed to prepare new ptv-files. In addition, for Q3 cases that include the CPM segments, the tunnel segments between the release point and the first fracture encountered were removed to enforce consistency between the ptv-file and the near-field release calculation, which defines Q3 release as flux into the fracture intersecting the tunnel nearest to the deposition hole.

The sensitivity studies described in this section were undertaken before SR-Site transport parameters were finalised. Consequently, SR-Can or preliminary SR-Site values are used for radionuclide inventories, near-field transport parameters, and far-field retention parameters. Details are provided in Appendix H.

6.4.2 Reference case

The reference case for this section assumes no sorption in the tunnels and no sorption in the soils. The CPM parts of the pathway, however, are included in the travel time. It is important to note that the inclusion of the CPM parts of the pathway in the advective travel time is in contrast to calculations presented elsewhere in this report. The flow-channelling factor is set to unity to represent no channelling within individual fractures. Colloids are not included.

The pinhole release scenario considers failure of one canister at an unknown deposition hole. To calculate the expected value of release, all canisters are forced to fail and an aggregate release is calculated. The expectation value for release is then calculated by dividing the aggregate release by the number of emplaced canisters. Note that deposition holes that do not have a connected pathway to the geosphere have zero release by definition. In addition, deposition holes for which a ConnectFlow pathway could not be defined because of numerical failure in the ConnectFlow particle tracking calculation (stuck particles, represented by OKFLAG > 0) are also assumed to result in no release. This assumption is based on the observation that stuck particles in the ConnectFlow particle tracking algorithm are caused by nearly stagnant pathways, and these pathways would not contribute significantly to the expected release. Deposition holes with the full perimeter criterion or effective full perimeter criterion flags set (FPC = 1) or (EFPC > 5) were assumed to not have emplaced canisters. That is, these contribute nothing to the aggregate release and were also not counted in the number of canisters emplaced.

Comparison of release path

Far-field releases expressed as equivalent doses are shown in Figure 6-41 for the three release paths. The Q1 release path results in the largest peak release, followed by Q2 and Q3. Peak release is almost an order of magnitude larger for the Q1 path compared with the Q3 path. The Q2 and Q3 paths result in flatter release histories compared with the Q1 path. At late times, differences between the release paths are much smaller, with the Q2 paths resulting in the largest releases.

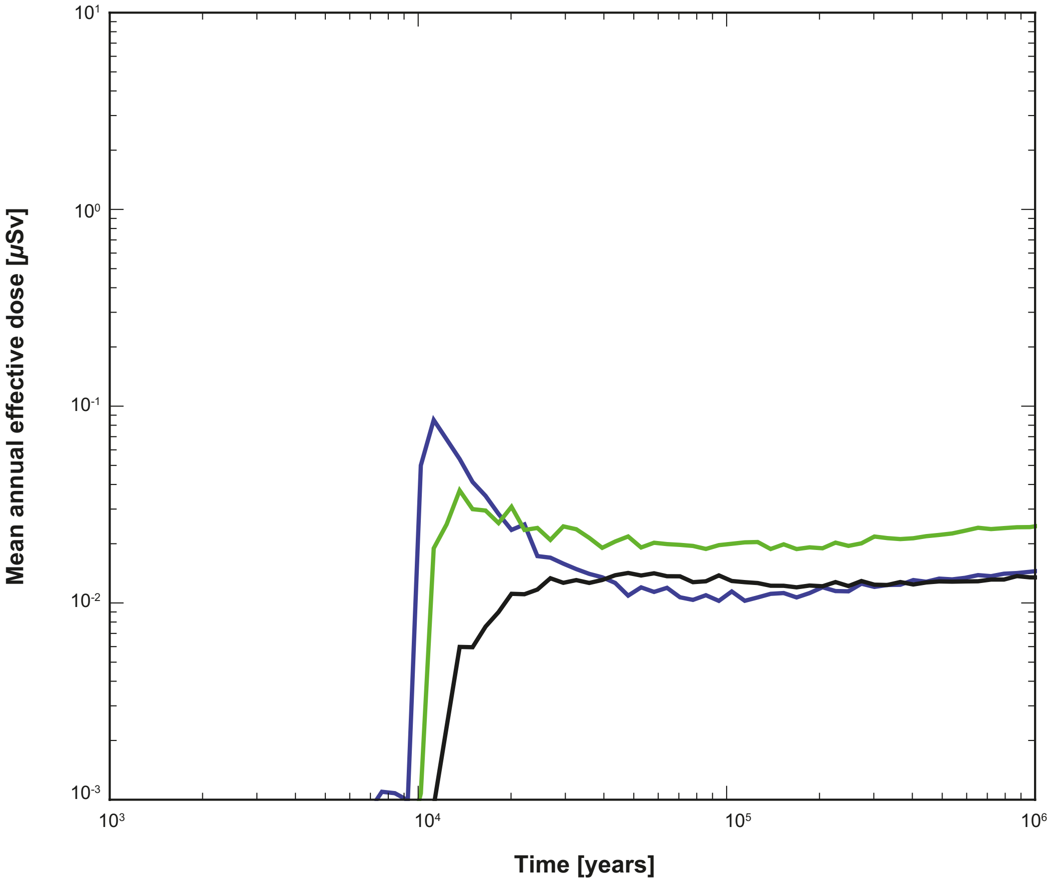

Figure 6-41. *All-nuclides far-field releases expressed as effective dose for the pinhole scenario and different release paths. Expected values are shown for all deposition holes versus time for Q1 (blue), Q2 (green), and Q3 (black) release paths.*

Details for the Q1 release path

Total far-field and near-field releases expressed as effective doses for the Q1 release path are shown in Figure 6-42. The far-field geosphere reduces peak dose by a factor of approximately 20. The dose at 1 million years is reduced by a factor of approximately 4 by the geosphere. Observable in Figure 6-42 is an increasing trend in the near-field release, which does not occur in the far field. This behaviour is attributable to ingrowth of Ra-226 at near-field release, which is then retarded in the far field.

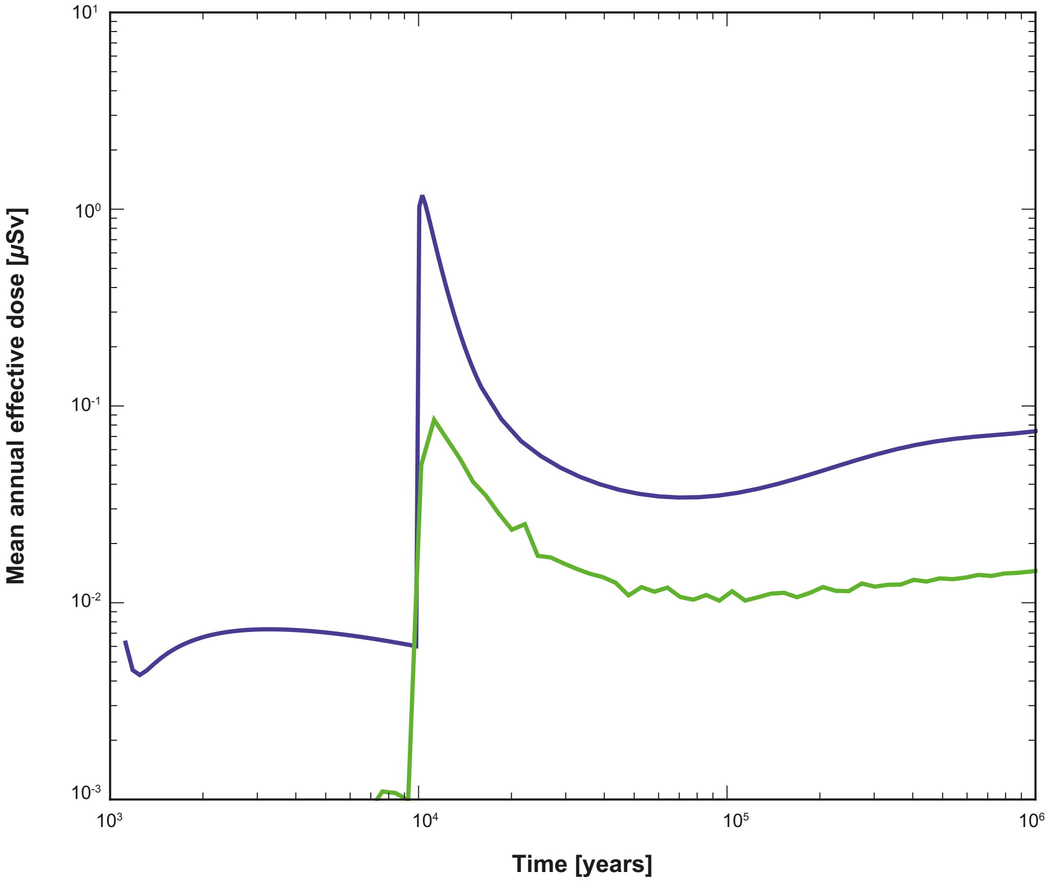

Figure 6-42. All-nuclides near-field and far-field releases expressed as effective dose for the pinhole scenario, Q1 release path. Expected values are shown for all deposition holes versus time: near-field dose equivalent release (blue) and far-field mean annual effective dose (green).

Trajectories for the 2% of pathways contributing the most by total instantaneous far-field release are shown in Figure 6-43. Each trajectory is colour-coded by maximum all-nuclides instantaneous dose as shown in the figure legend. Canister locations are shown as red or green dots. Red signifies that the deposition hole is not connected to the biosphere by a Q1 pathway. Green dots represent holes that contribute to transport through the Q1 pathway. It is noted that the majority of canisters have no connected Q1 pathway. Among those with connected pathways, the majority of radionuclide dose comes from a relatively small fraction of pathways.

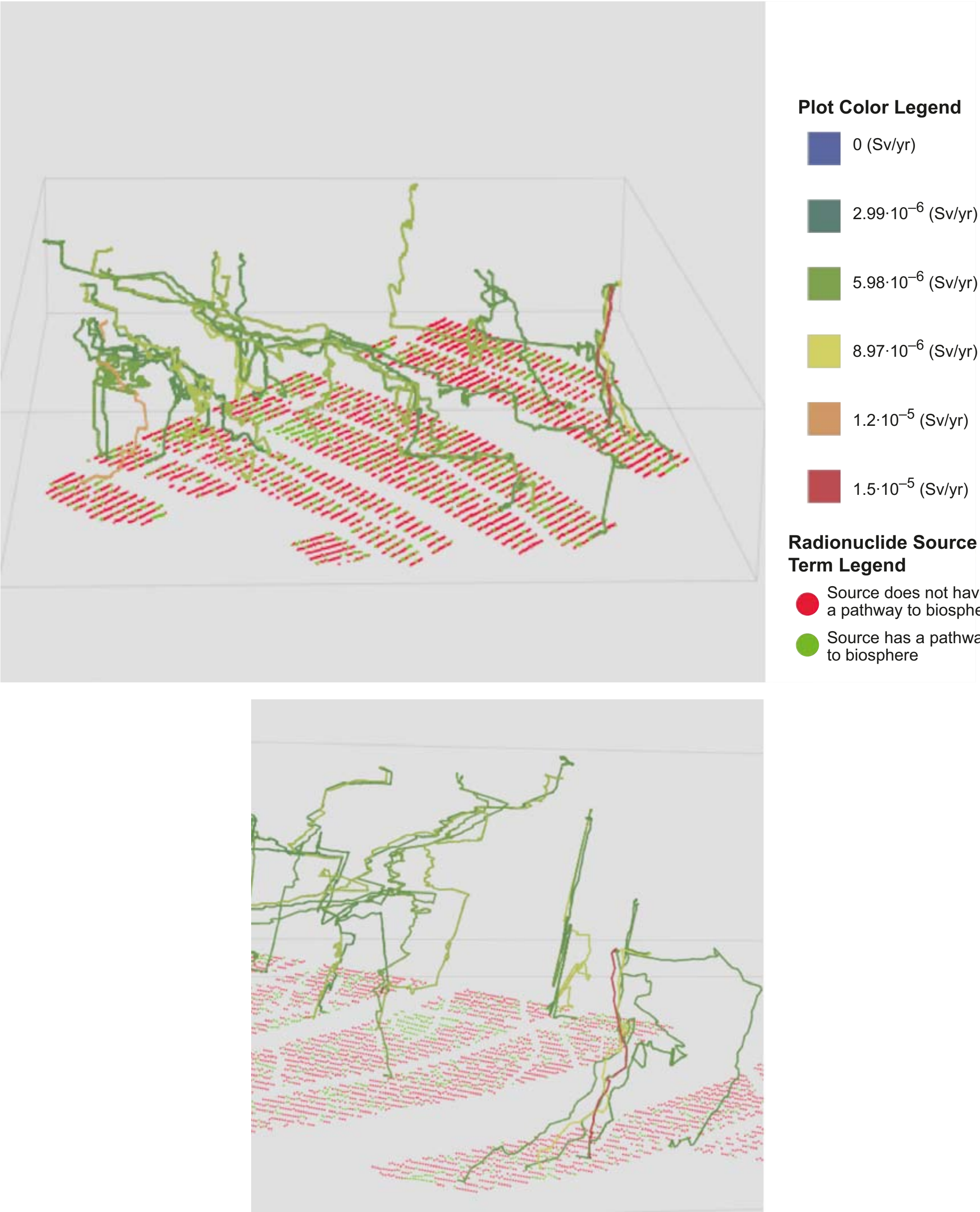

Figure 6-43. *Pathway trajectories for pinhole scenario, Q1 release path for the 2% of pathways contributing the most to the ensemble release. The top image shows the entire repository. The bottom image is a detail from the larger image (rotated). Trajectories and starting locations are colour-coded as shown in the legend.*

Near-field and far-field releases for the 12 radionuclides contributing most to far-field release are shown in Figure 6-44. It is clear that I-129, C-14, and Ra-226 account for almost all the far-field and near-field releases. Far-field attenuation factors range from about two orders of magnitude for Th-230 and Pa-231 to less than an order of magnitude for Se-79.

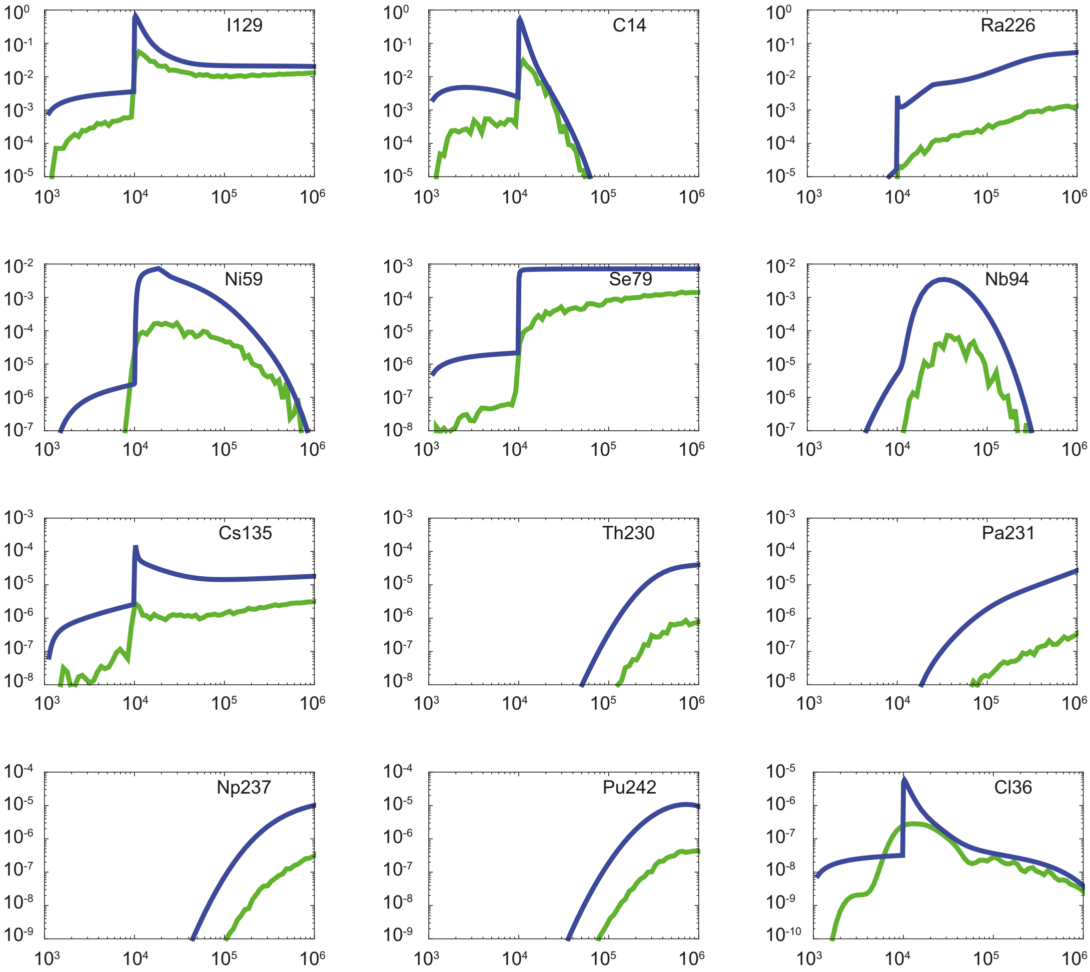

Figure 6-44. *Near-field (blue) and far-field (green) releases for the 12 radionuclides contributing most to the far-field release for the Q1 release path. Units are µSv/yr on the y-axis and year on the x-axis for each plot. Note the scale on the y-axis is different for different radionuclides.*

Details for the Q2 release path

Total far-field and near-field releases expressed as effective dose in Sv/yr for the Q2 release path are shown in Figure 6-45. The far-field geosphere reduces peak dose by a factor of approximately 5. The dose at 1 million years is reduced by a smaller factor. Near-field and far-field releases for the top six contributors (by far-field release) are shown in Figure 6-46. As is the case for the Q1 path, I-129, C-14, and Ra-226 are the largest contributors. The geosphere attenuates the release by factors of approximately 5 for I-129, 4.7 for C-14, and 40 for Ra-226.

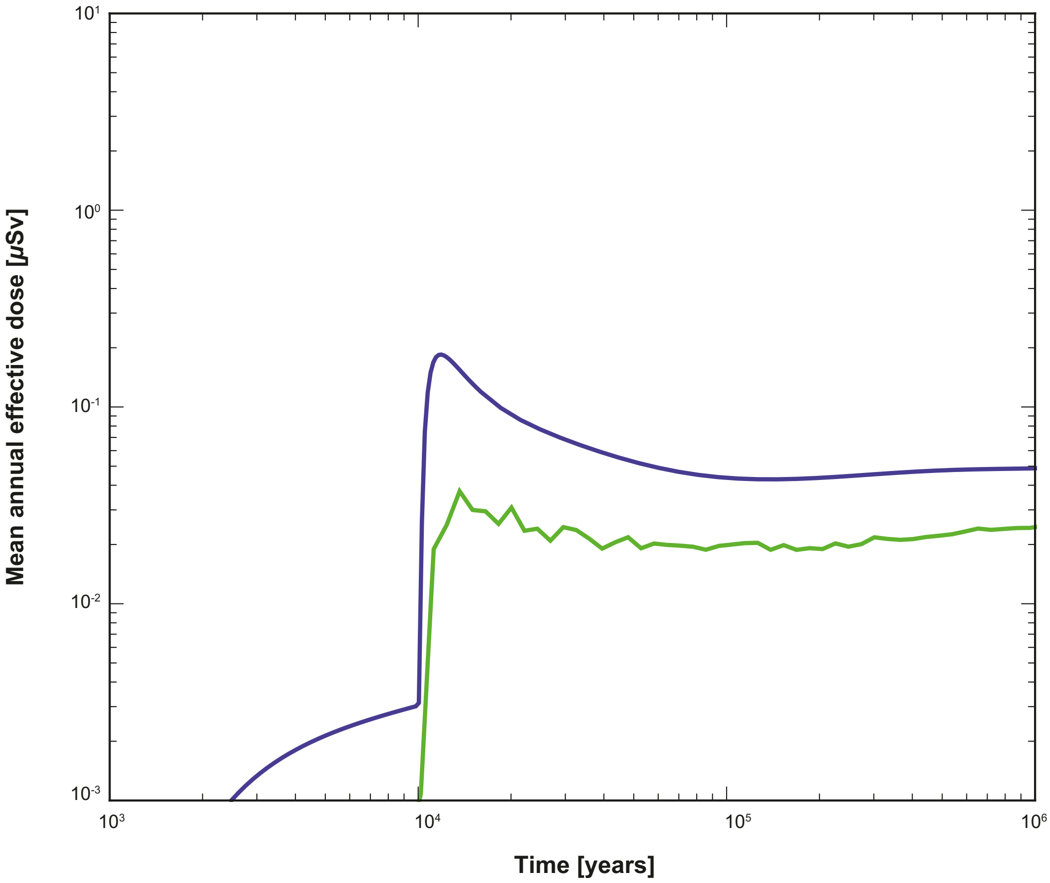

Figure 6-45. *All-nuclides near-field and far-field releases expressed as effective dose for the pinhole scenario, Q2 release path. Expected values are shown for all deposition holes versus time: near-field dose equivalent release (blue) and far-field mean annual effective dose (green).*

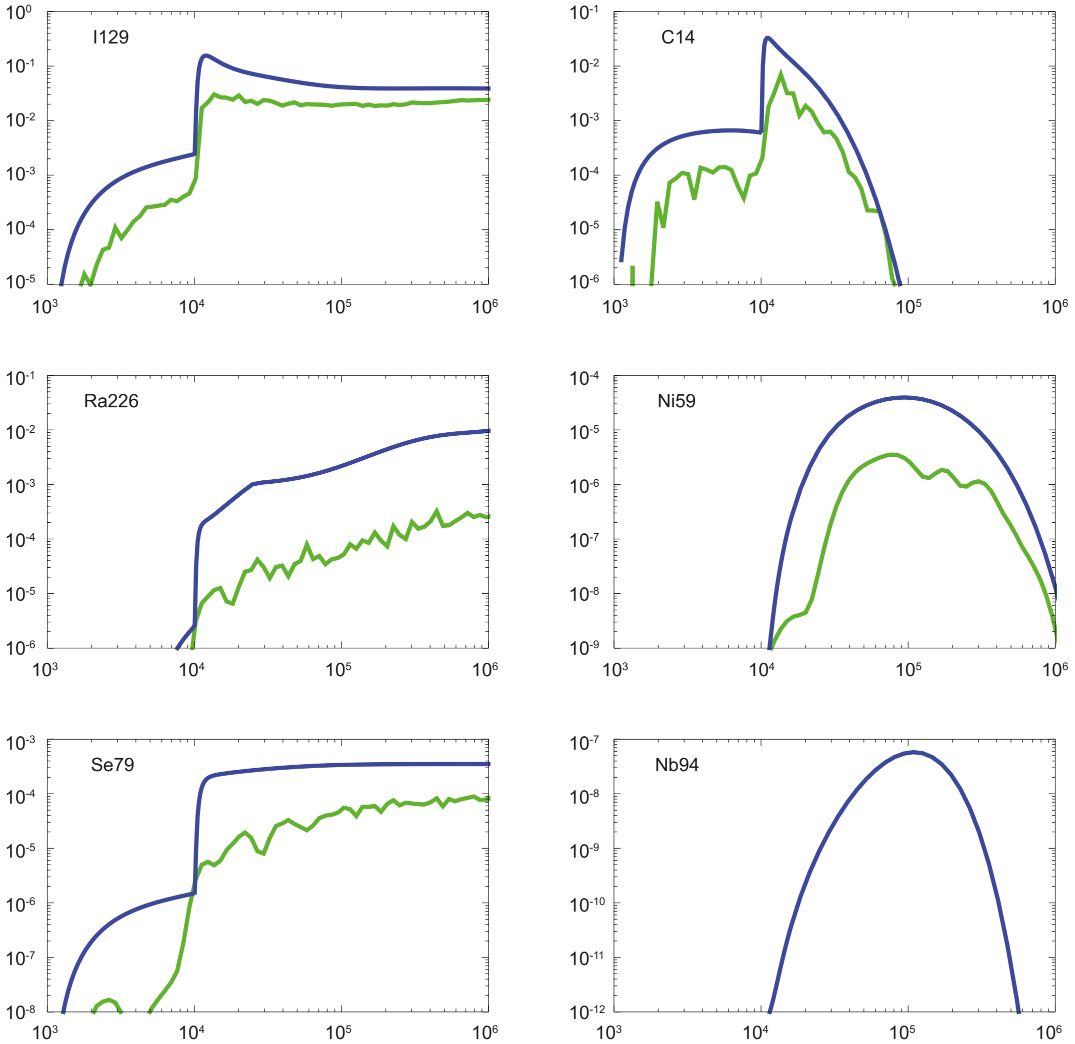

Figure 6-46. *Near-field (blue) and far-field (green) releases for the top six contributors (by far-field release) for the Q2 release path. Units are µSv/yr on the y-axis and year on the x-axis for each plot. Note the scale on the y-axis is different for different radionuclides.*

Details for the Q3 release path

Total far-field and near-field releases expressed as effective dose for the Q3 release path are shown in Figure 6-47. The far-field geosphere does not represent a significant barrier for this release path. However, the near-field Q3 release is smaller than that of the Q1 and Q2 paths.

Trajectories for the 2% of pathways contributing the most by total instantaneous far-field release are shown in Figure 6-48. Each trajectory is colour-coded by the maximum all-nuclides instantaneous dose as shown in the figure legend. Canister locations are shown as red or green dots. Red signifies that the deposition hole is not connected to the biosphere by a Q3 pathway or that the contribution from that pathway is negligible. Green dots represent holes that contribute to transport through the Q3 pathway. It is noted that in contrast to the Q1 path, many pathways contribute to dose for the Q3 path, primarily because the repository tunnels provide pathways to the fracture network backbone (see detail in lower left of Figure 6-48).

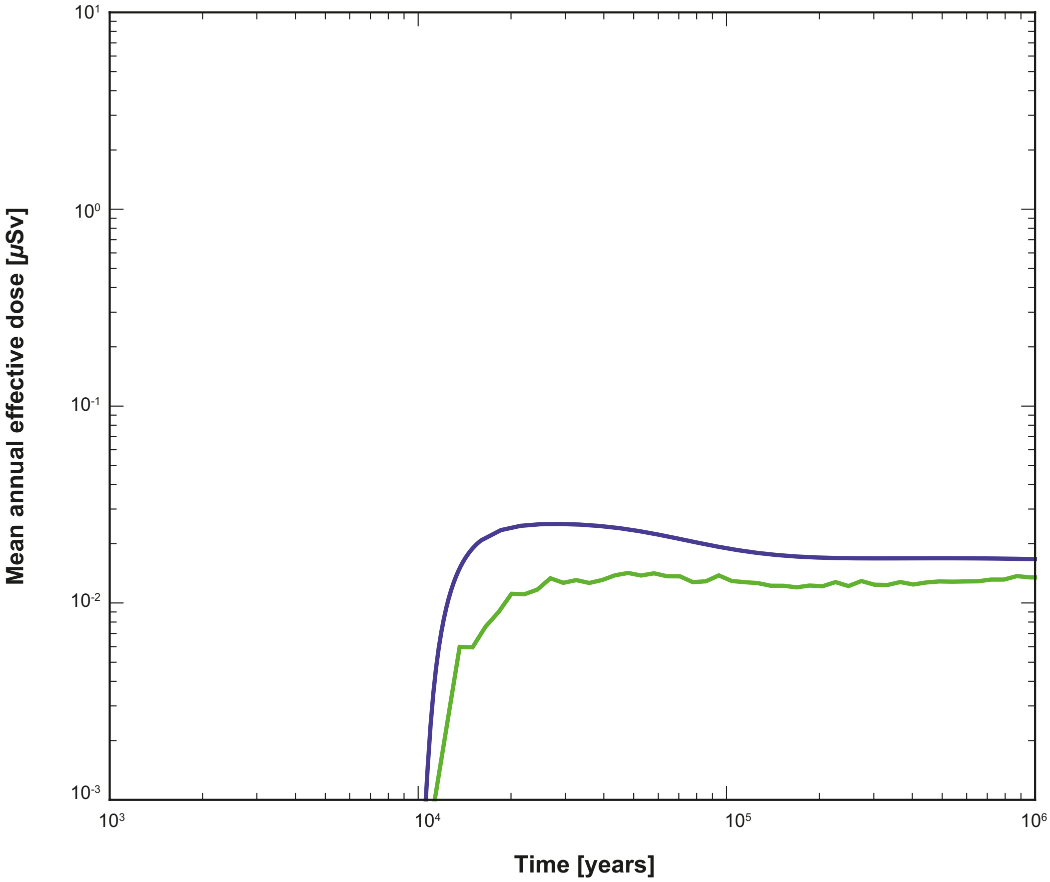

Figure 6-47. *All-nuclides near-field and far-field releases expressed as effective dose for the pinhole scenario, Q3 release path. Expected values are shown for all deposition holes versus time near-field dose equivalent release (blue) and far-field mean annual effective dose (green).*

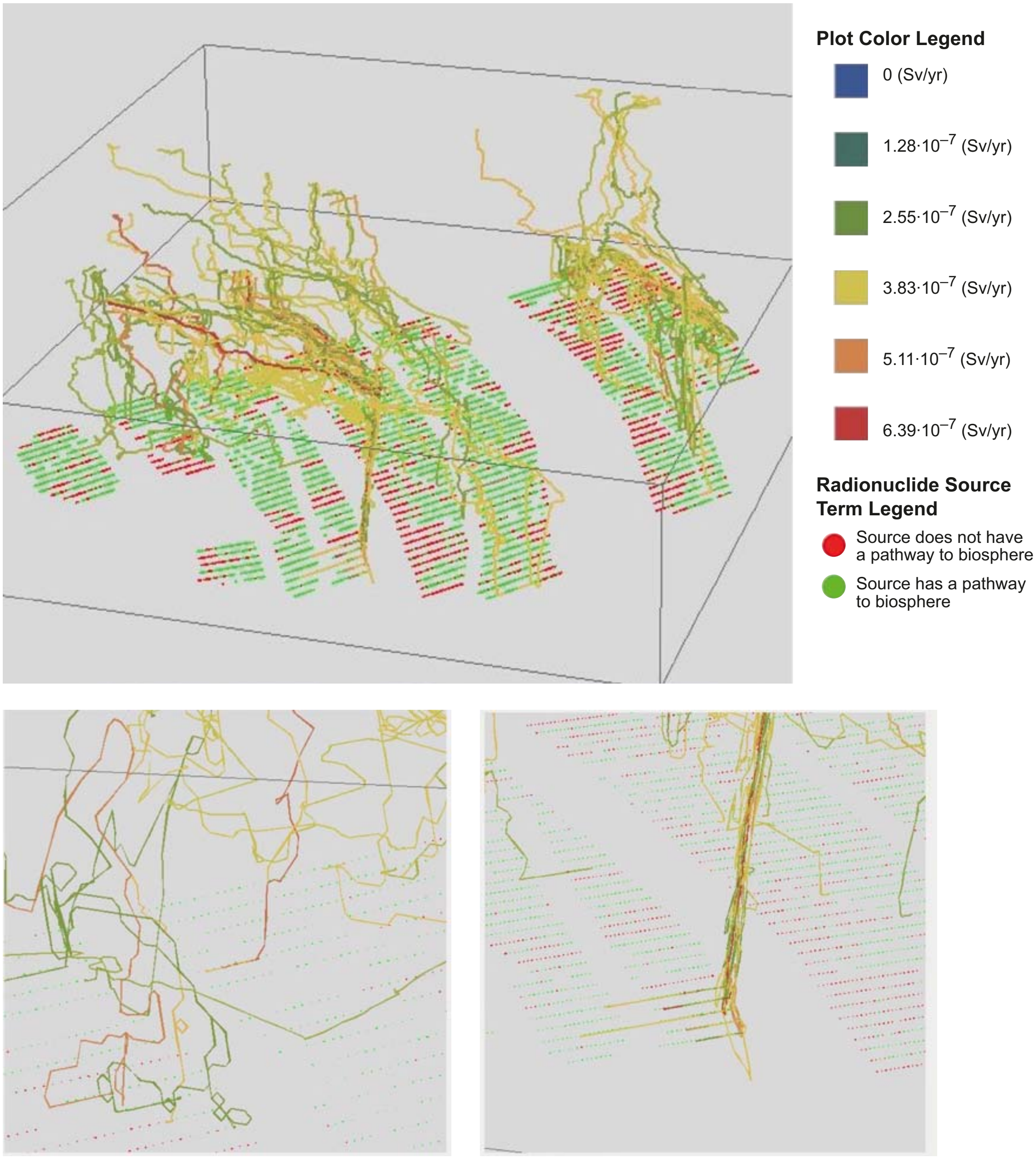

Figure 6-48. *Pathway trajectories for pinhole scenario, Q3 release path for top 2% of pathways by contribution to the all-nuclides release. The top image shows the entire repository. The bottom images are details from the larger image. Trajectories and starting locations are colour-coded as shown in the legend. Note the MARFA calculations used to calculate the dose rates shown in this figure used COMP23 outputs that were later found to be based on a ConnectFlow ptb-file that contained erroneous values for one parameter. These results should be considered qualitative only.*

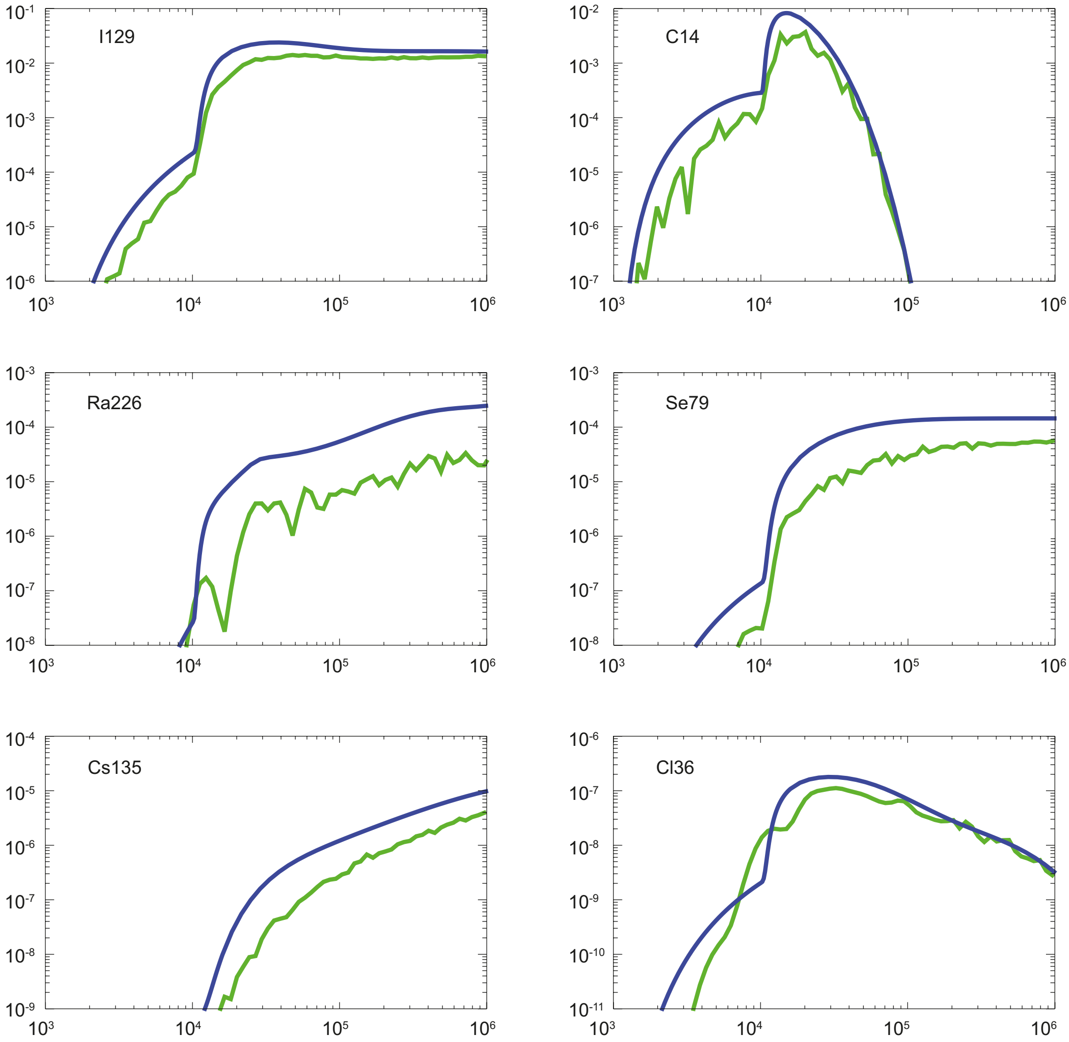

Figure 6-49. *Near-field (blue) and far-field (green) releases for the top six contributors (by far-field release) for the Q3 release path. Units are µSv/yr on the y-axis and year on the x-axis for each plot. Note the scale on the y-axis is different for different radionuclides.*

6.4.3 Issues related to the probabilistic nature of the calculations

Variability about the mean

The pinhole failure scenario presumes one failed canister at an unknown location. Results presented thus far and elsewhere in this report have been for the expected value of discharge averaged over all starting locations. Some locations will contribute much to the expected value and some will contribute little or nothing. For example, approximately 81% of deposition holes have no connected pathway to the biosphere and thus contribute nothing to the mean value for the Q1 path. To understand the variability about the mean, selected percentiles in the discharge were calculated at each time. Results for the Q1 release path are shown in Figure 6-50 (99th, 95th, 90th, and 85th percentiles in green and mean curve in blue).

More than half of the trajectories have zero release because of no release path. Thus, the median release is zero and is not shown. The peak of the 90th percentile is close to the peak of the mean, although the two peaks occur at different times. Thus, there is a less than 10% chance that the pinhole release scenario from one package will have a value greater than the peak of the mean. As already noted, there is a greater than 80% chance that the release will be exactly zero.

The shapes of the curves in Figure 6-50 are markedly different for the different percentiles. It is apparent that most of the deposition holes (90th and smaller percentiles) are either not connected to pathway or are connected to a pathway that provides sufficient retardation to allow key radionuclides to decay. Thus the peak of the mean is strongly influenced by the contributions from the few pathways that exhibit little retardation.

Another way to analyse the range of possible doses delivered to the biosphere is to plot the exceedance probability versus dose (Figure 6-51). This plot is based on a 1-million year interval. There is approximately a 2.7% probability that the maximum dose rate delivered to the biosphere will exceed 10^{-6} Sv/yr at some time in the 1-million year interval. For 10^{-5} Sv/yr dose, the exceedance probability is $4 \cdot 10^{-4}$.

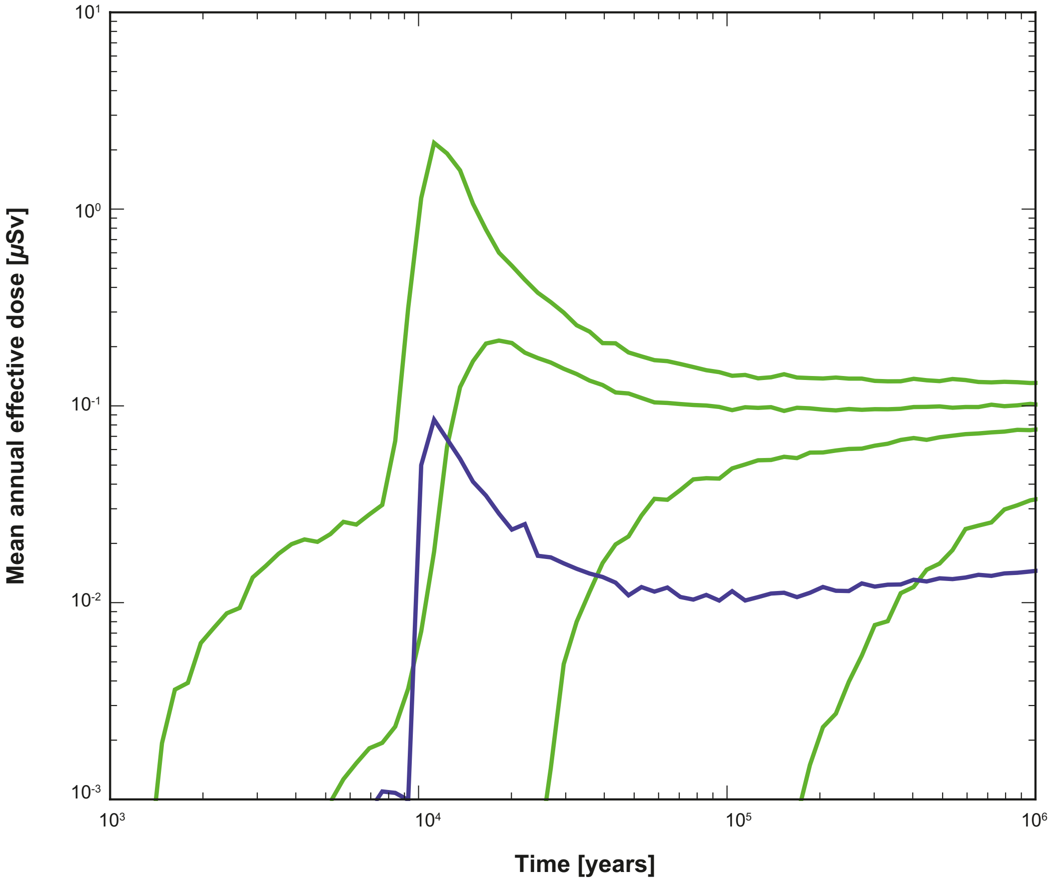

Figure 6-50. *Mean (blue curve) and selected percentiles (green curves) for pinhole Q1 release. Shown are the 99th, 95th, 90th, and 85th percentiles.*

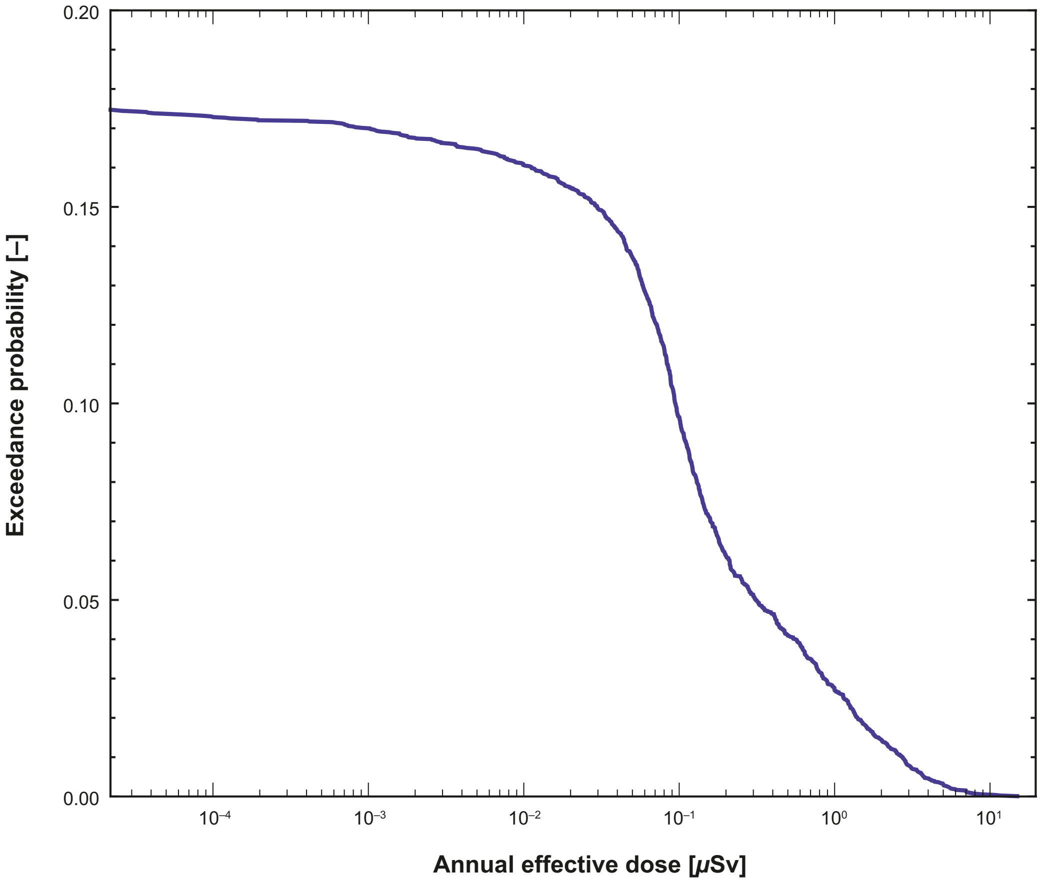

Figure 6-51. *Exceedance probability for a given dose rate (μSv/yr) for the pinhole Q1 release. A 1-million year time window was used to calculate the exceedance probability. Thus, for a given dose rate, the exceedance probability is the probability that the dose rate exceeds that value at some time during the 1-million year period.*

Multiple pathways for each deposition hole

The base case has one pathway per release point. The effect of this assumption was assessed by considering a variant case with 10 Q1 pathways per release point. This calculation was limited to the 25 release points contributing most to the total dose in the base case. Results are shown in Figure 6-52. The blue curve is near-field release. The solid green curve is the base case far-field release. The dashed green curve is the far-field release for the case with 10 pathways per release point. Although transport from any single release point may be different depending on whether 1 or 10 pathways are represented, these differences are averaged out in the ensemble.

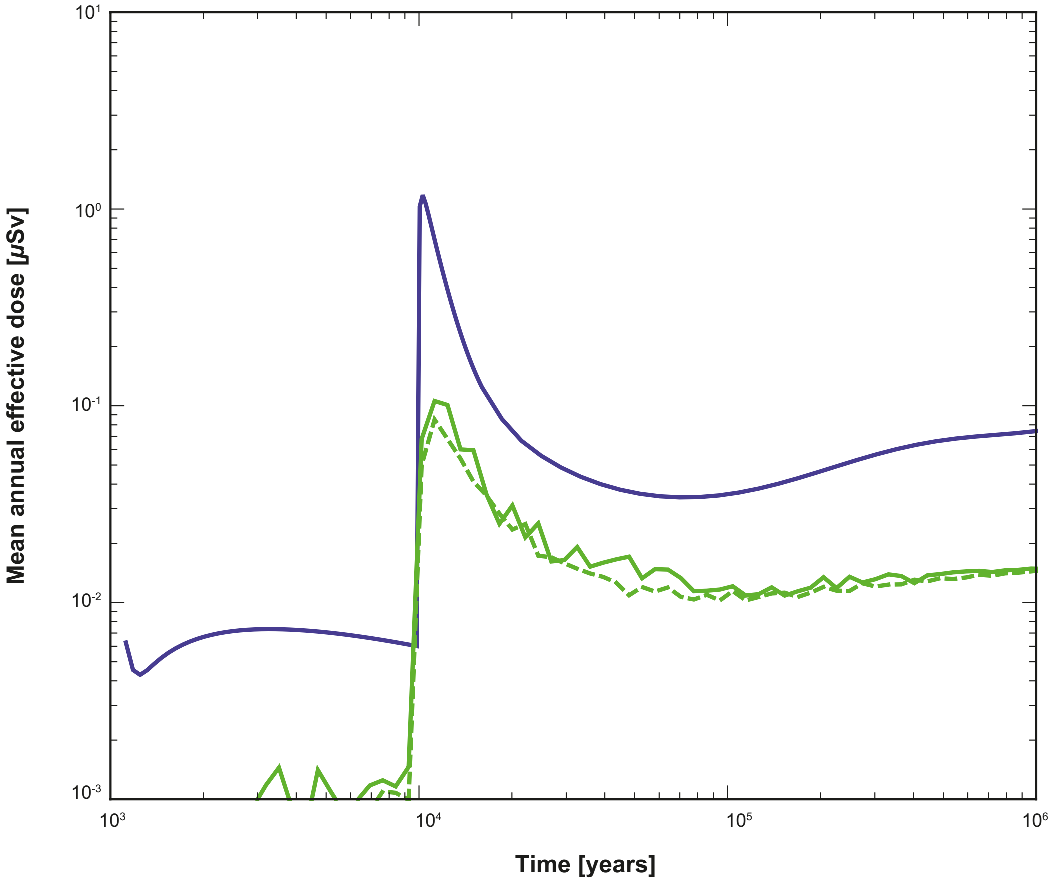

Figure 6-52. *Effect of having multiple Q1 pathways per release point. The blue curve is near-field release. The solid green curve is the base case far-field release. The dashed green curve is the far-field release for the case with 10 pathways per release point.*

6.4.4 Exploration of barrier function of geosphere components

Transport and retention in soils and tunnels

The reference case includes soils and tunnel segments in the transport pathway, but assigns these segments zero equilibrium partitioning coefficients for all elements. Thus, the delay introduced by a non-zero advective travel time through soils and tunnels is accounted for, but retardation of sorbing elements is ignored. Effects of the soils and tunnels are summarised in Figure 6-53 for the Q1 path. The blue curve is near-field release and the green curve is the base case. The pink curve neglects the effect of the CPM parts of the pathways (i.e., tunnels and soils). In calculating the pink curve, CPM segments were removed from the base case ptv-file and a new ptv-file was generated. The black curve uses the base case ptv-file, but with sorption turned on in tunnels and soil layers. There are two main conclusions to be drawn from Figure 6-53. First, the travel time in the CPM part of the pathways decreases the peak dose by a factor of approximately 5 (compare pink to green curves). This decrease is mostly due to the effect on the nonsorbing radionuclides I-129 and C-14. Second, sorption in tunnels and soils has no significant effect on total dose. This lack of sensitivity is a consequence of the dominant role that I-129 and C-14 play in determining the total dose. Indeed, examination of the far-field releases for individual nuclides (Figure 6-54) reveals that releases of sorbing radionuclides such as Ra-226 and Th-230 are significantly reduced by sorption in tunnels and soils.

Effects of the soils and tunnels are summarised in Figure 6-55 for the Q2 path. Without the delay provided by soils and tunnels, the geosphere is not a major barrier to radionuclide transport for a Q2 release. Other sensitivities are similar to the Q1 path.

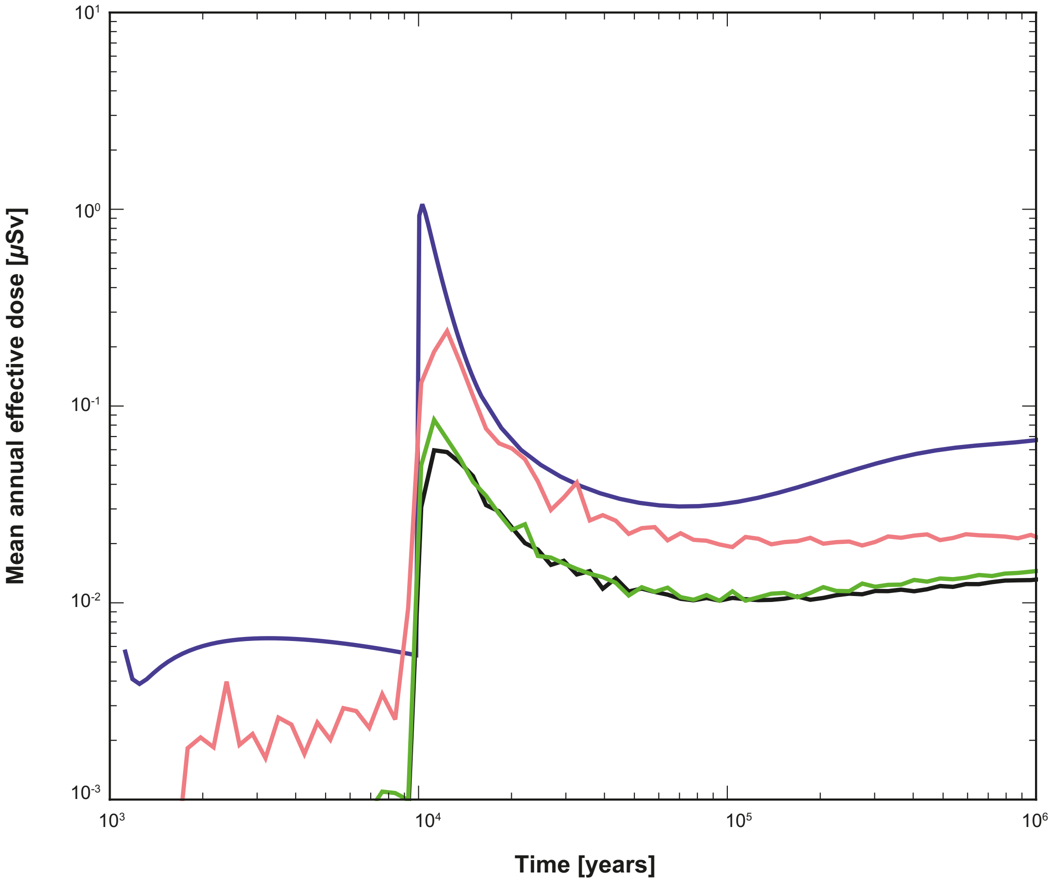

Figure 6-53. *Expected values for all-nuclides releases for the Q1 pinhole release, expressed as equivalent doses. The blue curve is near-field release and the other curves are far-field releases as follows: pink has no CPM segments in the pathway, green curve is the base case (CPM included but with no sorption), black has sorption in tunnels and soils.*

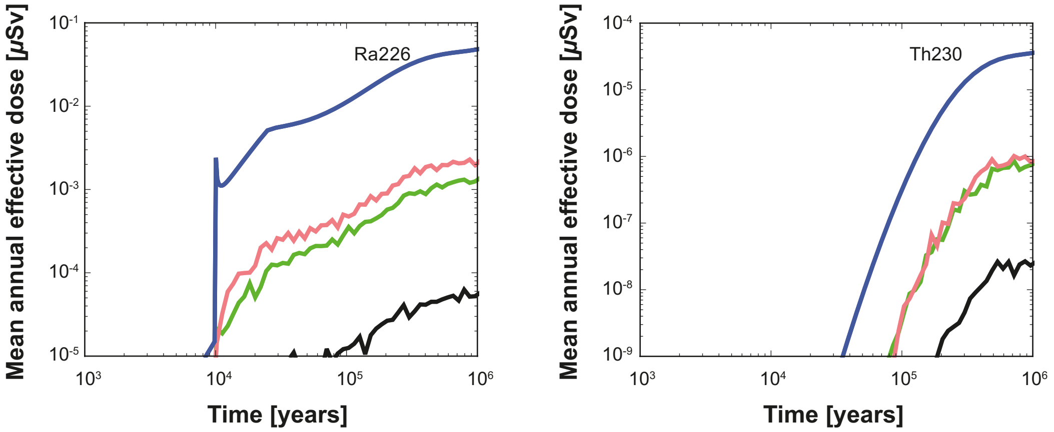

Figure 6-54. *Expected Ra-226 and Th-230 releases for pinhole Q1 release path and different assumptions about the role of tunnels and soils. The blue curve is near-field release and the other curves are far-field releases as follows: pink has no CPM segments in the pathway, green curve is the base case (CPM included but with no sorption), black has sorption in tunnels and soils.*

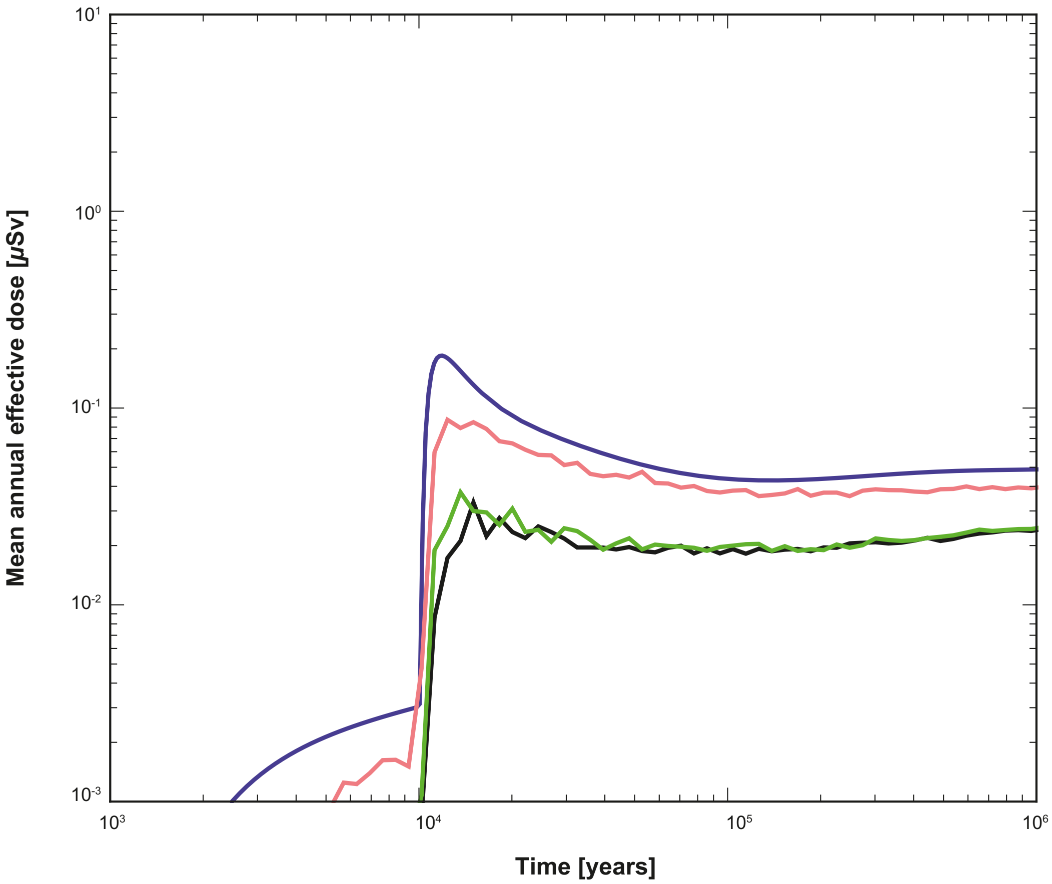

Figure 6-55. *Expected values for all-nuclides releases for the Q2 pinhole release, expressed as equivalent doses. The blue curve is near-field release and the other curves are far-field releases as follows: pink has no CPM segments in the pathway, green curve is the base case (CPM included but with no sorption), black has sorption in tunnels and soils.*

Crown space in tunnels

A variant flow model is considered in which tunnel backfill has compacted thus allowing a gap to form at the tunnel crown. Note that the tunnel crown case has different near-field releases as well as far-field releases, but the differences in near-field releases are small.

Results for the Q1 and Q3 release paths are shown in Figure 6-56 and Figure 6-57. In each figure, the green curve is the base case (i.e. no crown space). The black and pink curves have crown space. For the black curve, matrix diffusion into the neighbouring backfill is allowed. For the pink curve, this mitigating process is not active. Note that the differences between the crown space and no-crown space are not due to differences in the near-field releases; the base case has slightly higher near-field releases, but the differences are not large.

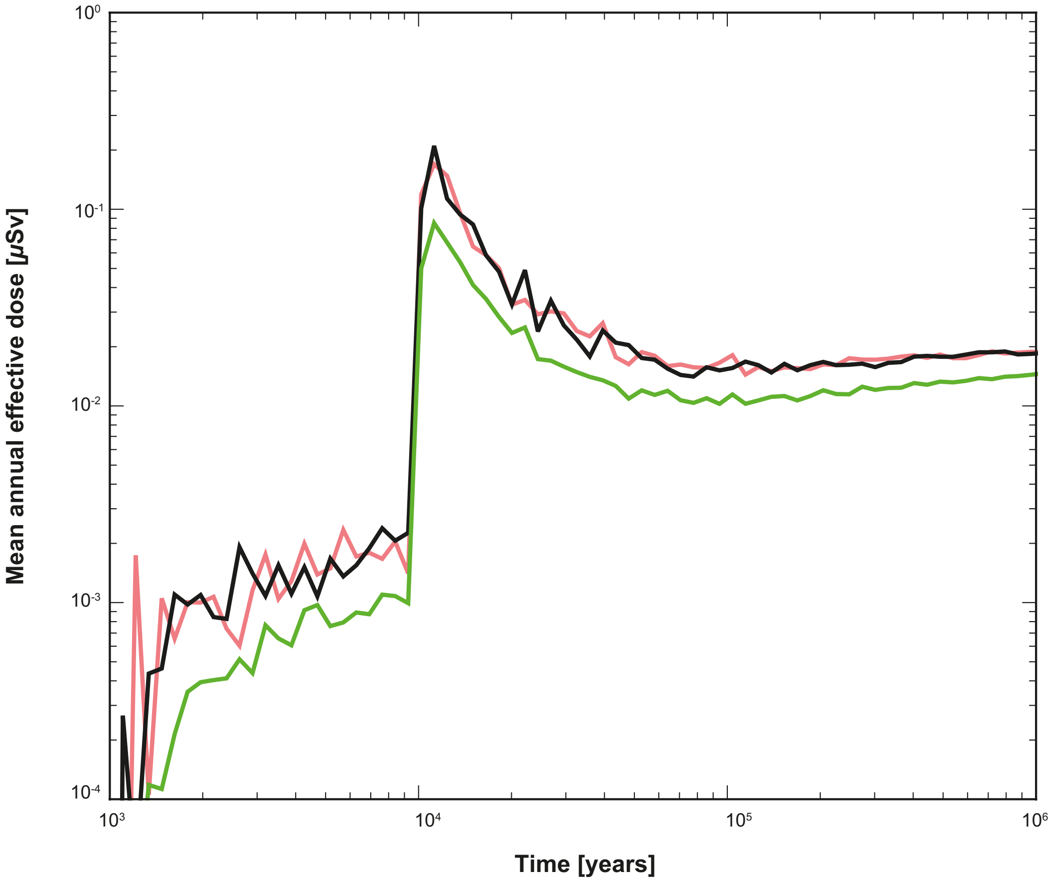

Figure 6-56. *Expected far-field release as equivalent dose for pinhole Q1 release path and different assumptions about the tunnel crown space. The green curve is the Q1 base case, which has no crown space represented. The black and pink curves are for cases with crown space with and without retention in the crown space.*

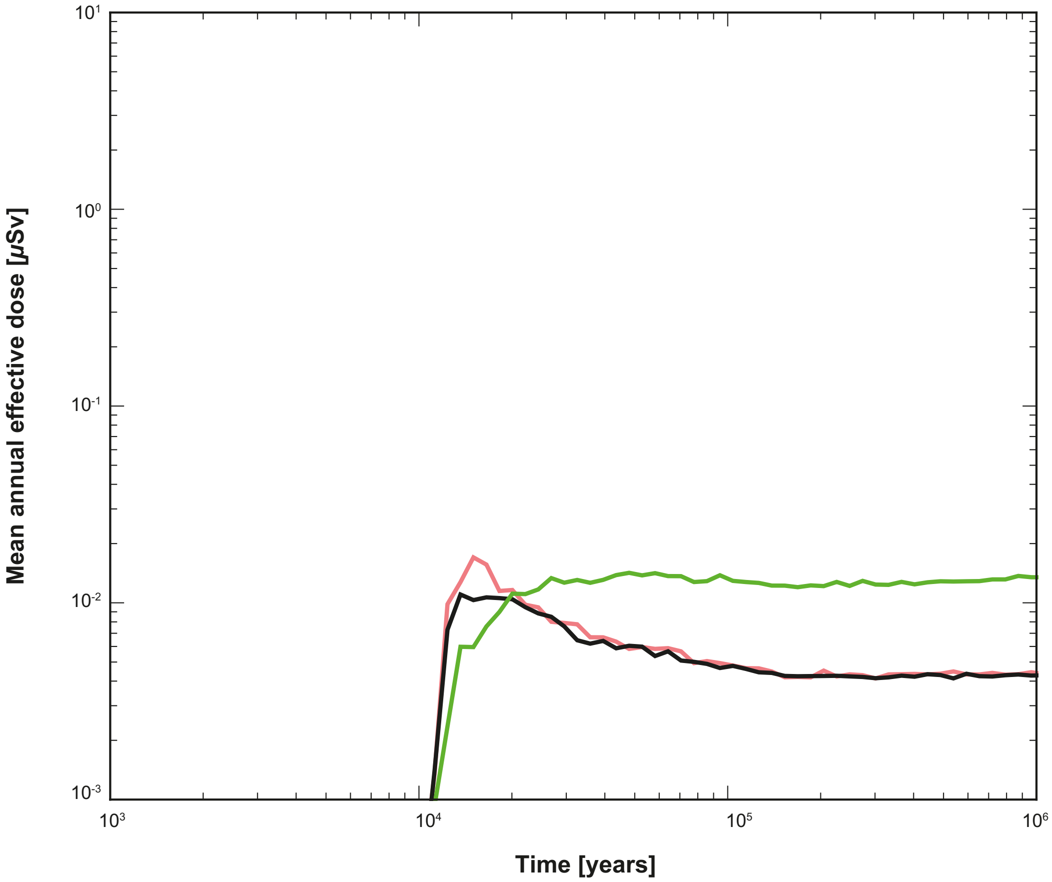

Figure 6-57. *Expected far-field release as equivalent dose for pinhole Q3 release path and different assumptions about the tunnel crown space. The green curve is the Q3 base case, which has no crown space represented. The black and pink curves are for cases with crown space with and without retention in the crown space.*

EDZ transmissivity

The base case has an excavation damage zone (EDZ) transmissivity of 10^{-8} m^2/s. The effects of different EDZ transmissivity for the Q1 release path are shown in Figure 6-58. The blue curve is the base case. The black curve is the case with no EDZ. The green and pink curves are results for EDZ transmissivity of 10^{-6} m^2/s and 10^{-7} m^2/s. The no-EDZ case is lower than the others. The presence of an EDZ increases the dose. Making the EDZ transmissivity larger than 10^{-8} m^2/s, however, does not further increase the dose. Instead, the dose drops slightly when going from an EDZ transmissivity of 10^{-7} m^2/s to 10^{-6} m^2/s, most likely because of subtle changes in flow paths. It is noted that the base case assumption for the uncertain EDZ transmissivity (10^{-8} m^2/s) results in the largest dose.

Effects of EDZ transmissivity on the Q2 releases are shown in Figure 6-59. Curves are coloured as in Figure 6-58. Note that the no-EDZ variant is not meaningful for the Q2 release path. Increasing the EDZ transmissivity above the base case value of 10^{-8} m^2/s does increase the dose somewhat, as expected. However, the effect is not large and quickly saturates; the doses for 10^{-7} m^2/s and of 10^{-6} m^2/s are not significantly different.

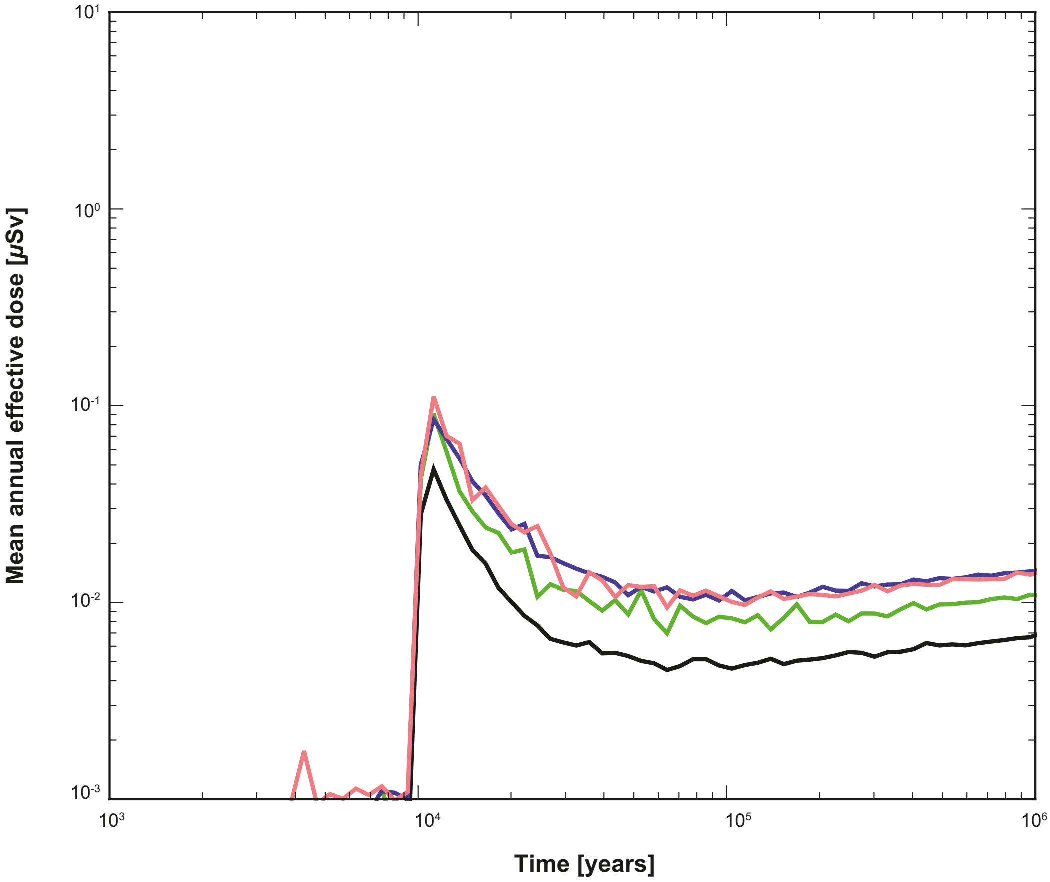

Figure 6-58. *Expected far-field release as equivalent dose for pinhole Q1 release path and different assumptions about the EDZ. The blue curve is the Q1 base case, which has EDZ transmissivity of 10^{-8} m^2/s. The black is the case for no EDZ. The green and pink curves are results for EDZ transmissivity of 10^{-6} m^2/s and 10^{-7} m^2/s, respectively.*

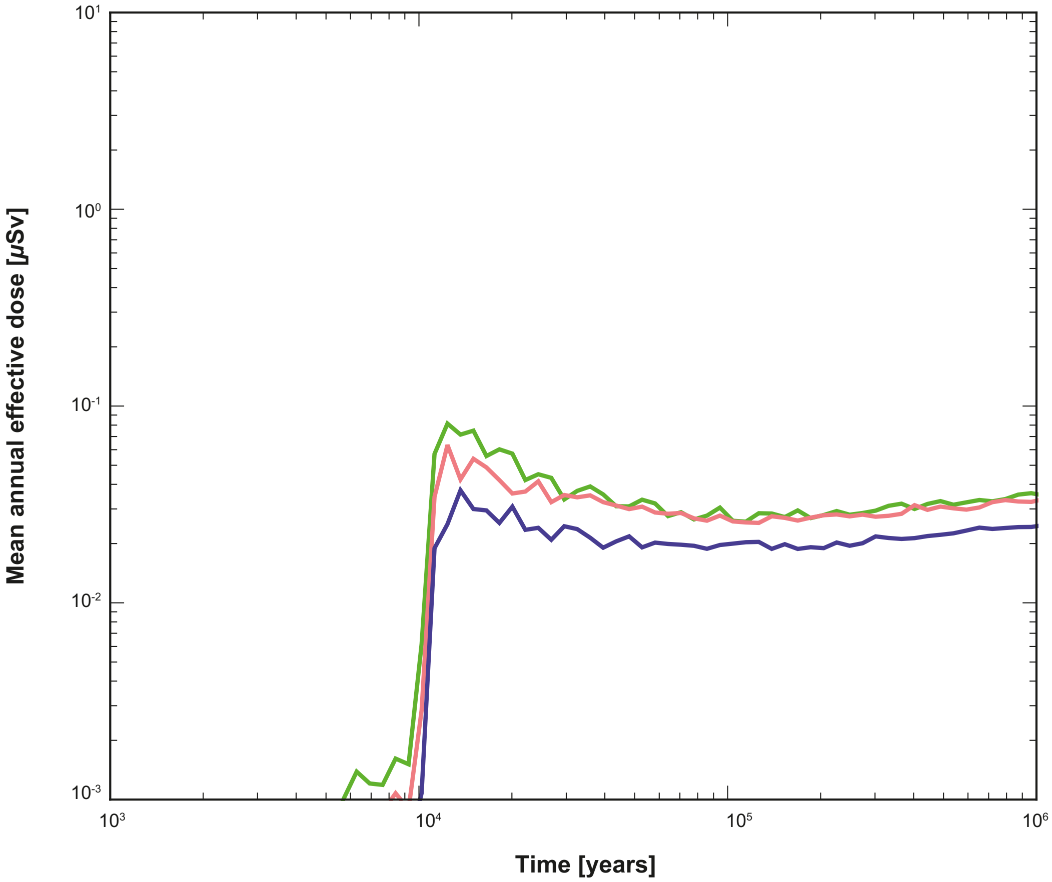

Figure 6-59. *Expected far-field release as equivalent dose for pinhole Q2 release path and different assumptions about the EDZ. The blue curve is the Q2 base case, which has EDZ transmissivity of 10^{-8} m²/s. The green and pink curves are results for EDZ transmissivity of 10^{-6} m²/s and 10^{-7} m²/s.*

6.4.5 Colloid-facilitated transport assuming irreversible sorption

As discussed in Section 4.5.6, sorption onto mobile bentonite colloids has the potential to increase the mobility of some radionuclides. Two limiting cases can be identified depending on the kinetics of desorption: (i) radionuclide desorption from colloids is rapid relative to the advective travel time, and (ii) radionuclide desorption from colloids is slow compared to the advective travel time and may thus be represented as irreversible. Sorption of radionuclides onto bentonite is understood to be reversible and rapid relative to the advective travel times of interest /**Buffer, backfill and closure process report**/; thus, irreversible sorption is not considered plausible. Nevertheless, consideration of irreversible sorption to bentonite colloids can help understand how the engineered and natural barriers function.

Several processes help mitigate the potential effects of irreversible sorption to colloids. These mitigating processes include permanent filtration of the colloids, colloid retardation, the fact that permanent sorption onto bentonite would dramatically reduce near-field release, and limited availability of sorption sites on bentonite colloids. The last process is considered and other mitigating processes neglected. The competitive Langmuir-type sorption model described in Appendix I.2 is used. In this model, radionuclides releases from the COMP23 code are partitioned between colloids and solution, taking into account competition for the limited number of available sites on colloids. Once partitioned, MARFA is used to transport colloid-associated radionuclides without retention processes. Radionuclides in solution are transported as in the reference case described in Section 6.4.2.

Dose-equivalent near-field releases based on the colloid-partitioning model are shown in Figure 6-60 for the pinhole reference case, Q1 release path. In this calculation, actinide species and transition metals were assumed to sorb irreversibly onto colloids that are present at a concentration of 10 mg/l. The blue curve is dose equivalent near-field release for all radionuclides. The solid green curve is release for all actinides and transition metals including both the dissolved and colloid-associated mass. The green dashed curve is the colloid-associated component. The actinide and transition metal portions of the total release are an order of magnitude smaller than the total release in the time period 20,000 to 50,000 years, and is even smaller before and after that time period. Moreover, when the actinide/transition metal release is largest, the availability of sites limits the colloid-associated release to even smaller fractions of the total release, mostly because Ni-59 and Nb-94 releases are large enough to saturate sorption sites. At late times, site limitations are less important, but the total actinide/transition metal release is small and not a significant contribution to the total.

Far-field effective doses for the same cases with and without colloids are shown in Figure 6-61. At its largest, the colloid-associated far-field release is approximately 1% of the total release.

Results in Figure 6-60 and Figure 6-61 are based on a colloid concentration of 10 mg/l. Although this number is representative of clay colloid concentrations in waters that are not highly dilute, it is an uncertain parameter. As discussed in Section 4.5.8, colloid concentrations may be higher during brief periods if dilute water reaches the repository horizon. An upper bound on colloid-facilitated transport for this situation can be established by allowing all actinides and transition metals to be transported unretarded through the geosphere. This modelling case assumes that colloids are transported unretarded through the geosphere, an unlimited supply of sorption sites on colloids, and no desorption from colloids. Even with this extreme bounding approximation, colloids have no significant effect on the all-nuclides dose (Figure 6-62). This lack of sensitivity is a consequence of the dominant role that the three nuclides I-129, C-14, and Ra-226 play in controlling the overall dose. I-129 and C-14 are already transported without sorbing in the MARFA far-field calculation, and their transport thus cannot be enhanced by colloids. Ra-226 sorbs by ion exchange, and is not expected to irreversibly sorb.

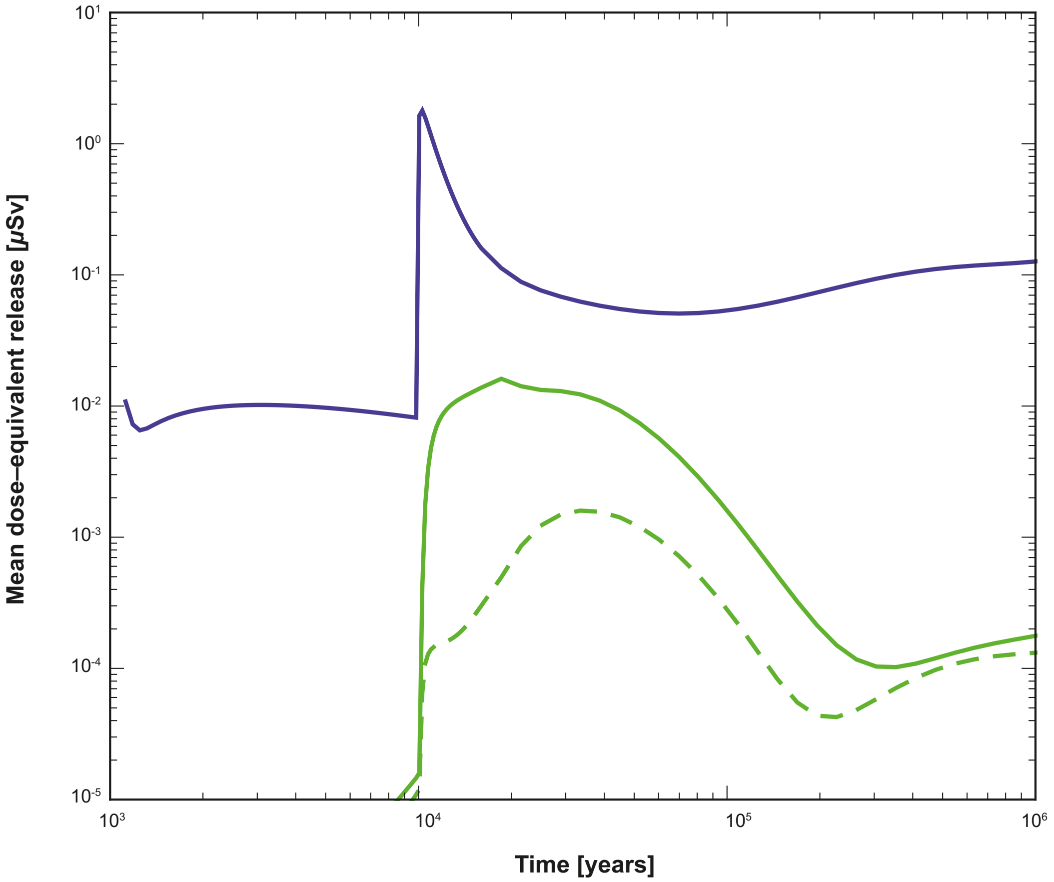

Figure 6-60. *Mean dose-equivalent near-field release for pinhole Q1 release path with irreversible sorption to colloids. The blue curve is total release, the solid green curve is the actinide and transition metal portion including the colloidal-associated and dissolved component, and the dashed green curve is the colloid-associated release of actinides and transition metals.*

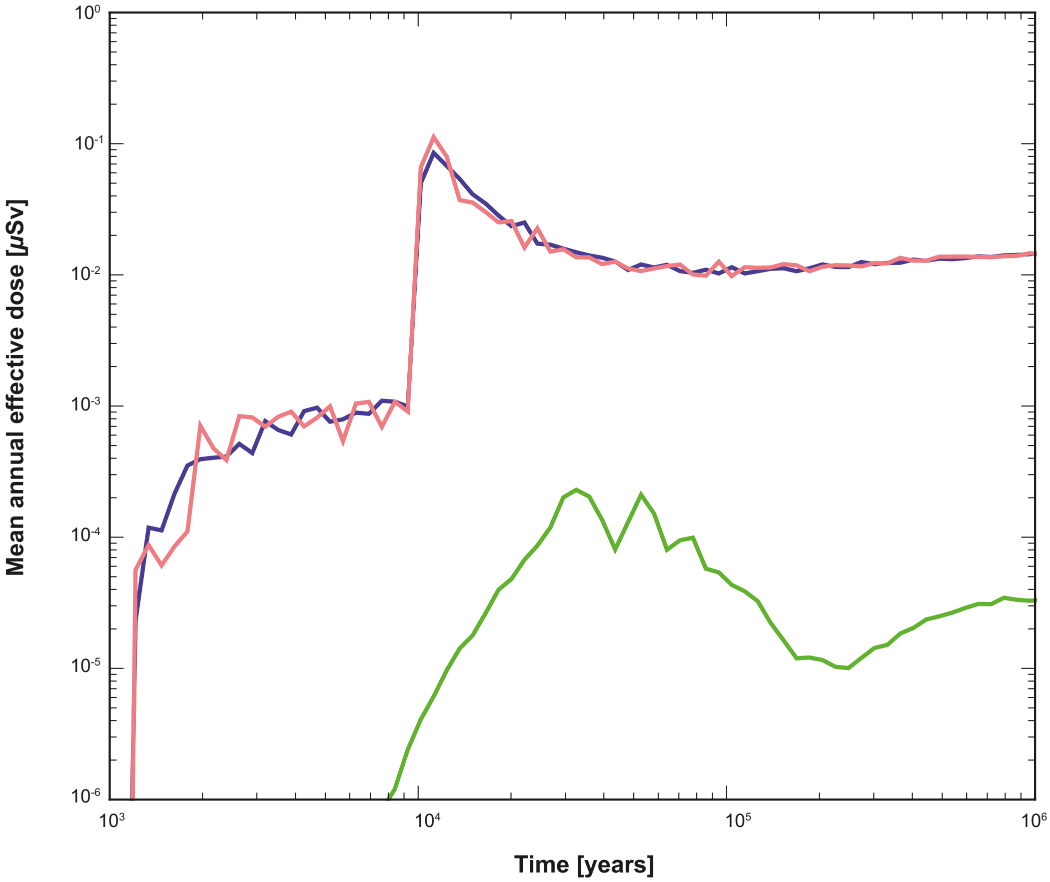

Figure 6-61. *Mean far-field effective dose for pinhole Q1 release path with and without irreversible sorption to colloids. The blue curve is total (all-nuclides) dose without colloids, while the pink curve is total dose with irreversible sorption to colloids at a concentration of 10 mg/l. The green curve is the dose due to the colloid-associated component.*

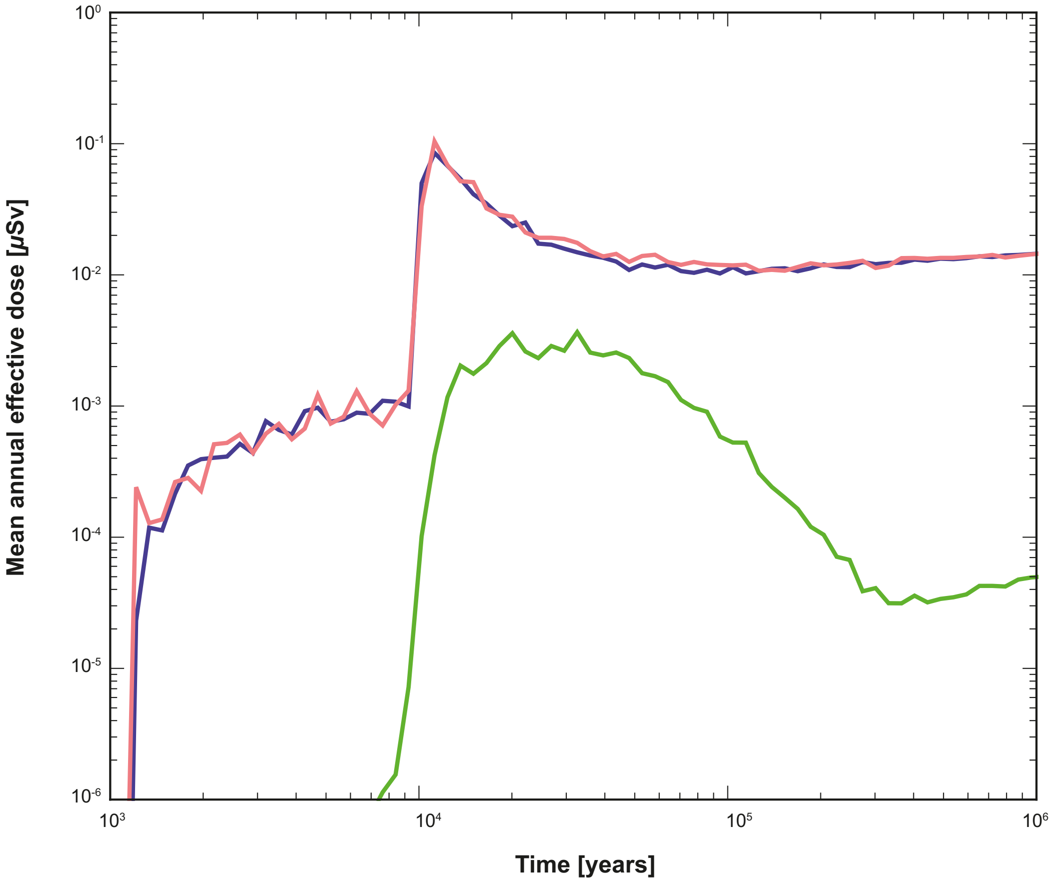

Figure 6-62. *Mean far-field effective dose for pinhole Q1 release path with irreversible sorption to colloids assuming unlimited sorption sites on colloids. The blue curve is total (all-nuclides) dose without colloids, while the pink curve is total dose with irreversible sorption to colloids. The green curve is the dose due to the colloid-associated component.*

6.5 Additional cases to illustrate barrier function

Some conclusions regarding loss of barrier functions can be drawn from the analyses already presented. In order to provide a fuller treatment, the following cases of barrier deficiencies are postulated:

A. An initial absence of enough buffer to cause advective conditions in the deposition hole for all deposition holes.

B. An initial pinhole in the copper shell for all canisters.

C. An initial, large opening in the copper shell and in the cast iron insert for all canisters.

D. A combination of cases A and C, i.e. an initial large opening in all canisters and advective conditions due to loss of buffer for all deposition holes.

E. A combination of case C with an assumption of fast fuel dissolution and fast corrosion of metal parts. An initial, large opening in every canister is combined with the assumption of complete fuel dissolution and metal corrosion in only 100 years.

A loss of the radionuclide retention capability of the rock is combined with each of the five cases, yielding a total of ten release situations. The cases without geosphere retention are denoted A* through E*.

In all cases it is assumed that the backfill and closure are installed and perform as expected. Also, all aspects of the rock other than those related to retention, e.g. the near-field groundwater flow, which is generally low and with only about one sixth of the deposition holes connected to water conducting fractures, as well as the stable and favourable groundwater composition in the near field, are assumed to be present. Elemental solubilities are imposed on concentrations of radionuclides in the canister void volume only if the buffer is in place.

Table 6-2 gives an overview of the status of the retardation related safety functions.

The transport and dose calculations are probabilistic, since it is desirable to take into account both uncertainties due to lack-of-knowledge in general and the spatial variability of the properties of the deposition holes and their associated transport paths in the geosphere. The semi-correlated hydrogeological DFN model is used for these stylised calculations. Except for the case specific assumptions regarding failed barrier functions, all transport data are taken from the **Data report**. This applies to e.g. corrosion rates, fuel dissolution rate, sorption and diffusion data and LDF values.

Table 6-2. Status of safety functions for the ten release situations. In cases denoted with an asterisk also geosphere retention is absent.

Green: Safety function intact
Yellow: Safety function deteriorates over time
Red: Safety function absent initially

	A. Buffer missing	A*	B. Pinhole damage	B*	C. Large canister defect	C*	D. Large canister defect and buffer missing	D*	E. Large canister defect, rapid fuel and metal conversion	E*
Limited fuel dissolution rate	🟩	🟩	🟩	🟩	🟩	🟩	🟩	🟩	🟥	🟥
Limited corrosion rate of metal parts	🟩	🟩	🟩	🟩	🟩	🟩	🟩	🟩	🟥	🟥
Limited solubilities	🟨	🟨	🟩	🟩	🟩	🟩	🟥	🟥	🟩	🟩
High transport resistance in canister/buffer interface	🟨	🟨	🟨	🟨	🟥	🟥	🟥	🟥	🟥	🟥
Retardation in buffer	🟥	🟥	🟩	🟩	🟩	🟩	🟥	🟥	🟩	🟩
High transport resistance in buffer/rock interface[1]	🟥	🟥	🟩	🟩	🟩	🟩	🟥	🟥	🟩	🟩
Geosphere retention	🟩	🟥	🟩	🟥	🟩	🟥	🟩	🟥	🟩	🟥

[1] When this safety function is present, spalling is still pessimistically assumed in all deposition holes. When this safety function is not present, i.e. when the buffer is missing, the groundwater turnover in the deposition hole is still limited by the hydraulic properties of the rock.

The biosphere is here represented by the constant LDF values obtained when the release is distributed in the landscape according to the time dependent distribution of release locations from the repository during an interglacial. Furthermore, since the LDF values are suited primarily to handle releases that are constant over periods of time that are comparable to the duration of an interglacial, i.e. typically 10,000 years, the releases for these cases are, as a variant, also evaluated with fully time dependent modelling of the biosphere. Here, the releases are distributed in the landscape and the time dependent doses are presented, rather than a time dependent release converted to dose by a constant LDF value.

In the following, each case is discussed briefly using distributed, constant LDFs. The section is concluded with summarising accounts of all cases both with LDFs and with time dependent modelling of the biosphere.

Cases A and A, initial absence of buffer*

A 0.5 m high section of the bentonite buffer is assumed to be missing, leaving a void in the form of a hollow cylinder between the canister and the wall of the deposition hole. The Q1 fracture, if it exists, intersects the deposition hole at the location of the void. The deposition hole is otherwise filled with buffer and the deposition tunnel backfill is assumed to be intact. For most of the deposition holes, the groundwater flow and sulphide concentrations are not sufficient to cause canister failure during the one million year assessment period. The corrosion calculation takes both the natural variability of flow rates for the ensemble of 6,000 deposition holes and the distribution of sulphide concentrations in the groundwater into account. This yields a calculated mean number of failed canisters of 0.17 at one million years, used also here. Only the deposition holes with the highest flow rates in the Q1 fracture contribute. This also means that releases to Q2 and Q3 release paths are negligible for these positions.

Radionuclide transport in the near field and far field is modelled as the semi-correlated case with initial advection, see Section 4.5.9. The consequences are similar to those shown in Figure 4-30 and Figure 4-31. The only differences is that the distributed LDF values are applied and the results are shown in Figure 6-69. Many of the radionuclides have decayed to insignificance when the first failures occur after close to 50,000 years. Near-field release equivalent doses are dominated by Nb-94 from metal parts of the fuel and Ra-226, Pb-210 and Np-237 from the fuel matrix. Far-field doses are dominated by Nb-94, Ra-226, Se-79 and I-129.

Cases B and B, initial, penetrating pinhole defect in all canisters*

The canister defects are assumed to be the same as the growing pinhole failure. Near-field and far-field radionuclide transport is modelled as the probabilistic calculation of the hypothetical pinhole failure mode including the effect of spalling, see Section 6.3.1, but with growing holes in all canisters. The deposition hole buffer and the deposition tunnel backfill are assumed to be intact. The dose consequences in the biosphere are calculated with the distributed LDF values since this is a more realistic approach when releases occur from all over the repository.

The consequences are similar to those in the pinhole scenario, see Figure 6-15 and Figure 6-17 for the near field and the far field, respectively. The only difference is that all canisters are now assumed to have defects, meaning that the probabilistic single-canister results should be multiplied by 6,000 and that the distributed LDF values are applied, leading to a reduction of the consequences by typically one order of magnitude. The far-field results with all 6,000 canisters are shown in the summary Figure 6-69 later in this section.

Cases C and C, initial, large opening in all canisters*

The canister defects are assumed to be in the form of a large opening in the copper shell and the cast iron insert. The deposition hole buffer and the deposition tunnel backfill are assumed to be intact.

In the reference evolution, some of the deposition holes are affected by buffer erosion to the extent that advective conditions occur in the hole. For the stylised case considered here, no such erosion is, however, assumed, in order to more clearly demonstrate the role of the canister if all other barriers are intact. Combinations of canister and buffer defects are analysed in one of the cases described below.

The calculation case is similar to the failure due to isostatic load, see Section 6.2. Near-field and far-field radionuclide transport is modelled as a probabilistic calculation case where the failure is postulated at 100 years for all canisters.

The dose equivalent release from the near field is shown in Figure 6-63. The dose is dominated the initial 10,000 years by C-14, Cs-137, Sr-90, Ag-108m, I-129 and Se-79. After about 10,000 years Se-79, C-14, Ra-226 and I-129 contribute most to the total dose. Releases of nuclides that sorb strongly in the buffer, e.g. Pu-238 and Pu-239, are strongly reduced compared to case D* below where the buffer is also assumed to be missing. There is a considerable reduction also of the release of Cs-137, Sr-90 and Ag-108m compared to the case in which the buffer is missing.

The dose from the far-field release is shown in Figure 6-64. The peak total dose is reduced by less than an order of magnitude compared to the near-field release, whereas doses from many of the short-lived or sorbing nuclides are considerably reduced.

It is noteworthy that this completely unrealistic case of initial loss of containment function for all canisters in the repository yields far-field releases, converted to doses, which never exceed the background radiation. However, the containment function is required for a majority of the canisters in order to fulfil the regulatory requirement on risk at Forsmark.

The long-term release rate of I-129 equals, to a good approximation, the release rate of this nuclide from the fuel matrix. This is caused by the assumed absence of sorption and long half-life of I-129. Regarding the calculated dose from I-129 for this and other hypothetical cases in this section, it is noted that the mitigating effect of mixing of I-129 with naturally occurring stable iodine is disregarded in the biosphere models.

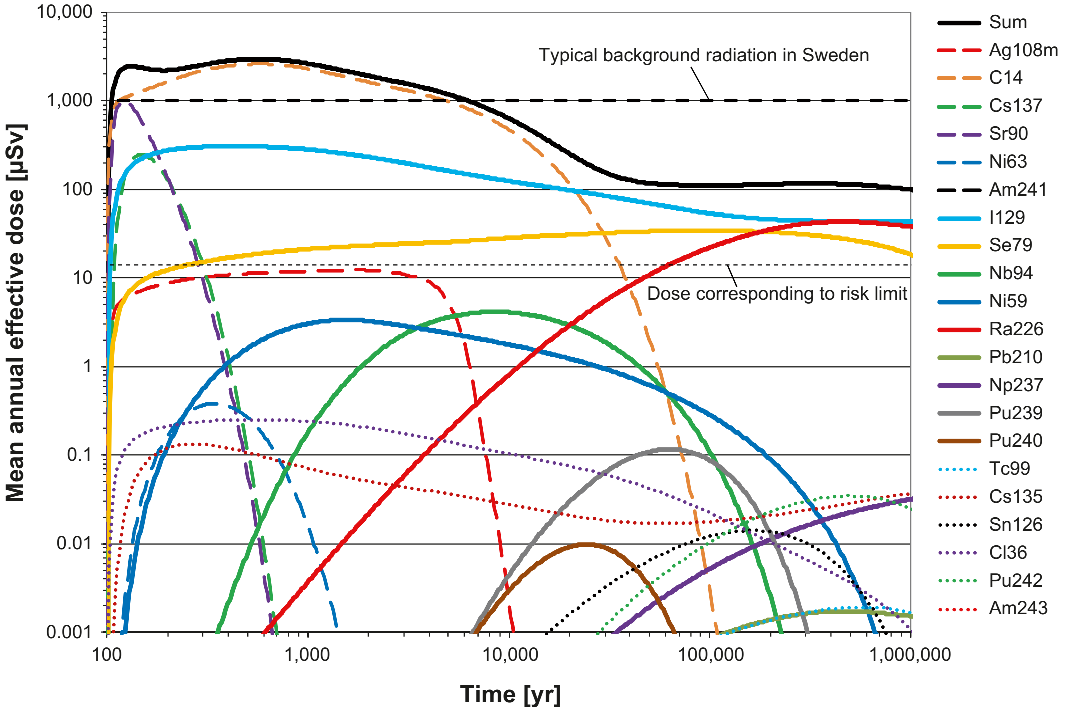

***Figure 6-63.** Near-field dose equivalent release for case C*, i.e. all canisters have an initial large defect and the buffer is intact.*

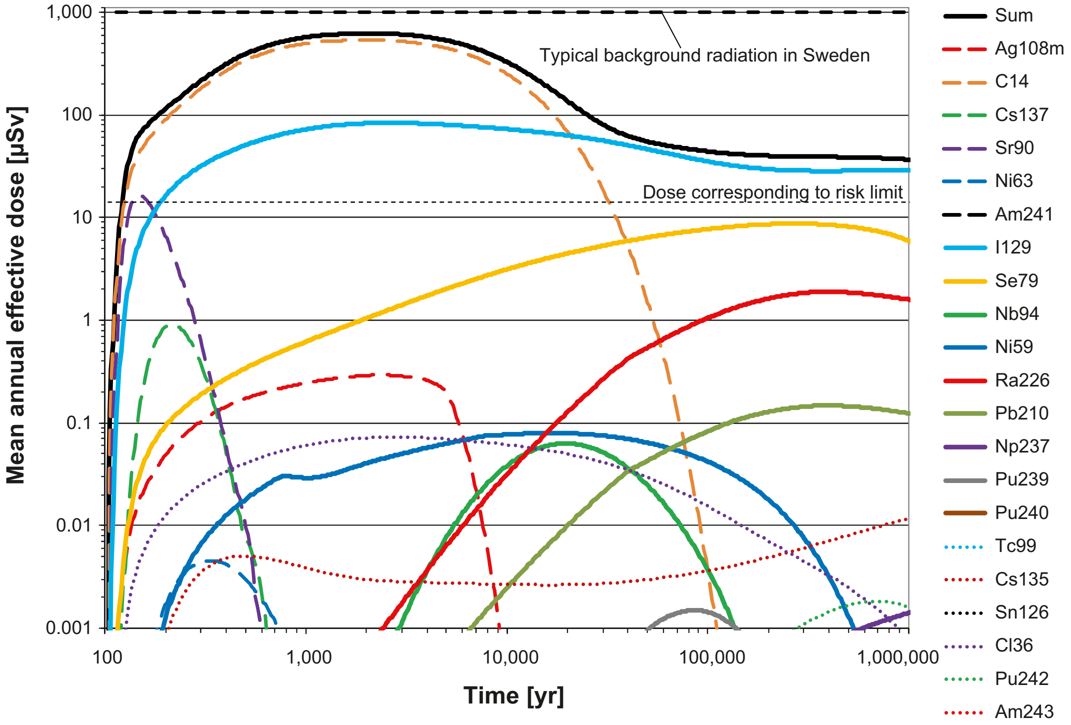

***Figure 6-64.** Far-field dose for case C, i.e. all canisters have an initial large defect and the buffer is intact.*

Cases D and D, initial large opening in all canisters and advective conditions due to loss of buffer for all deposition holes*

The defects are assumed to be the same as those modelled in the corrosion scenario, i.e. a large opening in the copper shell and the cast iron insert and a section of the bentonite buffer is missing where the canister is damaged, leaving a void between the canister and the wall of the deposition hole in the form of a hollow cylinder. The deposition hole is otherwise filled with buffer and the deposition tunnel backfill is assumed to be intact. This means that releases occur predominantly to the Q1 fracture, if it exists. Near-field and far-field radionuclide transport is modelled as a corrosion case where all canisters fail after 100 years.

Only the Q1 release path is evaluated in detail, since releases from Q1 will dominate in this situation. In the base case realisation of the semi-correlated hydrogeological DFN model used, 1,169 out of the 6,000 deposition holes have a Q1 fracture. This means that virtually all radionuclides will leave through Q1 from these deposition holes. The analysis is, for technical reasons, limited to the 1,000 deposition holes with the lowest F values and hence lowest geosphere retention. For the remaining 5,000 deposition holes, Q2 and Q3 releases need to be considered. The analysis of the isostatic load scenario shows i) that the Q1 release path dominates the initial approximately 10,000 years even with the buffer in place, ii) that I-129 dominates the total release after approximately 10,000 years and iii) that the retention of I-129 is close to zero. Therefore, the calculated release of I-129 from the 1,000 deposition holes with a Q1 path is multiplied by 6 to approximately account for releases through Q2 and Q3 from the remaining deposition holes.

The dose equivalent release from the near field is shown in Figure 6-65. The dose is dominated the initial 10,000 years by the IRF and/or CRF of Ag-108m, Cs-137, Sr-90, C-14 and Nb-94. Note that only the generally low flow rates at Forsmark limits the releases for the IRF/CRF. After about 10,000 years Nb-94, Pu-239, Pu-240, Np-237, Ra-226, Pb-210 and I-129 contribute most to the total dose.

The dose from the far-field release is shown in Figure 6-66. The total dose is reduced by about a factor of 10 compared to the near-field release. For the earliest releases this is an effect of the travel time in the geosphere. In the long term, strongly sorbing nuclides like Pu-239 and Pu-240 are retained in the geosphere. It is noteworthy that this completely unrealistic case of initial absence of all transport limitations in the engineered parts of the repository yields far-field releases, converted to doses, that exceed the background radiation by a factor of about five initially and that in the long term are less than a factor of ten above the risk limit.

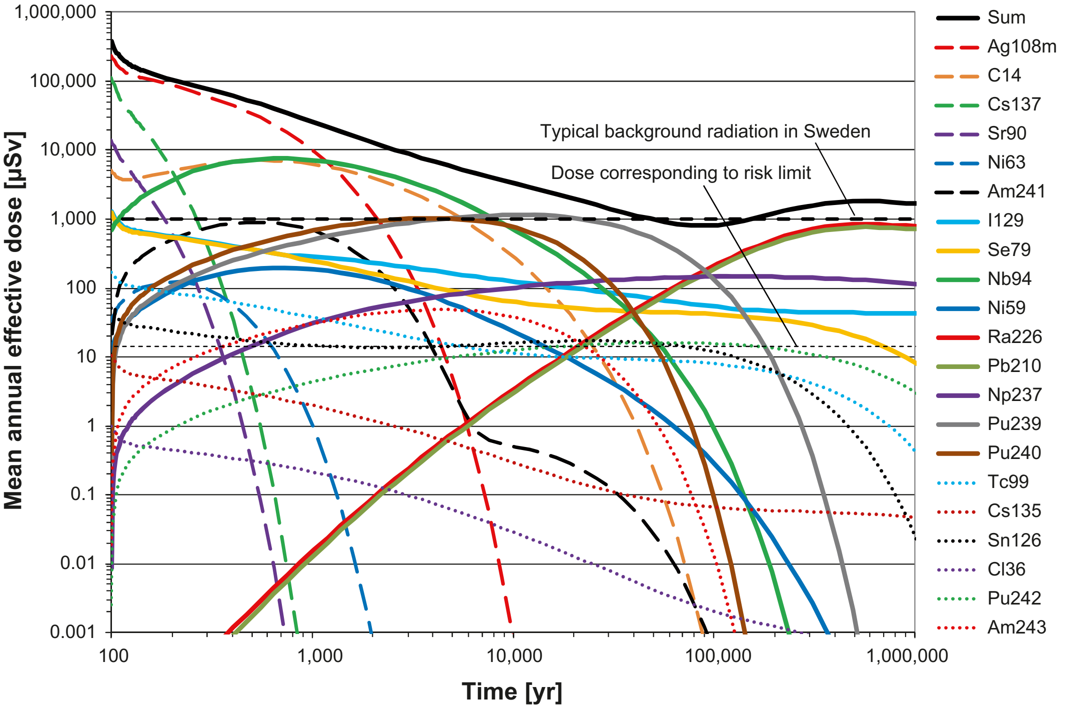

Figure 6-65. *Near-field dose equivalent release for case D*, i.e. all canisters have an initial large defect and the buffer is missing between the defect in the canister and the wall of the deposition hole.*

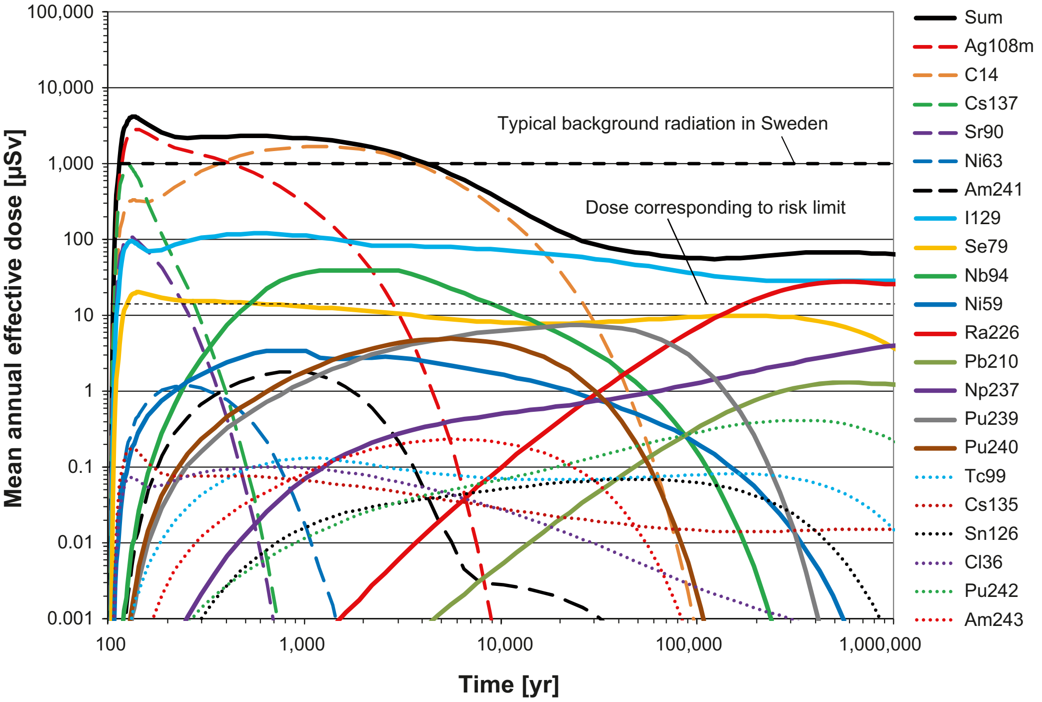

Figure 6-66. *Far-field dose for case D, i.e. all canisters have an initial large defect and the buffer is missing between the defect in the canister and the wall of the deposition hole.*

Cases E and E, initial, large opening in all canisters and rapid fuel dissolution and metal corrosion*

These cases are identical to cases C and C*, (all canisters have a large opening in the copper shell and the cast iron insert), except that for cases E and E* complete fuel dissolution and metal corrosion is assumed to occur in 100 years after water contacts the fuel. The containment function of not only the canister but also of the fuel matrix and the structural parts of the fuel is thus assumed to be absent. The deposition hole buffer and the deposition tunnel backfill are assumed to be intact.

The near-field and far-field developments for these cases are identical to those for cases C and C* with the exception of the fast conversion of the fuel and metal corrosion.

The dose equivalent release from the near field is shown in Figure 6-67. The dose is dominated by C-14, Cs-137, Sr-90 and I-129 for more than 10,000 years. In the longer term, Ra-226 and Se-79 together with I-129 contribute most to the total dose. Note that the release of Ag-108m is identical to that in case C* since this release is controlled by the solubility of Ag and not by corrosion in the model. The early releases of Sr-90, Cs-137 and I-129 have increased in inversed relation to the IRF values for these nuclides; cases E and E* are similar to assuming 100% IRF for all nuclides. The decrease of I-129 at very long times is caused by depletion of I-129 from the repository and the host rock through outward transport and not through decay.

The dose from the far field release is shown in Figure 6-68. The peak total dose is reduced by more than an order of magnitude compared to the near field release, whereas doses from many of the short-lived or sorbing nuclides are considerably reduced.

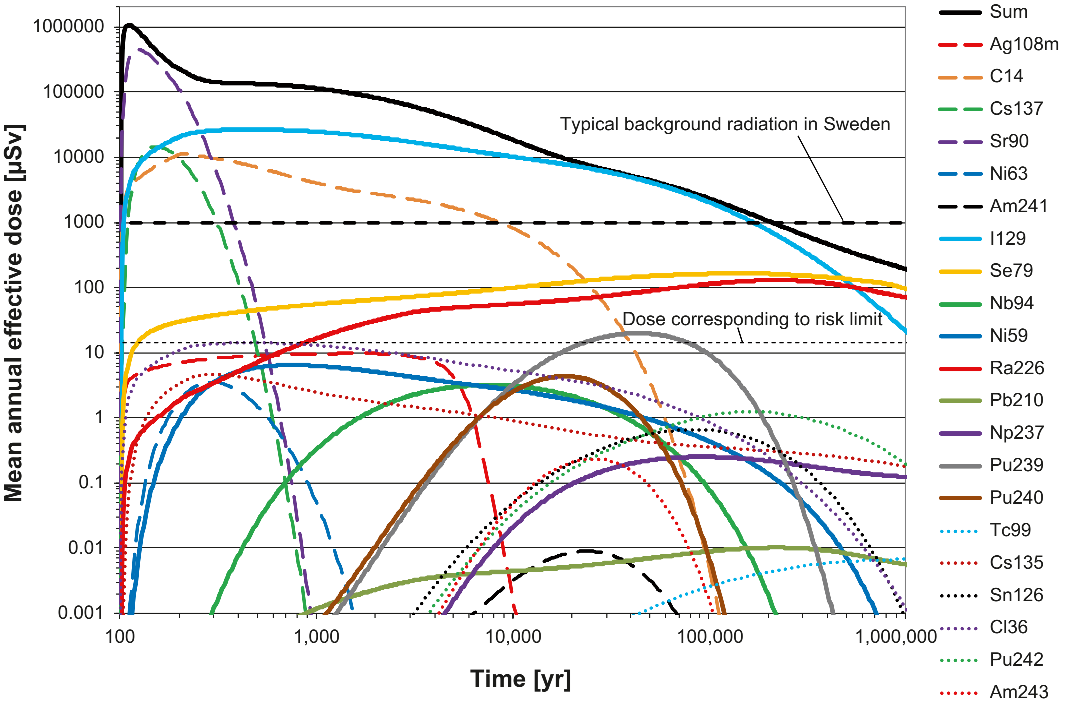

Figure 6-67. *Near-field dose equivalent release for case E*, i.e. all canisters have an initial large defect in combination with a rapid fuel and metal conversion and the buffer is intact.*

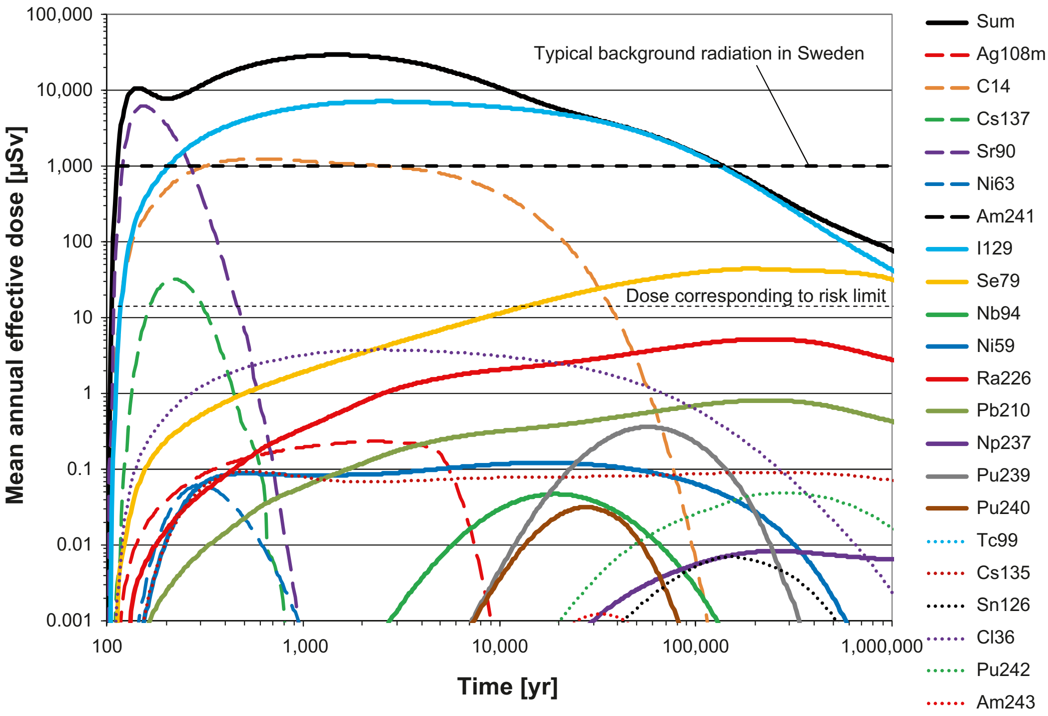

Figure 6-68. *Far-field dose for case E, i.e. all canisters have an initial large defect in combination with a rapid fuel and metal conversion and the buffer is intact.*

Summary of results with distributed LDF values

The summed dose for each case discussed above is given in Figure 6-69.

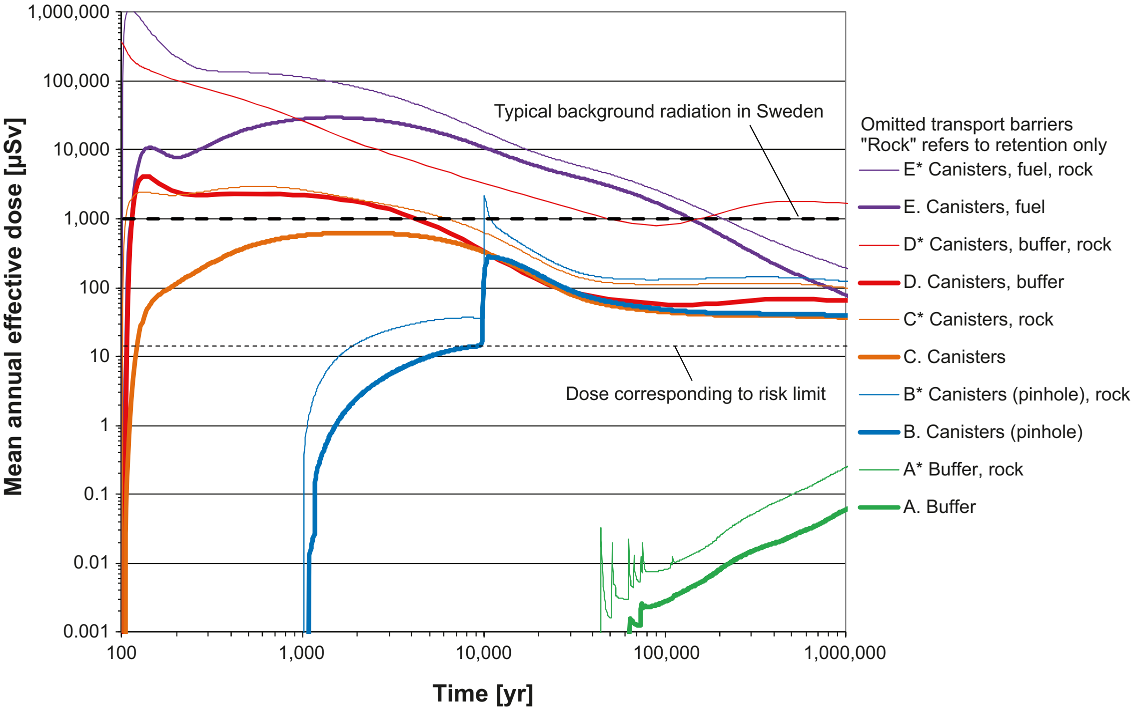

Figure 6-69. *Results of stylised cases to illustrate loss of barrier functions. Note that an omission of the "rock" barrier in these cases refers to omission of retention of radionuclides in the rock fractures only, whereas the favourable, low flow rate at repository depth and the favourable geochemical conditions are still taken into account.*

The following are noted.

After about 10,000 years, the doses for all cases are below the dose caused by typical background radiation in Sweden, except for the case in which retention properties of canisters, buffer and rock are all disregarded (case D*) and those with rapid fuel dissolution in combination with failed canisters (cases E and E*). The low flow and favourable groundwater chemistry of the rock and the presence of backfill and closure of the repository tunnel thus provide substantial protection from a fuel with unaltered dissolution rate.

If all canisters have large defects initially, but the barrier system is otherwise intact, case C, the peak annual dose to the most exposed individuals in the landscape does not exceed that caused by typical background radiation in Sweden, i.e. 1 mSv. Beyond 10,000 years this annual dose is less than an order of magnitude above the risk limit of 0.014 mSv.

If all canisters have large defects initially, and if also the buffer is assumed to be missing between the canister damage and the wall of the deposition hole, case D, the dose is around ten times the background radiation for the first few hundred years, but is after 1,000 years quite similar to the case where the buffer is in place, case C. This suggests that the buffer is, from the point of view of total dose, not important as a retention barrier in this time perspective. However, a comparison between Figure 6-64 and Figure 6-63 shows that the buffer has a considerable impact on near-field releases of many sorbing nuclides that do not dominate the dose.

With a large degree of damage to the canisters, the buffer missing and retention in the rock disregarded (case D*), the calculation results suggest annual doses in the Sievert range in the initial 1,000 years. This is a demonstration of the necessity of properly protecting man and the environment from the spent nuclear fuel, in particular in the 1,000 year time frame. It is noted that a more realistic treatment of corrosion of the AgInCd alloy of the PWR control rods would likely reduce the total dose, dominated by Ag-108m, by at least a factor of 10 the first 100 years and more between 100 and 1,000 years.

Beyond 10,000 years, the total dose is comparable to that caused by the background radiation even when neglecting the retention properties of all three barriers, case D*.

As expected, the cases with initial pinhole defects, case B, and those with large initial defects, case C, are quite similar beyond 10,000 years, when the pinhole defects are assumed to have grown into large defects. It is also noted that neglect of rock retention does not affect the total dose much for these cases after about 1,000 years. However, a comparison between Figure 6-66 and Figure 6-64 shows that the rock has a considerable impact on far-field releases of many sorbing nuclides that do not dominate the dose.

A comparison of cases C and E shows the considerable containment function of the waste form for more than 100,000 years.

Summary of results with time dependent modelling of the biosphere

As mentioned in the introduction, the LDF values are suited primarily to handle releases that are constant over periods of time that are comparable to the duration of an interglacial, i.e. typically 10,000 years. Therefore, the releases for most of the above cases were also evaluated with a fully time dependent modelling of the biosphere. Here, the releases are distributed in the landscape according to the time dependent spatial distribution of release points from the repository and the time dependent doses are presented, rather than a time dependent release converted to dose by a constant LDF value. This modelling was for assumed temperate conditions over a period of 60,000 years. The results are given in Figure 6-70. The solid curves are doses obtained with distributed LDF values (i.e. the same curves as in Figure 6-69) and the dashed curves are the corresponding doses obtained with time dependent modelling of the biosphere.

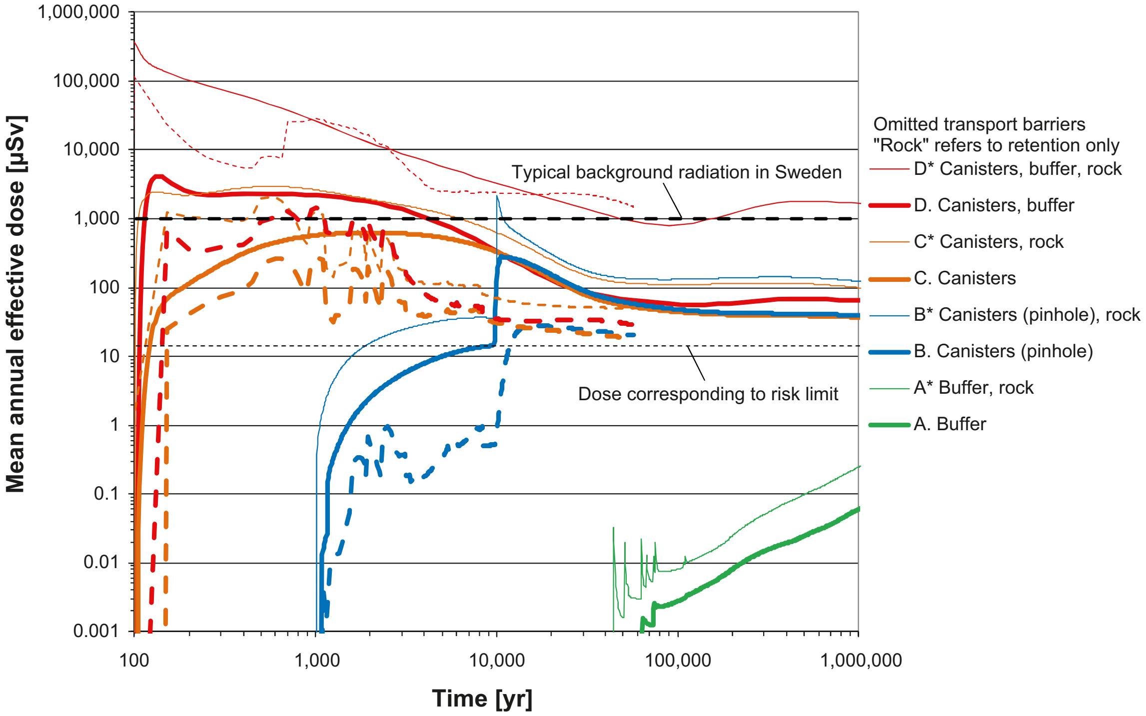

Figure 6-70. *Results of stylised cases to illustrate loss of barrier functions. Solid lines: Same as in Figure 6-69 (dose conversion through distributed LDF). Dashed lines: Corresponding cases with time dependent modelling of the biospehere.*

The results from time dependent modelling of the biosphere (dashed curves) are generally within an order of magnitude of, but below, the curves obtained with distributed LDF values. The one exception is the case where the retention properties of the canister, buffer and rock are all disregarded (case D*). In that case, the time dependent doses from Ag-108m around 1,000 years and from C-14 around 20,000 years exceed those obtained using the LDF. This exceedance is caused by accumulation and delay effects in the biosphere. The release of Ag-108m from the near field decreases rapidly over the initial hundreds of years and hence so does the release multiplied by the LDF value. In the time dependent case, some Ag-108m is accumulated in the landscape and this, in combination with the development of landscape objects, leads to a delayed release and hence dose that exceeds the dose obtained with the LDF values.

7 Summary and conclusions

Table 7-1 shows a summary of near-field and far-field maximum dose-equivalent releases for probabilistic numerical calculation cases discussed in this report. Contributions from the IRF are not included in the table. The maximum doses do not appear at the same time in all cases. In the corrosion cases and shear load cases the maximum normally appears at one million years while pinhole cases and isostatic load cases in general have their maximum shortly after the large failure in the canister is postulated.

For all probabilistic cases considered, the maximum over the one million year assessment time of the mean total far-field effective dose is smaller than the dose corresponding to the risk limit. Excluding hypothetical cases (e.g. growing pinhole and postulated failure at 100,000 years due to shear load) and the cases supporting the discussion of best available technique, the far-field effective dose is at least one order of magnitude smaller than the dose corresponding to the risk limit. The two scenarios contributing to the calculated risk, i.e. failure of the copper canister by corrosion and earthquake-induced shear failure of the copper canister, the peak of the mean annual effective dose is estimated to be 0.18 μSv/yr and 0.15 μSv/yr, respectively. These doses, which assume reference conditions, could be compared with the dose corresponding to the risk limit of 14 μSv/yr and the dose corresponding to typical background radiation of approximately 1,000 μSv/yr. Further discussion of dose estimates associated with these and other scenarios and results of risk summation can be found in the **Main report**.

In the scenario of failure of the copper canister due to corrosion, the geosphere provides only a modest (factor of 3) attenuation of the dose-equivalent release for the central case. The annual dose-equivalent release is relatively small because the geosphere provides benign geochemical and hydrological environments, thus limiting release from the waste form and engineered barriers. In variant corrosion cases that result in higher near-field releases, the far-field attenuation is somewhat stronger. This tendency to attenuate more strongly the larger near-field releases means that the geosphere also tends to reduce uncertainty in the far-field dose-equivalent releases.

The detailed numerical calculations are in good agreement with an analytical calculation using simplified modelling assumptions. This agreement significantly enhances confidence in the calculated dose-equivalent releases for two reasons. First, the comparison provides an important quality assurance check on the numerical modelling of dose-equivalent releases. This check applies not only to the numerical calculations but also to the data/parameter transfers, as the data for the analytical calculations were taken directly from the **Data report** independently of the numerical calculations. Second, it demonstrates that the effective dose for the corrosion cases and shear load case are controlled by relatively simple processes that are straightforward to understand.

Additional confidence in the calculated results is provided by extensive sensitivity analyses and detailed calculations used to screen out certain neglected processes. Analyses of the potential effect of flow channelling within individual fractures because of aperture variability, Appendix A, show that channelling is not sufficient to significantly alter the transport characteristics of the entire pathway. Calculations detailed in Appendix B justify the neglect of fracture mineral retention processes in the SR-Site transport calculations. The calculations in Appendix B indicate that sorption on chlorite and other clay minerals should dominate fracture mineral retention, although minor contributions from solid solutions involving calcite (and possibly barite) are feasible. These retention processes are neglected in SR-Site, which is a pessimistic assumption provided changes in groundwater chemistry do not result in pulse remobilization of radionuclides. The analyses demonstrate that pulse remobilization of radionuclides previously immobilized on fracture minerals is not expected to occur to any great extent for the relevant ranges of groundwater compositions.

Table 7-1. Summary of the results for all numerical probabilistic calculation cases.

Calculation case	Maximum total near-field dose equivalent release (μSv/yr)	Maximum total far-field mean effective dose (μSv/yr)
Dose corresponding to background radiation	1,000	1,000
Dose corresponding to risk limit	14	14
Canister failure due to corrosion		
Semi-correlated, central corrosion case	0.59	0.18
Semi-correlated, disregarding thorium in the near field	0.22	0.14
Semi-correlated including solubility limits	6.2	0.15
Semi-correlated, K_d for U(VI) instead of U(IV) in the geospehre	0.59	0.18
Semi-correlated, 10 mg/l colloids	0.59	0.19
Semi-correlated, 10 g/l colloids	0.59	0.33
Semi-correlated, varying climate, no colloids	0.59	0.19
Semi-correlated, varying climate, 10 g/l colloids	0.59	0.41
Semi-correlated, varying climate and colloid concentration	0.59	0.35
Semi-correlated with initial advection	1.0	0.27
Uncorrelated	3.1	0.45
Uncorrelated with initial advection	7.0	0.83
Fully correlated	3.2	0.63
Fully correlated with initial advection	6.0	0.96
Canister failure due to shear load		
Postulated failure of one canister at 100,000 years	4.2	4.2
Failure during the period 1,000 years to one million years	0.15	0.15
Early failure	0.0027	0.0027
Combination of shear load and buffer advection	0.34	0.34
Canister failure due to isostatic load		
Postulated failure of one canister at 10,000 years	2.5	0.63
Postulated failure of one canister at 100,000 years	1.5	0.39
The growing pinhole failure		
Including the effect of spalling	3.7	0.65
Disregarding the effect of spalling	0.85	0.41
Lost swelling pressure in tunnel backfill, “Crown space”	9.5	2.7
EDZ with a transmissivity of 10^{-6} m^2/s	5.8	2.0
EDZ with a transmissivity of 10^{-7} m^2/s	4.2	1.1
No EDZ	2.5	0.16
Cases addressing best available technique (BAT)		
Copper shell thickness 25 mm	1.2	0.36
Copper shell thickness 100 mm	0.25	0.078
No T/L-filtering	1.3	0.71
Neither T/L- nor EFPC-filtering	20	12

8 References

SKB's (Svensk Kärnbränslehantering AB) publications can be found at www.skb.se/publications.

References with abbreviated names

Buffer, backfill and closure process report, 2010. Buffer, backfill and closure process report for the safety assessment SR-Site. SKB TR-10-47, Svensk Kärnbränslehantering AB.

Climate report, 2010. Climate and climate related issues for the safety assessment SR-Site. SKB TR-10-49, Svensk Kärnbränslehantering AB.

Data report, 2010. Data report for the safety assessment SR-Site. SKB TR-10-52, Svensk Kärnbränslehantering AB.

Geosphere process report, 2010. Geosphere process report for the safety assessment SR-Site. SKB TR-10-48, Svensk Kärnbränslehantering AB.

Main report, 2011. Long-term safety for the final repository for spent nuclear fuel at Forsmark. Main report of the SR-Site project. SKB TR-11-01, Svensk Kärnbränslehantering AB.

Model summary report, 2010. Model summary report for the safety assessment SR-Site. SKB TR-10-51, Svensk Kärnbränslehantering AB.

Other public references

Abelin H, Birgersson L, Gidlund J, Neretnieks I, 1991a. A large-scale flow and tracer experiment in granite: 1. Experimental design and flow distribution. Water Resources Research, 27, pp 3107–3117.

Abelin H, Birgersson L, Moreno L, Widén H, Ågren T, Neretnieks I, 1991b. A large-scale flow and tracer experiment in granite: 2. Results and interpretation. Water Resources Research, 27, pp 3119–3135.

Abelin H, Birgersson L, Widen H, Ågren T, Moreno L, Neretnieks I, 1994. Channeling experiments in crystalline fractured rocks. Journal of Contaminant Hydrology, 15, pp 129–158.

Avila R, Ekström P-A, Åstrand P-G, 2010. Landscape dose conversion factors used in the safety assessment SR-Site. SKB TR-10-06, Svensk Kärnbränslehantering AB.

Cliffe K A, Kelly M, 2006. COMP23 version 1.2.2 user's manual. SKB R-04-64, Svensk Kärnbränslehantering AB.

Crawford J, 2010. Bedrock Kd data and uncertainty assessment for application in SR-Site geosphere transport calculations. SKB R-10-48, Svensk Kärnbränslehantering AB.

Cvetkovic V, Selroos J-O, Cheng H, 1999. Transport of reactive tracers in rock fractures. Journal of Fluid Mechanics, 378, pp 335–356.

Elert M, Gylling B, Lindgren M, 2004. Assessment model validity document FARF31. SKB R-04-51, Svensk Kärnbränslehantering AB.

EU, 1996. Council Directive 96/92/EURATOM of 13 May 1996 laying down basic safety standards for the protection of the health of workers and the general public against the dangers arising from ionizing radiation. Luxembourg: European Commission.

EU, 2002. Testing of safety and performance indicators (SPIN). EUR 19965, European Commission.

Follin S, 2008. Bedrock hydrogeology Forsmark. Site descriptive modeling, SDM-Site Forsmark. SKB R-08-95, Svensk Kärnbränslehantering AB.

Follin S, Johansson P-O, Hartley L, Jackson P, Roberts D, Marsic N, 2007. Hydrogeological conceptual model development and numerical modelling using CONNECTFLOW. Forsmark modelling stage 2.2. SKB R-07-49, Svensk Kärnbränslehantering AB.

Hamby D M, 1994. A review of techniques for parameter sensitivity analysis of environmental models. Environmental Monitoring and Assessment, 32, pp 135–154.

Hedin A, 2002a. Safety assessment of a spent nuclear fuel repository: sensitivity analyses for prioritisation of research. In: Bonano E J, Camp A L, Majors M J, Thompson R A (eds). Probabilistic Safety Assessment and Management, PSAM6: proceedings of the 6th International Conference on Probabilistic Safety Assessment and Management, 23–28 June 2002, San Juan, Puerto Rico. Amsterdam: Elsevier Science.

Hedin A, 2002b. Integrated analytic radionuclide transport model for a spent nuclear fuel repository in saturated fractured rock. Nuclear Technology, 138, pp 179–205.

Hedin A, 2003. Probabilistic dose calculations and sensitivity analyses using analytic models. Reliability Engineering & System Safety, 79, pp 195–204.

Helton J C, 1993. Uncertainty and sensitivity analysis techniques for use in performance assessment for radioactive waste disposal. Reliability Engineering & System Safety, 42, pp 327–367.

IAEA, 1996. International basic safety standards for protection against ionizing radiation and for the safety of radiation sources. Vienna: International Atomic Energy Agency. (Safety series 115)

ICRP, 1996. Age-dependent doses to members of the public from intake of radionuclides: Part 5. Compilation of ingestion and inhalation dose coefficients. Oxford: Pergamon for International Commission on Radiological Protection. (ICRP Publication 72)

Iman R L, Conover W J, 1979. The use of the rank transform in regression. Technometrics, 21, pp 499–509.

Joyce S, Simpson T, Hartley L, Applegate D, Hoek J, Jackson P, Swan D, Marsic N, Follin S, 2010. Groundwater flow modelling of periods with temperate climate conditions – Forsmark. SKB R-09-20, Svensk Kärnbränslehantering AB.

Kelly M, Cliffe K A, 2006. Validity document for COMP23. SKB R-06-76, Svensk Kärnbränslehantering AB.

Laaksoharju M, Smellie J, Tullborg E-L, Gimeno M, Hallbeck L, Molinero J, Waber N, 2008. Bedrock hydrogeochemistry Forsmark. Site descriptive modelling, SDM-Site Forsmark. SKB R-08-47, Svensk Kärnbränslehantering AB.

Lindgren M, Lindström F, 1999. SR 97. Radionuclide transport calculations. SKB TR-99-23, Svensk Kärnbränslehantering AB.

Lindgren M, Pettersson M, Karlsson S, Moreno L, 2001. Project SAFE. Radionuclide release and dose from the SFR repository. SKB R-01-18, Svensk Kärnbränslehantering AB.

Lindgren M, Gylling B, Elert M, 2002. FARF31 Version 1-2 – User's guide. SKB Arbetsrapport TS-02-03, Svensk Kärnbränslehantering AB.

Löfgren M, Sidborn M, 2010. Statistical analysis of results from the quantitative mapping of fracture minerals in Forsmark. Site descriptive modelling – complementary studies. SKB R-09-30, Svensk Kärnbränslehantering AB.

Norman S, Kjellbert N, 1990. FARF31 – A far field radionuclide migration code for use with the PROPER package. SKB TR 90-01, Svensk Kärnbränslehantering AB.

Painter S, 2006. Effect of single-fracture aperture variability on field-scale transport. SKB R-06-25, Svensk Kärnbränslehantering AB.

Painter S, Mancillas J, 2009. MARFA version 3.2.2 user's manual: migration analysis of radionuclides in the far field. SKB R-09-56, Svensk Kärnbränslehantering AB.

Romero L, 1995. The near-field transport in a repository for high-level nuclear waste. Ph. D. thesis. Department of Chemical Engineering and Technology, Royal Institute of Technology, Stockholm, Sweden.

Salas J, Gimeno M J, Molinero J, Auqué L F, Gómez J, Juárez I, 2010. SR-Site. Hydrogeochemical evolution of the Forsmark site. SKB TR-10-58, Svensk Kärnbränslehantering AB.

Saltelli A, Andres T H, Homma T, 1993. Sensitivity analysis of model output: an investigation of new techniques. Computational Statistics & Data Analysis, 15, pp 211–238.

Saltelli A, Chan K, Scott E M (eds), 2000. Sensitivity analysis. Chichester: Wiley.

Sandström B, Tullborg E-L, Smellie J, MacKenzie A B, Suksi J, 2008. Fracture mineralogy of the Forsmark site. SDM-Site Forsmark. SKB R-08-102, Svensk Kärnbränslehantering AB.

Serco, 2008. CONNECTFLOW, release 9.6. Technical summary document. Serco Report SA/ENV/CONNECTFLOW/15, Serco Assurance, United Kingdom.

SKB, 1995. SR 95. Template for safety reports with descriptive example. SKB TR 96-05, Svensk Kärnbränslehantering AB.

SKB, 1999. Deep repository for spent nuclear fuel. SR 97 – Post-closure safety. Main report – Volume I, Volume II and Summary. SKB TR-99-06, Svensk Kärnbränslehantering AB.

SKB, 2004. Interim main report of the safety assessment SR-Can. SKB TR-04-11, Svensk Kärnbränslehantering AB.

SKB, 2006a. Long-term safety for KBS-3 repositories at Forsmark and Laxemar – a first evaluation. Main report of the SR-Can project. SKB TR-06-09, Svensk Kärnbränslehantering AB.

SKB, 2006b. Data report for the safety assessment SR-Can. SKB TR-06-25, Svensk Kärnbränslehantering AB.

SKB, 2010. Corrosion calculations report for the safety assessment SR-Site. SKB TR-10-66, Svensk Kärnbränslehantering AB.

STUK, 2001. Long-term safety of disposal of spent nuclear fuel. Guide YVL 8.4, Radiation and Nuclear Safety Authority, Finland.

Vahlund F, Hermansson H, 2006. Compulink. Implementing the COMP23 model in Simulink. SKB R-06-86, Svensk Kärnbränslehantering AB.

Vidstrand P, Follin S, Zugec N, 2010. Groundwater flow modelling of periods with periglacial and glacial conditions – Forsmark. SKB R-09-21, Svensk Kärnbränslehantering AB.

Wold S, 2010. Sorption of prioritized elements on montmorillonite colloids and their potential to transport radionuclides. SKB TR-10-20, Svensk Kärnbränslehantering AB.